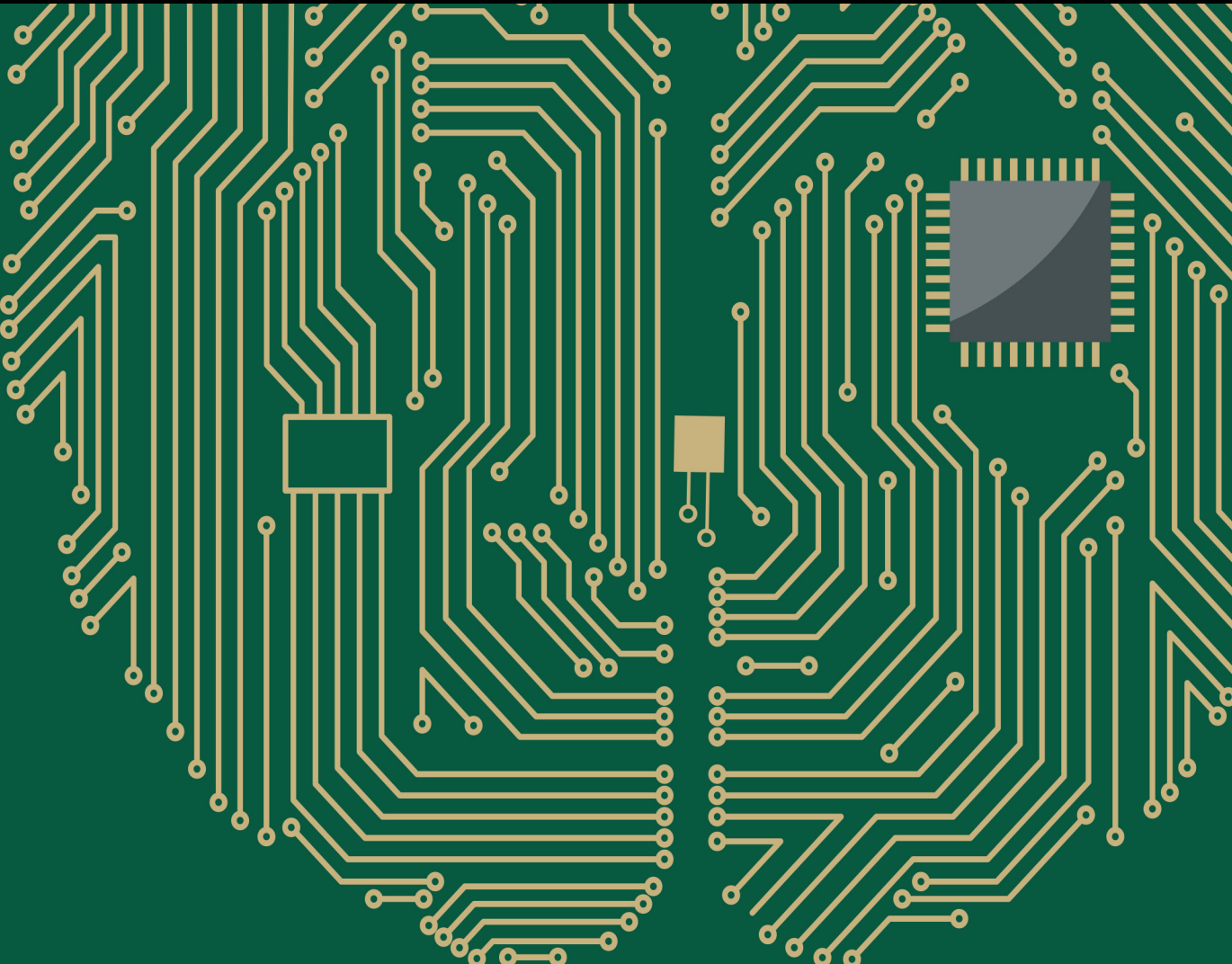


Recent Advances in Brain Signal Analysis: Methods and Applications

2018

Lead Guest Editor: Victor H. C. de Albuquerque

Guest Editors: Plácido R. Pinheiro, Roshan J. Martis,
and João Manuel R. S. Tavares



Recent Advances in Brain Signal Analysis: Methods and Applications 2018

Computational Intelligence and Neuroscience

Recent Advances in Brain Signal Analysis: Methods and Applications 2018

Lead Guest Editor: Victor H. C. de Albuquerque

Guest Editors: Plácido R. Pinheiro, Roshan J. Martis,
and João Manuel R. S. Tavares



Copyright © 2018 Hindawi. All rights reserved.

This is a special issue published in "Computational Intelligence and Neuroscience." All articles are open access articles distributed under the Creative Commons Attribution License, which permits unrestricted use, distribution, and reproduction in any medium, provided the original work is properly cited.

Editorial Board

Ricardo Aler, Spain	Paolo Gastaldo, Italy	Gerard McKee, Nigeria
Amparo Alonso-Betanzos, Spain	S. Ghosh-Dastidar, USA	Michele Migliore, Italy
Pietro Aricò, Italy	Manuel Graña, Spain	Paulo Moura Oliveira, Portugal
Hasan Ayaz, USA	Rodolfo E. Haber, Spain	Debajyoti Mukhopadhyay, India
Sylvain Baillet, Canada	Dominic Heger, Germany	Klaus Obermayer, Germany
Roman Bartak, Czech Republic	Stephen Helms Tillery, USA	Karim G. Oweiss, USA
Theodore W. Berger, USA	J. A. Hernández-Pérez, Mexico	Massimo Panella, Italy
Daniele Bibbo, Italy	Luis Javier Herrera, Spain	Fivos Panetsos, Spain
Vince D. Calhoun, USA	Etienne Hugues, USA	David M Powers, Australia
Francesco Camastra, Italy	Ryotaro Kamimura, Japan	Sandhya Samarasinghe, New Zealand
Michela Chiappalone, Italy	Pasi A. Karjalainen, Finland	Saeid Sanei, UK
Andrzej Cichocki, Japan	Elpida Keravnou, Cyprus	Michael Schmuker, UK
Jens Christian Claussen, UK	Raşit Köker, Turkey	Friedhelm Schwenker, Germany
Silvia Conforto, Italy	Dean J. Krusienski, USA	Victor R. L. Shen, Taiwan
António D. P. Correia, Portugal	Fabio La Foresta, Italy	Fabio Solari, Italy
Justin Dauwels, Singapore	Antonino Laudani, Italy	Jussi Tohka, Finland
Christian W. Dawson, UK	Maciej Lawrynczuk, Poland	Carlos M. Travieso-González, Spain
Carmen De Maio, Italy	Mikhail A. Lebedev, USA	Lefteri Tsoukalas, USA
Sergio Decherchi, Italy	Cheng-Jian Lin, Taiwan	Pablo Varona, Spain
Paolo Del Giudice, Italy	Giosuè Lo Bosco, Italy	Roberto A. Vazquez, Mexico
Maria Jose del Jesus, Spain	Ezequiel López-Rubio, Spain	Meel Velliste, USA
Arnaud Delorme, France	Bruce J. MacLennan, USA	Mario Versaci, Italy
Thomas DeMarse, USA	Reinoud Maex, Belgium	Francois B. Vialatte, France
Anastasios D. Doulamis, Greece	Kezhi Mao, Singapore	Thomas Villmann, Germany
Steven L. Fernandes, USA	Sergio Martinoia, Italy	Ivan Volosyak, Germany
Juan Carlos Fernández, Spain	Laura Marzetti, Italy	Cornelio Yáñez-Márquez, Mexico
Piotr Franaszczuk, USA	Elio Masciari, Italy	Michal Zochowski, USA
Leonardo Franco, Spain	Paolo Massobrio, Italy	Rodolfo Zunino, Italy

Contents

Recent Advances in Brain Signal Analysis: Methods and Applications 2018

Victor Hugo C. de Albuquerque , Plácido Rogerio Pinheiro , Roshan J. Martis, and João Manuel R. S. Tavares 

Editorial (2 pages), Article ID 5971086, Volume 2018 (2018)

Sparse Representation-Based Extreme Learning Machine for Motor Imagery EEG Classification

Qingshan She , Kang Chen, Yuliang Ma , Thinh Nguyen , and Yingchun Zhang 

Research Article (9 pages), Article ID 9593682, Volume 2018 (2018)

Pilot Study on Gait Classification Using fNIRS Signals

Hedian Jin , Chenguang Li , and Jiacheng Xu

Research Article (9 pages), Article ID 7403471, Volume 2018 (2018)

Neurophysiological Responses to Different Product Experiences

Enrica Modica , Giulia Cartocci , Dario Rossi , Ana C. Martinez Levy, Patrizia Cherubino , Anton Giulio Maglione , Gianluca Di Flumeri , Marco Mancini, Marco Montanari, Davide Perrotta, Paolo Di Feo , Alessia Vozzi, Vincenzo Ronca, Pietro Aricò , and Fabio Babiloni 

Research Article (10 pages), Article ID 9616301, Volume 2018 (2018)

Neurophysiological Profile of Antismoking Campaigns

Enrica Modica , Dario Rossi , Giulia Cartocci , Davide Perrotta, Paolo Di Feo , Marco Mancini, Pietro Aricò , Bianca M. S. Inguscio, and Fabio Babiloni 

Research Article (11 pages), Article ID 9721561, Volume 2018 (2018)

Decoding Motor Imagery through Common Spatial Pattern Filters at the EEG Source Space

Ioannis Xygonakis , Alkinoos Athanasiou , Niki Pandria , Dimitris Kugiumtzis , and Panagiotis D. Bamidis 

Research Article (10 pages), Article ID 7957408, Volume 2018 (2018)

Wireless Stimulus-on-Device Design for Novel P300 Hybrid Brain-Computer Interface Applications

Chung-Hsien Kuo , Hung-Hsuan Chen, Hung-Chyun Chou, Ping-Nan Chen, and Yu-Cheng Kuo

Research Article (13 pages), Article ID 2301804, Volume 2018 (2018)

Multiclass Motor Imagery Recognition of Single Joint in Upper Limb Based on NSGA-II OVO TWSVM

Shan Guan , Kai Zhao , and Fuwang Wang 

Research Article (11 pages), Article ID 6265108, Volume 2018 (2018)

Using Black Hole Algorithm to Improve EEG-Based Emotion Recognition

Roberto Munoz , Rodrigo Olivares , Carla Taramasco , Rodolfo Villarroel , Ricardo Soto , Thiago S. Barcelos , Erick Merino , and María Francisca Alonso-Sánchez 

Research Article (21 pages), Article ID 3050214, Volume 2018 (2018)

Spatial and Time Domain Feature of ERP Speller System Extracted via Convolutional Neural Network

Jaehong Yoon , Jungnyun Lee , and Mincheol Whang 

Research Article (11 pages), Article ID 6058065, Volume 2018 (2018)

A New Approach to Diagnose Parkinson's Disease Using a Structural Cooccurrence Matrix for a Similarity Analysis

João W. M. de Souza, Shara S. A. Alves, Elizângela de S. Rebouças, Jefferson S. Almeida, and Pedro P. Rebouças Filho 

Research Article (8 pages), Article ID 7613282, Volume 2018 (2018)

Brain State Decoding Based on fMRI Using Semisupervised Sparse Representation Classifications

Jing Zhang , Chuncheng Zhang , Li Yao , Xiaojie Zhao, and Zhiying Long 

Research Article (12 pages), Article ID 3956536, Volume 2018 (2018)

Assessment of Multivariate Neural Time Series by Phase Synchrony Clustering in a Time-Frequency-Topography Representation

M. A. Porta-Garcia , R. Valdes-Cristerna , and O. Yanez-Suarez 

Research Article (15 pages), Article ID 2406909, Volume 2018 (2018)

Liraglutide Activates the Nrf2/HO-1 Antioxidant Pathway and Protects Brain Nerve Cells against Cerebral Ischemia in Diabetic Rats

Caihong Deng , Jun Cao, Jiangquan Han , Jianguo Li, Zhaojun Li, Ninghua Shi, and Jing He

Research Article (7 pages), Article ID 3094504, Volume 2018 (2018)

Selection of the Optimal Algorithm for Real-Time Estimation of Beta Band Power during DBS Surgeries in Patients with Parkinson's Disease

Ángeles Tepper, Mauricio Carlos Henrich, Luciano Schiaffino, Alfredo Rosado Muñoz, Antonio Gutiérrez, and Juan Guerrero Martínez

Research Article (9 pages), Article ID 1512504, Volume 2017 (2018)

Editorial

Recent Advances in Brain Signal Analysis: Methods and Applications 2018

Victor Hugo C. de Albuquerque¹,² Plácido Rogerio Pinheiro¹,² Roshan J. Martis,² and João Manuel R. S. Tavares³

¹Programa de Pós-Graduação em Informática Aplicada, Universidade de Fortaleza, Fortaleza, Brazil

²Department of Electronics and Communication Engineering, Vivekananda College of Engineering and Technology, Puttur, India

³Instituto de Ciência e Inovação em Engenharia Mecânica e Engenharia Industrial, Departamento de Engenharia Mecânica, Faculdade de Engenharia, Universidade do Porto, Porto, Portugal

Correspondence should be addressed to Victor Hugo C. de Albuquerque; victor.albuquerque@unifor.br

Received 18 November 2018; Accepted 18 November 2018; Published 9 December 2018

Copyright © 2018 Victor Hugo C. de Albuquerque et al. This is an open access article distributed under the Creative Commons Attribution License, which permits unrestricted use, distribution, and reproduction in any medium, provided the original work is properly cited.

Signal processing and analysis has been extensively used in the field of neuroscience. For example, (semi)automatic brain-based systems have been increasingly used in various medical applications such as in disease prevention, detection, and diagnosis, rehabilitation, smart education environments, security and authentication, and biometry. These systems are suggested in the literature as accurate, fast, complementary, and alternative tools to aid specialists in their decision-making, by facilitating the analysis and interpretation of brain signals, and to reduce and/or eliminate errors.

The main objective of this special issue was to promote a discussion on the recent advances related to brain signal analysis, both in terms of novel methods and applications, in order to identify potential contributions to the field of neuroscience. This special issue of the *Computational Intelligence and Neuroscience* journal contains 13 original works selected from the 28 submitted. Hence, the selected studies address new trends in methods and techniques applied to different neuroscience applications.

In the first article, Á. Tepper et al. analyzed different power spectrum density methods with the aim to select one that minimizes the calculation time to be used in real time during deep brain stimulation surgery, concluding that the optimum method to perform the real-time spectral estimation of the beta band from the microelectrode recording signal is Welch with Hamming windows of 1.5 seconds and 50% overlap.

The second article, by J. Zhang et al., proposes a semi-supervised learning sparse representation classifier with an average coefficient method that performs the classification using the average coefficient of each class, instead of the reconstruction error, and selectively updates the training dataset using new testing data, to improve the performance of the sparse representation classifier. The proposed classifier achieved a better performance than the other three semi-supervised learning methods adopted for the comparison purpose.

The third article, by M. A. Porta-Garcia et al., proposes a framework for characterization of phase synchrony relationships between multivariate neural time series applied in EEG signals from P300 speller sessions of four subjects, relying on a proposed clustering algorithm, termed “multivariate time series clustering by phase synchrony.” The proposed solution is able to observe dynamics of phase changes and interactions among channels and can be applied to analyze other cognitive states rather than ERP vs. no event-related potential.

In the fourth article, J. W. M. de Souza et al. propose an approach to measure the similarity between the exam template and the handwritten trace of a patient following the exam template. The proposed solution uses the structural cooccurrence matrix to calculate how close the handwritten trace of the patient is to the exam template and is combined with Naïve Bayes, OPF, and SVM classifiers, showing to be a promising tool for the diagnosis of Parkinson’s disease.

The fifth article, by J. Yoon et al., explored the performance of a convolutional neural network on event-related potential (ERP) data to identify the key features that distinguish illiterates of the ERP speller system, in which the P700 peak may be the key feature of ERP as it appears in both illiterate and nonilliterate subjects.

In the sixth article, R. Munoz et al. describe a new method by means of metaheuristics based on the black hole algorithm to improve EEG-based emotion recognition, using the MAHNOB HCI Tagging Database, showing that the black hole algorithm used to optimize the feature vector of the support vector machine classifier obtained an accuracy of 92.56% over 30 executions.

The seventh article, by E. Modica et al., investigates cerebral and emotional reactions during the interaction with food products by EEG and autonomic activities, as caused by the cross-sensory interaction across a number of different products. The study has the obvious limitation of the number of the food packaging products tested, although the sample size of participants was sufficient to reveal significant statistical effects.

In the eighth article, I. Xygonakis et al. propose a multiclass brain-computer interfaces decoding algorithm that uses EEG source imaging, a technique that maps scalp potentials to cortical activations, in order to compensate for low spatial resolution of EEG. The authors obtained a mean accuracy increase of 5.6 % with respect to the conventional application method of a common spatial pattern on sensors.

The ninth article by E. Modica et al. evaluated the cerebral and emotional reaction to the exposure to selected antismoking public service announcements images in an adult sample, which have already been shown to be effective and ineffective for the promotion of an antismoking behaviour.

The tenth article, by H. Jin et al., proposes a method to identify motion intention of different walking states under normal environment, by using the functional near-infrared spectroscopy technology in twenty-two healthy subjects to walk with three different gaits (small step with low speed, small step with mid-speed, and mid-step with low speed), presenting a mean recognition rate of 78.79%.

In the eleventh article, S. Guan et al. describe a novel scheme that combines amplitude-frequency information of intrinsic mode function with a common spatial pattern, namely, AF-CSP, to extract motor imagery features and improve the classification performance. The second-generation nondominated sorting evolutionary algorithm is used to tune hyperparameters for linear and nonlinear kernel one versus one twin support vector machine. The proposed method is promising to achieve higher accuracy in brain-computer interface systems.

The last article of the special issue, by C.-H. Kuo et al., proposes a novel and practical P300-based hybrid stimulus-on-device brain-computer interface architecture for wireless networking applications. The authors showed that, for five subjects, the performance of classification and information transfer rate were improved after calibrations, for instance, 86.00% and 24.2 bits/min before calibrations and 90.25% and 27.9 bits/min after calibrations.

Conflicts of Interest

The guest editors declare that there are no conflicts of interest.

Acknowledgments

The guest editors wish to thank all the authors and reviewers for sharing and helping to improve the works published here, respectively.

*Victor Hugo C. de Albuquerque
Plácido Rogerio Pinheiro
Roshan J. Martis
João Manuel R. S. Tavares*

Research Article

Sparse Representation-Based Extreme Learning Machine for Motor Imagery EEG Classification

Qingshan She , **Kang Chen**, ¹ **Yuliang Ma** , ¹ **Thinh Nguyen** , ² and **Yingchun Zhang**  ^{1,2}

¹*Institute of Intelligent Control and Robotics, Hangzhou Dianzi University, Hangzhou, Zhejiang 310018, China*

²*Department of Biomedical Engineering, University of Houston, Houston, TX 77204, USA*

Correspondence should be addressed to Qingshan She; qsshe@hdu.edu.cn and Yingchun Zhang; yzhang94@uh.edu

Received 12 April 2018; Accepted 30 July 2018; Published 28 October 2018

Academic Editor: João M. R. S. Tavares

Copyright © 2018 Qingshan She et al. This is an open access article distributed under the Creative Commons Attribution License, which permits unrestricted use, distribution, and reproduction in any medium, provided the original work is properly cited.

Classification of motor imagery (MI) electroencephalogram (EEG) plays a vital role in brain-computer interface (BCI) systems. Recent research has shown that nonlinear classification algorithms perform better than their linear counterparts, but most of them cannot extract sufficient significant information which leads to a less efficient classification. In this paper, we propose a novel approach called FDDL-ELM, which combines the discriminative power of extreme learning machine (ELM) with the reconstruction capability of sparse representation. Firstly, the common spatial pattern (CSP) algorithm is adopted to perform spatial filtering on raw EEG data to enhance the task-related neural activity. Secondly, the Fisher discrimination criterion is employed to learn a structured dictionary and obtain sparse coding coefficients from the filtered data, and these discriminative coefficients are then used to acquire the reconstructed feature representations. Finally, a nonlinear classifier ELM is used to identify these features in different MI tasks. The proposed method is evaluated on 2-class Datasets IVa and IIIa of BCI Competition III and 4-class Dataset IIa of BCI Competition IV. Experimental results show that our method achieved superior performance than the other existing algorithms and yielded the accuracies of 80.68%, 87.54%, and 63.76% across all subjects in the above-mentioned three datasets, respectively.

1. Introduction

The brain-computer interface (BCI) is a system that allows its users to use their brain activity to control external devices which are independent of peripheral nerves and muscles [1, 2]. Motor imagery- (MI-) based sensorimotor rhythm (SMR) analysis, including mu (8–14 Hz) and/or beta (15–30 Hz) rhythms, recorded from the scalp over the sensorimotor cortex, is one of the widely used methods in the BCI field [3, 4]. However, these MI signals are highly non-stationary and inevitably contaminated with noise, and meanwhile, they strongly depend on subjects [5].

Sparse representation (SR), originally proposed by Olshausen et al. [6], attempts to simulate the working mechanism of primary visual cortex in the human visual system. The basic idea is to represent the data as a linear combination of atoms in a dictionary, whose requirement is that the coefficients are sparse, i.e., they contain only a small

number of nonzero elements. In the last two decades, SR has been widely studied for reconstruction, representation, and compression of high-dimensional noisy data, such as computer vision, pattern recognition, and bioinformatics [7–9]. Recently, the SR techniques have also yielded promising results in the BCI systems [10–15]. Although SR is a powerful tool to reconstruct the originals from noisy and imperfect data, using the original training samples as the dictionary may not fully exploit the discriminative information hidden in the training samples. To address the problem, Yang et al. [16] proposed a Fisher discrimination dictionary learning (FDDL) framework to learn a structured dictionary and had good reconstruction capability for the training samples, yielding a 3.2% improvement over the sparse representation-based classification (SRC) algorithm on AR datasets in face recognition.

Recently, Huang et al. developed a new efficient learning algorithm called extreme learning machine (ELM) [17, 18]

for training single-layer feedforward neural networks (SLFNs), featuring faster learning speed and better generalization capability in comparison with the well-known back propagation (BP) neural networks and support vector machines (SVMs). ELM has been applied to pattern recognition tasks in the BCI systems and has shown superior performance over traditional classification approaches [19–22]. In light of this advancement, efforts have been made in developing algorithms to integrate ELM and SR, thus exploiting the speed advantage and discriminative power of ELM and the antinoise performance and reconstruction ability of SR. A recent approach called extreme sparse learning (ESL) has been proposed in [23], which simultaneously learns sparse representation of the input signal and trains the ELM classifier. In the study by Yu et al. [24], the sparse coding technique is adopted to map the inputs to the hidden layer, instead of the random mapping used in classic ELM. Other ELM-SR hybrid models were also extensively studied, in which the ELM classifier is firstly employed to estimate noisy signals, and then a further identification for the estimated signals is carried out using the SRC algorithm [25–27].

Most of the existing ELM methods employ a single hidden layer network structure. While benefitting from a relatively fast training speed, it is well known that for a single hidden layer network, the training sample is always the original training sample set, which could limit the robustness of the network. Furthermore, due to its shallow architecture, feature learning using SLFNs may not be effective for natural signals (e.g., EEG). To incorporate a deeper network structure, a hierarchical-extreme learning machine (H-ELM) method has recently been developed, which allows for a layer-wise architecture design, and have shown to yield great classification performance [28]. In addition, multilayer structure has been extended into ELM in [29, 30] as well. Inspired by these works, we propose a new layer-wise structure framework called FDDL-ELM, which combines the idea of SR with ELM to learn a powerful nonlinear classifier. The proposed method first employs the Fisher discrimination criterion to learn a structured dictionary. With the learned dictionary, more discriminative sparse coding coefficients can be obtained, and more robust feature information can be extracted. Subsequently, the ELM classifier is utilized to discriminate the extracted features. The classification accuracy of the proposed method has been manifested by several benchmark datasets, as well as 2-class and 4-class real world EEG data from BCI Competition III Datasets IVa and IIIa and BCI Competition IV Dataset IIa.

The rest of the paper is organized as follows: Section 2 presents a brief introduction to basic ELM and FDDL and provides detailed description of the proposed FDDL-ELM algorithm. Section 3 evaluates the performance of the FDDL-ELM method through a series of experiments on several benchmark datasets, as well as motor imagery EEG datasets. Finally, we will conclude the paper and present some future work in Section 4.

2. Methodology

2.1. Classic ELM. ELM was originally implemented for single-hidden layer feedforward neural networks and then extended to generalize feedforward networks. By using random hidden node parameters and tuning-free strategy, ELM has some notable advantages, such as easy implementation, fast learning speed, and superior generalization performance [17], thus making it a suitable choice for the recognition problem of EEG signals in different motor imagery tasks.

Consider a dataset containing N training samples, $\{\mathbf{X}, \mathbf{Y}\} = \{\mathbf{x}_i, \mathbf{y}_i\}$, $i = 1, 2, \dots, N$, with the input $\mathbf{x}_i = [x_{i1}, x_{i2}, \dots, x_{ip}]^T \in R^p$ and its corresponding desired output $\mathbf{y}_i = [y_{i1}, y_{i2}, \dots, y_{iq}]^T \in R^q$, where T denotes a transpose operation. Assuming that m is the number of hidden neurons, and $g(\cdot)$ is the activation function, the output function of ELM is mathematically modeled as

$$\mathbf{y}_j = \sum_{i=1}^m \boldsymbol{\beta}_i g(\mathbf{a}_i^T \mathbf{x}_j + b_i), \quad j = 1, 2, \dots, N, \quad (1)$$

where $\boldsymbol{\beta}_i = [\beta_{i1}, \beta_{i2}, \dots, \beta_{iq}]^T$ is the weight vector that connects the i -th hidden neuron and the output neurons, $\mathbf{a}_i = [a_{i1}, a_{i2}, \dots, a_{ip}]^T$ is the randomly chosen input weight vector connecting the i -th hidden neuron and the input neurons, b_i is the randomly chosen bias of the i -th hidden node, and y_j is the actual output corresponding to input x_j .

For convenience of expression, the Equation (1) is written in matrix notation as

$$\mathbf{Y} = \mathbf{H}\boldsymbol{\beta}, \quad (2)$$

where $\mathbf{Y} = [y_1, y_2, \dots, y_N]^T_{N \times q}$ is the expected network output, $\boldsymbol{\beta} = [\boldsymbol{\beta}_1, \boldsymbol{\beta}_2, \dots, \boldsymbol{\beta}_m]^T_{m \times q}$ denotes the weight of output layer, and \mathbf{H} is the hidden layer output matrix which is defined as

$$\mathbf{H} = \begin{bmatrix} g(\mathbf{a}_1^T \mathbf{x}_1 + b_1) & \dots & g(\mathbf{a}_m^T \mathbf{x}_1 + b_m) \\ \dots & \dots & \dots \\ g(\mathbf{a}_1^T \mathbf{x}_N + b_1) & \dots & g(\mathbf{a}_m^T \mathbf{x}_N + b_m) \end{bmatrix}_{N \times m}. \quad (3)$$

To have better generalization performance, the regularization parameter C is introduced in [19], and its corresponding objective function is given by

$$\arg \min_{\boldsymbol{\beta}} (\|\boldsymbol{\beta}\|_2^2 + C\|\mathbf{H}\boldsymbol{\beta} - \mathbf{Y}\|_2^2), \quad (4)$$

where $\|\cdot\|_2$ denotes the l_2 -norm of a matrix or a vector. We can obtain the output weight vector $\boldsymbol{\beta}$ using the Moore-Penrose principle. The solution of Equation (4) is $\boldsymbol{\beta} = (\mathbf{I}/C + \mathbf{H}^T \mathbf{H})^{-1} \mathbf{H}^T \mathbf{Y}$ if $N > m$ and $\boldsymbol{\beta} = \mathbf{H}^T (\mathbf{I}/C + \mathbf{H} \mathbf{H}^T)^{-1} \mathbf{Y}$ if $N < m$.

2.2. Fisher Discrimination Dictionary Learning. Sparse representation-based classification (SRC) was proposed for face recognition, which directly used the training samples of all classes as the dictionary to code the query face image and

classified it by evaluating which class leads to the minimal reconstruction error [7]. However, the dictionary in use may not be effective enough to represent the query images due to the uncertain and noisy information in the original training images, and the discriminative information hidden in the training samples is not sufficiently exploited by such a naïve-supervised dictionary learning approach [16]. To address these problems, the FDDL method is proposed, utilizing both the discriminative information in the reconstruction error and sparse coding coefficients.

Denote $\mathbf{A} = [\mathbf{A}_1, \mathbf{A}_2, \dots, \mathbf{A}_c]$ as the training set, where \mathbf{A}_i is the subset of the training samples from class i , and c is the total number of classes, and an overcomplete dictionary $\mathbf{D} = [\mathbf{D}_1, \mathbf{D}_2, \dots, \mathbf{D}_c]$, where \mathbf{D}_i is the class-specified subdictionary associated with class i . Let \mathbf{X} be the coding coefficient matrix of \mathbf{A} over \mathbf{D} , we can write \mathbf{X} as $\mathbf{X} = [\mathbf{X}_1, \mathbf{X}_2, \dots, \mathbf{X}_c]$, where \mathbf{X}_i is the submatrix containing the coding coefficients of \mathbf{A}_i over \mathbf{D} . The objective function is written as follows:

$$J_{(\mathbf{D}, \mathbf{X})} = \arg \min_{\mathbf{D}, \mathbf{X}} \{r(\mathbf{A}, \mathbf{D}, \mathbf{X}) + \lambda_1 \|\mathbf{X}\|_1 + \lambda_2 f(\mathbf{X})\}, \quad (5)$$

where $r(\mathbf{A}, \mathbf{D}, \mathbf{X})$ is the discriminative fidelity term, $\|\mathbf{X}\|_1$ is the sparse constraint in which the notation $\|\cdot\|_1$ denotes the l_1 -norm, $f(\mathbf{X})$ is a discrimination constraint, and λ_1 and λ_2 are the scalar parameters.

$$r(\mathbf{A}_i, \mathbf{D}, \mathbf{X}_i) = \|\mathbf{A}_i - \mathbf{D}\mathbf{X}_i\|_F^2 + \|\mathbf{A}_i - \mathbf{D}_i \mathbf{X}_i^i\|_F^2 + \sum_{j=1, j \neq i}^c \|\mathbf{D}_j \mathbf{X}_i^j\|_F^2, \quad (6)$$

where $\|\cdot\|_F$ means the F -norm, \mathbf{X}_i^i is the coding coefficient of \mathbf{A}_i over the subdictionary \mathbf{D}_i , and \mathbf{X}_i^j is the coding coefficient of \mathbf{A}_i over the subdictionary \mathbf{D}_j . The minimization of $r(\mathbf{A}, \mathbf{D}, \mathbf{X})$ means that the reconstruction error of the i -th class of samples is minimized, and the reconstruction error through the i -th subdictionary is also minimized while the reconstruction by other subclass dictionaries should be minimized. Its purpose is to ensure that the reconstruction error constraint is minimized, and the sparse coefficient can be more discriminative.

$f(\mathbf{X})$ is a discriminative coefficient term which is given in the following:

$$f(\mathbf{X}) = \text{tr}(S_W(\mathbf{X})) - \text{tr}(S_B(\mathbf{X})) + \eta \|\mathbf{X}\|_F^2, \quad (7)$$

where $\text{tr}(\cdot)$ indicates the trace of subspace, $S_W(\mathbf{X})$ is the within-class scatter of \mathbf{X} , $S_B(\mathbf{X})$ is the between-class scatter of \mathbf{X} , and η is a parameter.

$$\begin{aligned} S_W(\mathbf{X}) &= \sum_{i=1}^c \sum_{\mathbf{x}_k \in \mathbf{X}_i} (\mathbf{x}_k - \mathbf{m}_i)(\mathbf{x}_k - \mathbf{m}_i)^T, \\ S_B(\mathbf{X}) &= \sum_{i=1}^c n_i (\mathbf{m}_i - \mathbf{m})(\mathbf{m}_i - \mathbf{m})^T, \end{aligned} \quad (8)$$

where \mathbf{m}_i and \mathbf{m} are the mean vectors of \mathbf{X}_i and \mathbf{X} respectively, and n_i is the number of samples in class \mathbf{A}_i .

2.3. The Proposed FDDL-ELM Method. In this section, we propose a novel nonlinear classification model that rests on a new ELM framework for multilayer perceptron (MLP), named FDDL-ELM. The framework consists of two stages: an encoding stage and a classification stage. The former stage uses the FDDL approach to map the input features into a midlevel feature space, and then the ELM algorithm is performed for final decision making in the latter stage. The framework of FDDL-ELM is shown in Figure 1.

Let \mathbf{A} be an input containing N training samples $\{\mathbf{A}, \mathbf{Y}\}$ with $\mathbf{A} = [\mathbf{A}_1, \mathbf{A}_2, \dots, \mathbf{A}_c]$, and \mathbf{Y} is the corresponding desired output, where \mathbf{A}_i is the subset of the input from class i , and c is the total number of classes.

Step (1): utilize the FDDL algorithm to learn a structured dictionary \mathbf{D} .

By incorporating Equations (6) and (7) into Equation (5), the objective function is rewritten as

$$\begin{aligned} J_{(\mathbf{D}, \mathbf{X})} = \arg \min_{(\mathbf{D}, \mathbf{X})} & \left\{ \sum_{i=1}^c r(\mathbf{A}_i, \mathbf{D}, \mathbf{X}_i) + \lambda_1 \|\mathbf{X}\|_1 \right. \\ & \left. + \lambda_2 (\text{tr}(S_W(\mathbf{X})) - \text{tr}(S_B(\mathbf{X})) + \eta \|\mathbf{X}\|_F^2) \right\}. \end{aligned} \quad (9)$$

The optimization of the objective function consists of two steps: First, update \mathbf{X} by fixing \mathbf{D} , and then update \mathbf{D} while fixing \mathbf{X} . The procedures are iteratively implemented for the desired discriminative dictionary \mathbf{D} and the discriminative coefficients \mathbf{X} as done in [16].

Step (2): reconstruct the signals for the high-level sparse feature information.

With the desired dictionary \mathbf{D} and the coefficients \mathbf{X} in the Step (1), we can get the reconstructed signals \mathbf{B} which can uncover important information hidden in the original signals and is simplified as follows:

$$\mathbf{B} = \mathbf{DX}. \quad (10)$$

Step (3): discriminate the reconstructed signals \mathbf{B} using the ELM classification method.

- (1) Randomly generate the hidden node parameters (\mathbf{a}_i, b_i) for $i = 1, 2, \dots, m$.
- (2) The new hidden-layer output matrix \mathbf{G} can be written as

$$\mathbf{G} = \begin{bmatrix} g(\mathbf{a}_1^T \mathbf{DX}_1 + b_1) & \dots & g(\mathbf{a}_m^T \mathbf{DX}_1 + b_m) \\ \dots & \dots & \dots \\ g(\mathbf{a}_1^T \mathbf{DX}_N + b_1) & \dots & g(\mathbf{a}_m^T \mathbf{DX}_N + b_m) \end{bmatrix}_{N \times m}. \quad (11)$$

- (3) The regularization parameter C is introduced, and the output weight β is calculated as follows:

$$\begin{aligned} \beta &= \left(\frac{\mathbf{I}}{C} + \mathbf{G}^T \mathbf{G} \right)^{-1} \mathbf{G}^T \mathbf{Y}, \quad \text{for } N > m, \\ \beta &= \mathbf{G}^T \left(\frac{\mathbf{I}}{C} + \mathbf{G} \mathbf{G}^T \right)^{-1} \mathbf{Y}, \quad \text{for } N < m. \end{aligned} \quad (12)$$

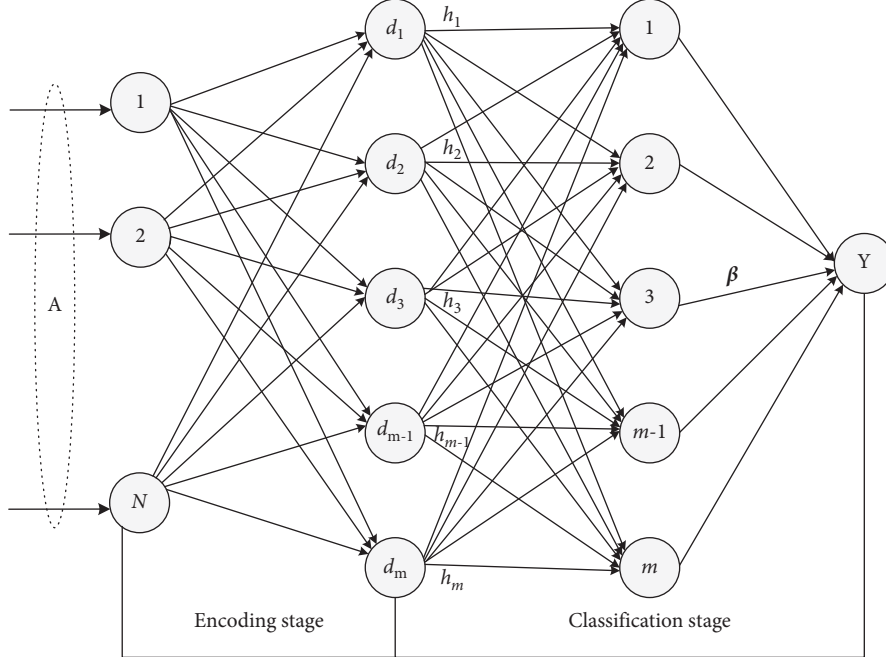


FIGURE 1: A schematic for the overall framework of the FDDL-ELM-learning algorithm.

Extensive efforts have been paid to the optimal selection of C and the leave-one-out (LOO) cross-validation strategy combining with the predicted residual sum of squares (PRESS) statistic is one of the most effective methods [26].

Step (4): For test data $\{A_{\text{test}}, Y_{\text{test}}\}$ and the learned dictionary D , we can reconstruct the A_{test} in the encoding stage and then calculate the labels Y_{predict} using the ELM classifier.

3. Experimental Results and Discussion

In this section, several experiments on benchmark datasets and EEG datasets were performed to evaluate the performance of the proposed FDDL-ELM method, as compared with the other state-of-the-art approaches. All methods were implemented using MATLAB 2014b environment on a computer with a 2.6 GHz processor and 8.0 GB RAM.

3.1. Experiment on Benchmark Datasets

3.1.1. Description. In order to evaluate its performance, the proposed FDDL-ELM method was first applied to four popular benchmark datasets in the UCI repository [31]. The details of these datasets are shown in Table 1.

The Liver Disorders dataset is a medical application, which consists of 345 samples belonging to 2 categories, and each sample extracts 6 features for representation. The Diabetes dataset contains 768 samples belonging to two categories. For each sample, 8 features are extracted. The Waveform dataset consists of 5000 samples from 3 classes of noisy waveforms, and each sample contains 21 attributes. The Columbia Object Image Library (COIL-20) is a multi-class image classification dataset and consists of 1440 grayscale image sample of 20 different objects, in which each

TABLE 1: Description of the benchmark datasets.

Datasets	Training	Testing	Features	Classes	Random perm
Liver Disorders	172	172	6	2	Yes
Diabetes	384	384	8	2	Yes
Waveform	2500	2500	21	3	Yes
COIL-20	720	720	1024	20	Yes

sample is a 32×32 grayscale image of one object taken from a specific view.

3.1.2. Experimental Setup. In Table 1, the column “Random perm” denotes whether the training and test data are randomly assigned. In each data partition, the ratio between training and test sample is 1 : 1. The classification process was repeated ten times, and the average of these outcomes was the final classification rate.

This proposed FDDL-ELM algorithm has 5 tuning parameters: λ_1 , λ_2 , and η in the encoding stage, as well as the number of hidden nodes m , and the regularization parameter C in the classification stage. In all the experiments, the optimal parameters λ_1 and λ_2 are searched using five-fold cross-validation from a small set $\{0.001, 0.005, 0.01, 0.05, 0.1\}$, and η is set to 1, as done in [16]. The optimal parameters m and C were determined from $m \in \{100, 200, \dots, 1500\}$ and $C \in \{e^{-5}, e^{-4}, \dots, e^5\}$ using the LOO cross-validation strategy based on the minimum MSE^{PRES} [27]. It is noted that C is automatically chosen and not fixed during the process of repeating ten times in the classification stage. The settings of these tuning parameters for four benchmark datasets are summarized in Table 2.

TABLE 2: Parameter settings of FDDL-ELM on the benchmark datasets.

Datasets	λ_1	λ_2	m
Liver Disorders	0.01	0.001	400
Diabetes	0.005	0.05	500
Waveform	0.001	0.01	100
COIL-20	0.05	0.001	900

3.1.3. Comparisons with Other State-of-the-Art Algorithms. In this experiment, we compare the proposed FDDL-ELM with three baseline algorithms, including ELM, FDDL, and H-ELM. The classification performance is evaluated in terms of average accuracy and standard deviation ($\text{acc} \pm \text{sd}$). Table 3 summarizes the performance results using four methods on the benchmark datasets.

From the results shown in Table 3, it is evidenced that the FDDL-ELM algorithm achieved comparable performance with other state-of-the-art methods, such as single-layer ELM, FDDL, and H-ELM with deep architecture. For the Diabetes dataset, the FDDL-ELM approach achieved more than 9% improvement over FDDL. For the Liver Disorders dataset, although the average classification accuracy of H-ELM (74.01%) was better than that of FDDL-ELM (72.38%), the accuracy of FDDL-ELM was higher than ELM by 0.23% and FDDL by 6.61%. For the Waveform dataset, the FDDL-ELM approach yielded a mean accuracy of 85.02%, a 0.57% improvement over ELM, and a 0.30% improvement over H-ELM. The average classification accuracy of COIL-20 dataset obtained by FDDL-ELM was 98.33%, higher than those of ELM (96.14%) and H-ELM (97.13%). Based on these observations, the proposed FDDL-ELM approach outperformed the original ELM and FDDL methods on all four datasets and had comparable performance on most of the four datasets compared with H-ELM.

3.1.4. The Impact of the Parameters. There are five parameters in our algorithm: λ_1 , λ_2 , η , m , and C . Since η is set to 1 [16], and C is automatically chosen [27], we will investigate the impact of the other three parameters (λ_1 , λ_2 , and m) on the performance of our algorithm in this section. λ_1 and λ_2 are respectively changed among $\{0.001, 0.005, 0.01, 0.05, 0.1\}$. The parameter m decides the number of hidden neurons, and its value is selected among $\{100, 200, \dots, 1500\}$.

Figures 2(a)–5(a) show the testing results of our algorithm as the parameter m changes on four datasets: Diabetes, Liver Disorders, Waveform, COIL-20 datasets, respectively. As can be seen, the performance of our algorithm is relatively stable with respect to m . Figures 2(b)–5(b) give the plots of testing accuracies as λ_1 and λ_2 vary on four datasets, respectively. From these results, it can be observed that the performance is more pronouncedly affected by the parameters λ_1 and λ_2 , relative to m . For a tradeoff between the classification performance and computation complexity, we can use a comparatively small number of nodes m when selecting λ_1 and λ_2 in real EEG applications.

TABLE 3: Comparisons of classification results on each dataset using different methods.

Method	Liver	Diabetes	Waveform	COIL-20
	Disorders	Acc \pm sd	Acc \pm sd	Acc \pm sd
ELM	72.15 ± 1.54	74.22 ± 1.10	84.45 ± 0.69	96.14 ± 1.03
FDDL	65.77 ± 4.45	65.43 ± 2.49	79.18 ± 1.19	96.48 ± 0.85
H-ELM	74.01 ± 0.87	71.67 ± 1.26	84.72 ± 0.30	97.13 ± 0.71
FDDL- ELM	72.38 ± 1.49	75.33 ± 0.68	85.02 ± 0.32	98.33 ± 0.62

3.2. Experiment on BCI Datasets

3.2.1. Description. This section evaluates the performance of the proposed FDDL-ELM method on MI EEG datasets. There are three datasets for analysis, including two datasets for binary classification and one dataset for multi-classification, as described below:

- (1) Dataset IVa, BCI competition III [32]: this dataset contains EEG signals from 5 subjects, who performed 2-class MI tasks: right hand and foot. EEG signals were recorded using 118 electrodes. A training set and a testing set were available for each subject. Their size was different for each subject. More precisely, 280 trials were available for each subject, among which 168, 224, 84, 56, and 28 composed the training set for subjects A1, A2, A3, A4, and A5, respectively, and the remaining trials composed the testing set.
- (2) Dataset IIIa, BCI competition III [33]: this dataset comprised EEG signals from 3 subjects who performed left hand, right hand, foot, and tongue MI. EEG signals were recorded using 60 electrodes. For the purpose of binary classification, only 2-class EEG signals (left and right hand MI) were used as done in [34]. Both the training and testing sets were available for each subject. Both sets contain 45 trials per class for subject B1, and 30 trials per class for subjects B2 and B3.
- (3) Dataset IIa, BCI competition IV [35]: this dataset consists of EEG signals from 9 subjects who performed 4-class MI tasks: left hand, right hand, foot, and tongue MI. EEG signals were recorded using 22 electrodes. The training and testing sets contain 288 trials for each class, respectively.

3.2.2. Experimental Setup. Data preprocessing was first performed on the raw EEG data. In particular, for each trial, we extracted features from the time-segment spanning from 0.5 s to 2.5 s after the cue instructing the subject to perform MI. Each trial was band-pass filtered in 8–30 Hz, using a fifth-order Butterworth filter. Next, the dimension of the EEG signal was reduced using the common spatial pattern (CSP) algorithm, a widely used feature selection method for MI-based BCIs [12, 34]. Finally, the filtered EEG signals by CSP were discriminated by different classification methods in our experiment.

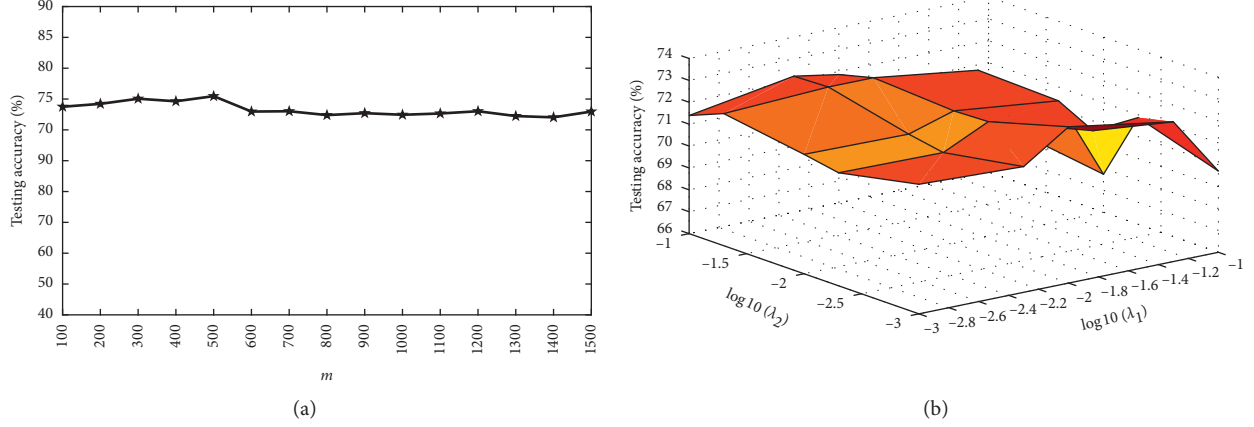


FIGURE 2: Testing accuracy with different parameters on Diabetes. (a) Accuracy in terms of m ; (b) accuracy curve in terms of (λ_1, λ_2) .

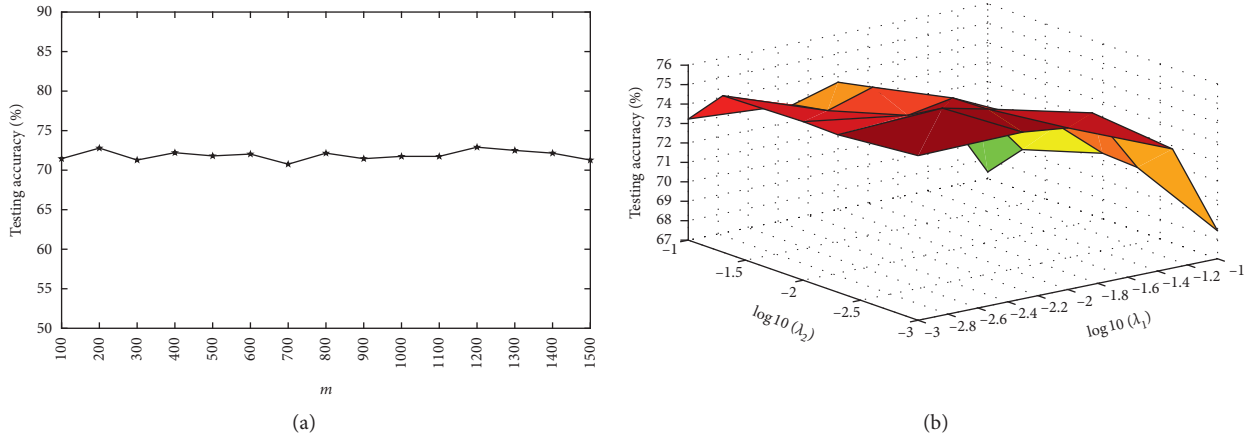


FIGURE 3: Testing accuracy with different parameters on liver disorders. (a) Accuracy in terms of m ; (b) accuracy curve in terms of (λ_1, λ_2) .

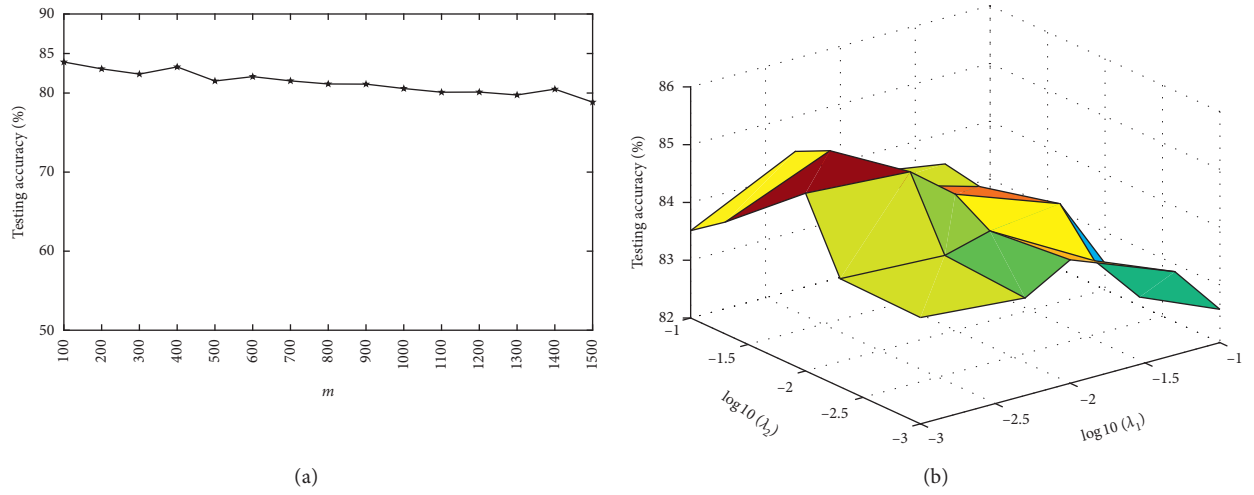


FIGURE 4: Testing accuracy with different parameters on waveform. (a) Accuracy in terms of m ; (b) accuracy curve in terms of (λ_1, λ_2) .

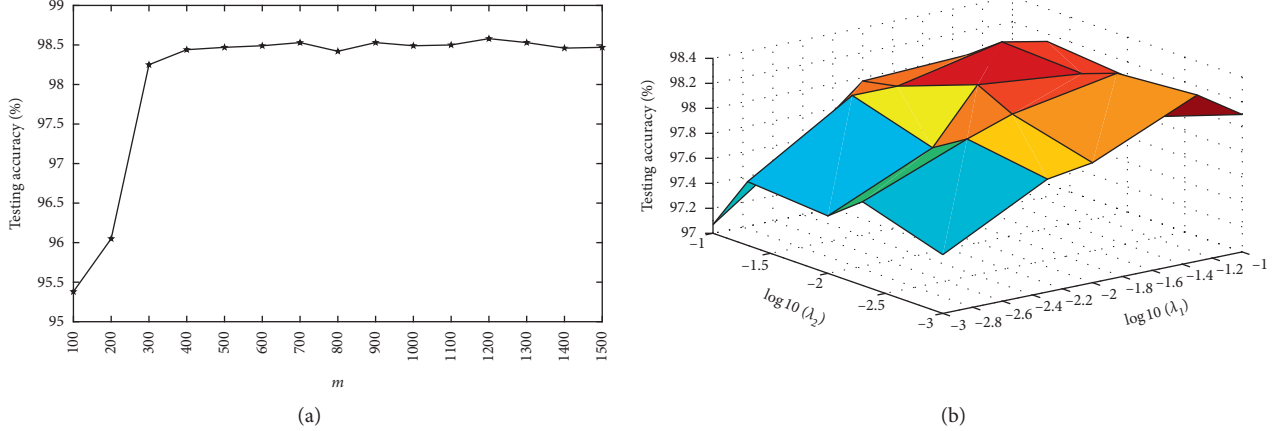


FIGURE 5: Testing accuracy with different parameters on COIL-20. (a) Accuracy in terms of m ; (b) accuracy curve in terms of (λ_1, λ_2) .

In this work, the classification process was repeated ten times, and the average accuracy was recorded for further analysis. The selection process of the parameters λ_1 , λ_2 , η , and C were the same as those described in Section 3.1.2, and the setting of the hidden node m was $\{10, 20, \dots, 100\}$.

3.2.3. Comparisons with Related Algorithms. We compared the proposed method FDDL-ELM with ELM, FDDL, and H-ELM on BCI Competition III Datasets IVa and IIIa and BCI Competition IV Dataset IIa. The average classification accuracies of all four algorithms are shown in Table 4.

From Table 4, it can be seen that the proposed method outperformed the ELM and FDDL algorithms on almost all subjects (except subject B2) in binary-classification applications. For subject B2, the ELM method obtained the average accuracy of 68.33%, a 0.33% improvement over FDDL-ELM. Compared with H-ELM which adopts a deep architecture, FDDL-ELM yielded comparable performance on all the 8 subjects and especially performed better in 4 subjects (A2, A3, A4, and B2). Furthermore, the proposed algorithm yielded the highest average accuracy on Datasets IVa and IIIa. For the Dataset IVa, the FDDL-ELM approach achieved a mean accuracy of 80.68%, a 0.73% improvement over ELM, and a 1.35% improvement over H-ELM. Moreover, a paired t -test revealed no significant difference between the FDDL-ELM and H-ELM approaches ($p = 0.626$) and a significant difference between the FDDL-ELM and ELM approaches ($p = 0.04$). For the Dataset IIIa, the average classification accuracy obtained by FDDL-ELM was 87.54%, higher than that of ELM (87.35%), FDDL (83.26%), and H-ELM (85.63%). Furthermore, a paired t -test revealed no significant difference between the FDDL-ELM and H-ELM approaches ($p = 0.596$). These results have shown that the FDDL-ELM method has achieved a great classification capacity in binary-classification applications.

In the 4-class-classification application for BCI Competition IV Dataset IIa, the average classification accuracies for the 9 subjects using four algorithms are also shown in Table 4. Note that our method also outperformed ELM and FDDL in 8 of the 9 subjects (except subject C8). For subject C8, ELM gained the best result (81.87%) compared with

TABLE 4: Comparisons of classification results on 2-class and 4-class BCI datasets using different methods.

Datasets	Methods				
	ELM	FDDL	FDDL-ELM	H-ELM	
Dataset IVa	A1	60.71	57.50	61.70	63.39
	A2	100	84.29	100	98.39
	A3	73.37	70.51	73.88	64.08
	A4	86.61	65.00	88.17	85.67
	A5	79.05	77.14	79.64	85.16
	Mean	79.95	70.89	80.68	79.33
Dataset IIIa	B1	96.89	93.11	97.78	98.56
	B2	68.33	60.33	68.00	60.00
	B3	96.83	96.33	96.83	98.33
	Mean	87.35	83.26	87.54	85.63
Dataset IIa	C1	76.43	62.77	76.74	75.69
	C2	45.38	32.92	45.70	47.74
	C3	76.32	70.76	77.13	76.98
	C4	59.24	45.59	60.50	61.84
	C5	37.12	31.42	36.24	37.85
	C6	45.90	35.28	47.57	47.08
	C7	78.99	66.91	80.30	80.07
	C8	81.87	63.72	80.60	76.46
	C9	67.36	65.48	69.10	76.42
	Mean	63.18	52.76	63.76	64.46

FDDL (63.72%), FDDL-ELM (80.60%), and H-ELM (76.46%). The FDDL-ELM approach performed the best in 4 subjects (C1, C3, C6, and C7), whereas H-ELM achieved the best result in 4 subjects (C2, C4, C5, and C9). The average classification accuracy of 9 subjects using FDDL-ELM was 63.76%, slightly lower than H-ELM (64.46%). A paired t -test revealed no significant difference between the FDDL-ELM and H-ELM approaches ($p = 0.519$) and a significant difference between the FDDL-ELM and FDDL approaches (p is less than 0.01). These results showed that when compared to the H-ELM algorithm, our method can achieve similar results without the deep architecture.

In these experiments, the proposed FDDL-ELM method exhibited an excellent performance in both binary-classification and multiclassification cases. The nonlinear property of FDDL-ELM allowed for its superior performance over the FDDL approach when processing the

nonstationary EEG signals. Furthermore, FDDL-ELM is more suitable in analyzing noisy EEG data than basic ELM because its encoding stage can acquire a higher representation of the raw signals and extract more effective feature information. Compared with the H-ELM, an algorithm with a deep architecture design, our method also yielded comparable results. In particular, on the binary-classification datasets (BCI Competition III Datasets IVa and IIIa), our method gained higher average accuracies (80.68% and 87.54%) than that of H-ELM (79.33% and 85.63%), respectively.

4. Conclusion

In this paper, we have proposed a new ELM framework called FDDL-ELM, which achieves a sparse representation of input raw data with layer-wise encoding, while still benefiting from the universal approximation capability of the original ELM. We verified the generalizability and capability of FDDL-ELM using publicly available benchmark databases and MI-BCI datasets. In these applications, FDDL-ELM demonstrated superior classification performance than the other relevant state-of-the-art methods. However, there are still several questions to be further investigated in future work. The nonstationary nature of EEG signals means that a classification model built earlier using the previous data is not able to well reflect the changes that have already taken place to the signals. Consequently, the online updates to the classification model are needed. Recently, the ensemble of subset online sequential extreme learning machine (ESOS-ELM) method is proposed for class imbalance learning [36]. In addition, an online sequential extreme learning machine with kernels (OS-ELMK) has been proposed for prediction of nonstationary time series [37]. In the study by Mirza et al.[38], a multilayer online sequential extreme learning machine has been proposed for image classification. In the future work, we will investigate the online learning algorithm of FDDL-ELM for analyzing MI EEG signals.

Data Availability

Three datasets were employed in this study, including two datasets for binary classification and one dataset for multiclassification, which are publicly available: (1) dataset IVa, BCI competition III [31]: this dataset contains EEG signals from 5 subjects, who performed 2-class MI tasks: right hand and foot. (2) Dataset IIIa, BCI competition III [34]: this dataset comprised EEG signals from 3 subjects who performed left hand, right hand, foot, and tongue MI. (3) Dataset IIa, BCI competition IV [32]: this dataset consists of EEG signals from 9 subjects who performed 4-class MI tasks: left hand, right hand, foot, and tongue MI.

Conflicts of Interest

The authors declare that there are no conflicts of interest regarding the publication of this article.

Acknowledgments

This work was supported by the National Nature Science Foundation under grants Nos. 61871427 and 61671197, Zhejiang Province Natural Science Foundation (LY15F010009), and the University of Houston. The authors would like to acknowledge the BCI Competition III Datasets IVa and IIIa and BCI Competition IV Dataset IIa which were used to test the algorithms proposed in this study.

References

- [1] S. Sun and J. Zhou, "A review of adaptive feature extraction and classification methods for EEG-based brain-computer interfaces," in *Proceedings of IEEE International Joint Conference on Neural Networks (IJCNN)*, pp. 1746–1753, Beijing, China, 2014.
- [2] J. Wolpaw and E. W. Wolpaw, *Brain-Computer Interfaces: Principles and Practice*, OUP, Oxford, UK, 2012.
- [3] Y. Wang, S. Gao, and X. Gao, "Common spatial pattern method for channel selection in motor imagery based brain-computer interface," in *Proceedings of IEEE International Conference on Engineering in Medicine and Biology Society*, vol. 5, pp. 5392–5395, Shanghai, China, 2005.
- [4] Q. She, H. Gan, Y. Ma et al., "Scale-dependent signal identification in low-dimensional subspace: motor imagery task classification," *Neural Plasticity*, vol. 2016, pp. 1–15, Article ID 7431012, 2016.
- [5] C. Park, D. Looney, N. ur Rehman et al., "Classification of motor imagery BCI using multivariate empirical mode decomposition," *IEEE Transactions on Neural Systems and Rehabilitation Engineering*, vol. 21, no. 1, pp. 10–22, 2013.
- [6] B. A. Olshausen and D. J. Field, "Sparse coding with an overcomplete basis set: a strategy employed by V1," *Vision Research*, vol. 37, no. 23, pp. 3311–3325, 1997.
- [7] J. Wright, A. Y. Yang, A. Ganesh et al., "Robust face recognition via sparse representation," *IEEE transactions on pattern analysis and machine intelligence*, vol. 31, no. 2, pp. 210–227, 2009.
- [8] J. Zhang, D. Zhao, and W. Gao, "Group-based sparse representation for image restoration," *IEEE Transactions on Image Processing*, vol. 23, no. 8, pp. 3336–3351, 2014.
- [9] Y. A. Huang, Z. H. You, X. Chen et al., "Sequence-based prediction of protein-protein interactions using weighted sparse representation model combined with global encoding," *BMC Bioinformatics*, vol. 17, no. 1, pp. 1–11, 2016.
- [10] Y. Shin, S. Lee, M. Ahn et al., "Noise robustness analysis of sparse representation based classification method for non-stationary EEG signal classification," *Biomedical Signal Processing and Control*, vol. 21, pp. 8–18, 2015.
- [11] Q. Yuan, W. Zhou, S. Yuan et al., "Epileptic EEG classification based on kernel sparse representation," *International Journal of Neural Systems*, vol. 24, no. 04, Article ID 1450015, 2014.
- [12] D. Wen, P. Jia, Q. Lian et al., "Review of sparse representation-based classification methods on EEG signal processing for Epilepsy detection, brain-computer interface and cognitive impairment," *Frontiers in Aging Neuroscience*, vol. 8, p. 172, 2016.
- [13] W. Zhou, Y. Yang, and Z. Yu, "Discriminative dictionary learning for EEG signal classification in brain-computer interface," in *Proceedings of IEEE Conference on Control Automation Robotics & Vision (ICARCV)*, pp. 1582–1585, Guangzhou, China, 2012.

- [14] Y. Li, Z. L. Yu, N. Bi et al., "Sparse representation for brain signal processing: a tutorial on methods and applications," *IEEE Signal Processing Magazine*, vol. 31, no. 3, pp. 96–106, 2014.
- [15] Y. Shin, S. Lee, J. Lee et al., "Sparse representation-based classification scheme for motor imagery-based brain-computer interface systems," *Journal of Neural Engineering*, vol. 9, no. 5, Article ID 056002, 2012.
- [16] M. Yang, L. Zhang, X. Feng et al., "Sparse representation based fisher discrimination dictionary learning for image classification," *International Journal of Computer Vision*, vol. 109, no. 3, pp. 209–232, 2014.
- [17] G. B. Huang, Q. Y. Zhu, and C. K. Siew, "Extreme learning machine: theory and applications," *Neurocomputing*, vol. 70, no. 1–3, pp. 489–501, 2006.
- [18] A. Lendasse, Q. He, Y. Miche et al., "Advances in extreme learning machines (ELM2012)," *Neurocomputing*, vol. 128, pp. 1–3, 2014.
- [19] L. Duan, M. Bao, J. Miao et al., "Classification based on multilayer extreme learning machine for motor imagery task from EEG signals," *Procedia Computer Science*, vol. 88, pp. 176–184, 2016.
- [20] S. Ding, N. Zhang, X. Xu et al., "Deep extreme learning machine and its application in EEG classification," *Mathematical Problems in Engineering*, vol. 2015, no. 1, pp. 1–11, 2015.
- [21] Y. Peng and B. L. Lu, "Discriminative manifold extreme learning machine and applications to image and EEG signal classification," *Neurocomputing*, vol. 174, pp. 265–277, 2016.
- [22] Y. Zhang, J. Jin, X. Wang et al., "Motor imagery EEG classification via Bayesian extreme learning machine," in *Proceedings of IEEE International Conference on Information Science and Technology (ICIST)*, pp. 27–30, Guangzhou, China, 2016.
- [23] S. Shojaeilangari, W. Y. Yau, K. Nandakumar et al., "Robust representation and recognition of facial emotions using extreme sparse learning," *IEEE Transactions on Image Processing*, vol. 24, no. 7, pp. 2140–2152, 2015.
- [24] Y. Yu and Z. Sun, "Sparse coding extreme learning machine for classification," *Neurocomputing*, vol. 261, no. SI, pp. 50–56, 2017.
- [25] M. Luo and K. Zhang, "A hybrid approach combining extreme learning machine and sparse representation for image classification," *Engineering Applications of Artificial Intelligence*, vol. 27, pp. 228–235, 2014.
- [26] J. Cao, J. Hao, X. Lai et al., "Ensemble extreme learning machine and sparse representation classification," *Journal of the Franklin Institute*, vol. 353, no. 17, pp. 4526–4541, 2016.
- [27] J. Cao, K. Zhang, M. Luo et al., "Extreme learning machine and adaptive sparse representation for image classification," *Neural networks*, vol. 81, pp. 91–102, 2016.
- [28] J. Tang, C. Deng, and G. B. Huang, "Extreme learning machine for multilayer perceptron," *IEEE Transactions on Neural Networks and Learning Systems*, vol. 27, no. 4, pp. 809–821, 2016.
- [29] T. V. Nguyen and B. Mirza, "Dual-layer kernel extreme learning machine for action recognition," *Neurocomputing*, vol. 260, pp. 123–130, 2017.
- [30] B. Mirza, S. Kok, Z. Lin et al., "Efficient representation learning for high-dimensional imbalance data," in *Proceedings of 2016 IEEE Conference on Digital Signal Processing*, pp. 511–515, Beijing, China, 2017.
- [31] C. C. Blake and C. J. Merz, "UCI repository of machine learning databases," <http://archive.ics.uci.edu/ml/>.
- [32] Graz University, "BCI competition III datasets Iva," <http://www.bbci.de/competition/iii/#datasetIva>.
- [33] Graz University, "BCI Competition III Datasets IIIa," <http://www.bbci.de/competition/iii/#datasetIIIa>.
- [34] F. Lotte and C. Guan, "Regularizing common spatial patterns to improve BCI designs: unified theory and new algorithms," *IEEE Transactions on Biomedical Engineering*, vol. 58, no. 2, pp. 355–362, 2011.
- [35] Graz University, "BCI competition IV datasets 2a," <http://www.bbci.de/competition/iv/#dataset2a>.
- [36] B. Mirza, Z. Lin, and N. Liu, "Ensemble of subset online sequential extreme learning machine for class imbalance and concept drift," *Neurocomputing*, vol. 149, pp. 316–329, 2015.
- [37] X. Wang and M. Han, "Online sequential extreme learning machine with kernels for nonstationary time series prediction," *Neurocomputing*, vol. 145, pp. 90–97, 2014.
- [38] B. Mirza, S. Kok, and F. Dong, "Multi-layer online sequential extreme learning machine for image classification," in *Proceedings in Adaptation, Learning and Optimization*, vol. 1, pp. 39–49, Springer, New York, NY, USA, 2016.

Research Article

Pilot Study on Gait Classification Using fNIRS Signals

Hedian Jin^{1,2}, Chunguang Li^{1,2} and Jiacheng Xu^{1,2}

¹*Key Laboratory of Robotics and System of Jiangsu Province, School of Mechanical and Electric Engineering, Soochow University, Suzhou, China*

²*Collaborative Innovation Center of Suzhou Nano Science and Technology, Suzhou, China*

Correspondence should be addressed to Chunguang Li; lichunguang@suda.edu.cn

Received 29 March 2018; Revised 23 July 2018; Accepted 27 August 2018; Published 17 October 2018

Academic Editor: Plácido R. Pinheiro

Copyright © 2018 Hedian Jin et al. This is an open access article distributed under the Creative Commons Attribution License, which permits unrestricted use, distribution, and reproduction in any medium, provided the original work is properly cited.

Rehabilitation training is essential for motor dysfunction patients, and the training through their subjective motion intention, comparing to passive training, is more conducive to rehabilitation. This study proposes a method to identify motion intention of different walking states under the normal environment, by using the functional near-infrared spectroscopy (fNIRS) technology. Twenty-two healthy subjects were recruited to walk with three different gaits (including small-step with low-speed, small-step with midspeed, midstep with low-speed). The wavelet packet decomposition was used to find out the main characteristic channels in different motion states, and these channels with links in frequency and space were combined to define as feature vectors. According to different permutations and combinations of all feature vectors, a library for support vector machines (libSVM) was used to achieve the best recognition model. Finally, the accuracy rate of these three walking states was 78.79%. This study implemented the classification of different states' motion intention by using the fNIRS technology. It laid a foundation to apply the classified motion intention of different states timely, to help severe motor dysfunction patients control a walking-assistive device for rehabilitation training, so as to help them restore independent walking abilities and reduce the economic burdens on society.

1. Introduction

Population aging is a prominent problem in today's society. In 2016, approximately 12% of the world's population was over the age of 60, and this percentage would rise to approximately 21% of the world's population by 2050 [1]. Aging leads to a significant decline in elderly body movement [2] and increase of body vulnerability. These would result in the probability of fractures or other accidents increased, causing severe motor dysfunction [3–5]. Similarly, spinal cord injury (SCI) is a common disease frequently resulting in severe motor dysfunction, forcing patients to depend on a wheelchair for mobility [6]. Moreover, the number of severe motor dysfunction victims of traffic accidents and accidental injuries has also increased rapidly as society develops. As a result, above patients often remain bedridden for extended periods of time, causing some complications and increasing the probability of degeneration of bodily functions. These problems would cause serious impact on rehabilitation and impose serious

economic burdens on society [7]. And the recovery of walking function is a primary desire of these patients [8]. Therefore, it is greatly meaningful to provide these patients with appropriate training to help them restore their walking ability.

However, most training instruments are passive-controlled. This leads to insufficient participation of patients and unobvious rehabilitation effect. Husemann et al. [9] conducted a controlled experiment on robotic training so as to motivate the initiative of subjects and conventional physiotherapy and found that walking ability was significantly improved by the robotic training. Veneman et al. [10] and Riener et al. [11] developed different strategies of orthotic devices to elicit greater voluntary participation of the subjects in the rehabilitation process, and it performed more effectively than a fixed repetitive pattern. Moreover, other studies had also demonstrated that training based on patient-active awareness can be more effective than passive for rehabilitation [12–14]. Therefore, the multitraining modes and patients' active participation play an important

role for advancing rehabilitation. And the biomechanical information and brain information can be used to judge subjects' motion intention so as to control a walking-assistive equipment to do rehabilitation training.

Progress has been made in recent years in using identified motion intention to control walking-assistive equipment, based on biomechanical information [15–18]. Lee and Sankai [15] and Hayashi et al. [16] used the lower limbs' electromyography (EMG) signal to identify the subjects' motion intention, to control walking-assistive equipment to drive movement. Limb-movement information and foot-pressure data that were tested by foot-pressure and angle-acceleration sensors were used to identify the motion intention of subjects, to control walking-assistive equipment [16–18]. These related studies can help patients control the exoskeleton to help them carry out rehabilitation training through their motion intention and have a better recognition accuracy. However, for these severe motor dysfunction patients, biomechanical signals were very weak or abnormal, and it was also very difficult to collect. Therefore, brain information can be used to identify the patients' motion intention to help them control the walking-assistance equipment to complete independent rehabilitation training.

In recent years, several studies have investigated brain activity based on electroencephalography (EEG) signals during walking [19–26]. According to an EEG signals' μ and β rhythms, three different walking speed levels were identified, with an average classification accuracy of 72.7% [22], this study also provides insight on the cortical involvement in human gait control and represents a step towards a brain-machine interface for poststroke gait rehabilitation [22]. Zhang et al. [23] used the multiple kernel learning algorithm to simultaneously learn the relative importance of different brain areas, so as to identify the region of importance, and it demonstrated that the frontal and frontocentral regions are the most important regions in controlling the exoskeleton. In addition, some studies noted that the intensity of neural activity in the motor cortex is positively correlated with walking speed, and it also proved that different motor states have different neural activities [21–25]. However, most experiments were based on treadmill, which differ from a normal gait. Moreover, the subjects often required external stimulus before experimentation, which was also not conducive to do rehabilitation training in normal environments [19–22,24–26].

On the contrary, fNIRS technology can support continuous testing under the normal environment and without external stimuli. Kim et al. [27] and Mihara et al. [28] found that the main activation areas during the change of walking speed are sensorimotor cortex (SMC), premotor cortex (PMC), and supplementary motor area (SMA). Caliandro et al. [29] demonstrated that the concentration of blood oxygen activity in the prefrontal cortex has a positive correlation with the step length, which establishes an important basis for the identification of step length. Holtzer et al. [30] also found that the activation of the PFC area is largely associated with increasing step length. A study of the pre-movement consciousness of the normal start and preparation determined that the proportion of oxyHb of the PFC

area and premotor cortex significantly increase [31]. These studies focus on which brain region was activated when the walking speed or step length changed, instead of status recognition, which lay a theoretical basis for this study in testing areas. In addition, fNIRS technology for the identification of similar patterns also has great application prospects. Sui et al. [32] identified three levels of bicycling speed, based on the difference of oxyHb and deoxyHb, with a corresponding classification accuracy of 74%. Hong et al. [33] identified mental arithmetic (MA), right-hand motor imagery (RI), and left-hand motor imagery (LI) with an average classification accuracy of 75.6% across ten subjects. The joint mutual information (JMI) criterion was used to extract the optimal features of hemodynamic responses, to identify three images of hand clenching associated with force and speed with a final accuracy of 76.7% [34]. Yin et al. [35] applied empirical mode decomposition to reduce the physiological noise during the task, and the intrinsic mode functions were used to extract the feature vectors, to identify the motor imagery tasks of right-hand clench force and speed, with a corresponding classification accuracy of 78.33%. Most of the fNIRS studies mainly focus on classifying the different states about upper limbs. For lower limbs, the study of different motion states of spontaneous walking is sparse, and the simultaneous classification of two-dimensional variables of walking speed and step length is still in the bank.

In this study, a method based on fNIRS signals is proposed, to identify the motion intention of two-dimensional variables of walking speed and step length simultaneously under the normal environment. During the whole experiment, in order to elicit greater voluntary participation of the subjects, all movements (the start and end of every task) were spontaneously controlled by themselves, and without external stimuli. It hopes to classify the two-dimensional states of walking speed and step length timely, based on the motion intention of movement. This study expects to apply a method to classify the motion intention of different states, so as to help patients control a walking-assistive device for rehabilitation training and let them restore independent walking abilities in the future.

2. Experiment Design

2.1. Subjects. Twenty-two healthy subjects (22 mean \pm 4 years old, seventeen males and five females) of Soochow University participated in this experiment. All participants were right-handed, without neurological abnormalities and other related conditions.

2.2. Instrument. A FOIRE-3000 optical topography system (Shimadzu Corporation, Kyoto, Japan) [32] with eight emitters and eight detectors was used to measure the light sources of wavelengths of 830 nm, 805 nm, and 780 nm, that represent the oxygenated hemoglobin (oxyHb), total hemoglobin (totalHb), and deoxygenated hemoglobin (deoxyHb), respectively. The sampling period of hemoglobin signals was 130 ms.

2.3. Cortical Regions. Prior fNIRS research determined that the PMC, SMA, and PFC areas are largely associated with walking speed or step length [27,29–31]. In addition, the PFC area plays an important role in identifying premovement consciousness [28]. According to the international 10–20 system [36, 37] and the Brodmann partition map [38], a 3×5 parietal flash holder was built, which was applied to fix emitters and detectors. Figure 1(a) shows the arrangement of the optodes, where the Cz point is the intersection of the left to right earlobe and nation to occipital tuberosity, with a distance to detector 7 of 3 cm. In the layout of the channel, the emitters 3 and 6, and detectors 1, 4, and 7 are on the connection of Nz-Cz-Lz, and the probe layout on the left and right is parallel to the connection of Nz-Cz-Lz, the distance between each detector and emitter is fixed at 3 cm. Based on the location of important region defined by above study and probe layout, it is defined that the channels 1 to 7 are in the PFC area, channels 8 to 12 are in the frontal eye cortex (FEC) area, channels 13 and 18 are in the PMC left (PMCL) area, channels 15 and 20 are in the PMC right (PMCR) area, and channels 14, 16, 17, 19, 21, 22 are in the SMA area.

2.4. Paradigm. The patient with very weak or no athletic ability finds it hard to undertake rehabilitation training, not to active training. According to the feedback from a rehabilitation doctor, these three walking states (contained the gait of small-step with low-speed (SL), small-step with midspeed (SM), and midstep with low-speed (ML)) were very helpful and necessary for these patients to improve their body function to restore their walking ability. Therefore, in this experiment, 22 health subjects' fNIRS signals under these three gait parameters were collected for initial research. During this experiment, because of the limited transmission lines, the walking distance was fixed at 4.4 m, and all the subjects could not exceed this range. So, the small-step was defined as approximately nine steps in fixed distance, and midstep was approximately about six or seven steps. But the walking speed depended on subjects' normal speed, and low-speed was defined that it must be slower than the normal gait obviously, about 30% to 50% of normal speed.

Before the experiment, all the subjects were asked to wash their hair, to make sure the scalp was clean. The experimental procedure and fNIRS' operating principle were also informed. And they were also told that they should maintain their heads in a steady position and their arms in a natural state when walking, without counting during the entire experiment.

Moreover, a researcher would walk with subjects carrying the fNIRS cables to reduce the effect of the cables' weight. Figure 1(b) shows the experiment setup. All the subjects were required to train these three gait parameters, and the researcher will calculate the walking speed and step number during the walking, to ensure the gait parameter subject walked was right. However, the subject would be arranged to train these three gait parameters randomly, based on the arrangement and combination of these three

states, in order to let the subject take a consideration of which gait parameter should be done during the experiment. When the subject can walk accurately, they would be told the specific process of the whole experiment. Each gait was consisted of four stages: rest, walk, rest, and retreat. During the whole experiment, each gait needed walking twice. In detail, at the beginning of the experiment, the starting point and ending point were marked previously, and all subjects stood at the starting point while resting for more than 30 s. Then, they began movement towards the ending point with the right foot. Next, the subjects did not retreat to the starting point until they stood at the ending point in a resting state for more than 30 s. The entire process of the experiment is shown in Figure 2. Moreover, the rest and start time were spontaneously controlled by the subjects. It is also stipulated that the subjects can not make a mistake in the order and gait parameters of the experiment, a researcher specializes in checking these; otherwise, the experiment will be cancelled and be redone next time. Finally, based on the feedback information after completing the experiment, the subject will take a consideration of which gait parameter they should do before walking.

3. Data Analysis

The totalHb and difference between the oxyHb and deoxyHb were used to extract feature vectors in the frequency domain. Eleven subjects were selected to calculate the highest recognition accuracy and its corresponding combination of feature vectors (ten for training and one for testing). When the best feature vectors combination was selected, these eleven subjects of training set were defined as training data, to calculate the final recognition accuracy of another eleven subjects. Due to various factors and maladjustments, only the second testing was used for analysis. All calculations and analysis were completed using Matlab R2016a.

3.1. Power Spectrum Analysis. For the eleven primary subjects in this study, power spectrum density analysis based on a rectangular window was used to analyze the rest time before and during the task segment. This method calculates the continuous frequency map of each channel in all states to determine the final analysis band and the band interval.

3.2. Data Preprocessing. Because the related researches on fNIRS are mainly focused on low-frequency components, over time, it will cause a zero drift in cerebral hemoglobin, significantly impacting the low-frequency component. In this study, the mathematical morphology method was proposed to remove this phenomenon [39], in order to reduce the influence of zero drift during the subsequent analysis. To identify the motion intention of all movements, 180 points before the task were analyzed. Corrosion and expansion are the main operations of this method, and their expressions are as follows, respectively:

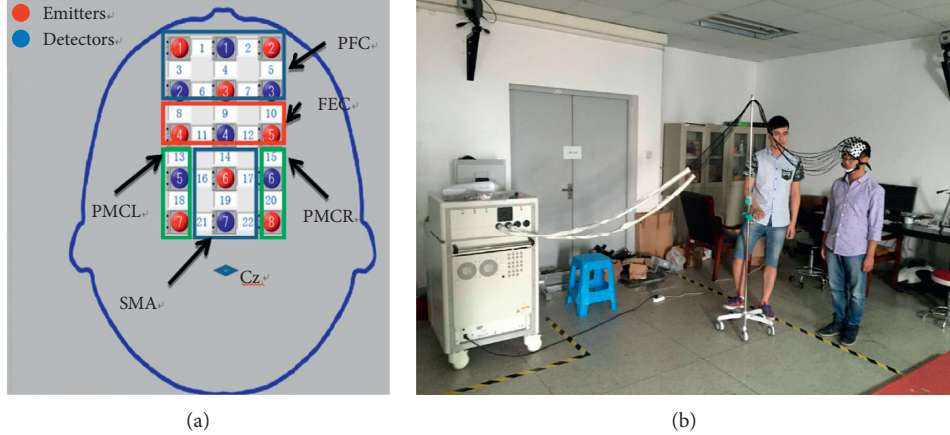


FIGURE 1: (a) The arrangement of the optodes. (b) The experimental setup. The person in the right was the subject; he was doing a rest for walking. The person in the left was a researcher who walked with the subject carrying the weight of the fNIRS cables.

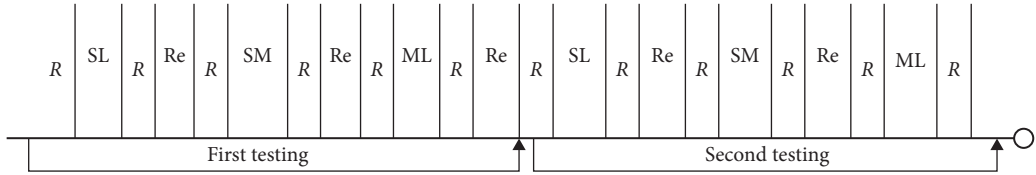


FIGURE 2: The process of the experiment. R represents the rest time. Re represents the backward process. SL represents the gait of small-step with low-speed. SM represents the gait of small-step with midspeed. ML represents the gait of midstep with low-speed. The first testing was a familiar process for the subjects, and the second testing was the analysis data.

$$(f \Theta k)(n) = \min_{m=0, \dots, M-1} \{f(n+m) - k(m)\}; \quad (1)$$

$$n = (0, 1, \dots, N-M),$$

$$(f \oplus k)(n) = \max_{m=0, \dots, M-1} \{f(n-m) - k(m)\}; \quad (2)$$

$$n = (M-1, M, N-1),$$

where $f(n)$ represents the original data, $(N-1)$ is the length of the data. $k(m)$ is a flat structure, and the length of $(M-1)$ is the number of points in ten sampling periods. Then, the opening and closing operations were calculated based on the corrosion and expansion, and their expressions are as follows:

$$(f^o k)(n) = (f \Theta k \oplus k)(n), \quad (3)$$

$$(f \circ k)(n) = (f \oplus k \Theta k)(n).$$

Then, the values of performing opening operation first and then the closing operation and performing closing operation first and then the opening operation were calculated, respectively. The final result was obtained by averaging the above two values because there is a big difference between individuals, such as hair, skull thickness, etc. These lead to a difference in the signal-to-noise ratio of the collected data; therefore, the data must be normalized before the extraction as

$$xN = 2 * \left[\frac{x - \min}{\max - \min} \right] - 1, \quad (4)$$

where x represents an original data point in one channel and \min and \max represent the minimum and maximum values of all channels of the analyzed data. The xN represents the normalized data.

3.3. Feature Extraction. The results of the power spectrum analysis can confirm the decomposition layers. Then, the preprocessing data are calculated in the frequency domain by wavelet packet decomposition [40, 41]. In this study, the wavelet basis is sym4. To obtain the more obvious features, the concentration changes of all channels of the totalHb and the difference between oxyHb and deoxyHb were calculated following wavelet packet decomposition. In the time domain, the motion intention occurred at the beginning of movement. Therefore, eight points (approximately 1 s) were used for analysis. For each state, the analyzed data were stored in a matrix ($M1$), where the columns represented the 22 channels and the rows represented the frequency bands.

For each state, each subject would admit a matrix ($M1$) after wavelet packet decomposition, but there is a huge difference between the values of different channels; in order to determine the significant channels and corresponding frequency bands of one state, each matrix was divided into three proportional parts based on the value of each element. In this research, the probability of 20%, 25%, 30%, 35%, and 40% were used, and based on the final accuracy of training and testing data, the probability of 30% was the best, so it was defined as the final percent. It means that the top 30% proportional parts were defined as digital “1”; the mid 40%

were digital “0”; and the bottom 30% were digital “−1” (M2). For the training set, eleven subjects were selected to find out the feature vectors. In detail, based on the frequency statistic, under each state, if the frequency of same digital number on one position of these eleven matrices was seven or more ($\geq 63.64\%$), this position was defined as the digital; otherwise, it was defined as digital “0” (M3). After that, the eleven matrices were combined into a new matrix under this state, which represents the features of this state. Next, the significant channels with links in frequency and space were combined to be defined as feature vectors, if the digital value was the same in this matrix. For the other states, the method of extracting of feature vectors was the same. The flow is shown in Figure 3.

3.4. State Classification. The libSVM algorithm [42] was used to classify these three states. To obtain the highest accuracy, the feature vectors of the totalHb and the difference between the oxyHb and deoxyHb were combined. For the primarily eleven participants, ten were selected for training data and one for testing data, a total of 11 combinations according to the different permutations. However, some feature vectors could improve the accuracy, and some could not, so all feature vectors needed requiring permutation and combination to find the best combination of feature vectors. For each of the feature vector permutations and combinations, the recognition accuracy of the 11 combinations was calculated. The final accuracy of this feature vectors combination was the average of these results. All feature vectors combinations were compared to select the highest recognition and its corresponding feature vectors. Then the eleven subjects were identified as the training data, and another eleven subjects were identified using the above feature vectors combination.

4. Results

4.1. Power Spectrum Analysis. The power spectrum density analysis method could get a continuous frequency map of each channel (Figure 4). By observing 11 subjects' continuous power spectrum of each channel of the totalHb and the difference between the oxyHb and deoxyHb. It was found that the main frequency band was approximately 0 to 0.18 Hz, so it was defined as the main frequency band in this study. Moreover, it was found that the distance between two peaks was about 0.03 Hz. Therefore, 0.03 Hz is the most reasonable frequency interval, which is also associated with the number of layers of wavelet packet decomposition.

4.2. Data Preprocessing. The zero drift of the original data was removed using a series of operations based on mathematical morphology (Figure 5). And to highlight the key channels, the 22 channels were normalized by Formula (1). The range of all values is −1 to 1 after normalization.

4.3. Feature Extraction. According to the power spectrum density analysis, the main frequency band was 0 to 0.18 Hz and the frequency interval was 0.03 Hz. Because the

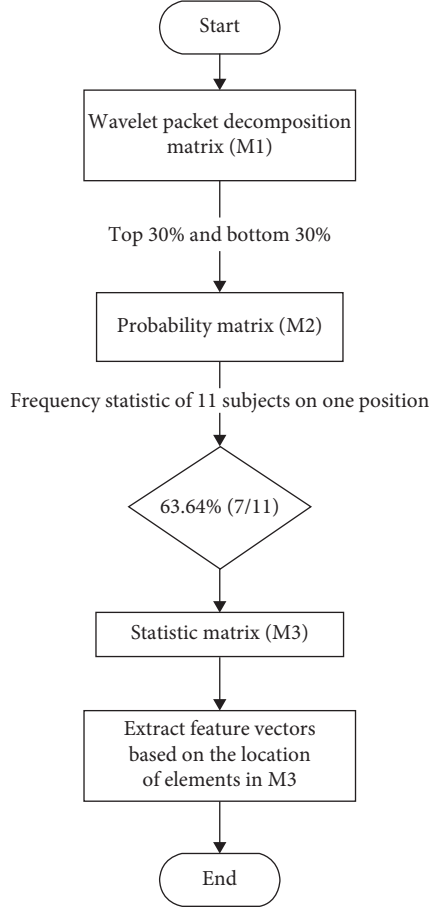


FIGURE 3: The flow of feature extraction.

sampling period of hemoglobin signals was 0.13 s, the signal's sampling frequency was approximately 7.7 Hz. Based on wavelet packet decomposition, the frequency band was divided into 128 groups, with each interval approximately 0.03 Hz. The first six groups (approximately 0 to 0.18 Hz) were used to extract feature vectors. The eight points at the end of the data were combined after calculating the concentration changes of all channels in the totalHb and the difference between the oxyHb and deoxyHb. For totalHb and the difference between oxyHb and deoxyHb of each subject, three 6×22 matrices representing the motion intention of the three gaits were created, respectively.

Based on the matrices of the last step and the above-mentioned method, the results of each state of the totalHb and the difference between oxyHb and deoxyHb are shown in Figure 6(a) and Figure 6(b). According to the spatial layout of the various channels in Figure 1(a), the channels with links in frequency or space were selected as feature vectors, if the digital value was the same. The isolated channel was not considered.

4.4. State Classification. For the different permutation and combination, the best average classification accuracy rate of training set was 78.79%. And under this features vector combination, the eleven training subjects were defined as the

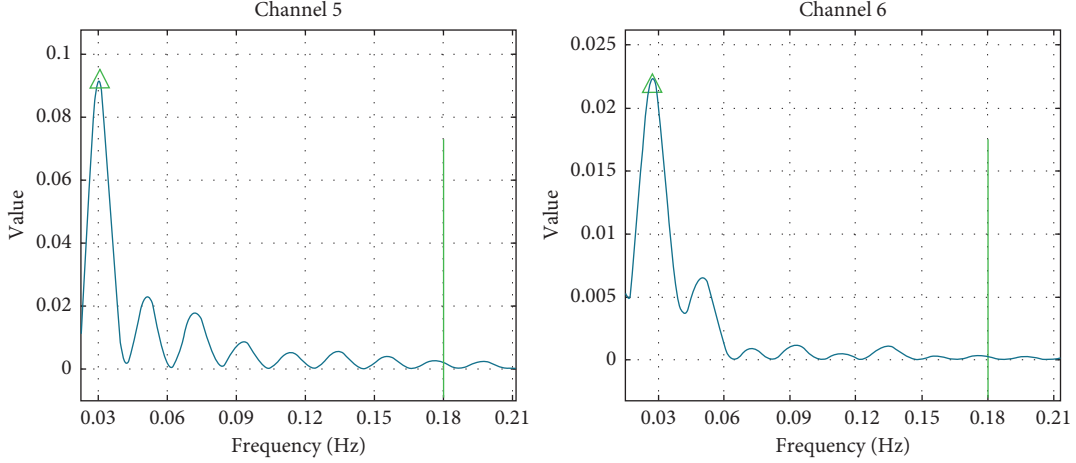


FIGURE 4: The continuous frequency maps of subject one's channel 5 and channel 6 under the ML gait of totalHb. The triangle represents the most active frequency point.

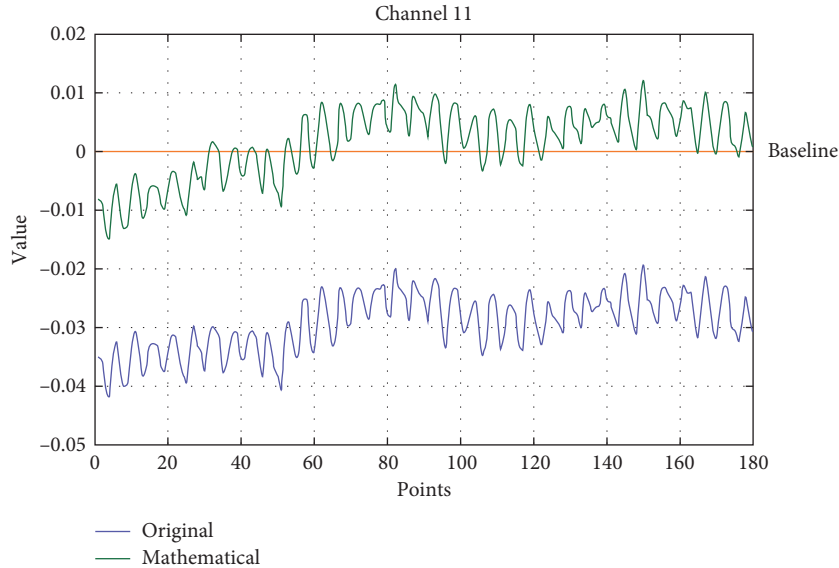


FIGURE 5: The sequence diagrams of subject one's channel 11 under the SM gait of totalHb. The blue line represents the original signal, and the green line represents the data after mathematical morphology.

training data to classify another eleven subjects (11 subjects' second tasks \times 3 states), with classification accuracy rates of 78.9% (26/33) (11 subjects' second tasks \times 3 states). The recognition rates of SL, SM, and ML states are 72.72% (8/11), 72.72% (8/11), and 90.9% (10/11), respectively.

5. Discussion

To date, most research on lower limbs focused on which brain region is activated when the walking speed or step length changed [21–25,27,29–31]. There is little research on the identifying motion intention of lower limbs, let alone several gaits with little difference. The test environment was one of the important reasons. The fNIRS technology overcomes this restriction and can be used in the natural environment. In this study, a method based on the fNIRS signal

was proposed to identify the motion intention of three similar motion states.

This study focuses on classifying the motion intention before movement of healthy subjects, and the final accuracy was 72.72% (8/11), 72.72% (8/11), and 90.9% (10/11), respectively. These results improved that the subjects' motion intention can be used to characterize the gait parameters. Moreover, through Figure 6, it can be found that there are obvious differences in the channel and frequency band under different motion intention of gait parameters. The motion intention prior to the movement initiation for patients is stronger than that for healthy subjects [43], and due to the defect of moving ability, the patient needs high attention for a certain action, whereas healthy subject does not. If one movement has been repeated for many times, it would be hard to extract the motion intention, and it will be

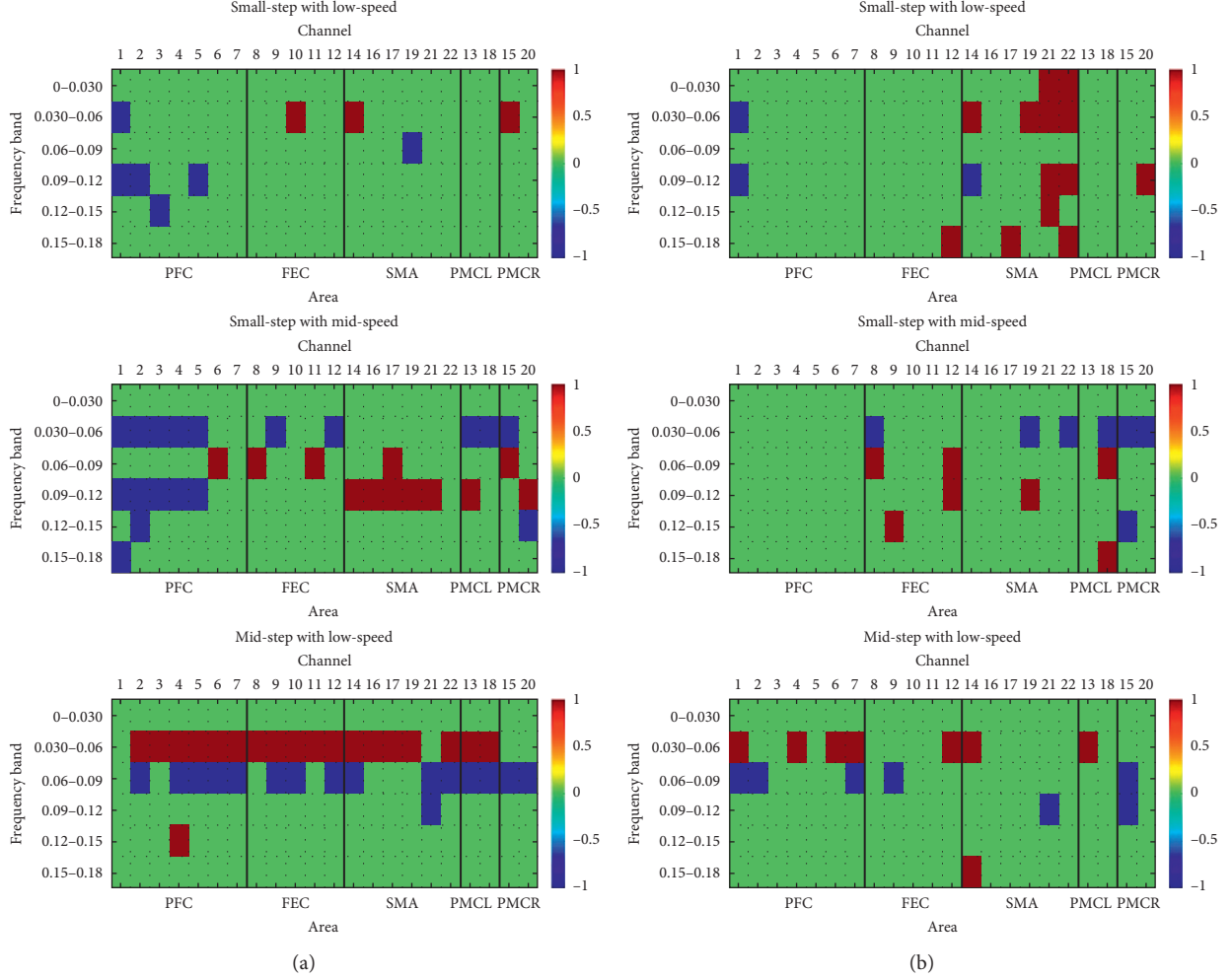


FIGURE 6: (a) The significant channels of three walking states under the total data. The red square represents digital 1: it means that the value of original seven matrices under this position has five or more under the top 30% proportion. The blue square represents digital -1: it means that the value of original seven matrices under this position has five or more under the bottom 30% proportion. The green square represents digital 0; it represents the all cases expert for above two. (b) The significant channels of three walking states under the difference between oxyHb and deoxyHb.

the main influence on the classification accuracy. Therefore, the paradigm of this experiment was designed specially (Figure 2); it was that the subject can not repeat one action continuously and each movement be done only twice, and the purpose of this design is to let the subject not take a movement unthoughtfully and have a consideration before the movement. This study was still in its infancy, and through the results of healthy subjects, it lays a foundation for later research on patients' motion intention.

For patients with weak or no athletic ability, the practice of small compensation and slow pace has great practical application value [6]. In rehabilitation, the patient's active participation and coordination are important, as good rehabilitation training methods ensure that patients receive the maximum rehabilitation in the shortest possible time. This provides them with the best chance of improving their quality of life, by reducing the burden on family and society [10]. This study uses spontaneous motion intention to classify minor gait, although it is in the initial stage of study

and the subjects are healthy men, but the results proved the feasibility of classifying the gait parameters through the motion intention before movement, which lays a good foundation for the patients to carry out the rehabilitation training through their motion intention and improve their walking ability in the future.

This study focused on the classification of walking intention before movement. So, all the movements were purely spontaneous, and the feature vectors used for classification were extracted before the actual movement. This method could compensate for the delay in the algorithm to communicate with external devices and lays a foundation for real-time BCI system. Although the classification accuracy was not very high, it confirmed the feasibility of controlling an exoskeleton to perform rehabilitation training for the further research.

However, there are many shortcomings in this study that need to be addressed in the future. First, the number of experiments was small, and all subjects were normal,

healthy, young people. For patients with weak or no athletic ability but intact brain function, their brain function is also different from normal function, and the same is true for the elderly [23,31,44–46]. Further research is required on a large number of patients and the elderly. Second, this study focused on identifying the motion intention of different gaits. However, the method of classifying the rest time and starting awareness and the rest and ending times is a difficult task. Only these three conditions were completed. The dynamic identification was performed for real-time data to realize the real BCI system. Third, the ending point was fixed due to the limitations of the institution. The stop-awareness part was controlled by external factors. Some companies have infrared wireless devices, which may be used to realize the true spontaneous gait in the future.

6. Conclusions

This study presented a method of classifying the motion intention of different spontaneous gaits based on fNIRS technology. And, three different walking states were presented with final recognition rates of 78.79%. In this study, only the subjects' motion intention was used to extract the feature vectors. And this study can classify the two-dimensional gait at the same time, instead of single changes of walking speed or step length. Moreover, a combination method of permutation and combination method and libSVM algorithm is considered, all combinations of feature vectors, to reduce the influence of extraneous feature vectors on the recognition result. These results confirmed it is feasible to classify the motion intention of advanced walking by using fNIRS technology, which adds the possibility of realizing the autonomous control of walking-assistive equipment based on the BCI system.

Data Availability

The data used to support the findings of this study are available from the corresponding author upon request.

Conflicts of Interest

The authors declare that they have no conflicts of interest regarding the publication of this paper.

Acknowledgments

This study was supported by the National Natural Science Foundation of China (61673286) and China Postdoctoral Science Foundation (nos. 2015M580461 and 2017T100397).

References

- [1] M. Wasay, W. Grisold, W. Carroll, and R. Shakir, "World brain day 2016: celebrating brain health in an ageing population," *Lancet Neurology*, vol. 15, no. 10, p. 1008, 2016.
- [2] W. K. Tang, E. Wong, H. F. K. Chiu, C. M. Lum, and G. S. Ungvari, "The Geriatric Depression Scale should be shortened: results of Rasch analysis," *International Journal of Geriatric Psychiatry*, vol. 20, no. 8, pp. 783–789, 2005.
- [3] A. Seichi, Y. Hoshino, T. Doi et al., "Development of a screening tool for risk of locomotive syndrome in the elderly: the 25-question geriatric locomotive function scale," *Journal of Orthopaedic Science*, vol. 17, no. 2, pp. 163–172, 2012.
- [4] K. Nakamura, "A "super-aged" society and the "locomotive syndrome"," *Journal of Orthopaedic Science*, vol. 13, no. 1, pp. 1-2, 2008.
- [5] C. I. Chang, D. C. Chan, and K. N. Kuo, "Prevalence and correlates of geriatric frailty in a northern Taiwan community," *Journal of the Formosan Medical Association*, vol. 110, no. 4, pp. 247–257, 2011.
- [6] K. Rockwood, X. Song, C. Macknight et al., "A global clinical measure of fitness and frailty in elderly people," *Canadian Medical Association Journal*, vol. 173, no. 5, pp. 489–495, 2005.
- [7] J. Diong, R. D. Herbert, L. K. Kwah, J. L. Clarke, and L. A. Harvey, "Mechanisms of increased passive compliance of hamstring muscle-tendon units after spinal cord injury," *Clinical Biomechanics*, vol. 27, no. 9, pp. 893–898, 2012.
- [8] R. Lapointe, Y. Lajoie, O. Serresse, and H. Barbeau, "Functional community ambulation requirements in incomplete spinal cord injured subjects," *Spinal Cord*, vol. 39, no. 6, pp. 327–335, 2001.
- [9] B. Husemann, F. Müller, C. Krewer, S. Heller, and E. Koenig, "Effects of locomotion training with assistance of a robot-driven gait orthosis in hemiparetic patients after stroke: a randomized controlled pilot study," *Stroke*, vol. 38, no. 2, pp. 349–354, 2007.
- [10] J. F. Veneman, R. Ekkelenkamp, H. V. D. Kooij, H. V. D. Kooij, and H. V. D. Kooij, "A series elastic- and bowden-cable-based actuation system for use as torque actuator in exoskeleton-type robots," *International Journal of Robotics Research*, vol. 25, no. 3, pp. 261–281, 2006.
- [11] R. Riener, L. Lunenburger, S. Jezernik et al., "Patient-cooperative strategies for robot-aided treadmill training: first experimental results," *IEEE Transactions on Neural Systems and Rehabilitation Engineering*, vol. 13, no. 3, pp. 380–394, 2005.
- [12] P. L. Jackson, M. F. Lafleur, F. Malouin, C. Richards, and J. Doyon, "Potential role of mental practice using motor imagery in neurologic rehabilitation," *Archives of Physical Medicine and Rehabilitation*, vol. 82, no. 8, pp. 1133–1141, 2001.
- [13] S. L. Wolf, C. J. Winstein, J. P. Miller et al., "Effect of constraint-induced movement therapy on upper extremity function 3 to 9 months after stroke: the EXCITE randomized clinical trial," *Journal of the American Medical Association*, vol. 296, no. 17, p. 2095, 2006.
- [14] J. H. Burridge and M. Ladouceur, "Clinical and therapeutic applications of neuromuscular stimulation: a review of current use and speculation into future developments," *Neuro-modulation Journal of the International Neuromodulation Society*, vol. 4, no. 4, pp. 147–154, 2001.
- [15] S. Lee and Y. Sankai, "Power assist control for walking aid with HAL-3 based on EMG and impedance adjustment around knee joint," in *Proceedings of IEEE/RSJ International Conference on Intelligent Robots and System*, pp. 1499–1504, Lausanne, Switzerland, September 2002.
- [16] T. Hayashi, H. Kawamoto, and Y. Sankai, "Control method of robot suit HAL working as operator's muscle using biological and dynamical information," in *Proceedings of 2005 IEEE/RSJ*

- International Conference on Intelligent Robots and Systems*, pp. 3063–3068, Alberta, Canada, August 2005.
- [17] T. Kagawa and Y. Uno, “A human interface for stride control on a wearable robot,” in *Proceedings of 2009 IEEE/RSJ International Conference on Intelligent Robots and Systems*, pp. 4067–4072, St. Louis, MO, USA, October 2009.
- [18] S. Tanabe, S. Hirano, and E. Saitoh, “Wearable Power-Assist Locomotor (WPAL) for supporting upright walking in persons with paraplegia,” *Neurorehabilitation*, vol. 33, no. 1, pp. 99–106, 2013.
- [19] T. M. Lau, J. T. Gwin, and D. P. Ferris, “Walking reduces sensorimotor network connectivity compared to standing,” *Journal of NeuroEngineering and Rehabilitation*, vol. 11, no. 1, pp. 1–14, 2014.
- [20] P. D. Sanctis, J. S. Butler, B. R. Malcolm, and J. J. Foxe, “Recalibration of inhibitory control systems during walking-related dual-task interference: a Mobile Brain-Body Imaging (MOBI) Study,” *Neuroimage*, vol. 94, no. 6, pp. 55–64, 2014.
- [21] J. Wagner, T. Solis-Escalante, R. Scherer, C. Neuper, and G. Müller-Putz, “It’s how you get there: walking down a virtual alley activates premotor and parietal areas,” *Frontiers in Human Neuroscience*, vol. 8, no. 1, p. 93, 2014.
- [22] G. Lisi and J. Morimoto, “EEG single-trial detection of gait speed changes during treadmill walk,” *Plos One*, vol. 10, no. 5, Article ID e0125479, 2015.
- [23] Y. Zhang, S. Prasad, A. Kilicarslan, and J. L. Contreras-Vidal, “Multiple kernel based region importance learning for neural classification of gait states from EEG signals,” *Frontiers in Neuroscience*, vol. 11, 2017.
- [24] A. Presacco, R. Goodman, L. Forrester, and J. L. Contreras-Vidal, “Neural decoding of treadmill walking from noninvasive electroencephalographic signals,” *Journal of Neurophysiology*, vol. 106, no. 4, pp. 1875–1887, 2011.
- [25] M. Severens, B. Nienhuis, P. Desain, and J. Duysens, “Feasibility of measuring event related desynchronization with electroencephalography during walking,” in *Proceedings of 2012 Annual International Conference of the IEEE Engineering in Medicine and Biology Society*, p. 2764, San Diego, CA, USA, August 2012.
- [26] J. T. Gwin, K. Gramann, S. Makeig, and D. P. Ferris, “Electrocortical activity is coupled to gait cycle phase during treadmill walking,” *Neuroimage*, vol. 54, no. 2, pp. 1289–1296, 2011.
- [27] H. Y. Kim, S. P. Yang, G. L. Park, E. J. Kim, and J. S. You, “Best facilitated cortical activation during different stepping, treadmill, and robot-assisted walking training paradigms and speeds: a functional near-infrared spectroscopy neuroimaging study,” *Neurorehabilitation*, vol. 38, no. 2, pp. 171–178, 2016.
- [28] M. Mihara, H. Yagura, M. Hatakenaka, N. Hattori, and I. Miyai, “Clinical application of functional near-infrared spectroscopy in rehabilitation medicine,” *Brain and Nerve*, vol. 62, no. 2, pp. 125–132, 2010.
- [29] P. Caliandro, M. Serrao, L. Padua et al., “Prefrontal cortex as a compensatory network in ataxic gait: a correlation study between cortical activity and gait parameters,” *Restorative Neurology and Neuroscience*, vol. 33, no. 2, pp. 177–187, 2015.
- [30] R. Holtzer, J. R. Mahoney, M. Izzenoglu, C. Wang, S. England, and J. Verghese, “Online fronto-cortical control of simple and attention-demanding locomotion in humans,” *Neuroimage*, vol. 112, pp. 152–159, 2015.
- [31] M. Suzuki, I. Miyai, T. Ono, and K. Kubota, “Activities in the frontal cortex and gait performance are modulated by preparation. an fNIRS study,” *Neuroimage*, vol. 39, no. 2, pp. 600–607, 2008.
- [32] Y. Sui, C. Li, J. Li et al., “Classification of desired motion speed-based on cerebral hemoglobin information,” in *Proceedings of 2nd International Conference on Advanced Robotics and Mechatronics (ICARM)*, pp. 320–324, Hefei, China, August 2017.
- [33] K. S. Hong, N. Naseer, and Y. H. Kim, “Classification of prefrontal and motor cortex signals for three-class fNIRS-BCI,” *Neuroscience Letters*, vol. 587, pp. 87–92, 2015.
- [34] X. Yin, B. Xu, C. Jiang et al., “Classification of hemodynamic responses associated with force and speed imagery for a brain-computer interface,” *Journal of Medical Systems*, vol. 39, no. 5, pp. 1–8, 2015.
- [35] X. Yin, B. Xu, C. Jiang, Y. Fu et al., “NIRS-based classification of clench force and speed motor imagery with the use of empirical mode decomposition for BCI,” *Medical Engineering and Physics*, vol. 37, no. 3, pp. 280–286, 2015.
- [36] M. Okamoto, H. Dan, K. Sakamoto et al., “Three-dimensional probabilistic anatomical cranio-cerebral correlation via the international 10-20 system oriented for transcranial functional brain mapping,” *Neuroimage*, vol. 21, no. 1, pp. 99–111, 2004.
- [37] D. Tsuzuki, V. Jurcak, A. K. Singh et al., “Virtual spatial registration of stand-alone fNIRS data to MNI space,” *Neuroimage*, vol. 34, no. 4, pp. 1506–1518, 2007.
- [38] G. Šimić and P. R. Hof, “In search of the definitive Brodmann’s map of cortical areas in human,” *Journal of Comparative Neurology*, vol. 523, no. 1, pp. 5–14, 2015.
- [39] Y. Sun, K. Chan, and S. M. Krishnan, “ECG signal conditioning by morphological filtering,” *Computers in Biology and Medicine*, vol. 32, no. 6, pp. 465–479, 2002.
- [40] Z. Li, J. Y. Leung, E. W. Tam, and A. F. Mak, “Wavelet analysis of skin blood oscillations in persons with spinal cord injury and able-bodied subjects,” *Archives of Physical Medicine and Rehabilitation*, vol. 87, no. 9, pp. 1207–1212, 2006.
- [41] D. Farina, O. F. do Nascimento, M. F. Lucas, and C. Doncarli, “Optimization of wavelets for classification of movement-related cortical potentials generated by variation of force-related parameters,” *Journal of Neuroscience Methods*, vol. 162, no. 1–2, pp. 357–363, 2007.
- [42] C. C. Chang and C. J. Lin, *LIBSVM: A Library for Support Vector Machines*, ACM, New York , NY, USA, 2011.
- [43] M. Lotze, H. Flor, W. Grodd et al., “Phantom movements and pain. An fMRI study in upper limb amputees,” *Brain*, vol. 124, no. 11, pp. 2268–2277, 2001.
- [44] J. Wu, B. A. Stoica, T. Luo et al., “Isolated spinal cord contusion in rats induces chronic brain neuroinflammation, neurodegeneration, and cognitive impairment: involvement of cell cycle activation,” *Cell Cycle*, vol. 13, no. 15, pp. 2446–2458, 2014.
- [45] J. Wu, Z. Zhao, B. Sabirzhanov et al., “Spinal cord injury causes brain inflammation associated with cognitive and affective changes: role of cell cycle pathways,” *Journal of Neuroscience*, vol. 34, no. 33, pp. 10989–11006, 2014.
- [46] M. Mihara, I. Miyai, M. Hatakenaka, K. Kubota, and S. Sakoda, “Role of the prefrontal cortex in human balance control,” *Neuroimage*, vol. 43, no. 2, pp. 329–336, 2008.

Research Article

Neurophysiological Responses to Different Product Experiences

Enrica Modica  ^{1,2}, **Giulia Cartocci**  ¹, **Dario Rossi**  ^{1,2}, **Ana C. Martinez Levy**, ³
Patrizia Cherubino  ¹, **Anton Giulio Maglione**  ¹, **Gianluca Di Flumeri**  ^{1,4,5}
Marco Mancini, ⁵ **Marco Montanari**, ^{1,5} **Davide Perrotta**, ¹ **Paolo Di Feo**  ¹, **Alessia Vozzi**, ¹
Vincenzo Ronca, ¹ **Pietro Aricò**  ^{1,4,5} and **Fabio Babiloni**  ^{1,5,6}

¹Department of Molecular Medicine, Sapienza University of Rome, Viale Regina Elena 291, 00161 Rome, Italy

²Department of Anatomical, Histological, Forensic & Orthopedic Sciences, Sapienza University of Rome, Piazzale Aldo Moro 5, 00185 Rome, Italy

³Department of Communication, Social Research, Sapienza University of Rome, Via Salaria 113, 00198 Rome, Italy

⁴IRCCS Fondazione Santa Lucia, Neuroelectrical Imaging and BCI Lab, Via Ardeatina 306, 00179 Rome, Italy

⁵BrainSigns Srl, Rome, Italy

⁶Department of Computer Science, Hangzhou Dianzi University, Xiangsha Higher Education Zone, 310018 Hangzhou, China

Correspondence should be addressed to Enrica Modica; enrica.modica@uniroma1.it

Received 9 March 2018; Revised 9 July 2018; Accepted 7 August 2018; Published 24 September 2018

Academic Editor: João M. R. S. Tavares

Copyright © 2018 Enrica Modica et al. This is an open access article distributed under the Creative Commons Attribution License, which permits unrestricted use, distribution, and reproduction in any medium, provided the original work is properly cited.

It is well known that the evaluation of a product from the shelf considers the simultaneous cerebral and emotional evaluation of the different qualities of the product such as its colour, the eventual images shown, and the envelope's texture (hereafter all included in the term “product experience”). However, the measurement of cerebral and emotional reactions during the interaction with food products has not been investigated in depth in specialized literature. The aim of this paper was to investigate such reactions by the EEG and the autonomic activities, as elicited by the cross-sensory interaction (sight and touch) across several different products. In addition, we investigated whether (i) the brand (Major Brand or Private Label), (ii) the familiarity (Foreign or Local Brand), and (iii) the hedonic value of products (Comfort Food or Daily Food) influenced the reaction of a group of volunteers during their interaction with the products. Results showed statistically significantly higher tendency of cerebral approach (as indexed by EEG frontal alpha asymmetry) in response to comfort food during the visual exploration and the visual and tactile exploration phases. Furthermore, for the same index, a higher tendency of approach has been found toward foreign food products in comparison with local food products during the visual and tactile exploration phase. Finally, the same comparison performed on a different index (EEG frontal theta) showed higher mental effort during the interaction with foreign products during the visual exploration and the visual and tactile exploration phases. Results from the present study could deepen the knowledge on the neurophysiological response to food products characterized by different nature in terms of hedonic value familiarity; moreover, they could have implications for food marketers and finally lead to further study on how people make food choices through the interactions with their commercial envelope.

1. Introduction

During a shopping experience in a supermarket, it has been suggested for consumers to have few seconds to get in touch with the product in the aisle and to decide whether buying or not the product on the basis of the gathered information in that time window [1].

There have been many studies which have demonstrated the role and the importance of packaging in terms of ability to communicate relevant product information, its influence on consumers' attention, perception, and purchase intention [2,3]. Expressions such as “the silent salesman” [4] are commonly used to describe the role of packaging. Packaging has become a significant marketing channel because of its

presence in the shop, combined with its strong influence on customers' decisions [5].

More recently, there has been a growing interest surrounding the influence of the sensory characteristics of packaging on consumers' expectations and on consumers' subsequent food experience [6, 7]. In fact, the product could be perceived as a combination of different items: the package, the brand, the aesthetic side (color, graphic, images, and shape), and the context of usage [8]. Each of these items may elicit different cognitive and emotional reactions with different meanings for consumers. Several studies have demonstrated that the role of the packaging is as important at the moment of the purchase as during the phase of usage and usability of product, known as the first and the second moment of truth, respectively [9,10]. The first one deals with the package's ability to grab the attention of customers, when the consumer builds his own expectations; this moment corresponds to the first time he looks at it, approaches, and deals with it. The second one is the experience itself, when the consumer uses and consumes the product. This is the moment of truth for the design of the prerequisites for services (i.e., information and functions). The package must be easy to use, the information on it must be relevant, so that consumers do not misuse the product, it must fit in storage spaces, and if the product should be dosed, the package has to facilitate this, and so on. Then, it is crucial for companies to design packages with user-friendly prerequisites for services since there are no employees present during the service consumption process. One could say that the package bridges the gap between production and consumption. If the visual exploration of food package provides information on the aesthetic side, the somatosensory inflow derived from its direct tactile exploration provides important information to the consumer [11]. In fact, touch gathers various data from perception, such as pressure, temperature, and texture [12], and it has a link to arousal [13]. Furthermore, arousal is the basis of emotion, motivation, and behavioural reactions; studies have shown that 95% of thinking is unconsciously realized where consumers make purchasing decisions based on emotion rather than rational thoughts [14]. Hurley's studies [15] showed that electrodermal activity, which in general is accepted as one of the more effective biomarkers of human arousal [16], is a possible measure to provide insight into customer preference of packaging and a support of a more holistic understanding of decision making. The correlation between vision and touch plays a very important role because the consumer develops a "feel" for the food package. In addition, the evaluation of the ingredients inside [17] would evoke memories of the food's taste and bring the somatic markers that were stored beside such memories back to the body. It is thus crucial in understanding consumer behaviour during evaluations of products, as studied in the literature, to study such variation of cerebral and emotional state of the consumers [18].

For years, the companies invested in traditional marketing researches, for example, surveys and focus groups, asking people to explain their consumption behaviour or to rate their preferences. Part of the recent growth on interest in multisensory packaging design is

undoubtedly due to the potential use of the innovative techniques in the field of cognitive neuroscience, which allow to deeply understand the cognitive perception toward stimuli. Most attention has been given to pricing, products, and branding, which have demonstrated some of the benefits by using neuroscientific methods, specifically fMRI, during a shopping task. Those studies found that adding the information of neural measures to self-report led to significantly more accurate predictions of subsequent purchasing decisions. Furthermore, Plassman and colleagues used fMRI to study whether information that creates expectations about product quality can influence product perceptions [19]. Results of this investigation found support for the latter, demonstrating that changing the prices of otherwise identical products (wines) affected brain regions involved in interpreting taste pleasantness after tasting the wines [17]. Neuroscientific techniques have been used to better understand consumer behaviour and nonconscious interactions with consumer products, and the role of emotions in the decision-making process [20, 21]. These techniques include the measure of electroencephalographic signals (EEG), the brain imaging (e.g., fMRI), and the measure of autonomic nervous system measures, for example, heart rate (HR) and electrodermal response (EDR). EEG is a noninvasive method of recording the electrical activity of the brain, by placing electrodes on the scalp. EEG-based studies, for instance, investigated the perceived pleasantness toward a stimulus, demonstrating the existence of an asymmetric activity of the prefrontal cortex in the alpha band [22], which implies a different motivational tendency toward the proposed stimuli. In particular, various studies evidenced a relative increase in the left prefrontal cortex (PFC) activation in the duration of the positive motivation, while an augmented right-sided anterior activation during the negative motivation [23]. From these considerations, it is possible to define the Approach Withdrawal Index (AW) as the difference of the brain activity between the right and the left PFC in the alpha band. The positive value of the AW Index suggests a positive motivation toward the stimulus, while higher right activity would be reflected by negative frontal alpha asymmetry values, suggesting a negative motivation in response to the stimulus [24].

It has been evidenced how the higher values of EEG spectral power over the frontal scalp areas in theta frequency band (4–7 Hz) have been connected to higher levels of task difficulty [25]. It has been also suggested that such increase of EEG frontal midline theta power spectra values (hereafter "frontal theta" for brevity) can represent a marker of cognitive processing, occurring in correspondence of mental fatigue during different visuocognitive task [26]. The frontal theta, used as index of effort and processing in regard to the task's complexity, has already been applied in different research fields: neuroaesthetics field [27]; avionic and car driving for the detection of the effort employed in the execution of flight simulation, air traffic management, and driving tasks [25–32]; and different challenging listening conditions both in normal hearing than in hearing-impaired participants [33] and to human-computer interaction [34] studies.

Similarly to the measurement of EEG activity, the measure of the autonomic nervous system's (ANS) activity can help researchers understand the psychophysiological reactions to stimuli, which have been associated with emotional processes in academic literature [35, 36]. For the emotions, discrete and dimensional theoretical models have been designed, respectively, implying for emotional states: peculiar physiological, behavioural, and experiential correlate with the discrete models, while a combination of affective dimensions, mainly valence and arousal, correlates with the dimensional models [13]. With the purpose of estimating the emotional reaction to stimuli, for this work, beyond EEG measures, we recorded the electrodermal response (EDR) and heart rate (HR). The first one is used to measure electrodermal activity, a property of the human body that causes continuous variation in the electrical characteristics across the skin. Skin conductance (SC) varies with the activity of sweat glands in the skin (the higher the sweating is, the higher the SC will be), controlled by the sympathetic nervous system; therefore, skin conductance is an indicator of psychological or physiological arousal [37]. In the present research, an autonomic index has been adopted, resulting from the combination of the electrodermal response (EDR) and the heart rate (HR). These two signals reflect the emotional response to stimuli, and the resulting Emotional Index (EI) has been conceived starting from Russell and Barrett's circumplex model of affect [38], where the HR is plotted on the *x*-axis, while the EDR is plotted on the *y*-axis, respectively, reflecting information concerning the stimuli' valence (positive or negative) and arousal (low or high activation).

In this way, it is possible to obtain a monodimensional variable, called the Emotional Index (EI), which provides information concerning the emotional status of participants, as shown in previous studies [39]. Studies demonstrated that knowledge in neuroscience can potentially enrich research in decision making and integrating neuroscience with decision making has a lot of potential [40].

According to these evidences, the aim of this paper was to investigate the cognitive and emotional reactions to the cross-sensory interaction (sight and touch) with products belonging to different categories. We estimated such cognitive and emotional reactions by using the Mental Effort, the AW, and the Emotional Indexes mentioned above. In particular, we investigated the influence of the following three features of the products:

- (1) The brand: Major Brand or Private Label
- (2) The familiarity: Foreign or Local Brand
- (3) The hedonic value of the products: Comfort Food or Daily Food

First, two phases have been investigated: visual exploration (VE) and visual and tactile exploration (VTE) during the interaction with (i) two Daily Food items (one representative of a Major Brand and one representative of a Private Label) and (ii) two Comfort Food items (one representative of a Foreign product and one of a Local product) (Experiment 1). Furthermore, we extended the

research to the study of the interaction between the brand and the familiarity by testing Comfort Food and Daily Food belonging to Major Brand, Private Label, and Foreign and Local products categories. Finally, in order to investigate the contribution of different sensory modalities, we added the tactile exploration (TE) phase to the already adopted VE and VTE phases (Experiment 2).

We made three working hypotheses:

HP1: Comfort Foods are a category of food, often characterized by high sugar and/or carbohydrate content, that should provide some psychological and specifically emotional reward (for a review, see [41]). Furthermore, since the prefrontal cortex (PFC) has been linked to the processing of hedonic aspects of taste [42], we predict higher AW values in response to the interaction with the Comfort Food than with the Daily Food. Furthermore, evidence shows that one sensory modality could be via by which the hedonic attributes of a product can be perceived and could bias the estimation of the quality and pleasantness of the product acquired by other sensory modalities [43]. Therefore, we would try to elucidate whether the visual or the tactile sensory modality would equally modulate the reaction (reflected by a similar pattern reported in both the VE and TE phases) or whether one of those would be predominant (higher values in one of the phases), or finally if they exerted a synergic effect (higher values in the VTE phase, but not in the TE and VE phases).

HP2: since (i) the higher complexity of a stimulus requests higher information processing, producing increased mental effort [25] and (ii) the increased tendency of approach, elicited by complex stimuli, raises the individual's interest [44], we hypothesize that the values of the investigated Cerebral Indexes for the participants would be higher during the interaction with Foreign products than with Local ones. In particular, it would occur during the VE and VTE phases, but not for the TE phase, due to the unfamiliarity of the products and because of the labels not being written in the native language.

HP3: literature evidences showed a differential activation pattern in the frontal lobe in response to the exposure to attractive and unattractive stimuli [45]. Typically, Major Brand products present more attractive packaging than products; therefore, we hypothesize that the former would elicit higher approach tendency than the Private Label items.

2. Materials and Methods

The project involved 32 healthy volunteers. Informed consent was obtained from each participant after the explanation of the study, which was approved by the local institutional ethics committee. The experiment was conducted following the principles outlined in the Declaration of Helsinki of 1975, as revised in 2000. During the entire experiment, the brain activity, heart rate, and the electrodermal response have been recorded. At the beginning of the recording, participants were asked to close and keep their eyes closed for 1 minute and after that to keep their eyes open, watching the black screen in front of them for 1 minute. This part of the recording was considered as baseline. For each product, the test protocol consisted of two

phases lasting 15 seconds each: in the first one, participants had to look at the product, and in the second one, they interacted with the product, by freely manipulating it. After each phase, the experimenter asked the participant to rate the extent to which they appreciated the interaction with the product on a scale from -5 to $+5$. The protocol then restarted with another item. Products have been randomly presented among participants. A subsample of 13 subjects performed a further phase: they also interacted with the product before the visual exploration, with the eyes closed.

Experiment 1: 19 healthy participants (10M, average age = 24.94 ± 3.40 , min = 21 years old and max = 31 years old) have been enrolled in the study. The selected products were (i) two Daily Food items (one representative of a Major Brand and one representative of a Private Label) and (ii) two Comfort Food items (one representative of a Foreign product and one of a Local product). The phases of interaction with the product lasted 15 seconds each and were the visual exploration (VE) and the visual and tactile exploration (VTE) phases.

Table 1 shows the examples of products belonging to each experimental category.

Experiment 2: 13 healthy participants (5 males, average age = 27.23 ± 7.30 , min = 21 years old and max = 44 years old) have been enrolled in the study. For this experiment, four different Comfort Foods (e.g., chocolate bars) and four different Daily Foods (e.g., rice) have been chosen. For each category of food, 2 Local products and 2 Foreign products have been selected: both Local and Foreign products belonged to either the Major Brand or the Private Label categories (Table 1).

The protocol was divided into three phases: tactile exploration (TE) with closed eyes (15 s), visual exploration (VE) (15 s), and visual and tactile exploration (VTE) (15 s). The aim of this experiment was to investigate how the aesthetic design, the familiarity, and the cross-perception influence the impression of a product as a variation of cognitive and emotional variables.

2.1. EEG Recordings and Signal Processing. The EEG activity was recorded using ten electrodes (Fpz, Fp1, Fp2, AFz, AF3, AF4, AF5, AF6, AF7, and AF8) placed on an EEG frontal headband by means of a portable 21-channel system (BEmicro, EBneuro, Italy). Although the system allowed to record up to 21 channels, a ready-made headband with ten electrodes placed over the prefrontal and frontal cortex, since (i) only this cortical area (prefrontal and frontal) was of interest in the present study, and (ii) the headband reduced the system's invasiveness and increased the comfort of the participant when compared with traditional EEG caps. The reference and the ground electrodes have been placed, respectively, on the left and right earlobes. The signals have been acquired at a sampling rate of 256 Hz, and the impedances were kept below $10\text{ k}\Omega$. After the acquisition phase, the raw EEG signal has been digitally preprocessed by using the EEGLAB [46] Matlab toolbox. Firstly, a notch filter (50 Hz) was applied in order to reject the main current interference. Secondly, the gathered signal has been

band-pass filtered by a fifth-order Butterworth filter ([2/30] Hz), in order to reject the continuous component as well as high-frequency interferences, such as muscular artefacts. Then, the independent component analysis (ICA), in particular the SOBI algorithm [47], has been applied to EEG data in order to identify and remove the component related to eye blinks and eye movements, since their contribution overlaps the EEG bands of interest [48]. The component (always one of ten) has been manually selected and removed, and after that the EEG signal has been reconstructed. Furthermore, in order to clean the EEG signal as much as possible, after these conservative steps (until now no EEG data has been lost), the EEG signal segments still affected by artefacts have been automatically detected and rejected. In particular, the EEG signal was segmented in 1-second-long epochs, shifted of 0.5 seconds. For each epoch, three automatic methods implemented in Matlab and based on “acceptability values” (in parentheses) have been used: the threshold criterion ($\pm 100\text{ }\mu\text{V}$), the trend estimation ($\pm 10\text{ }\mu\text{V/s}$, with $p=0.3$), and the sample-to-sample difference ($\pm 25\text{ }\mu\text{V}$). If for a specific epoch at least one criterion was not respected, that epoch was labelled as “artefact.” Thus, the EEG epochs marked as “artefacts” have been removed with the aim to have a clean EEG dataset [30, 31].

Finally, in order to take into account any subjective difference in terms of brain rhythms, for each subject the individual alpha frequency (IAF) was computed on the 60-second-long closed eyes segment, recorded at the beginning of the experimental task. It consists in the individual power spectrum peak within the conventional alpha domain [7/12] (Hz) [43], in order to define the EEG bands of interest according to the method suggested in the current scientific literature (i.e., each band is defined as “ $\text{IAF} \pm x$,” where IAF is the individual alpha frequency, in Hertz, and x an integer in the frequency domain) [25]. Consequently, the EEG signal of each channel for each subject was filtered, by using a fifth-order Butterworth filter, in own alpha [$\text{IAF} - 4/\text{IAF} + 2\text{ Hz}$] and theta bands [$\text{IAF} - 6/\text{IAF} - 4\text{ Hz}$] [25], since they represent the more interesting bands for the purpose of the present study.

To compute the activity of the cortical areas of interest in a specific frequency band, the global field power (GFP) was then computed. This is a measurement introduced by Lehmann and Michel [49] in 1990 to summarize the synchronization level of the brain activity over the scalp surface. GFP is computed from a specific set of electrodes (the set depends on the involved brain area; in the following, it will be specified for each index) by performing the sum of squared values of EEG potential at each electrode, averaged for the number of involved electrodes, resulting in a time-varying waveform related to the increase or decrease of the global power in the analysed EEG. The GFP formula is presented as follows:

$$\text{GPF} = \frac{1}{N} \sum_{i=1}^N x_{g_i}(t)^2, \quad (1)$$

where g is the considered EEG band, frontal is the considered cortical area, N is the number of electrodes included in the area of interest (in this example, the frontal area), and i is the electrodes' index.

TABLE 1

Comfort Food samples	Local products	Foreign products
Major Brand		
Private Label		
Daily Food samples	Local products	Foreign products
Major Brand		
Private Label		

The formula defining the frontal alpha asymmetry (Approach Withdrawal (AW)) index is as follows:

$$AW = GFP\alpha_{right} - GFP\alpha_{left}, \quad (2)$$

where the $GFP\alpha_{right}$ and $GFP\alpha_{left}$ stand for the GFP calculated among right (Fp2, AF4, AF8, and AF6) and left (Fp1, AF3, AF5, and AF7) electrodes, respectively, in the alpha (α) band. Higher frontal alpha asymmetry values, reported by the participants, stood for an approach motivation toward the stimulus, while lower frontal alpha asymmetry values stood for a withdrawal motivation [22, 23, 50, 51].

It may be argued that the tactile exploration, being characterized by the closed eyes condition, would be affected by an increase in the alpha range in comparison with both the visual exploration and visual and tactile exploration phases. However, the AW Index was calculated as the difference in the frontal alpha activity between the two hemispheres; therefore, alpha increase would not interfere with the estimation of the index.

To evaluate the mental effort/processing, EEG activity in the theta band of all the frontal electrodes has been considered for the GFP computation. An increase in the frontal theta (i.e., mental effort) would imply an increase in the task difficulty [33].

The AW Index and the Effort Index were estimated for each second and then normalized with respect to the index of the baseline (1 minute of open eyes).

It has been repeatedly evidenced in the literature, thanks to the application to several kinds of stimuli [29, 50, 52], that the frontal cortex constitutes an area of interest for the analysis of the approach or withdrawal attitude and the frontal theta as index of cerebral effort and processing.

The normalized AW and Effort values have been averaged along the whole duration of selected tasks for each subject: visual exploration (15 sec), tactile exploration (15 sec), and visual and tactile exploration (15 sec).

2.2. HR and EDR Recordings and Signal Processing

Electrodermal responses (EDR) and heart rate (HR) were recorded with a sampling rate of 64 Hz through a Shimmer (Shimmer Sensing, Ireland) system applied to the non-dominant hand of the subject. More in detail, the cardiac activity was recorded by recording a Photoplethysmogram (PPG) (i.e., a pulse oximeter which illuminates the skin and measures changes in light absorption due to the heart pump, at the thumb). In order to obtain the HR signal from the PPG, the Pan-Tompkins algorithm has been used [53]. The constant voltage method (0.5 V) was employed for the acquisition of the skin conductance. The electrodes were placed on the palmar side of the middle phalanges of the second and third fingers, on the nondominant hand of the participants, according to published procedures [54]. Employing the LEDAlab software [55], the tonic component of the skin conductance (Skin Conductance Level, SCL) was

estimated. The circumplex model of affect plane was adopted to collapse information about a stimulus deriving from SCL and HR[38,56]. In this model, the x axis reported the HR values, reflecting the valence dimension of a stimulus, while the y axis reported the SCL values, mirroring the arousal dimension of a stimulus [13]. Adopting this theoretical framework, it was possible to obtain a monodimensional variable, named the Emotional Index (EI), providing information concerning the emotional status of a participant, as defined in previous studies [39]. The EI results interpretation predict that higher values would mirror a more positive and engaging emotion experienced by the subject, and vice versa.

In the same way as the Cerebral Indexes, the Emotional Index value was estimated for each second and then standardized on the basis of the baseline (1 minute of open eyes).

2.3. Statistical Analysis. ANOVA was performed for each index (AW, Effort, and Emotional) for the factor phase with three levels (tactile exploration (TE), visual exploration (VE), and visual and tactile exploration (VTE)), singularly for each of the following means categories:

- (a) Comfort Food versus Daily Food
- (b) Major Brand versus Private Label
- (c) Foreign versus Local

For all the indexes (AW, Effort, and Emotional), paired t -test was performed singularly for each phase (tactile exploration (TE), visual exploration (VE), and visual and tactile exploration (VTE)), in order to compare the means of

- (a) Comfort Food versus Daily Food
- (b) Major Brand versus Private Label
- (c) Foreign versus Local

For the Major Brand versus Private Label comparison, we included only Local products in the analysis, due to the lack of knowledge of the Foreign labels that could bias the perception of the Brand level.

Since the correspondence between the phases, data from Experiments 1 and 2 were collapsed for the analyses performed on the VE and VTE phases (therefore, VE and VTE phases included 32 participants), while for the TE phase, only data from Experiment 2 were available (therefore including data from 13 participants).

In addition, Fisher's exact test was performed in order to analyse the distribution of the behavioural categorical data (e.g., the declared knowledge of the product).

3. Results and Discussion

3.1. Results

3.1.1. Comfort Food versus Daily Food Comparison. The comparison between these two categories of products showed a higher tendency of approach in response to Comfort Food than Daily Food as evaluated by the AW

Index both in the visual exploration phase (VE) ($p = 0.031$, $t = -2.26$, Cohen's $d = 0.297$, $df = 26$) and in the visual and tactile exploration (VTE) phase ($p = 0.027$, $t = -2.342$, Cohen's $d = 0.537$, $df = 26$) (Figure 1). The significance was not found for the AW Index during the tactile exploration (TE) phase ($p = 0.443$, $t = 0.794$). Concerning the Effort Index, a statistically significant effect of the phase has been found ($p = 0.003$, $F(2, 22) = 7.516$), with lower values reported for the TE in comparison with both the VTE ($p = 0.001$) and VE ($p = 0.016$) phases (Figure 2). The same ANOVA performed on AW and EI data considering the factor phase (TE, VE, and VTE) did not provide statistically significant results.

3.1.2. Major Brand versus Private Label Comparison. The comparison between the Major Brand and the Private Label products categories highlighted higher positive rating values for the Major Brand than for the Private Label products belonging to the Comfort Food category during the VE ($p = 0.001$, $t = -4.535$, Cohen's $d = 1.865$, $df = 11$) and VTE ($p = 0.001$, $t = -4.371$, Cohen's $d = 1.780$, $df = 11$) phases, but not during the TE phase ($p = 0.919$, $t = 0.104$). On the contrary, concerning the Daily Food category, the Private Label obtained higher rating values than the Major Brand category in the TE ($p = 0.019$, $t = 2.749$, Cohen's $d = 0.963$, $df = 11$) and in the VTE ($p = 0.018$, $t = 2.768$, Cohen's $d = 1.128$, $df = 11$) phases but not in the VE phase ($p = 0.186$, $t = 1.412$). In addition, the Fisher exact test evidenced higher values of product recognition for the Major Brand than for the Private Label products concerning both the Comfort Food ($p = 0.036$) and the Daily Food ($p = 0.003$) categories. Focusing on the rated products (data from Experiment 2), a higher AW value for the Private Label in comparison with the Major Brand products during the VTE phase has also been found ($p = 0.018$, $t = -2.788$, Cohen's $d = 0.364$, $df = 11$). Other paired t -test and ANOVA performed on AW, Effort, and Emotional Indexes did not report any statistical significance.

3.1.3. Foreign versus Local Products Comparison. The analysis demonstrated higher AW Index values for the Foreign products in comparison with the Local ones, supporting a higher tendency of approach toward the former products only during the VTE phase ($p = 0.034$, $t = -2.224$, Cohen's $d = 0.518$, $df = 29$) (Figure 3), but not in the TE ($p = 0.368$, $t = 0.938$) and VE ($p = 0.169$, $t = -1.409$) phases. Similarly, considering the Effort Index, an increased effort value for the Foreign products in comparison with the Local ones in the same VTE phase has been shown ($p = 0.003$, $t = -3.232$, Cohen's $d = 0.834$, $df = 29$) (Figure 4(b)), and also in the VE phase ($p < 0.001$, $t = -3.666$, Cohen's $d = 0.965$, $df = 29$) (Figure 4(a)), but not in the TE phase ($p = 0.266$, $t = 0.171$). Finally, concerning the EI, higher values were found in response to the Foreign products during the TE phase ($p = 0.010$, $t = -3.049$, Cohen's $d = 0.483$, $df = 12$), but not in the VE ($p = 0.508$, $t = -0.673$) and VTE ($p = 0.394$, $t = -0.868$) phases. ANOVA on the comparison among

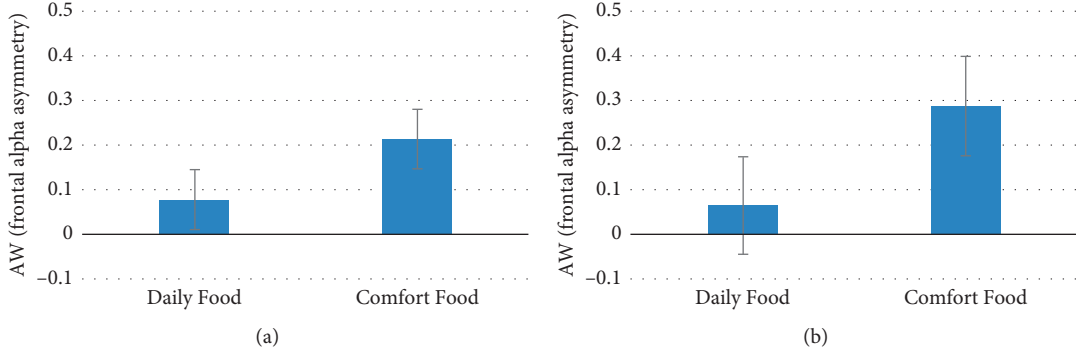


FIGURE 1: The graphs represent the statistical results for the AW Index values concerning the comparison between the Daily Food and Comfort Food categories. (a) Mean AW values during the visual exploration phase (statistically significant difference $p = 0.031$) and (b) mean AW values during the visual and tactile exploration phase (statistically significant difference $p = 0.027$). Error bars represent standard error.

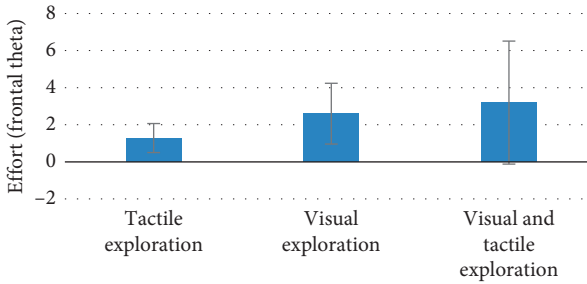


FIGURE 2: The graph represents the statistical results for the Effort Index values concerning the comparison among the experimental phases (visual exploration, tactile exploration, and visual and tactile exploration) (phase effect $p = 0.003$). The post hoc analysis evidenced how the tactile exploration phase presented lower effort values in comparison with both the visual exploration ($p = 0.016$) and the visual and tactile exploration phases ($p = 0.001$). Error bars represent standard error.

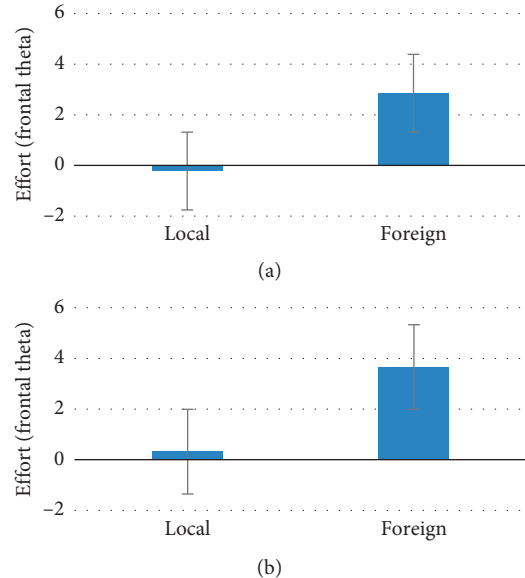


FIGURE 3: The graph represents the statistical results for the AW Index values concerning the comparison between the Local and Foreign products categories. Error bars represent standard error.

FIGURE 4: The graph represents the statistical results for the Effort Index values concerning the comparison between the Local and Foreign products categories. (a) represents mean Effort Index values during the visual exploration phase (statistically significant difference $p = 0.001$) and (b) represents mean Effort Index values during the visual and tactile exploration phase (statistically significant difference $p = 0.003$). Error bars represent standard error.

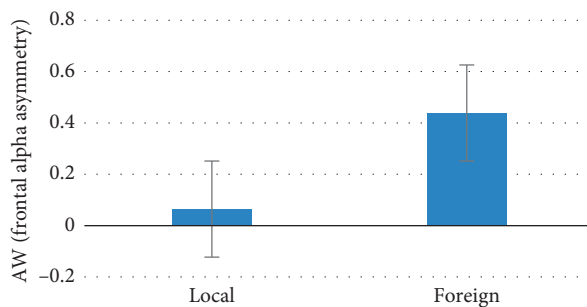


FIGURE 3: The graph represents the statistical results for the AW Index values concerning the comparison between the Local and Foreign products categories. Error bars represent standard error.

phases (TE, VE, and VTE) did not evidence any statistical significance for any of the indexes.

4. Discussion

The EEG results supported the hypothesis 1 that the Comfort Food category elicited a higher tendency of approach (higher

AW values) than the Daily Food category, as also found in previous evidences, reporting higher AW values for sweet foods, and in particular for chocolate, in comparison with other foods [57]. Moreover, it is interesting to note that this pattern was found for the VE and VTE phases but not for the TE phase, therefore suggesting that the visual modality was prominent over the touch for the hedonic evaluation of the tested products. This result was also supported by the evidence that there was a lower processing (as indexed by the mental effort values) during the TE phase in comparison with both the VE and VTE phases.

The lack of statistically significant differences in the comparison between Major Brand and Private Label products,

for what concerns the investigated neurometric indices, could be explained by the strong balance and correspondence between analogous products selected in the different categories. On the contrary, the identified differences between Major Brand and Private Label in the behavioural results displayed how the Major Brand products were the most recognized by participants. In addition, the higher verbally declared pleasantness reported for the Major Brand Comfort Food in comparison with the Private Label Comfort Food in correspondence of the VE and VTE phases suggest that for Comfort Food, the visual modality is prominent in the evaluation of Comfort Food quality. On the contrary, for the Daily Food, we found higher rated pleasantness for the Private Label Daily Food in comparison with the Major Brand Daily Food during the TE and VTE phases (both involving the tactile modality). This could be explained by the characteristics of the package, since the Private Label Daily Food was a plastic bag that allowed participants to “feel” the rice seeds when touching, while the Major Brand Daily Food was constituted by a carton box that did not confer direct information about the products inside.

Results on the comparison between Foreign and Local products verified hypothesis 2 and were consistent with Mandler’s theory [45], which demonstrated that a complex stimulus, so one requesting a high information processing, raised more interest than a simple one generating an approach toward itself (as shown by the highest AW value).

Mental effort results showed that the sample had higher effort value for the foreign product, during both the VE and VTE phases, probably because of not having familiarity with them. These results could be caused by the novelty of the visual features of the Foreign products, which requested higher cognitive activity to process the information. In fact, when the stimuli do not have sufficient attributes which call back a preexisting cognitive model, people spend more effort for acquiring the new information and for creating a new cognitive model [58]. In this case, because of the lack of familiarity with the foreign products, the sample spent more cognitive effort for processing information during the interaction with them. Interestingly, during the TE phase, we did not find any statistical difference between Foreign and Local products, possibly explained by the fact that the corresponding goods selected belonging to the Foreign and the Local categories were extremely similar from a haptic point of view.

Concerning the AW Index, the value reported for Foreign products was higher only during the VTE phase, maybe because of the presence of more appealing design and informative contents on the back of the packages; for instance, the Foreign Major Brand Daily Food product presented a naturalistic scenario on the back, instead of some extremely predictable information, as was the case on the Local Major Brand Daily Food one.

Furthermore, studies demonstrated that the novelty of a product, the difficulty in its categorization when compared to preexisting mental images of that product, and the incongruity between the novel product and the experienced known products belonging to the same category mirror to cognitive patterns underlying an increased curiosity toward the product and an increased tendency of

approach toward it. In particular, Olivero and Russo’s studies [59] demonstrated that when a product matched exactly the preexisting mental patterns, it loses its capacity to attract, causing boredom and avoidance from itself: the novelty stimulates the curiosity, interest, and the approach toward the product, especially for people called “*Sensation Seekers*,” who are easily bored without high levels of stimulation.

5. Conclusions

In summary, the results of the present study could be summarized as follows:

HP1 was confirmed, since different cognitive and emotional reactions have been obtained, in particular during the VTE phase in response to Comfort Food.

HP2 was also demonstrated, since the neuroelectrical indexes for the Foreign products showed higher values of Effort Index during all the phases in which the visual modality was involved and a higher approach tendency (AW Index) toward them during the free manipulation of such products.

HP3 was not confirmed; in fact, we did not detect any statistically significant difference in the neurophysiological reaction to the Major Brand and the Private Label items; however, this could be explained by the strong analogy and balance among the selected items.

The present study has the obvious limitations of the number of the food packaging products tested, although the sample size of participants was sufficient to reveal significant statistical effects. The future studies should preferably more focused address the study of different food packages, constituted by different materials (e.g., tetrapack bricks). Nevertheless, the study demonstrated the possibility to investigate the cerebral and emotional reactions of a group of normal subjects and potential buyer to the visual and tactile exploration of food products with a number of neurometric indexes.

Data Availability

The data used to support the study could be obtained by sending an email to Prof. Babiloni (fabio.babiloni@uniroma1.it).

Conflicts of Interest

The authors declare that they have no conflicts of interest.

Authors’ Contributions

Enrica Modica, Giulia Cartocci, and Dario Rossi contributed equally to the article.

Acknowledgments

This research was partly supported by the EU Project SmokeFreeBrain, through the definition and the study of the Cerebral and Emotional Indexes already used by Dr. Modica and Prof. Babiloni.

References

- [1] P. Silayoi and M. Speece, "Packaging and purchase decisions: an exploratory study on the impact of involvement level and time pressure," *British Food Journal*, vol. 106, pp. 607–628, 2004.
- [2] M. L. Kobayashi and M. De Toledo Benassi, "Impact of packaging characteristics on consumer purchase intention: instant coffee in refill packs and glass jars," *Journal of Sensory Studies*, vol. 30, pp. 169–180, 2015.
- [3] C. Delgado, A. Gomez-Rico, and J. Guinard, "Evaluating bottles and labels versus tasting the oils blind: effects of packaging and labelling on consumer preferences, purchase intentions and expectations for extra virgin olive oil," *Food Research International*, vol. 54, no. 2, pp. 2112–2121, 2013.
- [4] L Tangeland, K. Ø Schulte, and C. Boks, "Tactile qualities of materials in consumer product packaging," in *DS 50: Proceedings of Nord Design 2008 Conference*, Tallinn, Estonia, 21–23 August 2008.
- [5] R. L. Underwood and N. M. Klein, "Packaging as brand communication: effects of product pictures on consumer responses to the package and brand," *Journal of Marketing Theory and Practice*, vol. 10, no. 4, pp. 58–68, 2002.
- [6] B. Piqueras-Fiszman and C. Spence, "The influence of the feel of product packaging on the perception of the oral-somatosensory texture of food," *Food Quality and Preference*, vol. 26, pp. 67–73, 2012.
- [7] C. Spence and B. Piqueras-Fiszman, "The multisensory packaging of beverages," in *Food Packaging: Procedures, Management and Trends*, Nova Publishers, Hauppauge NY, USA, 2012, <https://ora.ox.ac.uk/objects/uuid:4e99ba7f-311b-4710-b741-35a1e442c230>.
- [8] H. N. J. Schifferstein and B. F. Howell, "Using color-odor correspondences for fragrance packaging design," *Food Quality and Preference*, vol. 46, pp. 17–25, 2015.
- [9] M. Löfgren, "Packaging and customer value: a service perspective," in *Division for Business and Economics*, 2004.
- [10] M. Gómez, D. M. Consuegra, and A. Molina, "The importance of packaging in purchase and usage behaviour," *International Journal of Consumer Studies*, vol. 39, no. 3, pp. 203–211, 2015.
- [11] K. R. Scherer, "What are emotions? And how can they be measured?," *Social Science Information*, vol. 44, pp. 695–729, 2005.
- [12] J. Berkley and C. H. Hubscher, "Are there separate central nervous system pathways for touch and pain?," *Nature Medicine*, vol. 1, no. 8, pp. 766–73, 1995.
- [13] B. Mauss and M. D. Robinson, "Measures of emotions: a review," *Cognition and Emotion*, vol. 23, no. 2, pp. 209–237, 2009.
- [14] G. Zaltman, *How Customers Think: Essential Insights into the Mind of the Market*, Harvard Business Press, Boston, MA, USA, 2003.
- [15] R. A. Hurley, J. Rice, G. Conlon, and L. O'Hara, "Measuring physiological arousal towards packaging: tracking electrodermal activity within the consumer shopping environment," *Journal of Applied Packaging Research*, vol. 7, no. 1, pp. 39–47, 2015.
- [16] W. Boucsein, *ElectrodermalActivity*, Springer Science & Business Media, 2012.
- [17] H. N. Schifferstein, A. Fenko, A. Desmet, D. Labbe, and N. Martin, "Influence of package design on the dynamics of multisensory and emotional food experience," *Food Quality and Preference*, vol. 27, pp. 18–25, 2013.
- [18] S. Little and U. R. Orth, "Effects of package visuals and haptics on brand evaluations," *European Journal of Marketing*, vol. 47, no. 1/2, pp. 198–217, 2013.
- [19] H. Plassmann, J. O'Doherty, B. Shiv, and A. Rangel, "Marketing actions can modulate neural representations of experienced pleasantness," *Proceedings of the National Academy of Sciences*, vol. 105, no. 3, pp. 1050–1054, 2008.
- [20] A. R. Damasio, *Descartes Error: Emotion Reason and the Human Brain*, Avon, New York, NY, USA, 1994.
- [21] E. T. Roll, *Emotion and Decision-Making Explained*, Oxford University Press, Oxford, UK, 2014.
- [22] G. Di Flumeri, G. Herrero, A. Trettel et al., "EEG frontal asymmetry related to pleasantness of olfactory stimuli in young subjects," in *Selected Issues in Experimental Economics*, pp. 373–381, Springer, Cham, Switzerland, 2016.
- [23] R. J. Davidson and K. Hugdahl, "Cerebral asymmetry, emotion, and affective style," in *Brain Asymmetry*, R. J. Davidson and K. Hugdahl, Eds., pp. 361–387, The MIT University, Cambridge, MA, USA, 1995.
- [24] R. J. Davidson, P. Ekman, C. D. Saron, J. A. Senulis, and W. V. Friesen, "Approach-withdrawal and cerebral asymmetry: emotional expression and brain physiology: I," *Journal of Personality and Social Psychology*, vol. 58, no. 2, pp. 330–341, 1990.
- [25] W. Klimesch, "EEG alpha and theta oscillations reflect cognitive and memory performance: a review and analysis," *Brain Research Reviews*, vol. 29, no. 2-3, pp. 169–195, 1999.
- [26] E. Wascher, B. Rasch, J. Sänger et al., "Frontal theta activity reflects distinct aspects of mental fatigue," *Biological Psychology*, vol. 96, pp. 57–65, 2014.
- [27] G. Cartocci, A. G. Maglione, E. Modica et al., "The Neuro-Dante project: neurometric measurements of participant's reaction to literary auditory stimuli from Dante's "Divina Commedia,"" in *Symbiotic Interaction*, pp. 52–64, Springer, Cham, Switzerland, 2016.
- [28] N. Sciaraffa, G. Borghini, P. Aricò et al., "Brain interaction during cooperation: Evaluating local properties of multiple-brain network," *Brain sciences*, vol. 7, no. 12, p. 90, 2017.
- [29] P. Aricò, G. Borghini, G. Di Flumeri et al., "Human factors and neurophysiological metrics in air traffic control: a critical review," *IEEE Reviews in Biomedical Engineering*, vol. 10, pp. 250–263, 2017.
- [30] P. Aricò, G. Borghini, G. Di Flumeri et al., "Adaptive automation triggered by EEG-based mental workload index: a passive brain-computer interface application in realistic air traffic control environment," *Frontiers in Human Neuroscience*, vol. 10, p. 539, 2016.
- [31] P. Aricò, G. Borghini, G. Di Flumeri et al., "A passive brain-computer interface application for the mental workload assessment on professional air traffic controllers during realistic air traffic control tasks," *Progress in Brain Research*, vol. 228, pp. 295–328, 2016.
- [32] G. Borghini, P. Aricò, G. Di Flumeri et al., "EEG-based cognitive control behaviour assessment: an ecological study with professional air traffic controllers," *Scientific Reports*, vol. 7, no. 1, p. 547, 2017.
- [33] M. G. Wisniewski, E. R. Thompson, N. Lyer et al., "Frontal midline θ power as an index of listening effort," *Neuroreport*, vol. 26, no. 2, pp. 94–99, 2015.
- [34] A. Gevins and M. E. Smith, "Neurophysiological measures of cognitive workload during human-computer interaction," *Theoretical Issues in Ergonomics Science*, vol. 4, no. 1-2, pp. 113–131, 2003.

- [35] S. D. Kreibig, "Autonomic nervous system activity in emotion: a review," *Biological Psychology*, vol. 84, no. 3, pp. 394–421, 2010.
- [36] P. Cherubino, A. Trettel, G. Cartocci et al., "Neuroelectrical indexes for the study of the efficacy of TV advertising stimuli," in *Selected Issues in Experimental Economics*, pp. 355–371, Springer, Cham, Switzerland, 2016.
- [37] K. Gouizi, F. BerekshiReguig, and C. Maaoui, "Emotion recognition from physiological signals," *Journal of Medical Engineering Technology*, vol. 35, no. 6-7, pp. 300–307, 2011.
- [38] J. A. Russell and L. F. Barrett, "Core affect, prototypical emotional episodes, and other things called emotion: dissecting the elephant," *Journal of Personality and Social Psychology*, vol. 76, no. 5, pp. 805–819, 1999.
- [39] G. Vecchiato, A. G. Maglione, P. Cherubino et al., "Neurophysiological tools to investigate consumer's gender differences during the observation of TV commercials," *Computational and Mathematical Methods in Medicine*, vol. 2014, Article ID 912981, 12 pages, 2014.
- [40] B. Shiv, A. Beehara, I. Levin et al., "Decision neuroscience," *Marketing Letters*, vol. 16, no. 3-4, pp. 375–386, 2005.
- [41] C. Spence, "Comfort food: a review," *International Journal of Gastronomy and Food Science*, vol. 9, pp. 105–109, 2017.
- [42] M. L. Kringelbach, "Food for thought: hedonic experience beyond homeostasis in the human brain," *Neuroscience*, vol. 126, no. 4, pp. 807–819, 2004.
- [43] C. Spence and A. Gallace, "Multisensory design: reaching out to touch the consumer," *Psychology & Marketing*, vol. 28, no. 3, pp. 267–308, 2011.
- [44] J. P. Schoormans and H. S. Robben, "The effect of new package design on product attention, categorization and evaluation," *Journal of Economic Psychology*, vol. 18, no. 2, pp. 271–287, 1997.
- [45] M. Stoll, S. Baecke, and P. Kenning, "What they see is what they get? An fMRI-study on neural correlates of attractive packaging," *Journal of Consumer Behaviour*, vol. 7, no. 4-5, pp. 342–359, 2008.
- [46] A. Delorme and S. Makeig, "EEGLAB: an open source toolbox for analysis of single-trial EEG dynamics including independent component analysis," *Journal of Neuroscience Methods*, vol. 134, no. 1, pp. 9–21, 2004.
- [47] A. Belouchrani, K. Abed-Meraim, J. F. Cardoso, and E. Moulines, "A blind source separation technique using second-order statistics," *IEEE Transactions on Signal Processing*, vol. 45, no. 2, pp. 434–444, 1997.
- [48] G. Di Flumeri, P. Aricò, G. Borghini et al., "A new regression-based method for the eye blinks artifacts correction in the EEG signal, without using any EOG channel," in *IEEE 38th Annual International Conference on Engineering in Medicine and Biology Society (EMBC)*, IEEE, pp. 3187–3190, 2016.
- [49] D. Lehmann and C. M. Michel, "Intracerebral dipole source localization for FFT power maps," *Electroencephalography and Clinical Neurophysiology*, vol. 76, no. 3, pp. 271–276, 1990.
- [50] R. J. Davidson, "What does the prefrontal cortex "do" in affect: perspectives on frontal EEG asymmetry research," *Biological Psychology*, vol. 67, no. 1-2, pp. 219–234, 2004.
- [51] G. Vecchiato, J. Toppi, L. Astolfi et al., "Spectral EEG frontal asymmetries correlate with the experienced pleasantness of TV commercial advertisements," *Medical and Biological Engineering and Computing*, vol. 49, no. 5, pp. 579–583, 2011.
- [52] A. G. Maglione, A. Scoppecci, P. Malerba et al., "Alpha EEG frontal asymmetries during audiovisual perception in Cochlear implant users. a study with bilateral and unilateral young users," *Methods of Information in Medicine*, vol. 54, no. 6, pp. 500–504, 2015.
- [53] J. Pan and W. J. Tompkins, "A real-time QRS detection algorithm," *IEEE Transactions on Biomedical Engineering*, vol. 32, no. 3, pp. 230–236, 1985.
- [54] W. Boucsein, D. C. Fowles, S. Grimnes, Society for Psychophysiological Research Ad Hoc Committee on Electrodermal Measures et al., "Publication recommendations for electrodermal measurements," *Psychophysiology*, vol. 49, no. 8, pp. 1017–1034, 2012.
- [55] M. Benedek and C. Kaernbach, "A continuous measure of phasic electrodermal activity," *Journal of Neuroscience Methods*, vol. 190, no. 1–5, pp. 80–91, 2010.
- [56] J. Posner, J. A. Russell, and B. S. Peterson, "The circumplex model of affect: an integrative approach to affective neuroscience, cognitive development, and psychopathology," *Development and Psychopathology*, vol. 17, no. 3, pp. 715–734, 2005.
- [57] G. Di Flumeri, P. Aricò, G. Borghini et al., "EEG-based approach-withdrawal index for the pleasantness evaluation during taste experience in realistic settings," in *Conference Proceedings: Annual International Conference of the IEEE Engineering in Medicine and Biology Society*, 2017.
- [58] L. Mannetti, *Psicologia Sociale: Lucia Mannetti Carocci*, 2005.
- [59] N. Olivero and V. Russo, *Manuale di Psicologia dei Consumi. Individuo*, Società, 2009.

Research Article

Neurophysiological Profile of Antismoking Campaigns

Enrica Modica ,^{1,2} Dario Rossi ,² Giulia Cartocci ,¹ Davide Perrotta,¹ Paolo Di Feo ,¹ Marco Mancini,³ Pietro Aricò ,^{1,3,4} Bianca M. S. Inguscio,¹ and Fabio Babiloni ,^{1,3,5}

¹Department of Molecular Medicine, Sapienza University of Rome, Viale Regina Elena 291, 00161 Rome, Italy

²Department Anatomical, Histological, Forensic & Orthopedic Sciences, Sapienza University of Rome, Piazzale Aldo Moro 5, 00185 Rome, Italy

³BrainSigns Srl, Rome, Italy

⁴IRCCS Fondazione Santa Lucia, Neuroelectrical Imaging and BCI Lab, Via Ardeatina, 306, 00179 Rome, Italy

⁵Department of Computer Science, Hangzhou Dianzi University, Xiangya Higher Education Zone, 310018 Hangzhou, China

Correspondence should be addressed to Enrica Modica; enrica.modica@uniroma1.it

Received 9 March 2018; Accepted 15 August 2018; Published 19 September 2018

Academic Editor: Plácido R. Pinheiro

Copyright © 2018 Enrica Modica et al. This is an open access article distributed under the Creative Commons Attribution License, which permits unrestricted use, distribution, and reproduction in any medium, provided the original work is properly cited.

Over the past few decades, antismoking public service announcements (PSAs) have been used by governments to promote healthy behaviours in citizens, for instance, against drinking before the drive and against smoke. Effectiveness of such PSAs has been suggested especially for young persons. By now, PSAs efficacy is still mainly assessed through traditional methods (questionnaires and metrics) and could be performed only after the PSAs broadcasting, leading to waste of economic resources and time in the case of Ineffective PSAs. One possible countermeasure to such ineffective use of PSAs could be promoted by the evaluation of the cerebral reaction to the PSA of particular segments of population (e.g., old, young, and heavy smokers). In addition, it is crucial to gather such cerebral activity in front of PSAs that have been assessed to be effective against smoke (Effective PSAs), comparing results to the cerebral reactions to PSAs that have been certified to be not effective (Ineffective PSAs). The eventual differences between the cerebral responses toward the two PSA groups will provide crucial information about the possible outcome of new PSAs before its broadcasting. This study focused on adult population, by investigating the cerebral reaction to the vision of different PSA images, which have already been shown to be Effective and Ineffective for the promotion of an antismoking behaviour. Results showed how variables as gender and smoking habits can influence the perception of PSA images, and how different communication styles of the antismoking campaigns could facilitate the comprehension of PSA's message and then enhance the related impact.

1. Introduction

Antismoking public service announcements (PSAs) have been proved to have success in reducing smoking habits in citizens [1] and this success is also reflected by the fact that the smoking rate is decreasing in several European countries. However, the EU's smoking rate among adults is falling too slowly to meet the EU government's goal. This "insufficient" success of antismoking campaigns could be due to ineffective antismoking messages [2] and/or the communication style which could have the boomerang effect among recipients [3]. On that basis, to increase the success of an antismoking campaign, it is important to evaluate the impact of a set of specific message features and how such features are

processed by the citizens in order to develop effective health messages [4]. Individuals' responses to different types of antismoking messages have been examined with the aim to identify certain features that enhance message effectiveness. In fact, there is evidence that antismoking advertising (ads) that activate strong negative emotions are better received and they are associated with a decreased intention to smoke [5], while messages that simply present health consequences of smoking might not work [6]. In addition, it has been suggested that also the thematic content of antismoking ads is also important [7]. For example, messages that dispose the manipulative and misleading nature of the tobacco industry (for more sophisticated audiences) and those that focus on the negative consequences of second-hand smoke were

found to be quite effective [6]. Norm-based messages were also found to be effective for young adolescents [8]. On the other hand, inconsistencies regarding the effectiveness of different types of antismoking ads have been also noted. Understanding antismoking messages that can enhance persuasion has long been of interest for communication researchers and those involved in the design of persuasive communication campaigns. O'Keefe's studies [9] noted that many of these studies assess effects of messages that induced some type of responses without exploring the message features that generate such responses. Nevertheless, a growing body of research explores the relationship between audio and visual features and the outcomes related to persuasion of the citizens [10]. It is crucial to understand the relationship between the arousing messages and the effective comprehension of them. In fact, exposure and comprehension alone are insufficient to facilitate persuasion [11].

A recent study investigated the relationship between fast-paced, evocative messages and message processing in the context of antidrug PSAs [12]. It was observed as fast-paced, intense, graphic, and suspenseful messages enhanced processing of antidrug PSAs. Such research provides the foundation for a theory of the relationship between arousing messages and persuasion.

In this scenario, efficient procedures for evaluating the effectiveness of antismoking messages could be a useful tool for designing public health campaigns. Encouragingly, research has shown that antismoking advertising can be successful in both adult [13] and young people [14].

In fact, it is important to understand the factors that could highlight Effective PSAs and, vice versa, to avoid features that could promote ineffectiveness in those PSAs, to develop efficient and cost-effective antismoking campaigns. Neuroscience techniques, rooted in consumer neuroscience studies, appeared a valid approach for achieving this goal. The antismoking PSA assessment can be performed through the study of the physiological and cerebral reactions to the exposure to the different kind of PSAs. Through such data collection techniques, several aspects related to the impact of commercial advertisings can be investigated with respect to target population's gender [15, 16], culture [17, 18], and age [19]; fragments of interest [15, 20, 21]; brand [22]; price [23]; scenes targeting and speaker's gender [24]; purchasing attitudes of the subjects [25]; and preretail testing [26]. The capability of assessing the impact of general advertising by EEG methods has been recently shown employing the support vector machine on EEG acquired through a frontal band [27]. In particular, the capability of EEG techniques to detect different cerebral patterns between smokers and nonsmokers has been already provided by event-related potential (ERP) studies, in which the amplitude of the P300 resulted lower in smokers than in nonsmokers [28, 29]. Importantly, this difference can be affected by the stimulus category, as evidenced by an ERP study in which it has been shown a significant smoking cue reactivity of the neural component P412, a P300-like wave correlated with unpleasantness-pleasantness in reaction to the cue [30]. In addition, the autonomic reaction to the vision of aversive and high-arousing videos has been already investigated,

highlighting a decrease of the heart rate in correspondence of stimuli characterized by negative content [31, 32]. A previous EEG and autonomic signals study investigating the reaction at the exposure to an Effective and an Ineffective antismoking video in a young sample, and employing the same indexes adopted in the present research, showed higher effort and emotional involvement levels in correspondence of the Effective video [33].

Based on these considerations, we employed different indexes related to the cerebral and emotional reactions of the participants to the stimuli provided, which will be explained in the following paragraphs.

The aim of this study was to investigate the cerebral and emotional reaction to the exposure to selected antismoking PSAs in an adult sample. In particular, we hypothesized the following:

- (i) On the basis of previous researches, which focused on antismoking campaigns evaluation [34] and their different effect on sample due to gender, age, and education variables [35], we presume the existence of distinct patterns of such indexes during the observation of Effective and Ineffective PSAs, by investigating an adult sample divided on the basis of smoking habit and gender
- (ii) Considering that the characteristics of a health campaign (text, images, and communication style) can influence its effectiveness [35, 36], we hypothesized a different cognitive and emotional response provided by those indexes in the evaluated sample toward the selected stimuli

The following paragraphs will explain the techniques and methodologies which allowed us to acquire the neurophysiological signal to develop the indexes for this article (Effort, Emotional, and Visual Attention Indexes), during the observation of antismoking images divided into Effective and Ineffective. Successively, the statistical results obtained for these indexes will be shown and discussed, and this will allow to confirm or not the initial hypothesis.

2. Materials and Methods

In this study, we employed different indexes related to the cerebral and emotional reactions of the subjects to the stimuli provided: the Effort, the Emotional, and the Visual Attention Indexes. In the following, we would like to describe the roots of such indexes in the already existing literature of the psychophysiological measurement of cognitive and emotional states, and how such indexes could be linked to the impact of the images related to Effective and Ineffective antismoking PSAs.

2.1. The Effort Index. It is known that the prefrontal cortex (PFC) plays a pivotal role in a cortical circuit involved in emotional and cognitive processes [31, 37]. The unbalance of the EEG spectral power in alpha frequency band (8–12 Hz) over left and right prefrontal areas is frequently used as a proxy of the involvement of PFC in the decision making. By using the PFC brain activity, the Effort Index has been

proposed as an efficient index of cognitive processing and mental fatigue occurring during the performance of task [38, 39]. In literature, the use of the Effort Index to evaluate the processing level and difficulty of task has been performed in a wide variety of field: neuroaesthetics [40], air traffic management, and driving tasks [41–48]; auditory [49–51]; and human-computer interaction [52] studies.

2.2. The Emotional Index. It has been demonstrated that emotional involvement has long been acknowledged as an essential ingredient in the recipe for persuasion; in fact, the study of persuasion has often examined the various influencing roles of emotion, suggesting how emotion plays an especially significant role in healthy campaigns [53–56].

Theoretical models have been designed to describe emotional states mainly including as independent variables the valence and the arousal experienced by the persons [32, 57, 58]. Typically, electrodermal (corresponding to the activity of the sweat glands) and cardiovascular responses are at the basis of the mostly used indices of activation of the autonomic nervous system. The electrodermal activity is often measured by the galvanic skin response (GSR), and it represents an index of changes in sympathetic arousal [58–65]. In addition, the heart rate (HR) has been evidenced as an index of sympathetic and parasympathetic activity (for a review, see [32]). Starting from this assumption, in the present research, it has been adopted an autonomic index, resulting from the matching of the galvanic skin response (GSR) and the heart rate (HR). These two signals reflect the emotional response to stimuli [32] and the resulting Emotional Index (EI) has been conceived starting from Russell and Barrett's circumplex model of affect [65], where the HR is plotted on the *x*-axis, while the GSR is plotted on the *y*-axis, reflecting information concerning the stimuli' valence (positive or negative) and arousal (low or high activation) [66–68]. The EI has been already applied for instance to the testing of auditory literary stimuli [38, 40] and to TV commercials [15, 19, 24, 69].

2.3. The Visual Attention Index. To increase the understanding of positive or negative attitudes toward social problems, eye-tracking (ET) techniques can be helpful in PSAs evaluation since they have the potentiality for increasing the effectiveness of social communications in different media. ET is a widely used tool in neuromarketing studies [70] since it can detect movements and position of the eyes that have been closely related to shifts of attention [71]. Such technique has already been used to understand how an antismoking cue is perceived in a natural environment by smokers and nonsmokers [72]. Furthermore, ET has been used assessing how the warning label on cigarette packs is perceived by adolescent smokers and nonsmokers [73] and how a social communication should be constructed in order to maximize the visual attention on the warning against tobacco consumption [74].

The experiment was performed in accord with the principles outlined in the Declaration of Helsinki of 1975, as revised in 2000, and it was approved by the University Ethical Committee.

The experimental sample was composed by 30 volunteers (15 M; average age = 34.16 ± 8.11 years old, min = 25 max = 55 years old), 15 Heavy Smokers (HS) and 15 Non-smokers (NS).

Participants were asked to watch a video sitting on a comfortable chair in front of a 19" flat screen with a distance varying from 50 to 60 cm. The proposed stimulus was composed by 6 neutral images taken from IAPS (International Affective Picture System) database [75] used as baseline, followed by a train of 11 antismoking PSA images displayed in a randomized order (so as to prevent in the participants reaction the eventual bias attributable to a positional effect), followed again by the baseline. Images were displayed for 9 seconds each and, between each pair of them, a white cross on a black field was shown, so as to reestablish a central fixation point.

For the EEG, autonomic responses and ET investigation four antismoking images have been selected from the stimuli set, as shown in Figure 1.

Data pertaining the promotion of health and economic improvements in the general population allowed their classification as "Effective" and "Ineffective" communication [76, 77].

The selected PSAs were as follows:

(i) Effective:

(a) NTC, Kids are fast learners (Australia 1997, paternalistic communication style) (Figure 1(a)): the image displays a child holding a cigarette in his right hand and carefully looking at it; on the bottom of the picture, there is the sentence "Kids are fast learners."

(b) CDC, Terry (USA 2012–2015, fear arousing appeal and narrative/experiential communication style) (Figure 1(b)): the image portraits a sick lady presenting the signs of a tracheotomy, flanked by the sentence "Don't tell people smoking is bad, show them."

(ii) Ineffective:

(a) "We won't let them spoil our fun!" "Who wants to be addicted?" Tobacco is wacko (USA 2000, paradoxical communication style) (Figure 1(c)): the picture is composed by a text element, illustrating the slogan of campaign, and the picture depicting a young man with a cigarette in the act of coughing.

(b) Feel free to say no (European Commission 2003, communication style aiming at the identification from young people with the represented young models) (Figure 1(d)): the picture is composed by three sections each depicting young people flanked by the icon of the campaign and the following antismoking sentences: "Who wants to be a looser?"

2.4. EEG Recordings and Signal Processing. The EEG activity was recorded by means of a portable 19-channel system

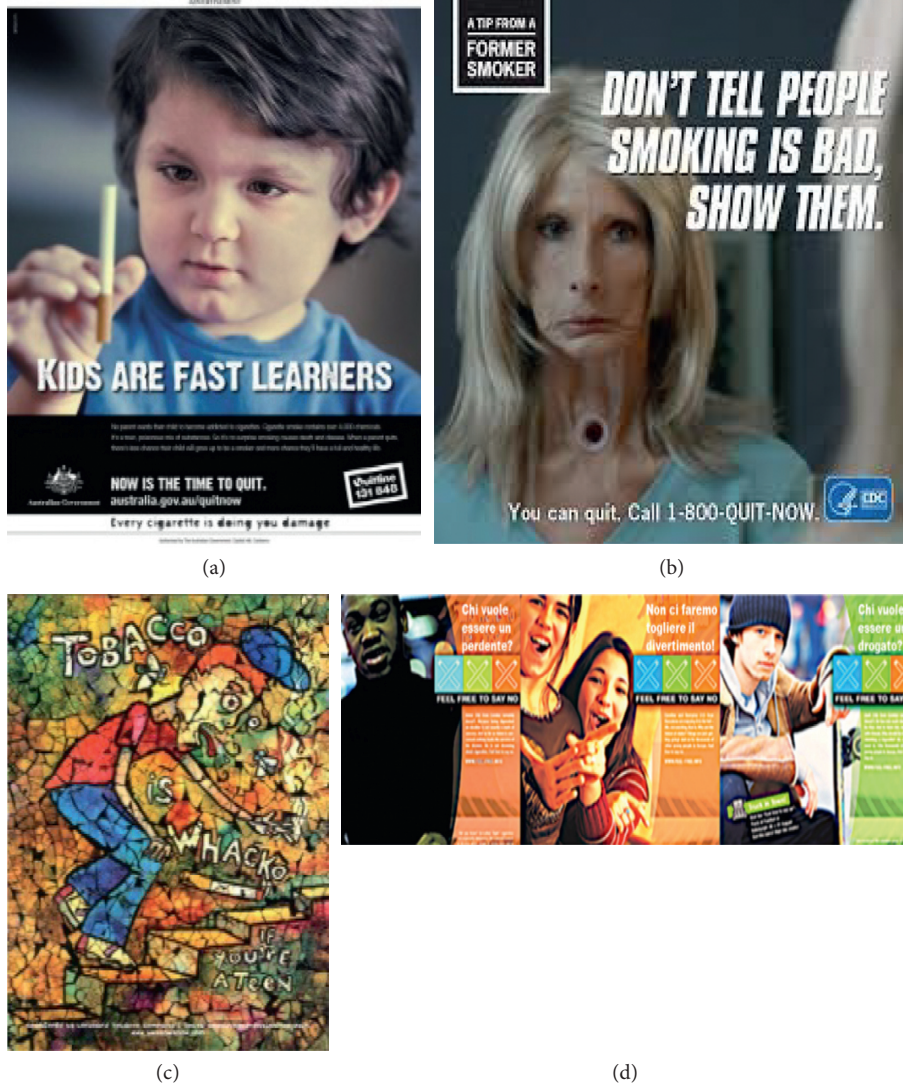


FIGURE 1: PSAs selected from the stimuli set. (a, b) Effective PSAs. (c, d) Ineffective PSAs.

(BEmicro, EBneuro, Italy). The impedances were kept below $10\text{k}\Omega$, and the signals have been acquired at a sampling rate of 256 Hz. A notch filter (50 Hz) has been applied in order to reject the main current interference, and then the gathered signal has been digitally band-pass-filtered by a fifth-order Butterworth filter ($[2 \div 30]$ Hz), in order to reject the continuous component as well as high-frequency interferences, such as muscular artefacts. To detect and remove components due to eye movement, blinks, the independent component analysis (ICA) procedure, in particular the SOBI algorithm [78], has been applied to EEG. For each subject, in order to take into account any subjective difference in terms of brain rhythms, it was collected 60-second-long open eyes segment, recorded at the beginning of the experimental task. This baseline data collection was performed in order to define the EEG bands of interest according to the methodology of the individual alpha frequency (IAF) [38]. With such methodology, that is, each band is defined as “ $\text{IAF} \pm x$,” where IAF is the individual alpha frequency, in Hertz, and x an integer in the frequency

domain [38]. Thus, the EEG activity was divided, by filtering the EEG signals in the time domain, in two main frequency bands: theta [$\text{IAF} - 6 \div \text{IAF} - 2$ Hz] and alpha [$\text{IAF} - 2 \div \text{IAF} + 2$ Hz]. To summarize, the activity of the cortical areas of interest in a specific frequency band, the global field power (GFP) was then computed. This is a measurement introduced by Lehmann and Michel [79] some decades ago to summarize the synchronization level of the brain activity over the scalp surface. GFP is computed from a specific set of electrodes by performing the sum of squared values of EEG potential at each electrode, averaged for the number of involved electrodes, resulting in a time-varying waveform related to the increase or decrease of the global power in the analysed EEG. The GFP formula is presented in the following equation:

$$\text{GFP}_{\vartheta, \text{Frontal}} = \frac{1}{N} \sum_{i=1}^N x_{\vartheta_i}(t)^2, \quad (1)$$

where ϑ is the considered EEG band, Frontal is the considered cortical area, N is the number of electrodes included

in the area of interest (in this example, the frontal area), and i is the electrodes' index.

To evaluate the mental effort/processing, GFP from such frontal electrodes in theta band has been used. Thus, the obtained values have been standardized on the basis of the baseline (the IAPS images) EEG activity acquired at the beginning and at the end of the experiment. An increase in the frontal theta (i.e., mental effort) would imply an increase in the task difficulty [49].

2.5. HR and GSR Recordings and Signal Processing. Galvanic skin responses (GSR) and heart rate (HR) have been acquired with a sampling rate of 128 Hz through a NeXus-10 (Mindmedia, the Netherlands) system. For these recordings, the electrodes were placed to the palmar side of the middle phalanges of the second and third fingers, on the nondominant hand of the participant, according to published procedures [80]. Employing the LEDAlab software [81], the tonic component of the skin conductance (Skin Conductance Level, SCL) was estimated. In order to obtain the HR signal, it has been used the Pan-Tompkins algorithm [82]. The constant voltage method (0.5 V) was employed for the acquisition of the skin conductance. The circumplex model of affect plane was adopted to collapse information about a stimulus deriving from SCL and HR [32, 67], as mentioned above. In this model, the x -axis reported the HR values, reflecting the valence dimension of a stimulus, while the y -axis reported the SCL values, mirroring the arousal dimension of a stimulus [59]. By matching HR and GSR, it is possible to obtain a one-dimensional variable, named the Emotional Index (EI), providing information concerning the emotional status of a participant, as defined in previous studies [15]. The EI results interpretation predict that higher values would mirror a more positive and engaging emotion experienced by the subject, and vice versa.

2.6. Eye-Tracking Recordings and Data Analysis. Eye-tracking data have been collected in order to establish where the gaze is directed when looking at the selected stimuli. A remote eye-tracker has been used (Eye Tribe) with the sampling frequency set at 30 Hz. From the raw data collected, all the artifactual or nonphysiological points of gaze were automatically removed. Then, an identification of the fixations on the images has been performed with an I-DT (Identification by Dispersion Threshold) algorithm [83] that uses two thresholds, a spatial one set at 60 pixels and a temporal one set at 100 ms, in order to identify all the fixations on the proposed images [84]. The analysis of the fixations was focused on the informative, antismoking-related areas of interest (AOIs) for each image, like the presence of the cigarette (Figure 1(a)), or a text or a claim against tobacco consumption (Figures 1(b) and (d)).

For each AOI, we obtained the Visual Attention (VA) Index that takes into account the percentage of total fixation duration (%TFD) for the selected AOI and the percentage of the area itself (%Area), calculated as in [85]:

$$VA = \frac{\%TFD}{\%Area}, \quad (2)$$

%TFD can give us information about how much attention is given to a particular area of the image (for a review, see [86]), but several studies highlighted the importance of the dimension of an area when dealing with attention deployment (for a review, see [86]). With this formula, we can obtain a nondimensional index suitable for the comparison of AOIs different in size.

3. Results

Data obtained for the Neuroelectrical Indexes and for the VA were analysed with ANOVA test. The between variable were "Smoking Habit," with two levels, Heavy Smokers (HS) and Nonsmokers (NS), and "Gender" with two levels, Female (F) and Male (M); the within variable was the "PSA kind," with two levels, Effective and Ineffective. Duncan post hoc has been employed on the statistically significant results from ANOVA. Concerning the results for the EI, t -test has been used. The statistical analysis was performed with the Holm protection against the alpha inflation error possibly occurring for the execution of multiple comparison [87].

Concerning the Effort Index, ANOVA showed a statistically significant effect for the interaction between the variables Smoking Habit and PSA kind ($F(1.27) = 7.836$, $p < 0.05$); the post hoc analysis highlighted an increase reported by HS group for Effective images when compared to HS for Ineffective ones ($p < 0.05$) and to NS for Effective ones ($p < 0.05$). Figure 2 shows these obtained results.

Moreover, the statistical results showed a difference for the Effort Index value between HS and NS group ($p = 0.002$) and between Effective and Ineffective ($p < 0.05$), which highlighted an increase of this index for HS participants and Effective PSA, as shown in Figure 3.

The EI analysis showed a statistically significant effect for the interaction between Gender (Female and Male) and the PSA images (Effective and Ineffective): in particular, concerning Effective images, the EI in females showed the lower value compared to males ($p < 0.014$), as shown in Figure 4.

The VA analysis showed a statistically significant difference between the PSA kind ($F = 4.9$, $p = 0.04$), with higher levels for the Ineffective PSAs as shown in Figure 5.

Concerning the "Gender" variable, the VA analysis showed a statistical difference in the perception between Female and Male subjects ($F = 6.9$, $p = 0.01$), with higher levels in the female population; Figure 6 highlights these results.

4. Discussion

Thanks to the use of neuroscience techniques, we measured the subject's EEG activity, autonomic response, and eye-tracker measurement, which allowed to obtain the indexes explained above, during the observation of selected PSA images. The information gathered by these indexes showed the different perception of the experimental sample toward the stimuli, on the basis of the different kind of the proposed PSA images (Effective and Ineffective) and the different variables of sample (Gender and Smoking Habit).

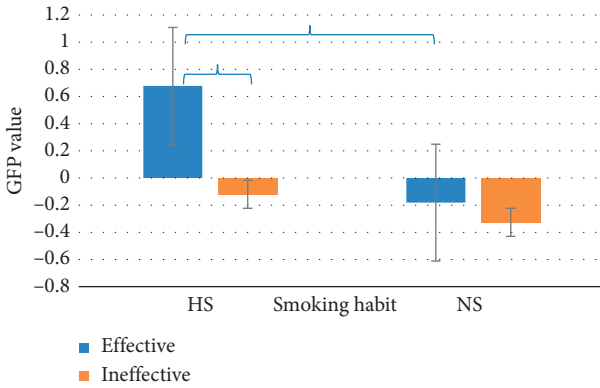


FIGURE 2: The graph represents the Effort Index value for both groups (Heavy Smokers (HS) and Nonsmokers (NS)) during the observation of PSA images (Effective and Ineffective) ($n = 30$). Brackets stand for a statistical significance equal to at least $p = 0.05$, or lower. Error bars represent standard error.

The aim of this paper was to evaluate the perception of adult sample of Effective PSAs compared to the Ineffective ones, on the basis of previous studies, which demonstrated the neurophysiological pattern existence in a young population sample during the observation of antismoking PSAs [88], evaluating the influence of the sample' characteristics. In fact, our results highlighted that the cognitive and emotional indexes were strongly correlated to smoking habit and gender, which confirmed the studies about the influence of socioeconomic variables (as gender, age, and income) on the smoking addiction [6, 7, 15, 18, 19].

Results related to the use of the VA Index suggest a tendency for the population to be more focused on the informative elements of the PSAs for the Ineffective ones. A possible explanation of such results is pointing at a poor delivery of the message, since the more an area of interest (AOI) is attended, the more the processing is made in order to grasp the information contained in it [84]. As a matter of fact, in the Ineffective PSAs, the antismoking message appears to be less clear, or to be hidden in a cluttered image, or poorly related to the issue.

The proposed study highlights also a different perception between the male and the female group in the population analysed: the female group attends more the informative parts of the selected PSAs, regardless of its kind. The presented stimuli put the sample population in front of a real and common problem: nicotine addiction and tobacco consumption, with related health and social problems. There is plenty of evidence in literature that suggest as males tend to avoid or deny health-related problems [89] or to have less tendency of seeking help [90], even for quit smoking [91], when compared to females. This could be reflected also in their fruition of communications concerning health problems such as in this case for antismoking PSAs. This observation leads to the necessity of creating a kind of PSA that do not detach the male population, but that encourage them to face the problem, against all kinds of perceived social stigma [92].

Concerning the Effort Index, results showed the highest value in the high smokers (HS) group during the observation

of PSA Effective images. Such result could be explained by the peculiar content and style of the images potentially requiring a higher frontal theta for gaining the antismoking information. Petty and colleagues' study [93] demonstrated that when people have opinions that do not fit with the receiving messages, they show a negative behaviour toward stimuli and they are not motivated to process the information. This could be occurred in with the case of nonsmoker participants during the observation of Effective PSAs. Their behaviour can be associated with a defence mechanism which strengthens nonsmokers' position regarding smoking [94]. These studies could explain the lowest Effort Index value obtained for NS group when compared to HS one ($p = 0.03$).

Concerning the two PSA kinds (Effective and Ineffective), results showed a statistically significant difference between Effective and Ineffective ($p < 0.05$). Specifically, the Effective PSAs selected for this paper, characterized by fear arousing appeal communication style, elicited higher cognitive processing of antismoking messages than the Ineffective ones, instead characterized by ironic and informative communication styles. These results are correlated with a previous study, which tested how the use of threatening and scary components in antitobacco messages increased mainly cognitive and emotional processes [95].

Concerning the EI, results showed a similar trend on the perception between PSA kind and Gender, where women showed a negative emotional involvement when exposed to Effective PSAs, while men showed a slightly positive emotional involvement. Statistical results highlighted a significant difference for Effective antismoking images between females and males ($p = 0.014$), according to literature, which highlighted a gender difference on the appreciation of TV advertisements [16], and how women are more influenced by advertisement that emphasize the health effects of smoking [96]. These researches showed that women seem generally influenced by antismoking PSAs, causing a more negative emotional involvement with respect to men. Furthermore, the lowest EI value for women reported in this study could be mainly explained by one of two Effective images, depicting a sick lady presenting the signs of a tracheotomy.

5. Conclusions

In summary, the results of the present study can respond to our hypothesis:

- (i) The Neuroelectrical and Emotional Indexes demonstrated the existence of a pattern on perception of PSA images, based on gender and smoking habit of the selected sample. The VA Index highlighted only the different trend between male and female groups regardless of PSA kind.
- (ii) All explained indexes showed a different reaction, in accordance with the style communication and the informative elements of campaigns, during the vision of antismoking campaigns.

Other studies are necessary to confirm the validity of the results of such study on a larger sample of population;

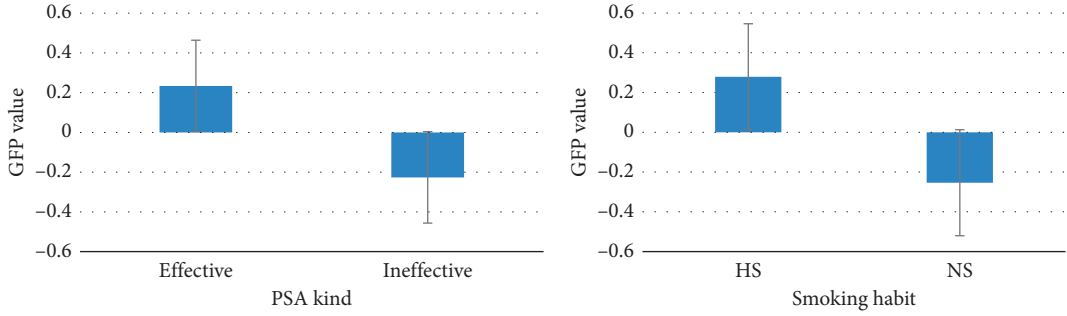


FIGURE 3: The graph represents the Effort Index value for the PSA kind images (Effective and Ineffective), on the left, and for Smoking Habit (Heavy Smokers (HS) and Nonsmokers (NS)), on the right ($n = 30$). All results plotted in the graphs are statistically significant with $p < 0.05$. Error bars represent standard error.

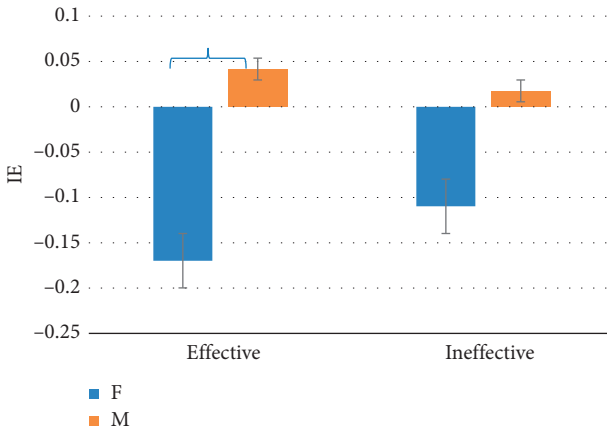


FIGURE 4: The graph represents the effect of the Gender (Female (F) and Male (M) on the EI values reported for both the PSAs selected (Effective and Ineffective) ($n = 30$). Brackets stand for a statistical significance equal to at least $p = 0.05$, or lower. Error bars represent standard error.

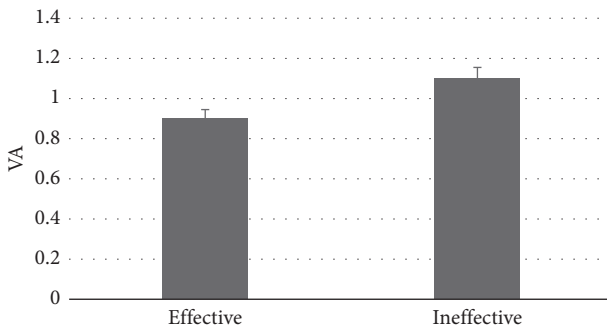


FIGURE 5: The graph represents the VA Index value for the PSA kind images ($n = 30$). All results plotted in the graphs are statistically significant with $p < 0.05$. Error bars represent standard error.

indeed, such results highlight the interest of the neurometric approach to the general issue of the PSA evaluation.

Furthermore, the obtained results have shown, through the estimation of the investigated indexes (i.e., Effort Index), the occurrence of a peculiar neural activation in the prefrontal cortex in response to antismoking advertising. There have been many studies which have demonstrated that the

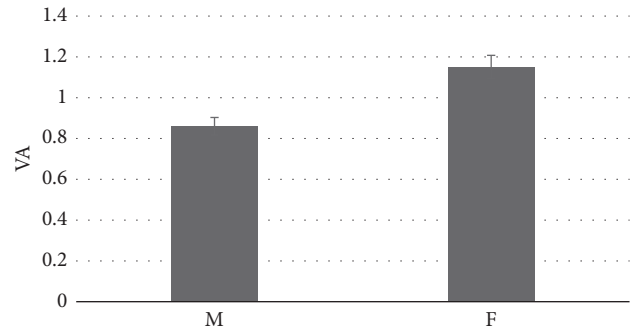


FIGURE 6: The graph represents the VA Index value for the “Gender” variable ($n = 30$). All results plotted in the graphs are statistically significant with $p < 0.05$. Error bars represent standard error.

average neural activity in the medial prefrontal cortex (MPFC) during messaging has been associated with future healthier behaviour change in individuals (e.g., for smoking reduction [97], physical activity [98]), as well as population measures of antismoking campaigns effectiveness (e.g., online click-through-rates [99] and calls to quit lines [100]). Given the multiple psychological functions supported by MPFC [101], examining the functional connectivity, specifically within the brain’s value system can provide additional information about why and how certain types of messages, like graphic warning messages, exert their effects. The meaning of the activity in a particular region changes depending on its interactions with other key regions [102], and examining the coherence of activity between brain regions during the exposure to different types of messages could provide new, complementary information about brain function [103]. In line with the importance of considering MPFC, Cooper and colleagues [104] found that the functional connectivity within investigated region during the exposure to health messages is linked to behaviour change.

Eye-tracking results highlighted a different perception during the vision of antismoking PSAs; therefore, it could be interesting to evaluate how this perception is mostly guided by the saliency or by the semantic content of the images. In fact, it is possible to evaluate the saliency of a picture, by applying one of the several methods developed during the last twenty years (for a review, see [105]). Through these

methods, it is indeed possible to obtain a description of the intrinsic low-level features (such as colour, shape, and direction) of the picture itself that lead to a bottom-up perception in the observer. By putting together eye-tracking data and saliency data could be therefore possible to understand if the perception is guided by the saliency of the picture, or alternatively by the semantic content of the objects depicted in the image itself.

Data Availability

The data relative to the study could be obtained by sending an e-mail to fabio.babiloni@uniroma1.it. Professor Babiloni will return directly the excel file related to the data gathered by the study.

Conflicts of Interest

The authors declare that there are no conflicts of interest regarding the publication of this paper.

Authors' Contributions

Enrica Modica, Dario Rossi, and Giulia Cartocci contributed equally to this article.

Acknowledgments

The present work was funded by the European Commission by Horizon2020 project HCO-06-2015, "SmokeFreeBrain," Grant no. 681120.

References

- [1] M. Siegel, "Mass media antismoking campaigns: a powerful tool for health promotion," *Annals of Internal Medicine*, vol. 129, no. 2, pp. 128–132, 1998.
- [2] M. C. Farrelly, C. G. Heaton, K. C. Davis, P. Messeri, J. C. Hersey, and M. Lyndon Haviland, "Getting to the truth: evaluating national tobacco countermarketing campaigns," *American Journal of Public Health*, vol. 92, no. 6, pp. 901–907, 2002.
- [3] J. Grandpre, E. M. Alvaro, M. Burgoon, C. H. Miller, and J. R. Hall, "Adolescent reactance and anti-smoking campaigns: a theoretical approach," *Health Communication*, vol. 15, no. 3, pp. 349–366, 2003.
- [4] M. Fishbein and J. N. Cappella, "The role of theory in developing effective health communications," *Journal of Communication*, vol. 56, no. 1, pp. S1–S17, 2006.
- [5] L. Biener, "Adult and youth response to the Massachusetts anti-tobacco television campaign," *Journal of Public Health Management and Practice*, vol. 6, no. 3, pp. 40–44, 2000.
- [6] L. K. Goldman and S. A. Glantz, "Evaluation of antismoking advertising campaigns," *Jama*, vol. 279, no. 10, pp. 772–777, 1998.
- [7] Y. Terry-Mcelrath, M. Wakefield, E. Ruel et al., "The effect of antismoking advertisement executional characteristics on youth comprehension, appraisal, recall, and engagement," *Journal of health communication*, vol. 10, no. 2, pp. 127–143, 2005.
- [8] C. Pechmann and S. J. Knight, "An experimental investigation of the joint effects of advertising and peers on adolescents' beliefs and intentions about cigarette consumption," *Journal of Consumer Research*, vol. 29, no. 1, pp. 5–19, 2002.
- [9] D. J. O'Keefe, "Message properties, mediating states, and manipulation checks: claims, evidence, and data analysis in experimental persuasive message effects research," *Communication Theory*, vol. 13, no. 3, pp. 251–274, 2003.
- [10] A. Lang, "The limited capacity model of mediated message processing," *Journal of communication*, vol. 50, no. 1, pp. 46–70, 2000.
- [11] W. J. McGuire, R. E. Rice, and C. K. Atkin, "Input and output variables currently promising for constructing persuasive communications," in *Public Communication Campaigns*, Sage, Thousand Oaks, CA, USA, vol. 3, pp. 22–48, 2001.
- [12] M. Stephenson and P. Palmgreen, "Sensation seeking, perceived message sensation value, personal involvement, and processing of anti-marijuana PSAs," *Communication Monographs*, vol. 68, no. 1, pp. 49–71, 2001.
- [13] M. Bala, L. Strzeszynski, and K. Cahill, "Mass media interventions for smoking cessation in adults," *Cochrane Database of Systematic Reviews*, vol. 1, 2008.
- [14] M. P. Brinn, K. V. Carson, A. J. Esterman, A. B. Chang, and B. J. Smith, "Cochrane Review: mass media interventions for preventing smoking in young people," *Evidence-Based Child Health: A Cochrane Review Journal*, vol. 7, no. 1, pp. 86–144, 2012.
- [15] G. Vecchiato, A. G. Maglione, P. Cherubino et al., "Neurophysiological tools to investigate consumer's gender differences during the observation of TV commercials," *Computational and Mathematical Methods in Medicine*, vol. 2014, Article ID 912981, 12 pages, 2014.
- [16] G. Cartocci, P. Cherubino, D. Rossi et al., "Gender and age related effects while watching TV advertisements: an EEG study," *Computational Intelligence and Neuroscience*, vol. 2016, Article ID 3795325, 10 pages, 2016.
- [17] S.-P. Han and S. Shavitt, "Persuasion and culture: advertising appeals in individualistic and collectivistic societies," *Journal of Experimental social Psychology*, vol. 30, no. 4, pp. 326–350, 1994.
- [18] G. Vecchiato, L. Astolfi, F. De Vico Fallani et al., "On the use of EEG or MEG brain imaging tools in neuromarketing research," *Computational Intelligence and Neuroscience*, vol. 2011, p. 3, 2011.
- [19] P. Cherubino, A. Trettel, G. Cartocci et al., "Neuroelectrical indexes for the study of the efficacy of TV advertising stimuli," in *Proceedings of the 2015 Computational Methods in Experimental Economics (CMEE) Conference: Selected Issues in Experimental Economics*, Springer, Switzerland, April 2016, pp. 355–371.
- [20] G. Vecchiato, L. Astolfi, and F. De Vico Fallani, "Changes in brain activity during the observation of TV commercials by using EEG, GSR and HR measurements," *Brain Topography*, vol. 23, no. 2, pp. 165–179, 2010.
- [21] G. Vecchiato, J. Toppi, and L. Astolfi, "Spectral EEG frontal asymmetries correlate with the experienced pleasantness of TV commercial advertisements," *Medical & Biological Engineering & Computing*, vol. 49, no. 5, pp. 579–583, 2011.
- [22] M. P. Paulus and L. R. Frank, "Ventromedial prefrontal cortex activation is critical for preference judgments," *NeuroReport*, vol. 14, no. 10, pp. 1311–1315, 2003.
- [23] M. Reimann, O. Schilke, B. Weber, C. Neuhaus, and J. Zaichkowsky, "Functional magnetic resonance imaging in consumer research: a review and application," *Psychology & Marketing*, vol. 28, no. 6, pp. 608–637, 2011.

- [24] P. Cherubino, "Marketing Meets Neuroscience: useful Insights for Gender Subgroups During the Observation of TV Ads," in *Applying Neuroscience to Business Practice*, IGI Global, Hershey, PA, USA, p. 163.
- [25] B. Knutson, S. Rick, G. Elliott Wimmer, D. Prelec, and G. Loewenstein, "Neural predictors of purchases," *Neuron*, vol. 53, no. 1, pp. 147–156, 2007.
- [26] D. Baldo, H. Parikh, Y. Piu, and K.-M. Müller, "Brain waves predict success of new fashion products: a practical application for the footwear retailing industry," *Journal of Creating Value*, vol. 1, no. 1, pp. 61–71, 2015.
- [27] Z. Wei, C. Wu, X. Wang, A. Supratak, P. Wang, and Y. Guo, "Using support vector machine on EEG for advertisement impact assessment," *Frontiers in Neuroscience*, vol. 12, p. 76, 2018.
- [28] A. P. Anokhin, A. B. Vedeniapin, E. J. Sirevaag et al., "The P300 brain potential is reduced in smokers," *Psychopharmacology*, vol. 149, no. 4, pp. 409–413, 2000.
- [29] F. Guney, B. O. Genc, R. Kutlu, and B. C. Ilhan, "Auditory P300 event-related potential in tobacco smokers," *Journal of Clinical Neuroscience*, vol. 16, no. 10, pp. 1311–1315, 2009.
- [30] C. A. Warren and B. E. McDonough, "Event-related brain potentials as indicators of smoking cue-reactivity," *Clinical Neurophysiology*, vol. 110, no. 9, pp. 1570–1584, 1999.
- [31] B. Baldaro, M. Mazzetti, M. Codispoti, G. TuoZZI, R. Bolzani, and G. Trombini, "Autonomic reactivity during viewing of an unpleasant film," *Perceptual and Motor Skills*, vol. 93, no. 3, pp. 797–805, 2001.
- [32] I. B. Mauss and M. D. Robinson, "Measures of emotion: a review," *Cognition and Emotion*, vol. 23, no. 2, pp. 209–237, 2009.
- [33] G. Cartocci, E. Modica, D. Rossi et al., "A pilot study on the neurometric evaluation of "effective" and "ineffective" antismoking public service announcements," in *Proceedings of IEEE 38th Annual International Conference of the Engineering in Medicine and Biology Society (EMBC)*, pp. 4597–4600, IEEE, Orlando, FL, USA, August 2016.
- [34] E. Bigsby, J. N. Cappella, and H. H. Seits, "Efficiently and effectively evaluating public service announcements: additional evidence for the utility of perceived effectiveness," *Communication Monographs*, vol. 80, no. 1, pp. 1–23, 2013.
- [35] L. Shen, "The effect of message frame in anti-smoking public service announcements on cognitive response and attitude toward smoking," *Health Communication*, vol. 25, no. 1, pp. 11–21, 2010.
- [36] J. D. Niederdeppe, "Syntactic indeterminacy, perceived message sensation value-enhancing features, and message processing in the context of anti-tobacco advertisements," *Communication Monographs*, vol. 72, pp. 324–344, 2005.
- [37] R. J. Davidson, "Anxiety and affective style: role of prefrontal cortex and amygdala," *Biological Psychiatry*, vol. 51, no. 1, pp. 68–80, 2002.
- [38] W. Klimesch, "EEG alpha and theta oscillations reflect cognitive and memory performance: a review and analysis," *Brain Research Reviews*, vol. 29, no. 2–3, pp. 169–195, 1999.
- [39] E. Wascher, B. Rasch, J. Sänger et al., "Frontal theta activity reflects distinct aspects of mental fatigue," *Biological Psychology*, vol. 96, pp. 57–65, 2014.
- [40] G. Cartocci, A. G. Maglione, E. Modica et al., "The "NeuroDante Project": neurometric measurements of participant's reaction to literary auditory stimuli from Dante's "Divina Commedia"," in *Proceedings of International Workshop on Symbiotic Interaction*, Springer, Padua, Italy, September 2016.
- [41] P. Aricò, G. Borghini, I. Graziani et al., "Towards a multimodal bioelectrical framework for the online mental workload evaluation," in *Proceedings of 36th Annual International Conference of the IEEE Engineering in Medicine and Biology Society (EMBC)*, IEEE, Chicago, IL, USA, August 2014.
- [42] G. Borghini, P. Aricò, L. Astolfi et al., "Frontal EEG theta changes assess the training improvements of novices in flight simulation tasks," in *Proceedings of 35th Annual International Conference of the IEEE Engineering in Medicine and Biology Society (EMBC)*, IEEE, Osaka, Japan, July 2013.
- [43] G. Borghini, P. Aricò, G. Di Flumeri et al., "Measuring neurophysiological signals in aircraft pilots and car drivers for the assessment of mental workload, fatigue and drowsiness," *Neuroscience & Biobehavioral Reviews*, vol. 44, pp. 58–75, 2014.
- [44] G. Borghini, P. Aricò, G. Di Flumeri et al., "EEG-based cognitive control behaviour assessment: an ecological study with professional air traffic controllers," *Scientific Reports*, vol. 7, no. 1, p. 547, 2017.
- [45] G. Di Flumeri, G. Borghini, P. Aricò et al., "On the use of cognitive neurometric indexes in aeronautic and air traffic management environments," in *Proceedings of International Workshop on Symbiotic Interaction*, Berlin, Germany, October 2015.
- [46] N. Sciaraffa, G. Borghini, P. Aricò et al., "Brain interaction during cooperation: evaluating local properties of multiple-brain network," *Brain Sciences*, vol. 7, no. 12, p. 90, 2017.
- [47] A. Maglione, G. Borghini, P. Aricò et al., "Evaluation of the workload and drowsiness during car driving by using high resolution EEG activity and neurophysiologic indices," in *Proceedings of the 36th Annual International Conference of the IEEE Engineering in Medicine and Biology Society*, pp. 6238–6241, Chicago, IL, USA, August 2014.
- [48] G. Borghini, P. Aricò, G. Di Flumeri et al., "Avionic technology testing by using a cognitive neurometric index: a study with professional helicopter pilots," in *Proceedings of the 37th Annual International Conference of the IEEE Engineering in Medicine and Biology Society (EMBC)*, Milano, Italy, August 2015.
- [49] M. G. Wisniewski, E. R. Thompson, N. Iyer, J. R. Estep, M. N. Goder-Reiser, and S. C. Sullivan, "Frontal midline θ power as an index of listening effort," *Neuroreport*, vol. 26, no. 2, pp. 94–99, 2015.
- [50] M. G. Wisniewski, E. R. Thompson, and N. Iyer, "Theta-and alpha-power enhancements in the electroencephalogram as an auditory delayed match-to-sample task becomes impossibly difficult," *Psychophysiology*, vol. 54, no. 12, pp. 1916–1928, 2017.
- [51] G. Cartocci, A. G. Maglione, G. Vecchiato et al., "Mental workload estimations in unilateral deafened children," in *Proceeding of 37th Annual International Conference of the IEEE Engineering in Medicine and Biology Society (EMBC)*, IEEE, Milano, Italy, August 2015.
- [52] A. Gevins and M. E. Smith, "Neurophysiological measures of cognitive workload during human-computer interaction," *Theoretical Issues in Ergonomics Science*, vol. 4, no. 1–2, pp. 113–131, 2003.
- [53] J. Kato, H. Ide, I. Kabashima, H. Kadota, K. Takano, and K. Kansaku, "Neural correlates of attitude change following positive and negative advertisements," *Frontiers in Behavioural Neuroscience*, vol. 3, p. 6, 2009.
- [54] A. H. Eagly and C. Shelly, *The Psychology of Attitudes*, Harcourt Brace Jovanovich College Publishers, San Diego, CA, USA, 1993.

- [55] R. E. Petty, D. DeSteno, and D. D. Rucker, "The role of affect in attitude change," in *Handbook of Affect and Social Cognition*, pp. 212–233, Psychology Press, Hove, UK, 2001.
- [56] J. P. Forgas, *Handbook of Affect and Social Cognition*, Psychology Press, Hove, UK, 2012.
- [57] J. Posner, J. A. Russell, and B. S. Peterson, "The circumplex model of affect: an integrative approach to affective neuroscience, cognitive development, and psychopathology," *Development and Psychopathology*, vol. 17, no. 3, pp. 715–734, 2005.
- [58] S. Hamann, "Mapping discrete and dimensional emotions onto the brain: controversies and consensus," *Trends in Cognitive Sciences*, vol. 16, no. 9, pp. 458–466, 2012.
- [59] H. D. Critchley, "Electrodermal responses: what happens in the brain," *The Neuroscientist*, vol. 8, no. 2, pp. 132–142, 2002.
- [60] M. M. Bradley and P. J. Lang, "Measuring emotion: behavior, feeling, and physiology," in *Cognitive Neuroscience of Emotion*, vol. 25, pp. 49–59, Oxford University Press, Oxford, UK, 2000.
- [61] M. M. Bradley, M. Codispoti, B. N. Cuthbert, and P. J. Lang, "Emotion and motivation I: defensive and appetitive reactions in picture processing," *Emotion*, vol. 1, no. 3, p. 276, 2001.
- [62] T. W. Frazier, M. E. Strauss, and S. R. Steinhauer, "Respiratory sinus arrhythmia as an index of emotional response in young adults," *Psychophysiology*, vol. 41, no. 1, pp. 75–83, 2004.
- [63] P. Gomez, P. Zimmermann, S. Guttormsen-Schär, and B. Danuser, "Respiratory responses associated with affective processing of film stimuli," *Biological Psychology*, vol. 68, no. 3, pp. 223–235, 2005.
- [64] Peter J. Lang, M. K. Greenwald, M. M. Bradley, and A. O. Hamm, "Looking at pictures: affective, facial, visceral, and behavioral reactions," *Psychophysiology*, vol. 30, no. 3, pp. 261–273, 1993.
- [65] J. A. Russell and L. F. Barrett, "Core affect, prototypical emotional episodes, and other things called emotion: dissecting the elephant," *Journal of Personality and Social Psychology*, vol. 76, no. 5, p. 805, 1999.
- [66] G. Vecchiato, P. Cherubino, A. G. Maglione et al., "How to measure cerebral correlates of emotions in marketing relevant tasks," *Cognitive Computation*, vol. 6, no. 4, pp. 856–871, 2014.
- [67] L. Astolfi, F. De Vico Fallani, F. Cincotti et al., "Neural basis for brain responses to TV commercials: a high-resolution EEG study," *IEEE Transactions on Neural Systems and Rehabilitation Engineering*, vol. 16, no. 6, pp. 522–531, 2008.
- [68] G. Vecchiato, A. G. Maglione, P. Cherubino et al., *Neuroelectrical Brain Imaging Tools for the Study of the Efficacy of TV Advertising Stimuli and their Application to Neuromarketing*, Springer, Heidelberg, Germany, 2013.
- [69] G. Vecchiato, A. G. Maglione, P. Cherubino et al., "Marketing and neuroscience: how electroencephalographic tools could help to design and analyze commercial advertising campaigns," *Micro & Macro Marketing*, vol. 23, no. 2, pp. 279–294, 2014.
- [70] R. O. J. Dos Santos, J. H. C. de Oliveira, J. B. Rocha, and J. M. E. Giraldi, "Eye tracking in neuromarketing: a research agenda for marketing studies," *International Journal of Psychological Studies*, vol. 7, no. 1, p. 32, 2015.
- [71] M. I. Posner, "Orienting of attention," *Quarterly Journal of Experimental Psychology*, vol. 32, no. 1, pp. 3–25, 1980.
- [72] J. S. Baschnagel, "Using mobile eye-tracking to assess attention to smoking cues in a naturalized environment," *Addictive Behaviors*, vol. 38, no. 12, pp. 2837–2840, 2013.
- [73] O. M. Maynard, M. R. Munafò, and U. Leonards, "Visual attention to health warnings on plain tobacco packaging in adolescent smokers and non-smokers," *Addiction*, vol. 108, no. 2, pp. 413–419, 2013.
- [74] A. A. Strasser, K. Z. Tang, D. Romer, C. Jepson, and J. N. Cappella, "Graphic warning labels in cigarette advertisements: recall and viewing patterns," *American Journal of Preventive Medicine*, vol. 43, no. 1, pp. 41–47, 2012.
- [75] P. J. Lang, M. M. Bradley, and B. N. Cuthbert, "International affective picture system (IAPS): affective ratings of pictures and instruction manual," Tech. Rep., NIMH, Center for the Study of Emotion & Attention, Bethesda, MD, USA, 2005.
- [76] J. Varcoe, "Assessing the effectiveness of social marketing," in *Proceedings of ESOMAR Public Sector Research Conference*, Berlin, Germany, May 2004.
- [77] J. Coffman, *Public Communication Campaign Evaluation*, Communications Consortium Media Center, Washington, DC, USA, 2002.
- [78] A. Belouchrani, K. Abed-Meraim, J.-F. Cardoso, and E. Moulines, "A blind source separation technique using second-order statistics," *IEEE Transactions on Signal Processing*, vol. 45, no. 2, pp. 434–444, 1997.
- [79] D. Lehmann and C. M. Michel, "Intracerebral dipole source localization for FFT power maps," *Electroencephalography and Clinical Neurophysiology*, vol. 76, no. 3, pp. 271–276, 1990.
- [80] W. T. Roth, M. E. Dawson, and D. L. Filion, "Publication recommendations for electrodermal measurements," *Psychophysiology*, vol. 49, no. 8, pp. 1017–1034, 2012.
- [81] M. Benedek and C. Kaernbach, "A continuous measure of phasic electrodermal activity," *Journal of Neuroscience Methods*, vol. 190, no. 1, pp. 80–91, 2010.
- [82] J. Pan and W. J. Tompkins, "A real-time QRS detection algorithm," *IEEE Transactions on Biomedical Engineering*, vol. BME-32, no. 3, pp. 230–236, 1985.
- [83] D. D. Salvucci and J. H. Goldberg, "Identifying fixations and saccades in eye-tracking protocols," in *Proceedings of the Eye Tracking Research & Application Symposium, ETRA 2000*, ACM, Palm Beach Gardens, FL, USA, November 2000.
- [84] K. Rayner, "Eye movements and attention in reading, scene perception, and visual search," *The Quarterly Journal of Experimental Psychology*, vol. 62, no. 8, pp. 1457–1506, 2009.
- [85] D. Rossi, A. G. Maglione, E. Modica et al., "An eye tracking index for the salience estimation in visual stimuli," in *Proceedings of 39th Annual International Conference of the IEEE Engineering in Medicine and Biology Society (EMBC)*, IEEE, Jeju Island, South Korea, July 2017.
- [86] A. O. Peschel and J. L. Orquin, "A review of the findings and theories on surface size effects on visual attention," *Frontiers in Psychology*, vol. 4, p. 902, 2013.
- [87] J. Zar, *Biostatistical Analysis*, Prentice Hall, New York, NY, USA, 2000.
- [88] G. Cartocci, M. Caratù, E. Modica et al., "Electroencephalographic, heart rate, and galvanic skin response assessment for an advertising perception study: application to anti-smoking public service announcements," *Journal of Visualized Experiments*, vol. 126, 2017.
- [89] P. M. Galdas, F. Cheater, and P. Marshall, "Men and health help-seeking behaviour: literature review," *Journal of Advanced Nursing*, vol. 49, no. 6, pp. 616–623, 2005.

- [90] M. E. Addis and J. R. Mahalik, "Men, masculinity, and the contexts of help seeking," *American Psychologist*, vol. 58, no. 1, pp. 5–14, 2003.
- [91] S.-H. Zhu, B. Rosbrook, C. Anderson, E. Gilpin, G. Sadler, and J. P. Pierce, "The demographics of help-seeking for smoking cessation in California and the role of the California Smokers' Helpline," *Tobacco Control*, vol. 4, no. 1, pp. S9–S15, 1995.
- [92] D. L. Vogel, N. G. Wade, and A. H. Hackler, "Perceived public stigma and the willingness to seek counseling: the mediating roles of self-stigma and attitudes toward counseling," *Journal of Counseling Psychology*, vol. 54, no. 1, p. 40, 2007.
- [93] R. E. Petty, J. T. Cacioppo, and R. Goldman, "Personal involvement as a determinant of argument-based persuasion," *Journal of Personality and Social Psychology*, vol. 41, no. 5, p. 847, 1981.
- [94] J. Lydon, M. P. Zanna, and M. Ross, "Bolstering attitudes by autobiographical recall: attitude persistence and selective memory," *Personality and Social Psychology Bulletin*, vol. 14, no. 1, pp. 78–86, 1988.
- [95] G. Leshner, F. Vultee, P. D. Bolls, and J. Moore, "When a fear appeal isn't just a fear appeal: the effects of graphic antitobacco messages," *Journal of Broadcasting & Electronic Media*, vol. 54, no. 3, pp. 485–507, 2010.
- [96] E. Yom-Tov, P. Muennig, and A. M. El-Sayed, "Web-based antismoking advertising to promote smoking cessation: a randomized controlled trial," *Journal of Medical Internet Research*, vol. 18, no. 11, p. e306, 2016.
- [97] M. Owens, J. MacKillop, J. C. Gray, B. E. Hawkshead, C. M. Murphy, and L. H. Sweet, "Neural correlates of graphic cigarette warning labels predict smoking cessation relapse," *Psychiatry Research: Neuroimaging*, vol. 262, pp. 63–70, 2017.
- [98] E. Falk, M. B. O'Donnell, C. N. Cascio et al., "Self-affirmation alters the brain's response to health messages and subsequent behavior change," *Proceedings of the National Academy of Sciences of the United States of America*, vol. 112, no. 7, pp. 1977–1982, 2015.
- [99] E. Falk, M. B. O'Donnell, S. Tompson et al., "Functional brain imaging predicts public health campaign success," *Social Cognitive and Affective Neuroscience*, vol. 11, no. 2, pp. 204–214, 2016.
- [100] E. B. Falk, E. T. Berkman, and M. D. Lieberman, "From neural responses to population behavior: neural focus group predicts population-level media effects," *Psychological Science*, vol. 23, no. 5, pp. 439–445, 2012.
- [101] A. De la Vega, L. J. Chang, M. T. Banich, T. D. Wager, and T. Yarkoni, "Large-scale meta-analysis of human medial frontal cortex reveals tripartite functional organization," *The Journal of Neuroscience*, vol. 36, no. 24, pp. 6553–6562, 2016.
- [102] J. M. Shine, P. G. Bissett, P. T. Bell et al., "The dynamics of functional brain networks: integrated network states during cognitive task performance," *Neuron*, vol. 92, no. 2, pp. 544–554, 2016.
- [103] J. D. Medaglia, M.-E. Lynall, and D. S. Bassett, "Cognitive network neuroscience," *Journal of Cognitive Neuroscience*, vol. 27, no. 8, pp. 1471–1491, 2015.
- [104] N. Cooper, D. S. Bassett, and E. B. Falk, "Coherent activity between brain regions that code for value is linked to the malleability of human behavior," *Scientific Reports*, vol. 7, no. 1, p. 43250, 2017.
- [105] A. Borji and L. Itti, "State-of-the-art in visual attention modeling," *IEEE Transactions on Pattern Analysis and Machine Intelligence*, vol. 35, no. 1, pp. 185–207, 2013.

Research Article

Decoding Motor Imagery through Common Spatial Pattern Filters at the EEG Source Space

Ioannis Xygonakis ,^{1,2} Alkinoos Athanasiou ,¹ Niki Pandria ,¹
Dimitris Kugiumtzis ,² and Panagiotis D. Bamidis ¹

¹Biomedical Electronics Robotics and Devices (BERD) Group, Lab of Medical Physics, School of Medicine,
Faculty of Health Sciences, Aristotle University of Thessaloniki (AUTH), 54124 Thessaloniki, Greece

²Department of Electrical and Computer Engineering, Faculty of Engineering, Aristotle University of Thessaloniki (AUTH),
54124 Thessaloniki, Greece

Correspondence should be addressed to Panagiotis D. Bamidis; pdbamidis@gmail.com

Received 9 March 2018; Revised 30 May 2018; Accepted 10 June 2018; Published 1 August 2018

Academic Editor: Victor Hugo C. de Albuquerque

Copyright © 2018 Ioannis Xygonakis et al. This is an open access article distributed under the Creative Commons Attribution License, which permits unrestricted use, distribution, and reproduction in any medium, provided the original work is properly cited.

Brain-Computer Interface (BCI) is a rapidly developing technology that aims to support individuals suffering from various disabilities and, ultimately, improve everyday quality of life. Sensorimotor rhythm-based BCIs have demonstrated remarkable results in controlling virtual or physical external devices but they still face a number of challenges and limitations. Main challenges include multiple degrees-of-freedom control, accuracy, and robustness. In this work, we develop a multiclass BCI decoding algorithm that uses electroencephalography (EEG) source imaging, a technique that maps scalp potentials to cortical activations, to compensate for low spatial resolution of EEG. Spatial features were extracted using Common Spatial Pattern (CSP) filters in the cortical source space from a number of selected Regions of Interest (ROIs). Classification was performed through an ensemble model, based on individual ROI classification models. The evaluation was performed on the BCI Competition IV dataset 2a, which features 4 motor imagery classes from 9 participants. Our results revealed a mean accuracy increase of 5.6% with respect to the conventional application method of CSP on sensors. Neuroanatomical constraints and prior neurophysiological knowledge play an important role in developing source space-based BCI algorithms. Feature selection and classifier characteristics of our implementation will be explored to raise performance to current state-of-the-art.

1. Introduction

Brain-Computer Interface (BCI) is emerging as a promising rehabilitation technology, that aims to establish a connection between brain activity and external devices. Recent advances in invasive BCIs have demonstrated the feasibility of performing complex motor tasks using brain signals by people with disability such as severe spinal cord injury and quadriplegia [1]. As invasive BCIs use intracranial electrodes to measure electrical activity of the cerebral cortex, either implanted or directly lying on the cortical surface such as electrocorticography (ECoG), their usage is limited due to ethical, medical, and physiological issues [2]. These limitations are not present with noninvasive BCIs, and the most

widely used noninvasive modality, electroencephalography (EEG), uses electrodes over the scalp to measure inferred cerebral cortical activity.

A variety of brain signal types and features have been used to decode user intent in noninvasive EEG-based BCIs, such as visual evoked potential (VEP), P300 response, slow cortical potentials (SCP), and sensorimotor rhythm (SMR), to name but a few [3]. SMR or mu (μ) rhythm, typically measured at the alpha band of 8–13 Hz over the scalp area overlying the sensorimotor cortex, can be modulated during motor execution or motor imagery (MI) tasks, and the BCIs decoding this type of signal are referred to as SMR-BCIs. Motor imagery displays similar patterns of brain activation and communication to motor execution [4, 5] while research

and development in the domain of SMR-BCIs has brought some remarkable applications ranging from the accurate control of a cursor in 2-D space [6], control of a quad-copter in 3D space [7], control a robotic arm for reach and grasp tasks [8], and control of a wheelchair [9] proving the potential of this technology.

Nonetheless, noninvasive BCIs also feature a number of limitations with regards to reliability, speed, and accuracy and have many challenges to overcome to meet both research and casual everyday use needs. Key features for the success of SMR-BCIs involve the classification accuracy, performance robustness, and asynchronous and intuitive control that requires the decoding of multiple motor imagery tasks. Control of an external complex device with multiple degrees of freedom, such as a robotic arm or an artificial limb, can be better achieved by utilizing motor imagery classes that are related to the intended end effector movement [10, 11], making control more intuitive and thus requiring less time for training.

Moreover, intrinsic drawbacks of EEG include low signal-to-noise ratio (SNR), low spatial resolution, and imprecise and indirect measuring of brain activity mainly attributed to the volume conduction effect. This effect describes the spread of the brain's electrical field while it is transmitted from the source space through the cerebrospinal fluid, skull, and scalp to reach the scalp surface where the electrodes lay, known as the sensor space [12]. To reduce the volume conduction effect and study the brain activity on the cortex, source imaging techniques are commonly used that map the scalp potentials measured by EEG sensors to cortical activations on the cortical mantle [13, 14]. Low SNR led the researches to search for spatial filters that extract the EEG components that reflect user intention. In this context, Common Spatial Pattern (CSP) method was proposed to extract spatial features of event related de/synchronization during motor imagery [15]. CSP filters are spatial filters designed to maximize the power difference on their outputs given different EEG classes [15]. CSP filters are considered as an effective way to discriminate classes and are one of the most popular feature extraction methods in the BCI field [16], which also have multiple extensions [17–20]. Remarkable classification results have already been reported by studies that implemented the CSP algorithm or its variants [21, 22].

In the current study, we describe the development of a BCI algorithm, aiming to decode multiple (4) MI tasks. In order to overcome the issues associated with low spatial resolution, we use source imaging and extract features in the cortical source space from selected Regions of Interest (ROIs), using Common Spatial Pattern filters. Finally, the classification is performed with an ensemble classification model that synergistically uses the classification models of selected ROIs, in order to increase classification accuracy.

2. Materials and Methods

2.1. BCI Competition Dataset. The BCI Competition IV 2a dataset was used to develop and test the BCI decoding algorithm. The dataset contains recordings from 9 healthy

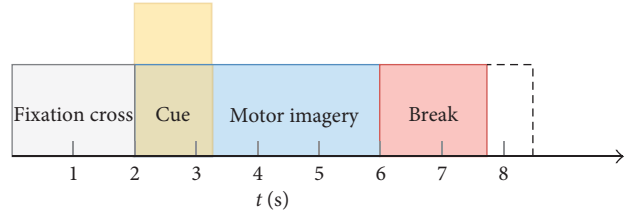


FIGURE 1: Diagram of a trial and timings during a session of the BCI Competition IV 2a dataset.

subjects that perform 4 motor imagery tasks, right arm, left arm, feet, and tongue [23]. The data of a subject consist of 2 sessions, one intended for training and the other for evaluation. Each session is comprised of 72 trials for each MI task, 288 trials in total, recorded with 22 EEG channels and 3 monopolar electrooculogram (EOG) channels (with left mastoid serving as reference). In our study, only data from the training session are used.

At the beginning of each trial ($t = 0$ s), a white cross on black background appeared, and after 2 s, an arrow oriented right, left up, or down informed the subject to perform the corresponding MI task (Figure 1). The arrow appeared for 1.25 s, and the subject was asked to keep on performing the MI task until the white cross disappeared ($t = 6$ s).

2.2. Signal Preprocessing. Signal analysis was performed solely on the EEG electrodes, and the EOG channels were excluded. Average reference was used, and the data were band-pass filtered at 7–15 Hz using a zero-phase FIR filter in order to capture the event related desynchronization and synchronization (ERD/ERS) activity [24]. Subsequently, data were down-sampled at 100 Hz and epoched for 500 msec after the visual cue with epoch duration of 3000 msec. Data were visually inspected for bad channels but none was excluded. All preprocessing was performed using a custom Fieldtrip script [25].

2.3. Inverse Problem Solution. EEG source imaging was deployed to mitigate low spatial resolution and low SNR caused by volume conduction. EEG source imaging maps sensor activity to brain neural current distribution at fixed positions over the cortex. The source activity is defined in terms of current dipoles, at a grid of vertices on the MNI cortical surface template, that model electrical activity of neuronal groups firing synchronously [26, 27]. The estimation of the sources from the EEG recordings constitutes the solution for the inverse problem, while the forward problem is described by the following equation (assuming zero noise) [27]:

$$M = GD, \quad (1)$$

where M is the $N_c \times T$ matrix of the EEG data, G is the lead-field matrix (also referred as gain matrix) that maps the source data to sensor data ($N_c \times N_d$), and D is the dipole current density ($N_d \times T$). N_d is the number of current dipoles, N_c is the number of EEG channels, and T is the number of measurements. Solving the forward problem

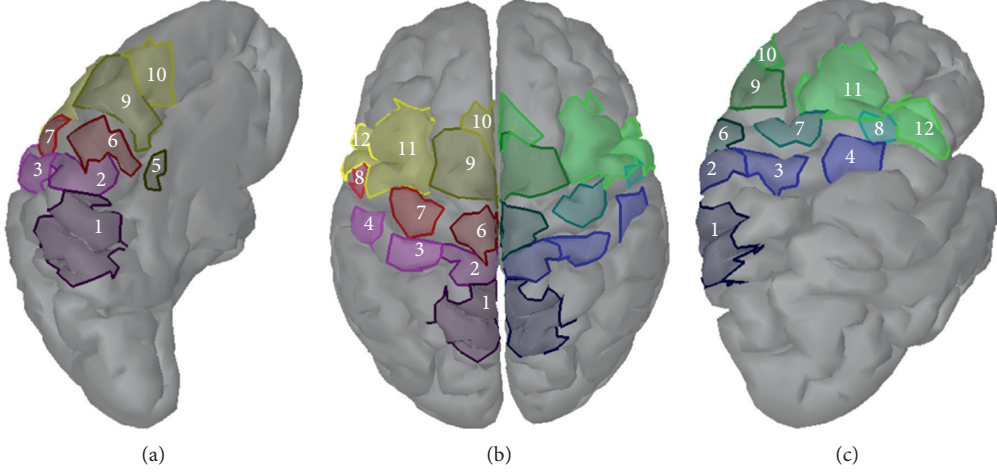


FIGURE 2: Regions of Interest (ROIs) at the cortical level: (a) midline surface, left hemisphere, (b) top view, both hemispheres, and (c) lateral view, right hemisphere. 1: SAC, 2: S1F, 3: S1H, 4: S2, 5: CMA, 6: M1F, 7: M1H, 8: M1L, 9: SMA, 10: pSMA, 11: PMd, 12: PMv [36].

consists of computing the lead-field matrix, referred to as head or forward model, that models how current flows from the sources through different head compartments (scalp, skull, and cortex) to the scalp surface.

The Montreal Neurological Institute (MNI) Colin 27 MRI generic template [28] was used as the default subject anatomy to compute a three-compartment (scalp, skull, and cortex) head model with symmetric boundary element method (BEM) using OpenMEG [29]. Default Brainstorm Colin 27 cortex was down-sampled using iso2mesh [30] to 5023 vertices, and the relative conductivity values of Scalp/Skull/Brain was assumed to be 1 : 1/15 : 1, with $\sigma_{\text{brain}} = \sigma_{\text{scalp}} = 0.33 \text{ S/m}$ and $\sigma_{\text{skull}} = 0.0042 \text{ S/m}$ [31]. All 5023 dipoles are assumed constrained to the cortical surface with an orientation perpendicular to the surface, based on the assumption that EEG primary signal sources are local groups of pyramidal neurons firing synchronously, located on the cortex and arranged perpendicular to its surface [26, 31].

Given the lead-field matrix, the inverse EEG problem consists of finding the dipole current density D in (1). This is a highly underdetermined problem since the number of dipoles (sources) is at the order of thousands and the number of EEG channels is at most at the order of hundreds, which in practice means that different current distributions (brain activity) can lead to exact EEG sensor values. Among different methods for solving the inverse problem, here it was solved with the weighted minimum norm estimate (wMNE) method using the Brainstorm toolbox [32–34]. Sensor noise covariance matrix, required for the computation of the solution, was calculated on the resting state period at the start of the session.

2.4. Regions of Interest. Cortical Regions of Interest (ROIs) were defined on the sensorimotor cortex to reduce the dimension of the source data derived from the inverse problem solution, having anatomical constraints and aiming at extracting valuable information related to MI tasks [11, 35]. 24 ROIs were defined based on neuroanatomical landmarks and Broadman areas and are depicted in Figure 2. Defined

ROIs include bilaterally presupplementary motor area (pSMA), supplementary motor area (SMA), cingulate motor area (CMA), dorsal premotor cortex (PMd) and ventral premotor cortex (Pmv), primary foot motor area (M1F), primary hand motor area (M1H) and primary lip motor area (M1L), primary foot somatosensory area (S1F), primary hand somatosensory area (S1H), secondary somatosensory area (S2), and somatosensory association cortex (SAC). During ROI analysis, source times-series that lay only on the defined ROIs on the mantle are analyzed, excluding from analysis all the other sources.

2.5. Feature Extraction. Feature extraction was performed at the source level, on ROIs data in particular. Common Spatial Pattern (CSP) filters are one of the most used feature extraction methods in BCI domain [16]. Assuming data of two classes, for example, the motor imagery of right and left, CSP algorithm calculates spatial filters that maximize the ratio of variance of data stemming from the two classes. Consequently, the extracted signals are optimally discriminating two different EEG classes while they are revealing spatial patterns of different classes [15, 17]. The spatially filtered signal S of an EEG trial is given by

$$S = WM, \quad (2)$$

where M is a $N_c \times T$ matrix representing the EEG measurement of data for the given trial and W is $L \times N_c$ matrix referred as CSP projection, whose rows are the spatial filters designed to output signals whose ratio of variances are maximally discriminating input data of two different classes.

Original CSP algorithm has been developed for two class problems, though there exist multiclass extensions [17, 37]. Since the classification problem of this work is multiclass, a multiclass extension of CSP was deployed using the One-vs-Rest scheme, with $L = 8$ filters, the last and the first eigenvectors of each class were selected [15]. CSP filters were calculated during training phase, on the mean covariance matrices of the data conditioned to the four classes.

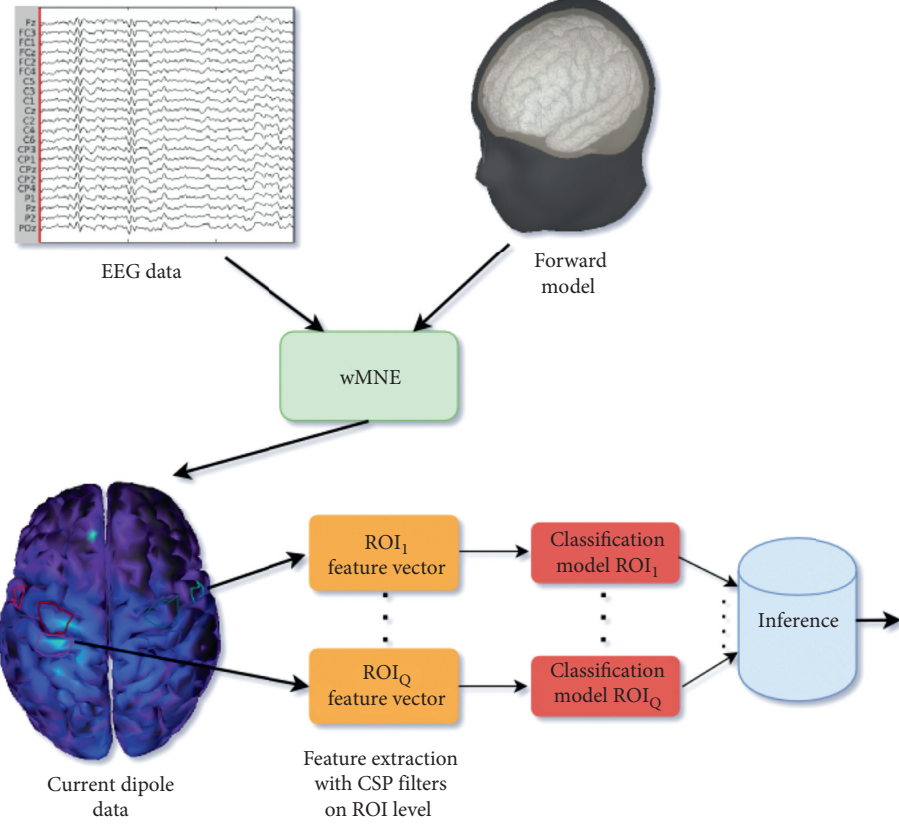


FIGURE 3: Outline of the implemented decoding algorithm. EEG sensor time series are transformed to current dipole time series. Data from the Regions of Interest (ROIs) are spatially filtered by ROI-CSP filters, to extract features to be classified by independent ROI classification models. Predicted class is the most voted class of the ROI classification models. On the classification model scheme, the predicted class is the outcome of an inference mechanism (majority vote). The inference mechanism takes as input the predicted class from the individual ROI classification models.

In this work, CSP filters were applied to the source data, and they were calculated on every ROI current dipole time-series. Assuming D_q the current dipole times-series of ROI_q, that resulted from the solution of the inverse problem (1), and W_q the CSP filter computed on the data of ROI_q, the output of the ROI-CSP filters is

$$Z = W_q D_q. \quad (3)$$

The feature vector of ROI_q, $v_{ROI_q} \in \mathbb{R}^L$ is extracted from CSP filters output, and each of its components, v_p , $p = 1, \dots, L$, is given as

$$v_p = \log\left(\frac{\text{var}(Z_p)}{\sum_{i=1}^L \text{var}(Z_i)}\right) \in \mathbb{R}, p \in [1, L], \quad (4)$$

where Z_p is the p row of the matrix Z , that is, the output signal of the p th CSP filter output. Repeating this procedure for each selected ROI results to Q feature vectors of $L = 8$ elements, where Q is the number of selected ROIs.

2.6. Classification. An ensemble classification model was used for the prediction of the MI task [38], illustrated in Figure 3. It is supported that an ensemble method using multiple independent classification models can increase the

classification performance [39, 40]. An independent classification model was built for each of the selected ROIs, and the final classification outcome was selected by an inference (fusion) mechanism. K -nearest neighbors (kNN), Naive Bayes, Decision Tree, and Linear Discriminant Analysis (LDA) classifier were tested with LDA having superior performance as it is demonstrated in the Results section. The ROI classification model was based on LDA, and the inference mechanism was the majority vote of the selected ROI classification models. The selected ROIs were the Q most accurate ROIs according to a selection procedure that is presented in the next section.

2.7. ROI Selection. The defined ROIs extend all over the motor cortex, while the cortical activity related to the performed motor imagery tasks is derived only from a subset of the defined ROIs. ROIs were selected based on their classification model accuracy. In order to select the most accurate ROIs, 10-fold cross-validation using the LDA classifier was performed on ROI level, and this was repeated 10 times to ensure more robust results (in every run, CSP filters are calculated on different data). The $Q = 8$ most accurate ROIs were selected. The number is based on parametric analysis results of the inference mechanism

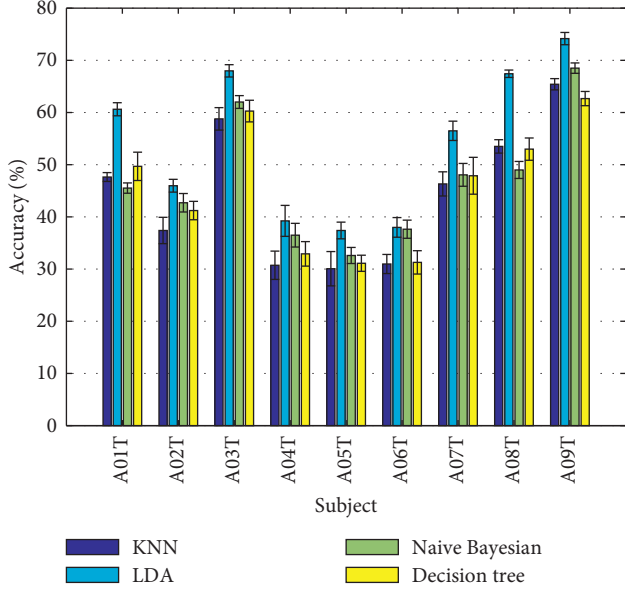


FIGURE 4: Classification accuracy of kNN, LDA, Naïve Bayesian, and Decision Tree classifiers across all subject data.

accuracy. Parametric analysis was run for different subjects, and the number of selected ROIs was set to $Q = 8$.

The performance of the classification scheme on the source space was further compared to the performance on the sensor space using the same setting (10-fold cross-validation of the LDA classification repeated 10 times). For the sensor space, the CSP filters are computed on the preprocessed EEG data. Moreover, to better assess the developed method, performance in terms of Cohen's kappa statistic, a useful metric for multiclass prediction problems, was compared to the winner of BCI Competition IV of dataset 2a [23, 33]. The winner of the competition deploys CSP on multiple frequency bands (FBCSP) as feature extraction method, Mutual Information-based Best Individual Feature (MIBIF) algorithm for feature selection, and Naïve Bayesian Parzen Window (NBPW) classifier [21, 41].

3. Results and Discussion

3.1. Classification Accuracy. Four different classifiers were tested to select the classifier to make the predictions. LDA, kNN, Naïve Bayesian, and Decision Tree were tested by performing 10-fold cross-validation, 10 times on all subjects. LDA had superior performance with the highest prediction accuracy among all subjects, with mean accuracy 54.1%. Naïve Bayesian was second with 46.9%, followed by Decision Tree and kNN with 45.5% and 44.5%, respectively (Figure 4).

The source method of classification achieved consistently higher accuracy rates across all subjects (43.7% to 74.5%), when compared to the sensor method (37.7% to 73.4%), as illustrated in Figure 5 and displayed in Table 1 below. Comparison of the developed method's performance to the winner of BCI Competition IV of dataset 2a in terms of Cohen's kappa statistic [42, 43] (multiclass prediction) is presented in Table 2.

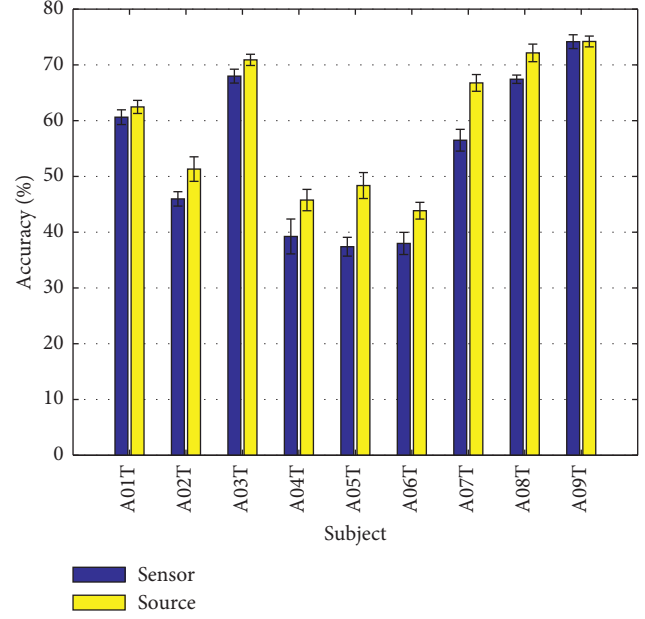


FIGURE 5: Classification accuracy of the developed source method and the equivalent traditional sensor approach, on the BCI Competition IV, 2a dataset.

Classification sensitivity and specificity, also referred to as true positive and true negative rate respectively, between the source and sensor method are demonstrated in Tables 3–6. Among the subjects, the source method has mean 11.1% higher true positive rate for the left arm, 5.2% higher for right arm, and 3.3% and 1.9% better rate for foot and tongue imagery, respectively. The mean differences of sensor to source true negative rate metric are low for all classes, −1.2%, 1.9%, 2.9%, and 3.6% for left, right arm, foot, and tongue imagery, respectively.

3.2. Selected ROIs. The ROI selection procedure was performed for all the subjects, exhibiting interesting inter-subject properties. As illustrated in Figure 6, the symmetrical left and right S1H, M1L, M1H, and CMA ROIs were the, $Q = 8$, most selected among all the subjects, with the left and right S1H, and left M1L, M1H, and CMA being selected for all 9 subjects. For the subjects A02T, A06T, A09T the pMd_R, SAC_L, and S2_R were selected instead of M1L_R, M1H_R, and CMA_R, respectively, with still 7 out of 8 selected ROIs being on the most frequent ones. Most frequently selected ROIs are illustrated on Figure 7 on the cortical mantle model.

3.3. Discussion. Noninvasive BCI systems emerge as a promising and safe solution for rehabilitation purposes in contrast with invasive BCIs that are associated to health risks and ethical issues [44], but their commercial use is still hindered by low performance and instability. Despite a number of already demonstrated SMR-BCI applications [8, 9, 45], noninvasive BCIs still suffer from low SNR. In our work, we investigate the use of source imaging and

TABLE 1: 10×10 -fold cross-validation performance in terms of mean classification accuracy (%) of the developed source method and the equivalent sensor method.

Subject	A01T	A02T	A03T	A04T	A05T	A06T	A07T	A08T	A09T	Mean
Sensor	61.0	45.8	68.2	39.4	38.0	37.7	56.3	67.3	73.4	54.1
Source	62.4	51.3	70.9	46.3	47.6	43.7	67.2	71.9	74.5	59.7

TABLE 2: 10×10 -fold cross-validation performance in terms of mean Cohen's kappa value, of the developed method in source and sensor level, and the method developed by the winner of BCI Competition IV, dataset 2a.

Subject	A01T	A02T	A03T	A04T	A05T	A06T	A07T	A08T	A09T	Mean
Sensor	0.48	0.27	0.57	0.19	0.17	0.17	0.42	0.56	0.64	0.39
Source	0.50	0.34	0.61	0.30	0.30	0.26	0.56	0.63	0.66	0.46
Winner FBCSP	0.76	0.47	0.83	0.48	0.60	0.34	0.86	0.80	0.78	0.65

TABLE 3: Sensor method classification sensitivity (true positive rate).

Sensitivity	Left (%)	Right (%)	Foot (%)	Tongue (%)
A01T	49.03	70.00	47.92	75.56
A02T	38.75	41.11	61.81	42.22
A03T	80.14	80.83	50.14	60.83
A04T	34.86	37.64	37.92	46.53
A05T	43.33	48.33	25.83	32.08
A06T	35.42	38.33	50.56	27.64
A07T	68.61	57.08	44.03	56.25
A08T	73.47	61.67	65.28	69.31
A09T	81.67	68.89	67.64	78.47
Mean	56.14	55.99	50.12	54.32

TABLE 5: Source method classification sensitivity (true positive rate).

Sensitivity	Left (%)	Right (%)	Foot (%)	Tongue (%)
A01T	55.97	70.56	52.64	70.69
A02T	49.72	38.33	67.08	50.14
A03T	81.25	81.39	57.92	63.06
A04T	49.44	38.61	48.47	46.53
A05T	71.39	59.17	25.00	37.92
A06T	47.36	44.58	59.03	24.44
A07T	88.47	72.50	45.56	60.56
A08T	77.22	75.14	60.14	76.11
A09T	84.58	70.28	65.00	76.94
Mean	67.27	61.17	53.43	56.27

TABLE 4: Sensor method classification specificity (true negative rate).

Specificity	Left (%)	Right (%)	Foot (%)	Tongue (%)
A01T	85.28	84.86	88.33	89.03
A02T	79.63	80.83	87.64	79.86
A03T	91.67	93.47	86.76	85.42
A04T	78.94	77.31	82.59	80.14
A05T	79.40	80.83	79.03	77.27
A06T	80.93	77.96	79.91	78.52
A07T	87.04	85.14	82.50	87.31
A08T	94.21	87.55	83.98	90.83
A09T	93.47	92.78	86.67	92.64
Mean	85.62	84.53	84.16	84.56

TABLE 6: Source method classification specificity (true negative rate).

Specificity	Left (%)	Right (%)	Foot (%)	Tongue (%)
A01T	86.20	85.88	88.80	89.07
A02T	76.90	84.07	88.33	85.79
A03T	89.63	93.29	89.63	88.66
A04T	75.46	84.07	84.40	83.75
A05T	79.12	80.37	86.76	84.91
A06T	78.15	78.75	82.08	86.16
A07T	88.15	89.17	87.69	90.69
A08T	93.70	90.51	86.99	91.67
A09T	92.27	91.85	88.52	92.96
Mean	84.40	86.44	87.02	88.18

subsequent application of CSP on the source space to compensate for the head volume conduction by mapping scalp potentials to cortical activations [46]. There are several studies supporting that BCI algorithms based on source space features are superior to the sensor ones [11, 47], an observation that is confirmed in our study, comparing the classification results on the sensor and source space. Our BCI algorithm uses, in particular, sources belonging to select Regions of Interest (ROIs) on motor cortex for feature extraction and an ensemble classification model to take advantage of ROI data.

Despite the fact that our algorithm did not reach the accuracy levels of the winning method of the BCI Competition, during the ROI selection procedure, common ROIs emerged among all subjects. The emerged ROIs are anatomically and neurophysiologically related to the MI tasks, linking the method results with neurological data. Given that

the motor tasks of the competition involved motor imagery of both arms, tongue, and feet, consistent selection of primary hand motor areas and primary lip motor area (cortical representations of hands and face on the primary motor cortex) seems very promising. Cingulate motor areas are also considered very important nodes of the sensorimotor network, having been demonstrated to drive the sensorimotor process [48, 49]. It is our conviction that selected ROIs, as produced by the developed algorithm, validate our results since there is a clear neuroanatomical and neurophysiological link between these ROIs and the Motor Imagery tasks performed in the dataset.

Our method appeared to improve mean accuracy by 5.6% and by 0.07 Cohen's kappa value among all subjects, with respect to sensor method. When our algorithm is compared

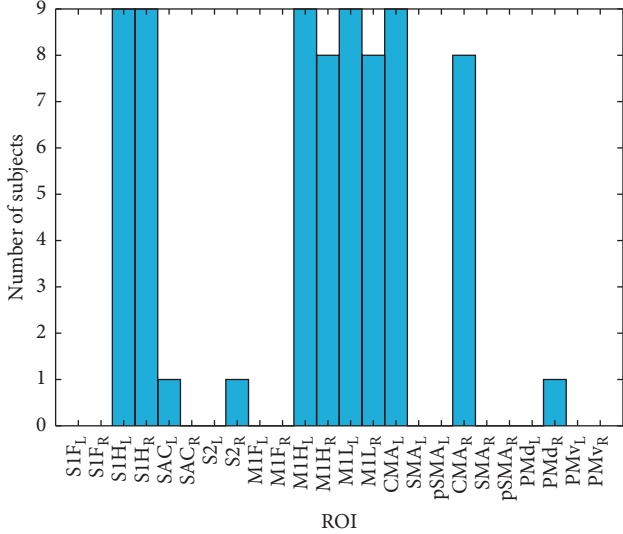


FIGURE 6: Histogram of the selected regions of interest (ROI), across all subjects.

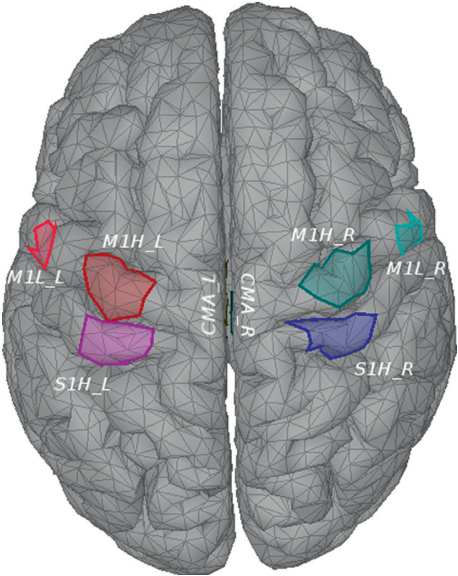


FIGURE 7: Positions of the most commonly selected ROIs among subjects (right and left M1L, M1H, S1H, and CMA), displayed on the cortical model.

with the winner of the BCI Competition (FBCSP), the mean accuracy is considerably lower by 0.19 Cohen's kappa value. The performance of our algorithm based on kappa value is considered moderate while that of the winning implementation is considered substantial [40]. We believe this difference is attributed to feature selection and classifier used by the winner. FBCSP generates CSP features in different frequency bands resulting to multiple features, while feature selection procedure is a vital component to detect the most discriminable features [41]. On the other hand, our source-based algorithm seems to increase the classification accuracy of subjects with the worst performance, namely the A04, A05, & A06, as it can be illustrated in Figure 5, outperforming sensor

algorithm by a mean accuracy rate of 7.5%. Nevertheless, the trend identified cannot lead to safe conclusions yet, since we cannot infer statistical significance of the results, requiring further investigation on data with larger population of subjects. Moreover, ensemble classification was used, in an effort to increase classification accuracy, by synergistically deploying the independent ROI classification models. Majority vote of ROI classification models was used as final classification outcome, although a weighted vote taking into account the ROI-MI task relation could be considered in the future.

3.4. Limitations and Future Steps. In this study, a generic template three-compartment BEM head model was utilized to solve the forward problem. Forward problem solution induces an important error in the source estimation, as has been explored extensively in previous studies [50, 51]. Main forward problem error inducing factors are (a) the use of the MNI template MRI data rather than the subjects' individual neuroanatomy and (b) the absence of cerebrospinal fluid (CSF) in the forward modeling. Template anatomy was used for all subjects, missing important geometrical information for every subject, producing a lead-field matrix that transforms the EEG sensor data into a template cortical manifold different from the real one. CSF compartment has big influence on both signal topography and magnitude, resulting in strong signal attenuation for superficial sources on gyral crowns [52]. This effect is termed to the high increase of conductivity between the sensors and sources. In a future effort to address this problems, a 4- or 5-compartment head model including CSF and skull anisotropy will be used, modeled with finite elements [53].

There are two main shortcomings in the use of CSP method that were not dealt in this work. The first is that the CSP filters are prone to noise and overfitting, and the second is that the CSP performance is highly dependent on the input signal frequency band the individual subject BCI performance is dependable on individual frequency band used [20, 21]. There are many variants of conventional CSP algorithm designed to overcome the limitations, with popular variants being the RCSP that tackle noise and overfitting with regularization and the FBCSP that better capture the individual subject multiple frequency band filters feature selection, respectively, while a newly introduced method combines aforementioned methods [20, 21, 39].

Future work will focus on better CSP filters extraction and use feature selection and more sophisticated ensemble models, in an effort to increase the performance of the algorithm. Since the anatomy used for the forward model is common among all subjects and the selected ROIs are common among all subjects, we would like to check the potential of the algorithm in transfer learning between subjects. There is a study supporting that transfer learning between different subjects by means of source space can achieve higher average single-trial classification accuracy than with a conventional method [54]. Beyond the BCIC IV 2a dataset that is a common ground for the evaluation of methods decoding multiple MI, we aim to evaluate the improved method on dataset we compiled for the

CSI: Brainwave project, containing EEG data of healthy or subjects with spinal cord injury performing multiple motor imagery mainly of the upper limbs [36, 55].

4. Conclusions

Source estimation and application of CSP filters at the source space constitute a promising solution to increasing classification accuracy of noninvasive BCIs. Our method has demonstrated capability in decoding multiple motor imagery tasks with better accuracy than the equivalent sensor method. While our implementation still is not superior to the state of the art of BCI algorithms, feature selection and classifier characteristics can improve performance. Neuroanatomical constraints and prior neurophysiological knowledge has been shown to play an important role in developing source space-based BCI algorithms. Our results indicate that the selected ROIs are common among all subjects, which worth further investigation probably in the context of transfer learning between different subjects.

Data Availability

The BCI Competition IV dataset is available at <http://www.bbci.de/competition/iv/>. The data from the hereby described analysis can be made available from the authors upon request.

Ethical Approval

This study describes a novel analysis of a publicly available dataset. It does not describe new experiments on human subjects.

Conflicts of Interest

The authors declare that there are no conflicts of interest regarding the publication of this article.

Acknowledgments

This study was conducted as part of the development of the project CSI:Brainwave and was supported by the “Brihaye” 2018 EANS Research Grant. This study was supported by the European Union’s Horizon 2020 Research and Innovation Program under Grant Agreement no. 681120 for the SmokeFreeBrain Project.

References

- [1] L. R. Hochberg, D. Bacher, B. Jarosiewicz et al., “Reach and grasp by people with tetraplegia using a neurally controlled robotic arm,” *Nature*, vol. 485, no. 7398, pp. 372–375, 2012.
- [2] B. Lee, C. Y. Liu, and M. L. J. Apuzzo, “A primer on brain-machine interfaces, concepts, and technology: a key element in the future of functional neurorestoration,” *World Neurosurgery*, vol. 79, no. 3-4, pp. 457–471, 2013.
- [3] L. F. Nicolas-Alonso and J. Gomez-Gil, “Brain computer interfaces, a review,” *Sensors*, vol. 12, no. 12, pp. 1211–1279, 2012.
- [4] J. Harris and A. Hebert, “Utilization of motor imagery in upper limb rehabilitation: a systematic scoping review,” *Clinical Rehabilitation*, vol. 29, no. 11, pp. 1092–1107, 2015.
- [5] S. Kraeutner, A. Gionfriddo, T. Bardouille, and S. Boe, “Motor imagery-based brain activity parallels that of motor execution: evidence from magnetic source imaging of cortical oscillations,” *Brain Research*, vol. 1588, pp. 81–91, 2014.
- [6] J. J. Shih, D. J. Krusinski, and J. R. Wolpaw, “Brain-computer interfaces in medicine,” *Mayo Clinic Proceedings*, vol. 87, no. 3, pp. 268–279, 2012.
- [7] A. Saimpont, M. F. Lafleur, F. Malouin, C. L. Richards, J. Doyon, and P. L. Jackson, “The comparison between motor imagery and verbal rehearsal on the learning of sequential movements,” *Frontiers in Human Neuroscience*, vol. 7, 2013.
- [8] J. Meng, S. Zhang, A. Bekyo, J. Olsoe, B. Baxter, and B. He, “Noninvasive electroencephalogram based control of a robotic arm for reach and grasp tasks,” *Scientific Reports*, vol. 6, no. 1, article 38565, 2016.
- [9] F. Galán, M. Nuttin, E. Lew et al., “A brain-actuated wheelchair: asynchronous and non-invasive Brain-computer interfaces for continuous control of robots,” *Clinical Neurophysiology*, vol. 119, no. 9, pp. 2159–2169, 2008.
- [10] B. He, B. Baxter, B. J. Edelman, C. C. Cline, and W. W. Ye, “Noninvasive brain-computer interfaces based on sensorimotor rhythms,” *Proceedings of the IEEE*, vol. 103, no. 6, pp. 907–925, 2015.
- [11] B. J. Edelman, B. Baxter, and B. He, “EEG source imaging enhances the decoding of complex right-hand motor imagery tasks,” *IEEE Transactions on Biomedical Engineering*, vol. 63, no. 1, pp. 4–14, 2016.
- [12] P. L. Nunez and R. Srinivasan, *Electric Fields in the Brain: The Neurophysics of EEG*, Oxford University Press, New York, NY, USA, 2006.
- [13] C. M. Michel, M. M. Murray, G. Lantz, S. Gonzalez, L. Spinelli, and R. Grave de Peralta, “EEG source imaging,” *Clinical Neurophysiology*, vol. 115, no. 10, pp. 2195–2222, 2004.
- [14] B. He, L. Yang, C. Wilke, and H. Yuan, “Electrophysiological imaging of brain activity and connectivity-challenges and opportunities,” *IEEE Transactions on Biomedical Engineering*, vol. 58, no. 7, pp. 1918–1931, 2011.
- [15] H. Ramoser, J. Müller-Gerking, G. Pfurtscheller, J. Muller-Gerking, and G. Pfurtscheller, “Optimal spatial filtering of single trial EEG during imagined hand movement,” *IEEE Transactions on Rehabilitation Engineering*, vol. 8, no. 4, pp. 441–446, 2000.
- [16] A. Bashashati, M. Fatourechi, R. K. Ward, and G. E. Birch, “A survey of signal processing algorithms in brain-computer interfaces based on electrical brain signals,” *Journal of Neural Engineering*, vol. 4, no. 2, pp. R32–R57, 2007.
- [17] S. Lemm, B. Blankertz, G. Curio, and K.-R. Müller, “Spatiospectral filters for improving the classification of single trial EEG,” *IEEE Transactions on Biomedical Engineering*, vol. 52, no. 9, pp. 1541–1548, 2005.
- [18] K. P. Camilleri, O. Falzon, T. Camilleri, and S. G. Fabri, “Phase variants of the common spatial patterns method,” in *Modern Electroencephalographic Assessment Techniques, Neuro-methods*, V. Sakkalis, Ed., Vol. 91, pp. 249–265, Humana Press, New York, NY, 2014.
- [19] T. H. Brandon, S. T. Tiffany, K. M. Obremski, and T. B. Baker, “Postcessation cigarette use: the process of relapse,” *Addictive Behaviors*, vol. 15, no. 2, pp. 105–114, 1990.
- [20] F. Lotte and C. Guan, “Regularizing common spatial patterns to improve BCI designs: unified theory and new algorithms,”

- IEEE Transactions on Biomedical Engineering*, vol. 58, no. 2, pp. 355–362, 2011.
- [21] K. K. Ang, Z. Y. Chin, C. Wang, C. Guan, and H. Zhang, “Filter bank common spatial pattern algorithm on BCI competition IV datasets 2a and 2b,” *Frontiers in Neuroscience*, vol. 6, 2012.
- [22] X. Bai, X. Wang, S. Zheng, and M. Yu, “The offline feature extraction of four-class motor imagery EEG based on ICA and Wavelet-CSP,” in *Proceedings of the 33rd Chinese Control Conference*, pp. 7189–7194, Nanjing, China, July 2014.
- [23] M. Tangermann, K.-R. Müller, A. Aertsen et al., “Review of the BCI Competition IV,” *Frontiers in Neuroscience*, vol. 6, p. 55, 2012.
- [24] G. Pfurtscheller, C. Brunner, A. Schlogl, and F. H. Lopes da Silva, “Mu rhythm (de)synchronization and EEG single-trial classification of different motor imagery tasks,” *Neuroimage*, vol. 31, no. 1, pp. 153–159, 2006.
- [25] R. Oostenveld, P. Fries, E. Maris, and J.-M. Schoffelen, “FieldTrip: open source software for advanced analysis of MEG, EEG, and invasive electrophysiological data,” *Computational Intelligence and Neuroscience*, vol. 2011, Article ID 156869, 9 pages, 2011.
- [26] G. Buzsaki, C. A. Anastassiou, and C. Koch, “The origin of extracellular fields and currents—EEG, ECoG, LFP and spikes,” *Nature Reviews Neuroscience*, vol. 13, no. 6, pp. 407–420, 2012.
- [27] H. Hallez, B. Vanrumste, R. Grech et al., “Review on solving the forward problem in EEG source analysis,” *Journal of NeuroEngineering and Rehabilitation*, vol. 4, no. 1, p. 46, 2007.
- [28] C. J. Holmes, R. Hoge, L. Collins, R. Woods, A. W. Toga, and A. C. Evans, “Enhancement of MR images using registration for signal averaging,” *Journal of Computer Assisted Tomography*, vol. 22, no. 2, pp. 324–333, 1998.
- [29] A. Gramfort, T. Papadopoulou, E. Olivi, and M. Clerc, “Open-MEEG: opensource software for quasistatic bioelectromagnetics,” *BioMedical Engineering Online*, vol. 9, no. 1, p. 45, 2010.
- [30] Q. Fang and D. A. Boas, “Tetrahedral mesh generation from volumetric binary and grayscale images,” in *Proceedings of the 2009 IEEE International Symposium on Biomedical Imaging: From Nano to Macro*, pp. 1142–1145, Boston, MA, USA, July 2009.
- [31] L. A. Geddes and L. E. Baker, “The specific resistance of biological material—a compendium of data for the biomedical engineer and physiologist,” *Medical & Biological Engineering*, vol. 5, no. 3, pp. 271–293, 1967.
- [32] R. Grech, T. Cassar, J. Muscat et al., “Review on solving the inverse problem in EEG source analysis,” *Journal of Neuro-Engineering and Rehabilitation*, vol. 5, no. 1, p. 25, 2008.
- [33] M. S. Hämäläinen and R. J. Ilmoniemi, “Interpreting magnetic fields of the brain: minimum norm estimates,” *Medical & Biological Engineering & Computing*, vol. 32, no. 1, pp. 35–42, 1994.
- [34] F. Tadel, S. Baillet, J. C. Mosher, D. Pantazis, and R. M. Leahy, “Brainstorm: a user-friendly application for MEG/EEG Analysis,” *Computational Intelligence and Neuroscience*, vol. 2011, Article ID 879716, 13 pages, 2011.
- [35] F. Cincotti, D. Mattia, F. Aloise et al., “High-resolution EEG techniques for brain-computer interface applications,” *Journal of Neuroscience Methods*, vol. 167, no. 1, pp. 31–42, 2008.
- [36] A. Athanasiou, I. Xygonakis, N. Pandria et al., “Towards rehabilitation robotics: off-the-shelf BCI control of anthropomorphic robotic arms,” *Biomed Research International*, vol. 2017, Article ID 5708937, 17 pages, 2017.
- [37] G. Dornhege, B. Blankertz, G. Curio, and K.-R. Muller, “Boosting bit rates in noninvasive EEG single-trial classifications by feature combination and multiclass paradigms,” *IEEE Transactions on Biomedical Engineering*, vol. 51, no. 6, pp. 993–1002, 2004.
- [38] L. Rokach, “Ensemble-based classifiers,” *Artificial Intelligence Review*, vol. 33, no. 1–2, pp. 1–39, 2010.
- [39] S.-H. Park, D. Lee, and S.-G. Lee, “Filter bank regularized common spatial pattern ensemble for small sample motor imagery classification,” *IEEE Transactions on Neural Systems and Rehabilitation Engineering*, vol. 26, no. 2, pp. 498–505, 2018.
- [40] C.-H. Chuang, L.-W. Ko, Y.-P. Lin, T.-P. Jung, and C.-T. Lin, “Independent component ensemble of EEG for brain-computer interface,” *IEEE Transactions on Neural Systems and Rehabilitation Engineering*, vol. 22, no. 2, pp. 230–238, 2014.
- [41] K. K. Ang, Z. Y. Chin, H. Zhang, and C. Guan, “Filter Bank Common Spatial Pattern (FBCSP) in brain-computer interface,” in *Proceedings of the 2008 IEEE International Joint Conference on Neural Networks (IEEE World Congress on Computational Intelligence)*, pp. 2390–2397, Hong Kong, China, 2008.
- [42] J. Cohen, “A coefficient of agreement for nominal scales,” *Educational and Psychological Measurement*, vol. 20, no. 1, pp. 37–46, 1960.
- [43] J. R. Landis and G. G. Koch, “The measurement of observer agreement for categorical data,” *Biometrics*, vol. 33, no. 1, pp. 159–174, 1977.
- [44] S. I. Ryu and K. V. Shenoy, “Human cortical prostheses: lost in translation?,” *Neurosurgical Focus Other Titles*, vol. 27, no. 1, p. E5, 2009.
- [45] J. R. Wolpaw, N. Birbaumer, D. J. McFarland, G. Pfurtscheller, and T. M. Vaughan, “Brain-computer interfaces for communication and control,” *Clinical Neurophysiology*, vol. 113, no. 6, pp. 767–791, 2002.
- [46] B. He and L. Ding, “Electrophysiological mapping and neuroimaging,” in *Neural Engineering*, pp. 499–543, Springer, Boston, MA, USA, 2013.
- [47] B. Kamousi, A. N. Amini, and B. He, “Classification of motor imagery by means of cortical current density estimation and Von Neumann entropy,” *Journal of Neural Engineering*, vol. 4, no. 2, pp. 17–25, 2007.
- [48] A. Athanasiou, M. A. Klados, C. Styliadis, N. Foroglou, K. Polyzoidis, and P. D. Bamidis, “Investigating the role of alpha and beta rhythms in functional motor networks,” *Neuroscience*, vol. 378, pp. 54–70, 2016.
- [49] D. Mattia, F. Cincotti, L. Astolfi et al., “Motor cortical responsiveness to attempted movements in tetraplegia: evidence from neuroelectrical imaging,” *Clinical Neurophysiology*, vol. 120, no. 1, pp. 181–189, 2009.
- [50] Z. Akalin Acar and S. Makeig, “Effects of forward model errors on eeg source localization,” *Brain Topography*, vol. 26, no. 3, pp. 378–396, 2013.
- [51] C. Ramon, P. Schimpf, J. Haueisen, M. Holmes, and A. Ishimaru, “Role of soft bone, CSF and gray matter in EEG simulations,” *Brain Topography*, vol. 16, no. 4, pp. 245–248, 2003.
- [52] J. Vorwerk, J.-H. Cho, S. Rampp, H. Hamer, T. R. Knösche, and C. H. Wolters, “A guideline for head volume conductor modeling in EEG and MEG,” *Neuroimage*, vol. 100, pp. 590–607, 2014.
- [53] J. Vorwerk, R. Oostenveld, M. C. Piastra, L. Magyari, and C. H. Wolters, “The FieldTrip-SimBio pipeline for EEG

- forward solutions," *BioMedical Engineering Online*, vol. 17, no. 1, p. 37, 2018.
- [54] M. Wronkiewicz, E. Larson, and A. K. C. Lee, "Leveraging anatomical information to improve transfer learning in brain-computer interfaces," *Journal of Neural Engineering*, vol. 12, no. 4, article 46027, 2015.
- [55] A. Athanasiou, G. Arfaras, N. Pandria et al., "Wireless brain-robot interface: user perception and performance assessment of spinal cord injury patients," *Wireless Communications and Mobile Computing*, vol. 2017, Article ID 2986423, 16 pages, 2017.

Research Article

Wireless Stimulus-on-Device Design for Novel P300 Hybrid Brain-Computer Interface Applications

Chung-Hsien Kuo ,^{1,2,3} Hung-Hsuan Chen,¹ Hung-Chyun Chou,¹ Ping-Nan Chen,³ and Yu-Cheng Kuo¹

¹Department of Electrical Engineering, National Taiwan University of Science and Technology, Taipei, Taiwan

²Center for Cyber-Physical System Innovation, National Taiwan University of Science and Technology, Taipei, Taiwan

³Department of Biomedical Engineering, National Defense Medical Center, Taipei 114, Taiwan

Correspondence should be addressed to Chung-Hsien Kuo; chkuo@mail.ntust.edu.tw

Received 20 April 2018; Accepted 28 June 2018; Published 18 July 2018

Academic Editor: Roshan J. Martis

Copyright © 2018 Chung-Hsien Kuo et al. This is an open access article distributed under the Creative Commons Attribution License, which permits unrestricted use, distribution, and reproduction in any medium, provided the original work is properly cited.

Improving the independent living ability of people who have suffered spinal cord injuries (SCIs) is essential for their quality of life. Brain-computer interfaces (BCIs) provide promising solutions for people with high-level SCIs. This paper proposes a novel and practical P300-based hybrid stimulus-on-device (SoD) BCI architecture for wireless networking applications. Instead of a stimulus-on-panel architecture (SoP), the proposed SoD architecture provides an intuitive control scheme. However, because P300 recognitions rely on the synchronization between stimuli and response potentials, the variation of latency between target stimuli and elicited P300 is a concern when applying a P300-based BCI to wireless applications. In addition, the subject-dependent variation of elicited P300 affects the performance of the BCI. Thus, an adaptive model that determines an appropriate interval for P300 feature extraction was proposed in this paper. Hence, this paper employed the artificial bee colony- (ABC-) based interval type-2 fuzzy logic system (IT2FLS) to deal with the variation of latency between target stimuli and elicited P300 so that the proposed P300-based SoD approach would be feasible. Furthermore, the target and nontarget stimuli were identified in terms of a support vector machine (SVM) classifier. Experimental results showed that, from five subjects, the performance of classification and information transfer rate were improved after calibrations (86.00% and 24.2 bits/ min before calibrations; 90.25% and 27.9 bits/ min after calibrations).

1. Introduction

According to World Health Organization (WHO) statistics, in 2013, there were between 250,000 and 500,000 people suffering from spinal cord injuries (SCIs) [1]. Due to difficulty with mobility, an estimated 20% to 30% of people with SCIs show clinically significant signs of depression. Negative mental conditions lead to negative impacts on improvements in function and overall health. Negative attitudes and physical barriers obstruct basic mobility and result in the exclusion of people from participation in society. Improvement in the independent living ability of people suffering from SCIs is one method to overcome the disability's barriers.

Brain-computer interfaces (BCIs) are systems that interpret the brain's electrical activities to command external

devices [2–6]. Thus, BCIs provide subjects with a nonmuscular method to connect with the world. Particularly for disabled people who suffer from SCIs and strokes, BCIs improve their independence in daily life. Several studies have proven that there is a great potential to develop BCIs with wide applications, such as assistive spelling systems, robotics, and rehabilitation tools. Reviewing the achievements of the past several decades, BCIs have been widely discussed. Faster, more user-friendly and more robust BCIs had been proposed by several research groups worldwide. With fast-paced technical developments, BCI studies have reached a critical point and continue to seek innovative applications.

P300 [7] is one of the conventional BCIs. P300 is an event-related potential (ERP), and the most significant feature of the potential waveform is the positive peak occurred around

300ms after a stimulus. Hence, P300 has been widely used to provide communication capabilities for healthy users, wheelchair users, and disabled people with SCIs and strokes. In addition to P300, steady state visually evoked potential (SSVEP) is another common BCI modality. SSVEP is an evoked signal that responds to visual flickering stimuli at a specific frequency. Because SSVEP is a phase-locked evoked potential, different phases of flickering stimuli are generated to obtain more stimulus targets.

Hybrid BCI is a novel architecture that integrates different BCI modalities, such as ERP, SSVEP, and motor imagery [8–11]. Particularly, auditory and tactile based P300 BCI and SSVEP BCI studies were practically proposed [12, 13]. In general, hybrid BCIs have the advantages of BCI modalities and compensate for their shortcoming. Thus, hybrid BCIs are expected to increase the accuracy and information transfer rates (ITRs). For example, P300 is a major peak and one of the most-used ERP features. The presentation of a stimulus in an oddball paradigm can elicit a positive peak in EEG. Stimuli could be visual, auditory, or somatosensory. P300 has the advantages of requiring less initial user training and being easy to observe in a simple and discriminative task. However, due to irrelative stimuli, P300-based BCI has a reported decrease in performance after long-term operation. Compared to P300, SSVEP-based BCIs [13] feature high ITRs, high signal-to-noise ratios, and relatively obvious patterns and do not require prior training procedures. However, SSVEP-based BCI requires accurate control of the subject's eye muscles and hardware that allows precisely flickering stimuli. Therefore, different paradigms of hybrid BCIs are proposed to improve single BCI modality-based systems.

A robust classifier acts an important role to recognize EEG patterns. Viewing proposed literatures, SVM [14–16], Linear Discriminant Analysis (LDA) [17–20], Bayesian Analysis [21–25], and Artificial Neural Network (ANN) [26–30] classifiers were discussed. Generally, a specific model for a user is trained before using BCI. Users are asked to follow a defined paradigm, and acquired EEG epochs are labeled particular events. Classification algorithms are trained by a labeled dataset that is called supervised learning traditionally. Type-1 fuzzy logic was proposed by Dr. Zadeh and has been discussed widely in many fields [31–35]. Type-1 fuzzy sets express the degree to which an input belongs to a fuzzy set by a crisp value. In 1975, Dr. Zadeh proposed type-2 fuzzy sets to model uncertainties. IT2FLS features interval membership functions, known as the footprint of uncertainty (FoU). FoU is expressed by two boundary functions, including a lower membership function and a higher membership function. It is robust to more uncertainties in real environments. For BCI research, because the brain's electrical signals are small and easily affected by the environment and any movement artifact, type-2 fuzzy systems show a great potential to resolve those problems. Instead of subjective fuzzy models defined by developers' knowledge, adaptive fuzzy logic systems, such as Fuzzy-Neural Network (FNN), Genetic Algorithm (GA), and swarm-based fuzzy systems, were proposed. ABC algorithm was proposed by Karaboga et al. in 2005 and was inspired by the foraging behavior of honey bee colonies [36]. It features fast convergence, less parameters, and strong robustness.

Finally, the proposed P300-based hybrid BCI with latency calibration for wireless SoD applications is elaborated in five sections in this paper, and the structure is stated as follows. In Section 1, this work specifies people with SCIs and proposes a wireless networking BCI for wireless home automation applications. In Section 2, the adopted methodologies of the proposed BCI are described. EEG processing techniques and adaptive IT2FLS for BCI calibrations are introduced. In Section 3, the experimental paradigm is specified. In Section 4, several experiments are conducted to assess the proposed hypotheses and approaches. Subjects participated in experiments to evaluate the performance of the proposed hybrid BCI. Section 5 reviews the proposed system according to experimental results. Moreover, improved strategies and future prospections are discussed.

2. Methodology

This paper aims at presenting a new stimulus-on-device (SoD) design with combining the wireless sensor network (WSN) and P300-based BCI applications. Such a WSN and P300 combination forms a novel BCI application rarely seen in literatures. Such a SoD exhibits the variation of latency between target stimuli and elicited P300. Hence, this paper adopts our previous work [37] that discussed the latency problems occurred in the conventional P300 studies to deal with the subjects' P300 peak latency variation as well as the WAS transmission delay to make the SoD design practically feasible.

2.1. SoD Design Concept and Protocol. Considering visual-based hybrid BCI, P300 and SSVEP are two of the most discussed BCI modalities. Two main paradigms, including sequential [36, 38] and simultaneous systems [39, 40], are usually discussed. As shown in Figure 1, a sequential hybrid BCI separates a BCI system into a number of blocks. The output signals of blocks are the input signals of the next BCI system. On the other hand, a simultaneous hybrid BCI benefits individual users by obtaining a higher responded efficiency through the utilizing of an appropriate BCI modality [41]. A stimulation panel containing a number of visual stimuli is a common layout for visual-based BCIs. Stimuli responding to a defined task are arranged and presented in front of users. Users are able to select a target stimulus by gazing one of visual stimuli on a panel or a monitor. Here, this BCI layout is called SoP architecture. Instead of SoP architecture, the proposed SoD architecture embeds visual stimuli in target devices and a coordinator controller sends trigger signals to those stimulation-embedded devices through wireless communication. SoD architecture benefits the mobility of users when without using a multistimuli stimulation panel. Additionally, without the limited dimension of stimulation panel, more tasks are able to be defined by adding visual stimuli in target devices. SoD is a flexible and user-friendly BCI architecture that provides an intuitive control scheme.

Based on the SoD architecture, a scenario that applies a P300-based BCI to a wireless home automation system for appliance controls, such as lighting, electric curtains, and air

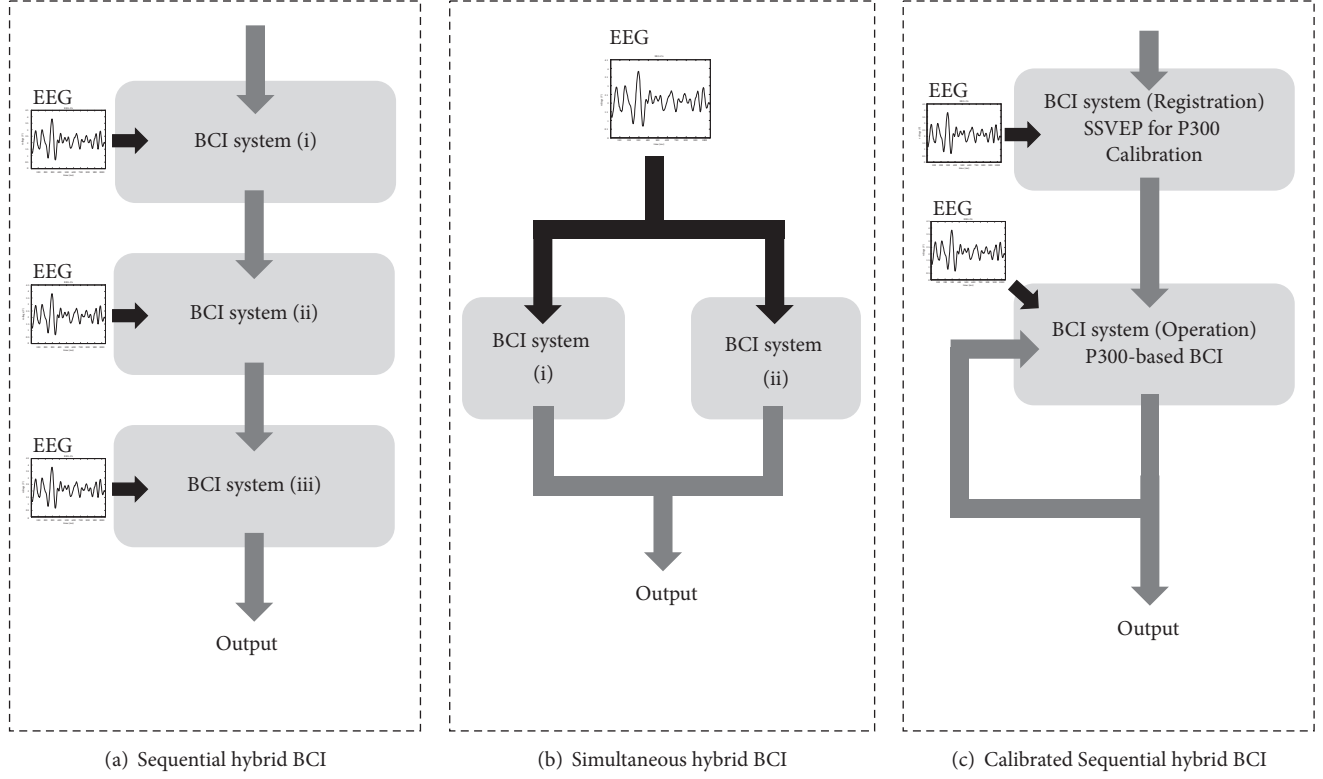


FIGURE 1: Block diagram of sequential (a), simultaneous (b), and calibrated sequential (c) (proposed) hybrid BCIs.

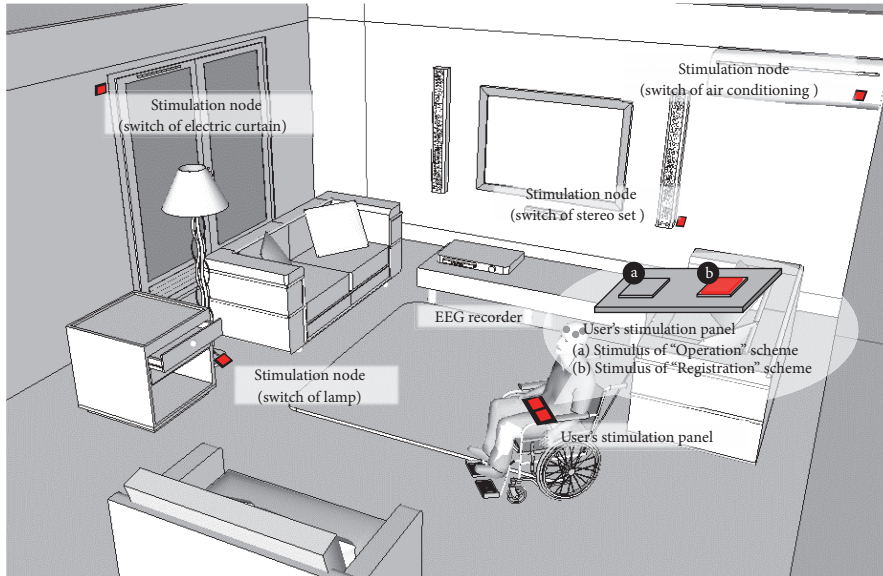


FIGURE 2: The scenario of wireless home automation based on BCI.

conditioning, is shown in Figure 2. A user is outfitted with an EEG recorder, and a coordinator controller featuring a built-in wireless communication module handles the EEG stream. A visual stimulus panel is placed in front of the user. There are two sets of LED modules that generate 16 Hz flickering visual stimuli with different phase delays. The user is able to start the BCI system by gazing at the stimulus of “Operation”

and applying the P300-based BCI to the appliance controls. Then, the coordinator controller sends trigger signals to stimulation-embedded appliances. Here, each stimulation-embedded appliance is regarded as a stimulation node. The controller coordinates the latency of flashing stimuli through wireless communication and extracts epochs that respond to flashing stimuli.

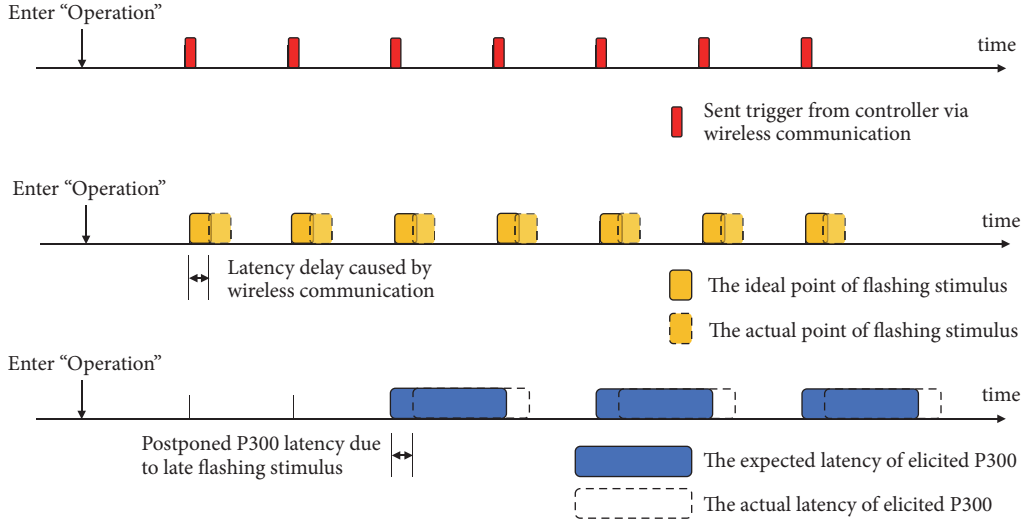


FIGURE 3: The latency of sent triggers, flashing stimuli, ideal P300 latency, and actual P300 latency.

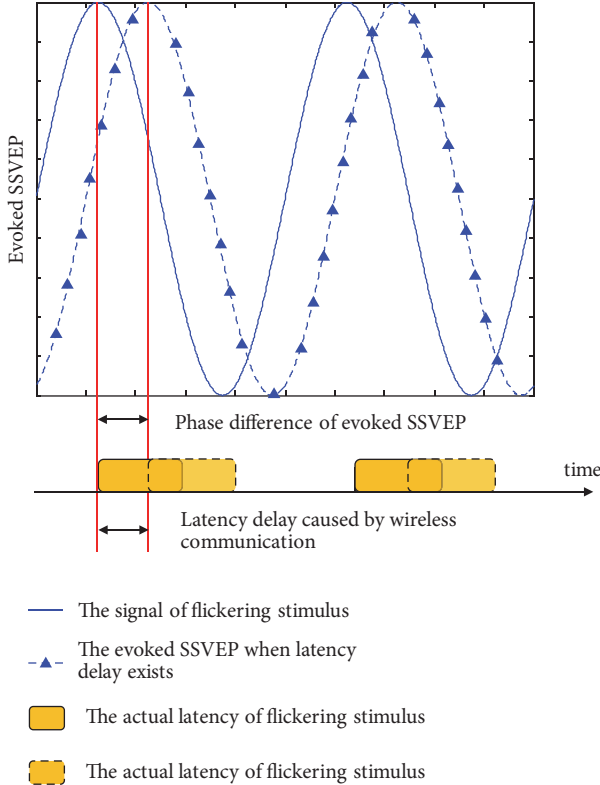


FIGURE 4: The latency of flickering stimuli and evoked SSVEP.

However, distances, transmission qualities, and hardware processing are uncertain factors that cause latency delays for this kind of SoD applications. Synchronization is influenced by any jitter between the clocks of an EEG recorder and the stimulation nodes and varies over time. The timeline of sent triggers, flashing stimuli, ideal P300 latency, and actual P300 latency are shown in Figure 3. Induced by the uncertainties of wireless communication, there are differences in

the expected and actual latencies of the elicited P300 for different subjects and applied situations. Additionally, latency differences might fluctuate due to the changing quality of wireless communication. As a result, the accuracy of P300 recognition is affected while the acceptances of users decrease because of unstable performance. Therefore, a scheme of “Registration” is proposed. “Registration” allows users to access a BCI system by identifying the SSVEP. The phase lag of evoked SSVEP due to communication delays is depicted in Figure 4. This work attempts to assess how the latency of the elicited P300 correlates with the phase lag of the evoked SSVEP. A trained regression model is applied to estimate the possible latency of the elicited P300 according to phase lag analysis of the evoked SSVEP. Thus, the uncertainty of latency caused by wireless communication is resolved. Before starting “Operation”, users are asked to gaze at the stimulus of “Registration” to register their model. Users are asked to register every stimulation node item by item. A trained regression model is applied to estimate the possible latency of elicited P300 for each stimulation node. The proposed wireless P300-based BCI is calibrated when “Registration” is finished.

The proposed wireless networking BCI includes “Registration” and “Operation” schemes. “Registration” allows users to access the BCI system by identifying the SSVEP, and “Operation” allows users to control stimulation-embedded devices via P300. A block diagram of “Registration” and “Operation” is shown in Figure 5.

2.2. EEG Acquisition. This paper used the V-amp (Brain Products, German) EEG instrument to collect the subject EEG signal. The experiments were done based on the 4–20 Hz bandpass filtering frequency range. The EEG signal was acquired with 500 Hz sampling rate. Five electrodes were placed at P3, Pz, P4, O1, and O2 according to the 10/20 system. P3, Pz, P4, O1, and O2 are channels that respond to visual stimuli. The acquired EEGs were used for the phase lag analyses of SSVEP and P300 recognitions. Five electrodes

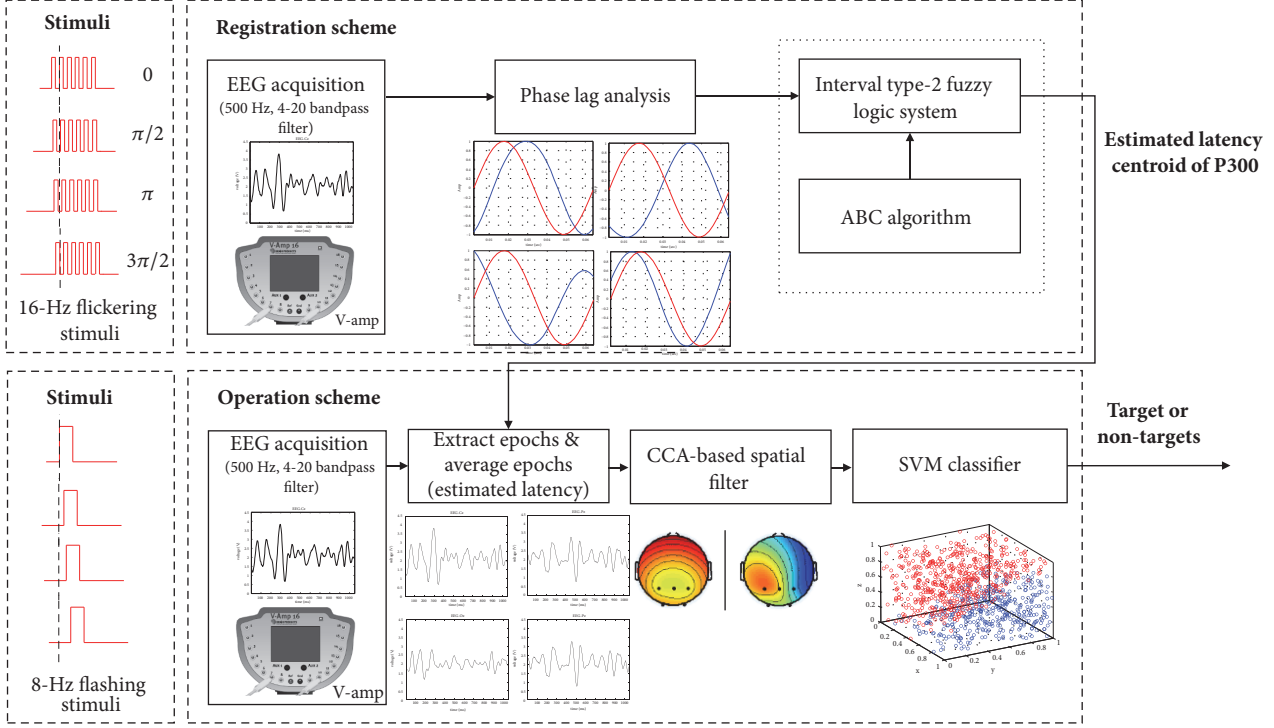


FIGURE 5: The block diagram of “Registration” and “Operation”.

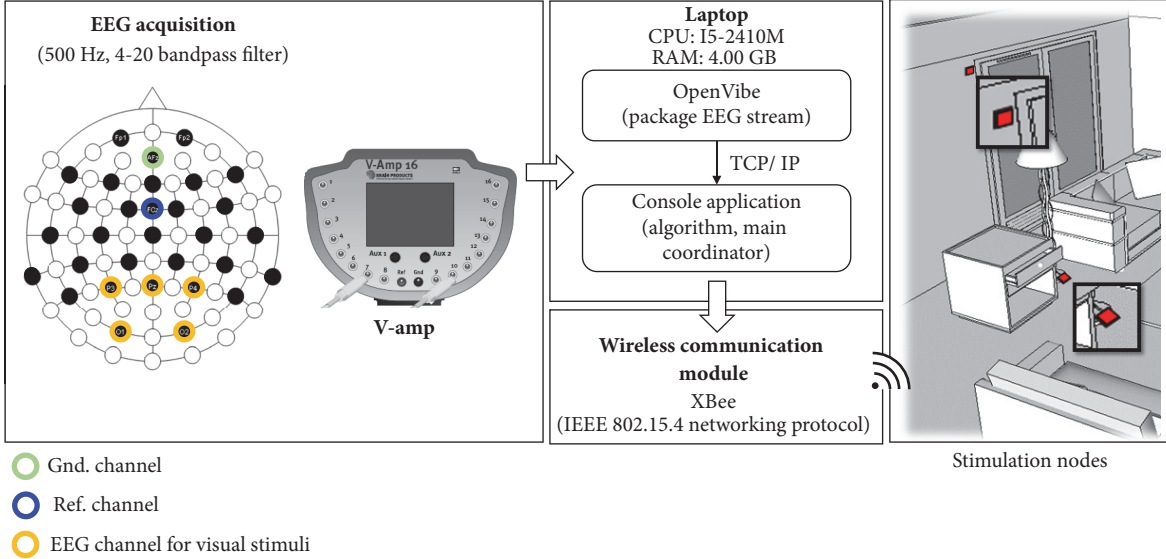


FIGURE 6: The system architecture.

were distributed in the occipital area. A reference electrode was placed at FCz, and a ground electrode was placed at AFz according to the recommended placement of the EasyCap (Standard Cap for V-amp, German). The system architecture is shown in Figure 6.

2.3. Signal Processing and Target/Nontarget Classification. As mentioned in the Introduction section, this paper adopts our previous work [37] to deal with the subjects’ P300 peak

latency variation and the WAS transmission delay. Hence, the signal processing and target/nontarget classification followed the approaches proposed in [37] as well as the experiment protocol elaborated in Section 2.1. The approaches for signal processing and target/nontarget classification are briefly described as follows.

- (1) IT2FLS for BCI calibrations: the proposed calibration approach is to predict the latency of the elicited P300

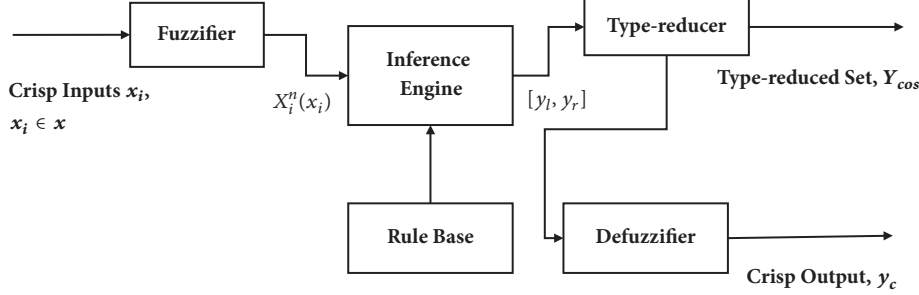


FIGURE 7: Operation of IT2FLS.

in terms of the phase lag appeared at the $0, \pi/2, \pi, 3\pi/2$ of a conventional SSVEP waveform. Figure 7 illustrated the operation of the IT2FLS, where x_i is crisp inputs, $x_i^n(x_i)$ is the interval fuzzy set, y_l and y_r are the maximum and minimum values, respectively, Y_{cos} is generated in terms of a center-of-sets type reducer, and y_c is a crisp output which was obtained after the defuzzifier with respect to y_l and y_r . As a consequence, the regression model based on an IT2FLS was used. The calibration was done through the analysis of phase delays. Evoked phase lags were the inputs of IT2FLS, and a calibrated latency centroid of P300 was the output for the future application bases of the SoD approach. The details can be found in [37].

- (2) ABC algorithm: in this paper, the parameters of IT2FLS were evaluated in terms of the swarm-based ABC algorithm that was inspired by the honey bee colonies' foraging behaviors. The scheme of the ABC algorithm is shown in Figure 8. The details can be found in [37].
- (3) Adaptive IT2FLS for BCI calibration: the block diagram of the proposed ABC-based adaptive IT2FLS is shown in Figure 9. A labeled training dataset is required to train the appropriate parameters of adaptive IT2FLS. A labeled training dataset includes a number of training trials. Each trial is a pair consisting of input values (the phase lag of evoked SSVEP) and a desired output value (the latency centroid of elicited P300). In the ABC algorithm, a fitness function describes the level of fitness of the m th food source, which is a D-dimensional vector consisting of the parameters of IT2FLS. The fitness function in this work is defined as (1).

$$\text{fitness} = \frac{1}{\sum_{k=1}^K g(y_{m,k}, y_{t \arg et,k})} \quad (1)$$

$$m = 1, 2, \dots, M \quad k = 1, 2, \dots, K$$

where $y_{m,k}$ is the output of the m th IT2FLS when the k th dataset is imported, $y_{t \arg et,k}$ is the desired output of the k th dataset, and g is the objective function that calculates mean square errors of the difference between $y_{m,k}$ and $y_{t \arg et,k}$, as

shown in (2). Thus, the m th food source is evaluated by a labeled training dataset that contains K datasets.

$$g(y_{m,k}, y_{t \arg et,k}) = \sqrt{(y_{m,k} - y_{t \arg et,k})^2} \quad (2)$$

$$m = 1, 2, \dots, M \quad k = 1, 2, \dots, K$$

2.4. CCA-Based Spatial Filter for Event-Related Potentials. Spatial filters are usually applied to improve the SNR of the EEG. CCA-based spatial filters have previously been used to increase the classification accuracy of evoked potentials, such as SSVEP. Spüler et al. proposed a CCA-based spatial filter for ERP [42]. Here, a CCA-based spatial filter is used to improve P300 classifications. CCA is a multivariate statistical method and can be applied to find linear transformations that maximize the correlation between the two datasets. There are two multidimensional datasets, M and N , with q variables. CCA is used to find two transformations, W_M and W_N , to maximize the canonical correlation ρ , as described in

$$U = W_M^T M \quad (3)$$

$$V = W_N^T N \quad (4)$$

$$\rho = \frac{\text{cov}(U, V)}{\sqrt{\text{var}(U) \text{var}(V)}} \quad (5)$$

where W_M and W_N are two transformations that maximize the canonical correlation ρ between canonical variables U and V . The canonical correlations of M and N are obtained by solving eigenvalue equations, as shown in

$$C_{MM}^{-1} C_{MN} C_{NN}^{-1} C_{NM} W_M = \rho^2 W_M \quad (6)$$

$$C_{NN}^{-1} C_{MN} C_{MM}^{-1} C_{NM} W_N = \rho^2 W_N \quad (7)$$

where C_{MM} and C_{NN} are covariance matrices of M and N , C_{MN} and C_{NM} are covariance matrices between M and N , ρ^2 is a squared canonical correlation value, and eigenvectors W_M and W_N are two transformation matrices. Here, W_M^T is used as the spatial filter. The CCA-based spatial filter acts as a whitening filter that decorrelates signals. By maximizing the canonical correlation, the CCA finds a spatial filter that improves the SNR of the elicited potentials.



FIGURE 8: The scheme of the ABC algorithm.

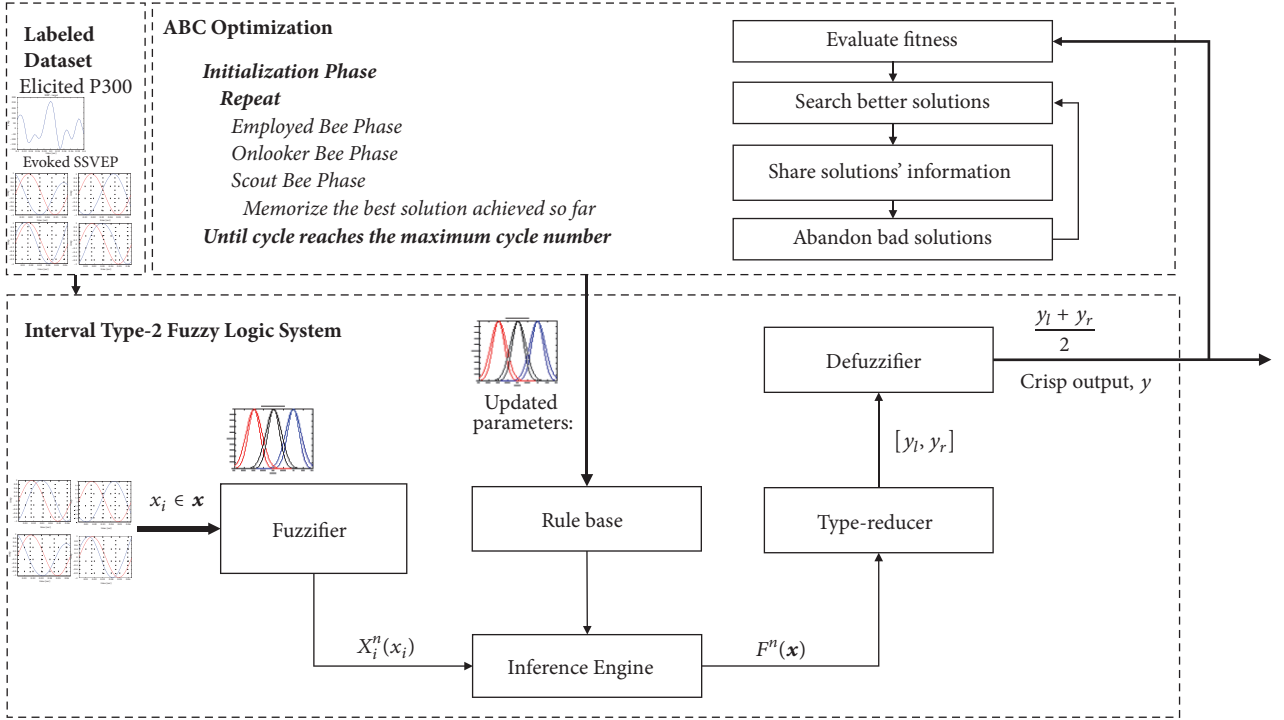


FIGURE 9: The block diagram of the proposed ABC-based adaptive IT2FLS.

2.5. SVM Classifier. Given a labeled dataset $\{(\mathbf{p}_i, q_i)\}_{i=1}^n, q_i \in \{1, -1\}$, where p_i are sampled EEG and q_i are class labels, SVM algorithm is trained by solving the following optimization problem:

$$\text{Minimize} \quad \frac{1}{2} \|\mathbf{w}\|^2 + C \sum_{i=1}^n \xi_i \quad (8)$$

$$\text{Subject to} \quad q_i (\mathbf{w}^T \phi(\mathbf{p}_i) + b) - 1 + \xi_i \geq 0 \quad (9)$$

w and b are the weight vector and the bias of hyperplane. ϕ maps p_i to a higher dimensional space and ξ_i are slack

variables. In this work, the radial basis function (RBF) is adopted to perform nonlinear classifications for BCI.

3. Experimental Paradigm

Eight healthy subjects, composed of 6 males and 2 females (mean age 22 years, standard deviation three years), participated in the experiments. All subjects were students at the National Taiwan University of Science and Technology and had minimal prior experience operating visual-based BCI. All subjects had normal or corrected to normal vision.

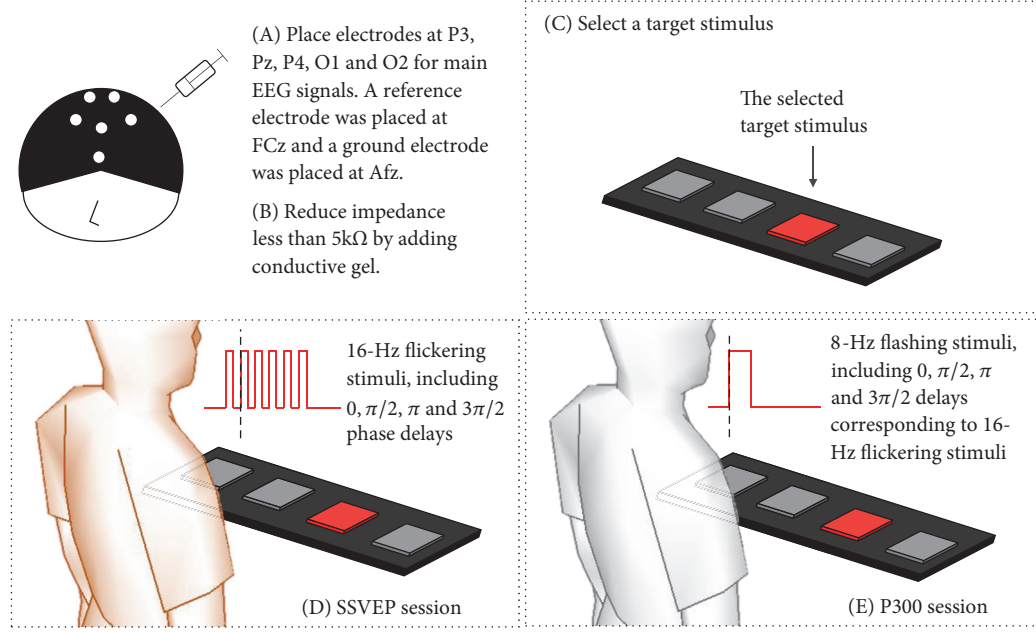


FIGURE 10: The experimental setup and paradigm.

Subjects were asked to view a stimulation panel of a 1×4 matrix. The stimulation panel was composed of four modules of LED arrays with the same dimensions of $3(\text{cm}) \times 3(\text{cm})$, which were placed with an interval of 8 cm between them. Each LED array presented visible red light on a black background and used moderate intensity. There was a 50 cm distance between the stimulation panel and the subjects, who were in comfortable positions. The experiments include two major components. First, a flickering stimulus was presented to observe SSVEP. A phase lag analysis was performed to realize the difference in evoked SSVEP when applying different stimulus phases. Second, a flashing stimulus was presented to observe the elicited P300. The averaging method was used to realize the difference in the elicited P300 between target and nontarget epochs. In addition, a certain delay was applied to realize the change of latency of the elicited P300. Finally, this work assessed how the latency of the elicited P300 correlated with the phase lag of SSVEP. The experimental setup is summarized in Figure 10.

3.1. SSVEP Session. To realize the phase lag of SSVEP when providing $0, \pi/2, \pi$, and $3\pi/2$ phase delays, a 16 Hz flickering stimulus was generated. To meet the scenario of the proposed BCI, the SSVEP sessions were conducted before the P300 sessions. There was a 1-minute break between the SSVEP and P300 sessions. Before starting the experiments, subjects were able to select any LED array module based on their comfort level. Each flickering stimulus continued for 5 seconds, and there was a 2-second interval between different phase stimuli.

3.2. P300 Session. To realize the responded latency of the elicited P300 when adding $0, \pi/2, \pi$, and $3\pi/2$ delays corresponding to 16 Hz flickering stimuli, an 8 Hz flashing stimulus was generated. Subjects were allowed to select an LED array

module that generated the flashing stimulus. The selected LED array module was regarded as the target stimulus, and the remaining LED array modules were regarded as nontarget stimuli. To improve the SNR of the elicited P300, each stimulus flashed 30 times, and extracted epochs were further averaged. Therefore, 120 epochs in total, including 30 target and 90 nontarget epochs, were collected.

3.3. SVM Classifier for P300-Based BCI. An SVM classifier was used to classify extract epoch into target or nontarget stimuli. In order to evaluate the implemented BCI, an online session was simulated. P300 dataset contained an amount of 10 sessions (5 subjects with two sessions each), and there were 100 trials for each session (100 targets and 300 nontargets). The epochs of first session were used as training dataset, and the epochs of second session were used as test dataset.

4. Experimental Results and Discussions

4.1. Correlation between Elicited P300 and Evoked SSVEP. To determine how the evoked SSVEP correlated with the latency of the elicited P300, phase delays, including $0, \pi/2, \pi$, and $3\pi/2$, for SSVEP and flashing delays, including 0.000 (ms) , 15.625 (ms) , 31.250 (ms) , and 46.875 (ms) , for P300 were evaluated. Because a 16 Hz flickering stimulus was adopted, the reference signal peaks at 15.625 ms ($t_{\text{ref}} = 15.625$) and the phase lags were obtained according to (10), where t_{res} is the latency of peak of the evoked SSVEP, and T is the period of flickering stimuli. Additionally, the latency of the elicited P300 was recognized according to the highest response elicited potential.

$$\theta = \frac{t_{\text{res}} - t_{\text{ref}}}{T} \times 360^\circ \quad (10)$$

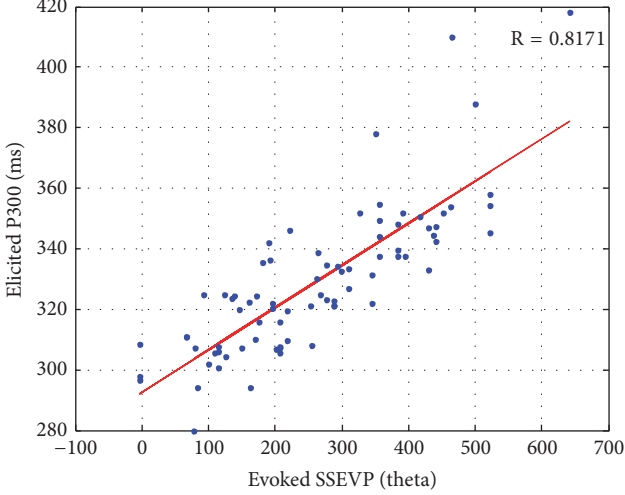


FIGURE 11: The scatter plot of elicited P300 and evoked SSVEP (8 subjects).

Eight subjects were involved in this experiment. Two datasets were collected on different days for each subject. A scatter plot showing the elicited P300 and evoked SSVEP is depicted in Figure 11. It reveals how the elicited P300 correlates with the evoked SSVEP. The correlation coefficient is computed by

$$R = \frac{\text{cov}(X_{P300}, Y_{SSVEP})}{\sigma_{X_{P300}} \sigma_{Y_{SSVEP}}} \quad (11)$$

where X_{P300} is the latency of the elicited P300, Y_{SSVEP} is the phase of the evoked SSVEP, and $\sigma_{X_{P300}}$ and $\sigma_{Y_{SSVEP}}$ are their standard deviations. Here, the correlation coefficient is 0.8171, which indicates high correlation between the evoked SSVEP and elicited P300.

4.2. The Adaptive IT2FLS for BCI Calibration Based on Evoked SSVEP. An adaptive IT2FLS was used to calibrate the latency centroid of the extracted epochs for P300 recognitions. Phase lags were the inputs of IT2FLS, and an estimated latency centroid of P300 was the output. An adaptive IT2FLS based on ABC optimization was trained by a labeled dataset. The labeled dataset consisted of evoked phase lags (features) and P300 latency centroids (target). Collected datasets were further divided into two groups (60% for training instances; 40% for evaluation instances). The training performance is shown in Figure 12. There were three membership functions for each fuzzy set (number of fuzzy sets = 4; number of membership functions = 3), as shown in Figure 13.

4.3. P300 Recognition with and without Calibrations. Here, a trained IT2FLS model was used to estimate the latency centroid of the elicited P300 according to the evoked SSVEP. Different lengths of extracted epochs, including 160 (ms), 140 (ms), 120 (ms), 100 (ms), 80 (ms), and 60 (ms), based on estimated centroid, were evaluated. If an estimated latency centroid was located at t_c , an extracted epoch ranged from $t_c - 80(\text{ms})$ to $t_c + 80(\text{ms})$ when the length of the extracted

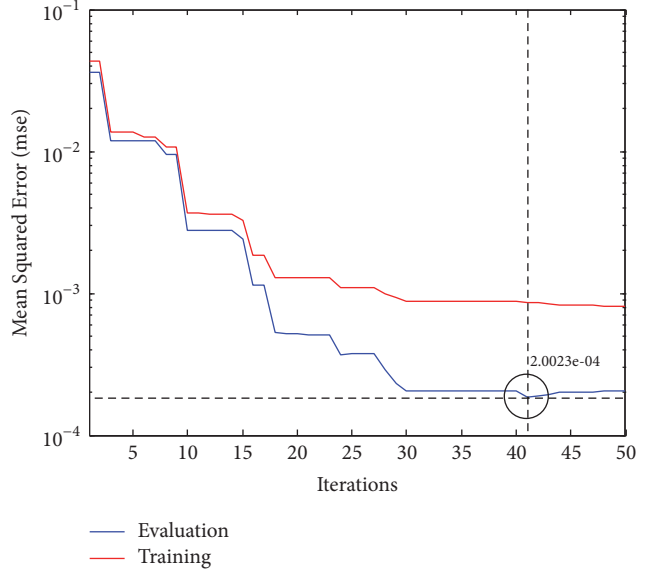


FIGURE 12: The training performance of ABC-based IT2FLS for BCI calibration.

epoch was 160 (ms). On the other hand, without calibrations, fixed intervals, including $t_s + 300$ to $t_s + 460$ (ms), $t_s + 300$ to $t_s + 440$ (ms), $t_s + 300$ to $t_s + 420$ (ms), $t_s + 300$ to $t_s + 400$ (ms), $t_s + 300$ to $t_s + 380$ (ms), and $t_s + 300$ to $t_s + 360$ (ms), were adopted. Here, t_s was the time of flashing stimulus. It was noted that 5 repetitions were conducted in this experiment, and the extracted epochs were downsampled at 62.5 Hz. The SVM classifier was employed to classify extracted epochs into target and nontarget stimuli. The accuracy rates of the SVM classifier and the ITRs with and without calibrations are shown in Figures 14–16 and Table 1. According to the experimental results, the performance of classification improves after calibration. In addition, the adopted classifier maintains satisfactory accuracy rates when decreasing the length of the extracted epoch.

5. Conclusion and Future Work

This work presented a wireless networking hybrid BCI to address the issue of improving the independence of individuals with SCIs. A scheme based on SoD architecture, which applies a P300-based BCI to wireless applications, was presented. However, because P300 recognitions rely on the synchronization between stimuli and elicited potential, the variation of latency between the target stimuli and elicited potential is a concern. Therefore, this work proposed “Registration” and “Operation” schemes that calibrated the latency centroid of P300 according to the evoked SSVEP and control stimulation-embedded appliances via P300. Therefore, the experiments attempted to assess how the latency of the elicited P300 correlates with the phase lag of the evoked SSVEP. Five subjects participated in the experiments, and a trained IT2FLS-based model was applied to estimate the possible latency centroid of the elicited P300 according to a phase lag analysis of the evoked SSVEP. In addition, an

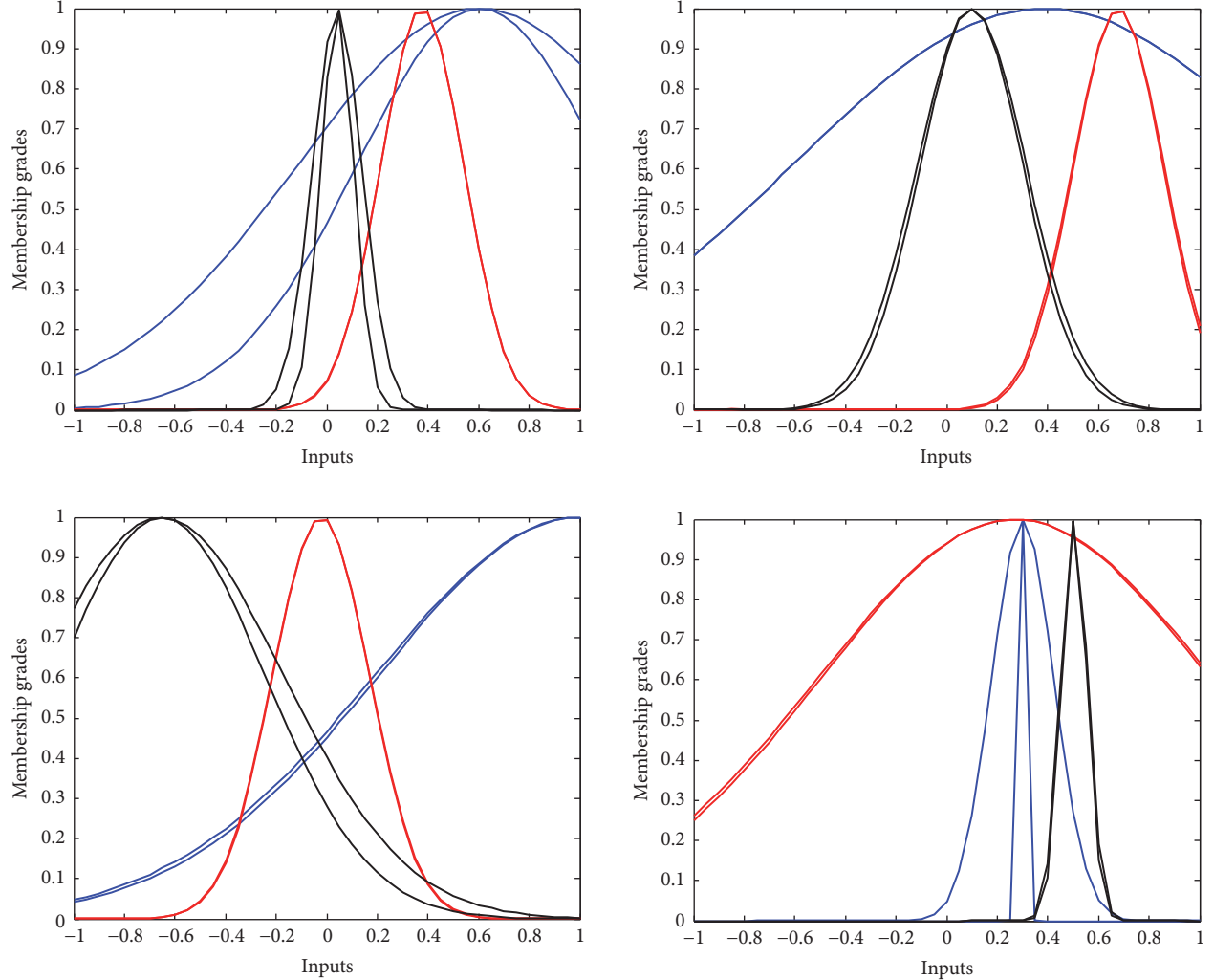


FIGURE 13: Antecedent membership functions for window calibrations.

TABLE 1: ITR (bits/min) comparisons between with and without calibrations.

Subject #	With calibrations					Without calibrations						
	1	2	3	4	5	Average	1	2	3	4	Average	
Length of epoch										ITR		
160	31.3	35.8	35.8	31.3	27.5	32.3	22.0	25.2	34.2	16.7	16.7	22.9
140	28.7	34.2	34.2	27.5	27.5	30.4	23.0	26.3	34.2	18.3	21.1	24.6
120	28.7	34.2	34.2	27.5	25.2	29.9	22.0	26.3	34.2	19.2	24.1	25.2
100	28.7	31.3	31.3	23.0	25.2	27.9	21.1	26.3	29.9	17.5	26.3	24.2
80	28.7	29.9	28.7	20.1	24.1	26.3	21.1	27.5	28.7	17.5	19.2	22.8
60	21.1	26.3	29.9	15.8	16.7	22.0	20.1	23.0	20.1	15.8	15.8	19.0

SVM classifier was employed to judge either target or non-target stimuli. Based on calibrated latency centroids, different lengths of extracted epochs were discussed. Classification performances showed that the accuracy rates improve after calibration.

In the future, the uncertainty of the ERP amplitude due to different distances between users and stimulation nodes is an interesting topic. In addition, the light intensity of the operating environment is another issue in real-world applications. The modulation of appropriate stimulus intensity related to

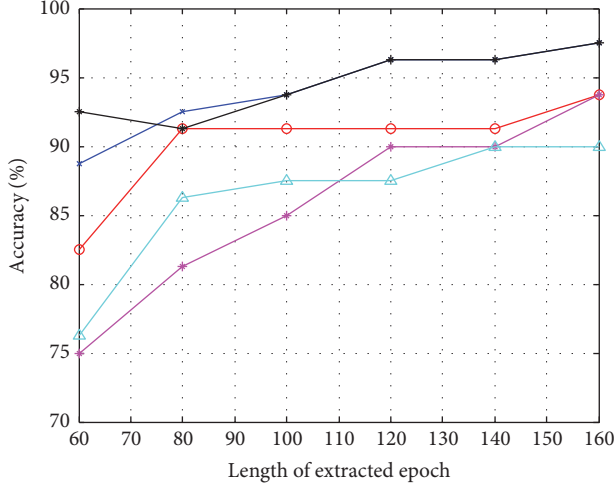


FIGURE 14: The accuracy of P300 classification depending on different lengths of extracted epochs with calibrations.

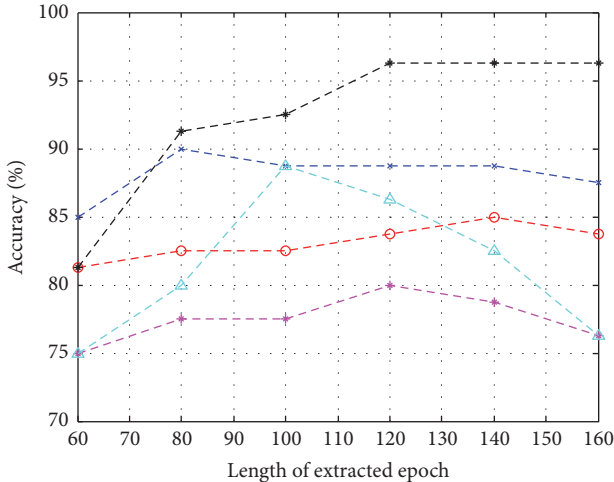


FIGURE 15: The accuracy of P300 classification depending on different lengths of extracted epochs without calibrations.

users' comfort and system performance would be another future work of this paper.

Data Availability

The data used to support the findings of this study are available from the corresponding author upon request.

Conflicts of Interest

The authors declare no conflicts of interest.

Acknowledgments

This work was financially supported by the “Center for Cyber-physical System Innovation” from The Featured Areas Research Center Program within the framework of the

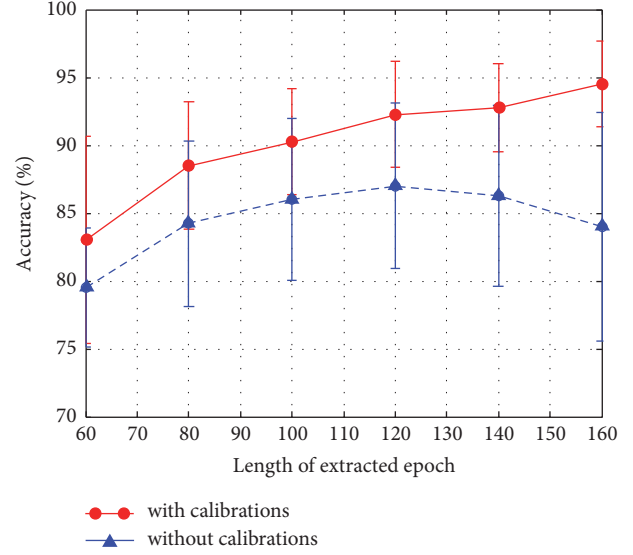


FIGURE 16: The comparison between with and without calibrations depending on different lengths of extracted epochs.

Higher Education Sprout Project by the Ministry of Education (MOE) in Taiwan.

References

- [1] W. H. O., “Spinal cord injury,” <http://www.who.int/media-centre/factsheets/fs384/en>, [Aug. 14, 2015], 2013.
- [2] C. Escolano, J. M. Antelis, and J. Minguez, “A telepresence mobile robot controlled with a noninvasive brain-computer interface,” *IEEE Transactions on Systems, Man, and Cybernetics, Part B: Cybernetics*, vol. 42, no. 3, pp. 793–804, 2012.
- [3] Y. Chae, J. Jeong, and S. Jo, “Toward brain-actuated humanoid robots: asynchronous direct control using an EEG-Based BCI,” *IEEE Transactions on Robotics*, vol. 28, no. 5, pp. 1131–1144, 2012.
- [4] V. Gandhi, G. Prasad, D. Coyle, L. Behera, and T. M. McGinnity, “EEG-Based mobile robot control through an adaptive brain-robot interface,” *IEEE Transactions on Systems, Man, and Cybernetics: Systems*, vol. 44, no. 9, pp. 1278–1285, 2014.
- [5] D. P. McMullen, G. Hotson, K. D. Katyal et al., “Demonstration of a semi-autonomous hybrid brain-machine interface using human intracranial EEG, eye tracking, and computer vision to control a robotic upper limb prosthetic,” *IEEE Transactions on Neural Systems and Rehabilitation Engineering*, vol. 22, no. 4, pp. 784–796, 2014.
- [6] A. Frisoli, C. Loconsole, D. Leonardis et al., “A new gaze-BCI-driven control of an upper limb exoskeleton for rehabilitation in real-world tasks,” *IEEE Transactions on Systems, Man, and Cybernetics, Part C: Applications and Reviews*, vol. 42, no. 6, pp. 1169–1179, 2012.
- [7] J.-C. Liu, H.-C. Chou, C.-H. Chen, Y.-T. Lin, and C.-H. Kuo, “Time-Shift Correlation Algorithm for P300 Event Related Potential Brain-Computer Interface Implementation,” *Computational Intelligence and Neuroscience*, vol. 2016, pp. 1–22, 2016.
- [8] B. Z. Allison, C. Brunner, V. Kaiser, G. R. Müller-Putz, C. Neuper, and G. Pfurtscheller, “Toward a hybrid brain-computer interface based on imagined movement and visual attention,” *Journal of Neural Engineering*, vol. 7, no. 2, Article ID 026007, 2010.

- [9] G. Pfurtscheller, T. Solis-Escalante, R. Ortner, P. Linortner, and G. R. Muller-Putz, "Self-paced operation of an SSVEP-based orthosis with and without an imagery-based "brain switch": a feasibility study towards a hybrid BCI," *IEEE Transactions on Neural Systems and Rehabilitation Engineering*, vol. 18, no. 4, pp. 409–414, 2010.
- [10] B. Rebsamen, E. Burdet, Q. Zeng et al., "Hybrid P300 and mu-beta brain computer interface to operate a brain controlled wheelchair," in *Proceedings of the 2nd Int. Conf. Rehab. Eng. Assist. Tech.*, pp. 51–55, 2008.
- [11] E. Yin, T. Zeyl, R. Saab, T. Chau, D. Hu, and Z. Zhou, "A hybrid brain—computer interface based on the fusion of P300 and SSVEP scores," *IEEE Transactions on Neural Systems and Rehabilitation Engineering*, vol. 23, no. 4, pp. 693–701, 2015.
- [12] E. Yin, Z. Zhou, J. Jiang, Y. Yu, and D. Hu, "A dynamically optimized SSVEP brain-computer interface (BCI) speller," *IEEE Transactions on Biomedical Engineering*, vol. 62, no. 6, pp. 1447–1456, 2015.
- [13] E. Yin, T. Zeyl, R. Saab, D. Hu, Z. Zhou, and T. Chau, "An auditory-tactile visual saccade-independent P300 brain-computer interface," *International Journal of Neural Systems*, vol. 26, no. 1, Article ID 1650001, 2016.
- [14] M. A. Oskoei, J. Q. Gan, and H. Hu, "Adaptive schemes applied to online SVM for BCI data classification," in *Proceedings of the 2009 IEEE Ann. Int. Conf. Eng. Med. Biol. Soc. (EMBC)*, pp. 2600–2603, 2009.
- [15] Z. Gu, Z. Yu, Z. Shen, and Y. Li, "An online semi-supervised brain-computer interface," *IEEE Transactions on Biomedical Engineering*, vol. 60, no. 9, pp. 2614–2623, 2013.
- [16] S. Siuly and Y. Li, "Improving the separability of motor imagery EEG signals using a cross correlation-based least square support vector machine for brain-computer interface," *IEEE Transactions on Neural Systems and Rehabilitation Engineering*, vol. 20, no. 4, pp. 526–538, 2012.
- [17] Y. Zhang, G. Zhou, Q. Zhao, J. Jin, X. Wang, and A. Cichocki, "Spatial-temporal discriminant analysis for ERP-based brain-computer interface," *IEEE Transactions on Neural Systems and Rehabilitation Engineering*, vol. 21, no. 2, pp. 233–243, 2013.
- [18] R. Xu, N. Jiang, C. Lin, N. Mrachacz-Kersting, K. Dremstrup, and D. Farina, "Enhanced low-latency detection of motor intention from EEG for closed-loop brain-computer interface applications," *IEEE Transactions on Biomedical Engineering*, vol. 61, no. 2, pp. 288–296, 2014.
- [19] A. Barachant, S. Bonnet, M. Congedo, and C. Jutten, "Multiclass brain-computer interface classification by Riemannian geometry," *IEEE Transactions on Biomedical Engineering*, vol. 59, no. 4, pp. 920–928, 2012.
- [20] C. Vidaurre, M. Kawanabe, P. Von Bünnau, B. Blankertz, and K. R. Müller, "Toward unsupervised adaptation of LDA for brain-computer interfaces," *IEEE Transactions on Biomedical Engineering*, vol. 58, no. 3, pp. 587–597, 2011.
- [21] B. Rivet, A. Souloumiac, V. Attina, and G. Gibert, "xDawn algorithm to enhance evoked potentials: application to brain-computer interface," *IEEE Transactions on Biomedical Engineering*, vol. 56, no. 8, pp. 2035–2043, 2009.
- [22] X. Lei, P. Yang, and D. Yao, "An empirical bayesian framework for brain-computer interfaces," *IEEE Transactions on Neural Systems and Rehabilitation Engineering*, vol. 17, no. 6, pp. 521–529, 2009.
- [23] M. Higger, M. Akcakaya, H. Nezamfar, G. LaMountain, U. Orhan, and D. Erdogmus, "A Bayesian framework for intent detection and stimulation selection in SSVEP BCIs," *IEEE Signal Processing Letters*, vol. 22, no. 6, pp. 743–747, 2014.
- [24] H.-I. Suk and S.-W. Lee, "A novel bayesian framework for discriminative feature extraction in brain-computer interfaces," *IEEE Transactions on Pattern Analysis and Machine Intelligence*, vol. 35, no. 2, pp. 286–299, 2013.
- [25] Y. J. Chen, A. R. A. See, and S. C. Chen, "SSVEP-based BCI classification using power cepstrum analysis," *IEEE Electronics Letters*, vol. 50, no. 10, pp. 735–737, 2014.
- [26] R. Palaniappan, "Utilizing gamma band to improve mental task based brain-computer interface design," *IEEE Transactions on Neural Systems and Rehabilitation Engineering*, vol. 14, no. 3, pp. 299–303, 2006.
- [27] G. Pfurtscheller and C. Neuper, "Motor imagery and direct brain-computer communication," *Wireless SoD P300 Hybrid BCI*, vol. 89, no. 7, pp. 1123–1134, 2001.
- [28] J.-M. Cano-Izquierdo, J. Ibarrola, and M. Almonacid, "Improving motor imagery classification with a new BCI design using neuro-fuzzy S-dFasArt," *IEEE Transactions on Neural Systems and Rehabilitation Engineering*, vol. 20, no. 1, pp. 2–7, 2012.
- [29] H. Cecotti and A. Gräser, "Convolutional neural networks for P300 detection with application to brain-computer interfaces," *IEEE Transactions on Pattern Analysis and Machine Intelligence*, vol. 33, no. 3, pp. 433–445, 2011.
- [30] D. Coyle, G. Prasad, and T. M. McGinnity, "Faster self-organizing fuzzy neural network training and a hyperparameter analysis for a brain-computer interface," *IEEE Transactions on Systems, Man, and Cybernetics, Part B: Cybernetics*, vol. 39, no. 6, pp. 1458–1471, 2009.
- [31] C.-L. Lin, Y.-M. Chang, C.-C. Hung, C.-D. Tu, and C.-Y. Chuang, "Position Estimation and Smooth Tracking with a Fuzzy-Logic-Based Adaptive Strong Tracking Kalman Filter for Capacitive Touch Panels," *IEEE Transactions on Industrial Electronics*, vol. 62, no. 8, pp. 5097–5108, 2015.
- [32] H.-Y. Chung, C.-C. Hou, and Y.-S. Chen, "Indoor intelligent mobile robot localization using fuzzy compensation and kalman filter to fuse the data of gyroscope and magnetometer," *IEEE Transactions on Industrial Electronics*, vol. 62, no. 10, pp. 6436–6447, 2015.
- [33] S.-C. Wang and Y.-H. Liu, "A PSO-Based Fuzzy-Controlled Searching for the Optimal Charge Pattern of Li-Ion Batteries," *IEEE Transactions on Industrial Electronics*, vol. 62, no. 5, pp. 2983–2993, 2015.
- [34] Z. Li, C.-Y. Su, L. Wang, Z. Chen, and T. Chai, "Nonlinear Disturbance Observer-Based Control Design for a Robotic Exoskeleton Incorporating Fuzzy Approximation," *IEEE Transactions on Industrial Electronics*, vol. 62, no. 9, pp. 5763–5775, 2015.
- [35] E. Kayacan, E. Kayacan, and M. Ahmadieh Khanesar, "Identification of nonlinear dynamic systems using type-2 fuzzy neural networks - A novel learning algorithm and a comparative study," *IEEE Transactions on Industrial Electronics*, vol. 62, no. 3, pp. 1716–1724, 2015.
- [36] D. Karaboga and B. Basturk, "A powerful and efficient algorithm for numerical function optimization: artificial bee colony (ABC) algorithm," *Journal of Global Optimization*, vol. 39, no. 3, pp. 459–471, 2007.
- [37] C.-H. Kuo, Y.-C. Kuo, H.-C. Chou, and Y.-T. Lin, "P300-based Brain-Computer Interface with Latency Estimation Using ABC-based Interval Type-2 Fuzzy Logic System," *International Journal of Fuzzy Systems*, vol. 19, no. 2, pp. 529–541, 2017.
- [38] R. C. Panicker, S. Puthuserypady, and Y. Sun, "An asynchronous P300 BCI with SSVEP-based control state detection,"

- IEEE Transactions on Biomedical Engineering*, vol. 58, no. 6, pp. 1781–1788, 2011.
- [39] E. Yin, Z. Zhou, J. Jiang, F. Chen, Y. Liu, and D. Hu, “A speedy hybrid BCI spelling approach combining P300 and SSVEP,” *IEEE Transactions on Biomedical Engineering*, vol. 61, no. 2, pp. 473–483, 2014.
- [40] X.-A. Fan, L. Bi, T. Teng, H. Ding, and Y. Liu, “A brain-computer interface-based vehicle destination selection system using P300 and SSVEP signals,” *IEEE Transactions on Intelligent Transportation Systems*, vol. 16, no. 1, pp. 274–283, 2015.
- [41] Y. Li, J. Pan, F. Wang, and Z. Yu, “A hybrid BCI system combining P300 and SSVEP and its application to wheelchair control,” *IEEE Transactions on Biomedical Engineering*, vol. 60, no. 11, pp. 3156–3166, 2013.
- [42] M. Spüler, A. Walter, W. Rosenstiel, and M. Bogdan, “Spatial filtering based on canonical correlation analysis for classification of evoked or event-related potentials in EEG data,” *IEEE Transactions on Neural Systems and Rehabilitation Engineering*, vol. 22, no. 6, pp. 1097–1103, 2014.

Research Article

Multiclass Motor Imagery Recognition of Single Joint in Upper Limb Based on NSGA- II OVO TWSVM

Shan Guan , Kai Zhao , and Fuwang Wang 

School of Mechanical Engineering, Northeast Electric Power University, 132012 Jilin, China

Correspondence should be addressed to Shan Guan; guanshan1970@163.com

Received 19 April 2018; Accepted 7 June 2018; Published 28 June 2018

Academic Editor: Plácido R. Pinheiro

Copyright © 2018 Shan Guan et al. This is an open access article distributed under the Creative Commons Attribution License, which permits unrestricted use, distribution, and reproduction in any medium, provided the original work is properly cited.

In the study of the brain computer interface (BCI) system, electroencephalogram (EEG) signals induced by different movements of the same joint are hard to distinguish. This paper proposes a novel scheme that combined amplitude-frequency (AF) information of intrinsic mode function (IMF) with common spatial pattern (CSP), namely, AF-CSP to extract motor imagery (MI) features, and to improve classification performance, the second generation nondominated sorting evolutionary algorithm (NSGA-II) is used to tune hyperparameters for linear and nonlinear kernel one versus one twin support vector machine (OVO TWSVM). This model is compared with least squares support vector machine (LS-SVM), back propagation (BP), extreme learning machine (ELM), particle swarm optimization support vector machine (PSO-SVM), and grid search OVO TWSVM (GS OVO TWSVM) on our dataset; the recognition accuracy increased by 5.92%, 22.44%, 22.65%, 8.69%, and 5.75%. The proposed method has helped to achieve higher accuracy in BCI systems.

1. Introduction

BCI is a technology that enables the brain to establish communication and control directly between human brain and computer or other electronic devices without the help of peripheral nerves and limbs [1, 2]. BCI technology not only enhances the ability of disabled patients to communicate with the outside world in the field of medical rehabilitation [3, 4], but also has wide applications in smart home, mass consumption and entertainment, military, and other fields. At present, the research direction of BCI system is mainly in the following aspects: sensorimotor (SMR) [5], slow cortical potential (SCP) [6], P300 event-related potential [7], and steady-state visual evoked potential (SSVEP) [8]. The most widely used is the SMR BCI system based on motor imagery.

The μ (8–13Hz) and β (13–30Hz) rhythms in EEG signals will cause a phenomenon named event-related desynchronization (ERD) and event-related synchronization (ERS) when motor imagery occurs [9, 10]. This means that the rhythmic activities of the brain represent frequency specific changes may consist either of decreases or of increases of

power in given frequency bands. The ERD/ERS phenomenon is an important basis for the BCI systems of motor imagery.

In order to improve the classification accuracy of the BCI system, researchers have studied the feature extraction methods and classification methods of EEG signals [11–15]. The most commonly used feature extraction methods include wavelet packet transform (WT), Fourier transform (FT), CSP [16, 17], and autoregressive (AR) model. The classification methods include linear discriminant analysis (LDA), support vector machine (SVM), neural network (NN), and so on. Wang et al. used the convolution neural network (CNN) to recognize the image of the brain topographic map of three kinds of motor imagery movements of the upper limb, flexion wrist, and wrist external rotation, and the highest recognition rate in the three classification experiments is 67.89% [18]. Roy et al. carried out Hilbert transform for two kinds of motor imagery of shoulder and elbow joint and used discrete wavelet transformation to extract features; SVM gets the highest recognition rate of 84.91% in the five recognition methods [19]. Sachin et al. used empirical mode decomposition (EMD) to extract the energy features of left and right hand motor

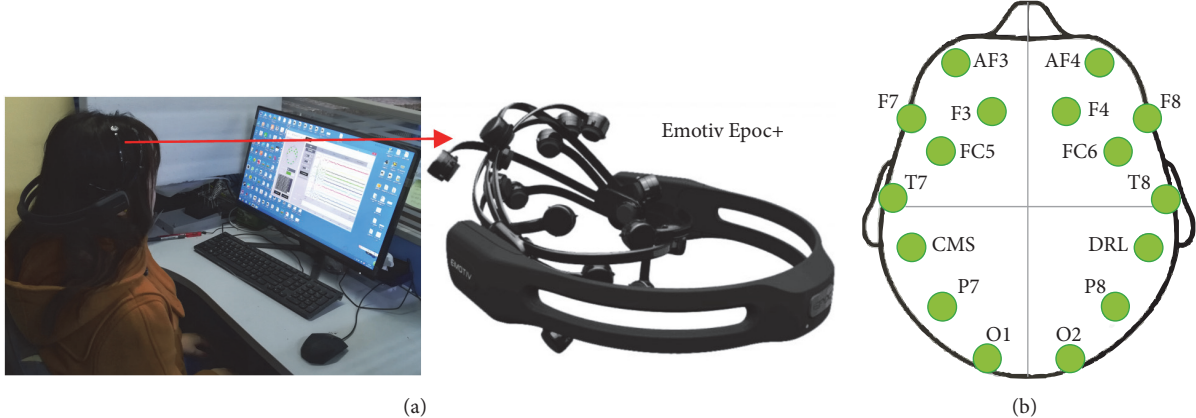


FIGURE 1: (a) Experimental photos and Emotiv Epoc+ and (b) Emotiv 14 electrodes located over 10-20 international system positions.

imagery EEG signals and classified them using LS-SVM; the recognition rate is no less than 95.56% [20]. Tang et al. used PSO to optimize the hidden-layer visible deep stacking network (HVDSN) to recognize the left and right hand motor imagery EEG signals; the recognition rate is no less than 89.84% [21]. Although the above studies have achieved high recognition results, most of the research focuses on hands and feet motor imagery, few studies have been conducted based on multiclass motor imagery of single joint.

In this paper, we propose a method to improve accuracy of motor imagery BCI using AF-CSP and an optimized OVO TWSVM classifier. The proposed method is composed of a total of four stages. First, a notch filter and common average reference (CAR) are used to remove noise in EEG signal. Second, EMD is used to obtain IMF, and FFT is used to obtain AF information of the IMF. Third, the NSGA-II is used to tune hyperparameters for linear and nonlinear OVO TWSVM. Finally, an optimized OVO TWSVM classifier is evaluated using laboratory data sets (three kinds of motor imagery of shoulder flexion, extension, and abduction) and compared with state-of-the-art algorithms (LS-SVM, BP, ELM, PSO-SVM, and GS OVO TWSVM).

2. Materials and Methods

Emotiv Epoc+ is used to collect EEG data of motor imagery. It is a portable EEG acquisition device with a sampling rate of 128Hz. It has fourteen electrode channels (AF3, F7, F3, FC5, T7, P7, O1, O2, P8, T8, FC6, F4, F8, and AF4) and two inference electrodes (CMS, DRL), and the electrode placement follows the international 10-20 standard. Experimental photos, equipment, and the Emotiv 14 electrodes are located over 10-20 international system positions as shown in Figure 1. This experiment collected three kinds of EEG signals of one joint: imagination of shoulder flexion, extension, and abduction, as shown in Figure 2.

Seven subjects participated in this experimental study. These subjects were in good health. During the experiment, subjects were naturally placed with both hands, trying to avoid body or head movement. During the experiment, subjects carried out motor imagery under the outside cue,

a single experiment collected EEG signal for 5 seconds, and then take 5-7 seconds to have a rest; each action repeated acquisition 20 times. The experimental process is shown in Figure 3. The dimension of EEG is high and the amount of data is large, in order to reduce the computational complexity. In this paper, the EEG signals collected from four electrode channels of FC5, F3, F4, and FC6 were selected for the following motor imagery analysis.

3. Theories and Methods

3.1. Data Preprocessing. EEG signals contain a variety of noise, and it is necessary to perform spatial filtering before feature extraction of the signal. First, the 50Hz notch filter is used to remove the power frequency noise. McFarland et al. compared four kinds of spatial filtering technology to improve the SNR of EEG signal, and the conclusion shows the superiority of CAR and large Laplacian methods [21]; this paper uses CAR method as the spatial filter. The calculation of CAR is to subtract the average of all the electrodes from the selected channel. The formula for calculation is as follows:

$$V_i^{CAR} = V_i^{RAW} - \frac{1}{4} \sum_{j=1}^4 V_j^{RAW} \quad (1)$$

where V_i^{CAR} is filtered potential and V_i^{RAW} is the potential of the i electrode.

3.2. Empirical Mode Decomposition. EMD is used to stabilize the nonstationary signals and obtain IMF. The specific EMD decomposition process is given in document [22]. EEG signal can be decomposed into IMF components after the empirical mode decomposition, and the expression is as follows:

$$S(t) = \sum_{i=1}^N C_i(t) + R_n(t) \quad (2)$$

where $S(t)$ represents the original EEG signal, $C_i(t)$ is the i^{th} IMF, and $R_n(t)$ is residual components after screening.

Taking the 1-4s data of the F3 electrode channel in Figure 3, as an example, use EMD method to decompose

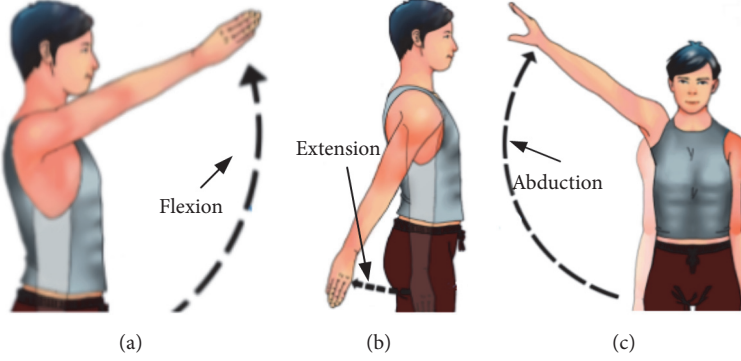


FIGURE 2: Three movements of shoulder joint: (a) flexion, (b) extension, and (c) abduction.



FIGURE 3: Timing for experimental process.

the denoised signal, and the IMF component is shown in Figure 4(a). Figure 4(b) is the AF domain information for the IMF component after FFT. From Figure 4(b), we can see that the μ and β rhythms of the motor imagery are mainly distributed in IMF1 and IMF2. In this paper, the sampled data of the selected 4 electrode channels are decomposed by EMD, respectively, do FFT to IMF1 and IMF2 of each electrode channel, and construct the i^{th} experiment EEG data matrix X_i ($i = N \times M$), where N corresponds to this article is 8 and M is the selected information of μ and β rhythms.

3.3. Common Spatial Pattern. The traditional CSP algorithm is essentially looking for a spatial filter to obtain more obvious eigenvectors after the signal passed through the filter, which makes a kind of signal variance reach a maximum, and another signal reaches a minimum. This method achieves the purpose of distinguishing two types of signals. Combining AF information of IMF with CSP to form AF-CSP and applying one versus one (OVO) strategy to AF-CSP make AF-CSP suitable for multiple classification problems, and the specific process is as follows:

$$R = \frac{X_i X_i^T}{\text{trace}(X_i X_i^T)} \quad (3)$$

where T is transpose operator. Then calculate the mixed space covariance matrix R_c of the two types motor imagery R_l , R_r as follows:

$$R_C = R_l + R_r \quad (4)$$

Eigenvalue decomposition for covariance of mixed space is as follows:

$$R_C = U_C A_C U_C^T \quad (5)$$

where U_C is the eigenvector matrix and A_C is the eigenvalue diagonal matrix. Whitening matrix P is calculated in

$$P = A_C^{-1/2} U_C^T \quad (6)$$

The whitening matrix causes eigenvalues of transformed matrix be equal one, so we calculate transformed covariance matrixes S_j and S_k in

$$S_j = P R_l P^T \quad (7)$$

$$S_k = P R_r P^T \quad (8)$$

After whitening, the matrixes S_j and S_k have the same eigenvector, and the following formula can be obtained after the eigenvalue decomposition:

$$S_j = B A_T B^T \quad (9)$$

$$S_k = B A_R B^T \quad (10)$$

The desired spatial filter is obtained by the upper form $W = (B^T P)^T$, and we can get a new data matrix after filtering by W : $Z_{N \times M} = W_{N \times M} X_i$. Feature vectors can be obtained by

$$f_p = \log \left(\frac{\text{var}(Z_p)}{\sum_i^{2m} \text{var}(Z_i)} \right) \quad (11)$$

where Z_p ($p = 1, \dots, 2m$). The dimension of f_p can not exceed N at most; in this paper, we set $m = 2$, so we can get a vector of four dimensions.

Combined with OVO strategy, eigenvectors constructed between every two types of actions are

$$f_1 = [F_1, E_1] \quad (12)$$

$$f_2 = [F_2, A_1] \quad (13)$$

$$f_3 = [E_2, A_2] \quad (14)$$

where f_1 represents the eigenvector obtained after AF-CSP transformation of flexion (F_1) and extension (E_1) of shoulder

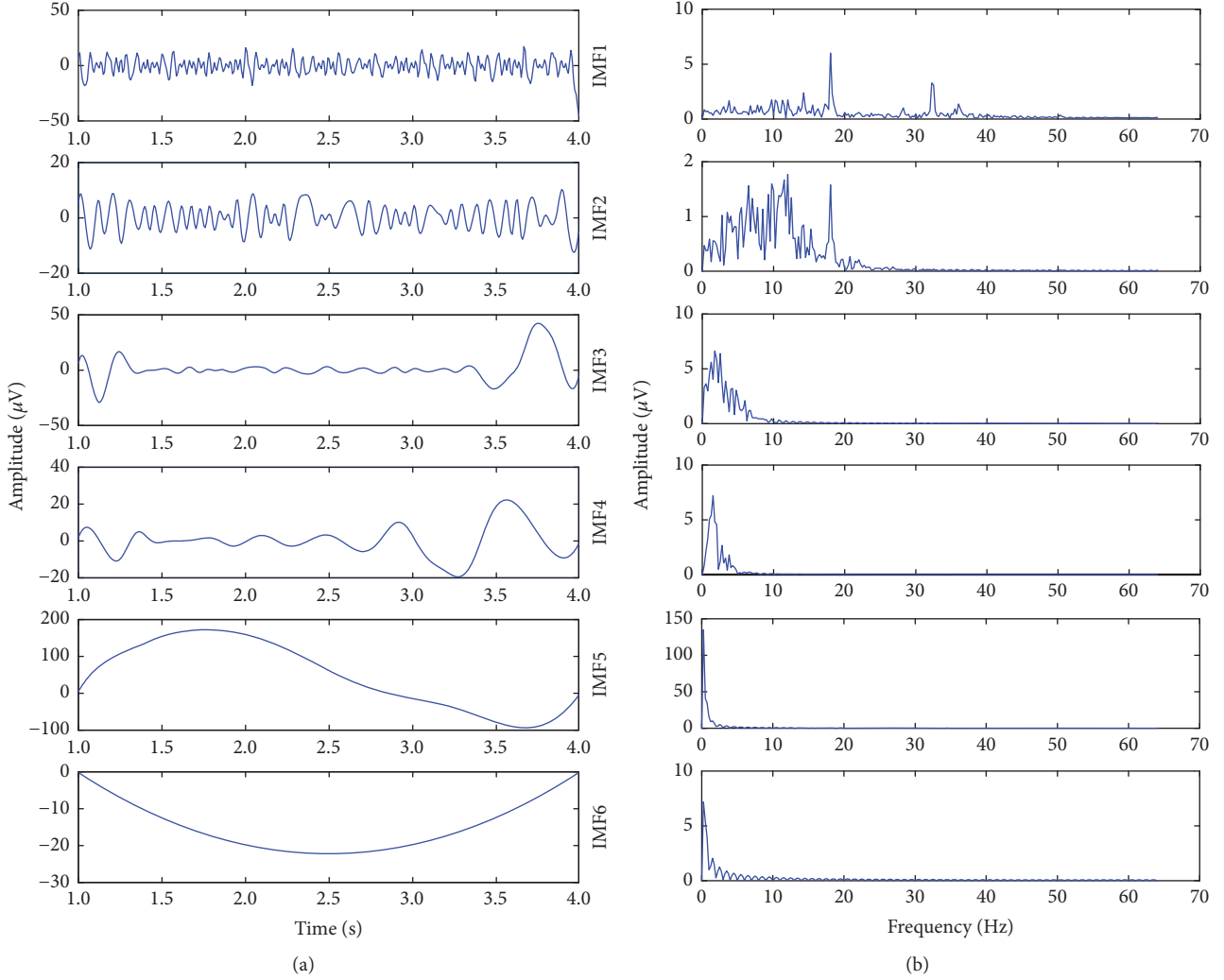


FIGURE 4: (a) IMF obtained from 3s EEG signals after EMD decomposition. (b) Amplitude-frequency domain information corresponds to per IMF of Figure 4(a).

joint. f_2 represents the eigenvector obtained after AF-CSP transformation of flexion (F_2) and abduction (A_1) of shoulder joint. f_3 represents the eigenvector obtained after AF-CSP transformation of extension (E_2) and abduction (A_2) of shoulder joint.

Figure 5 shows one example of the eigenvector f_1 constructed by AF-CSP of subject B, and f_1 is constructed by two MI tasks of shoulder joint flexion and extension. In Figure 5, the lateral axis represents the sequence number of experiments and the vertical axis represents the eigenvalue. We can see clearly from Figure 5 that the selected 4-dimensional feature vectors constructed by AF-CSP are distinctly distinguishable. The final eigenvector constructed by the AF-CSP method is

$$f = \begin{bmatrix} F_1 & F_2 \\ E_1 & E_2 \\ A_1 & A_2 \end{bmatrix} \quad (15)$$

3.4. Twin Support Vector Machine. TWSVM, which is developed on the basis of traditional SVM, is a new machine learning method [23]. For the two-classification problem, TWSVM constructs a hyperplane for every class of samples, so that each class sample is closest to its own hyperplane and far away from another hyperplane. TWSVM solves two-classification problem by solving a set of quadratic programming problems (QPPs), and SVM solves all classification problems by solving one QPP. This strategy makes TWSVM work 4 times faster than a standard SVM [24].

Combine OVO strategy with standard TWSVM to get OVO TWSVM, and the OVO TWSVM has a better classification performance than the OVO SVM [25]. For k class classification problem, the algorithm constructs a two-classification TWSVM subclassifier between any two classes of samples. Each subclassifier in OVO TWSVM needs only two classes of samples for training. Two hyperplanes are needed to train two types of sample i and j , such as

$$x^T w_{ij} + b_{ij} = 0 \quad (16)$$

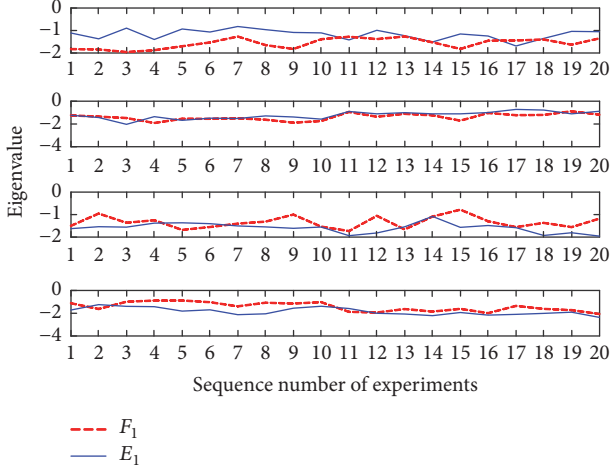


FIGURE 5: Twenty sets of four-dimensional eigenvectors f_1 obtained by AF-CSP method of flexion and extension of shoulder joint.

$$x^T w_{ji} + b_{ij} = 0 \quad (17)$$

where w_{ij} and w_{ji} are two normal vectors of hyperplanes and b_{ij} and b_{ji} are two hyperplanes. It is generally obtained by solving the following two-quadratic programming problem:

$$\begin{aligned} \min \quad & \frac{1}{2} \|A_i w_{ij} + e_{ij}^{(1)} b_{ij}\|^2 + \frac{c_{ij}}{2} e_{ij}^{(2)T} \xi_{ij} \\ \text{s.t.} \quad & (A_i w_{ij} + e_{ij}^{(2)} b_{ij}) + \xi_{ij} \geq e_{ij}^{(2)}, \quad \xi_{ij} \geq 0 \end{aligned} \quad (18)$$

$$\begin{aligned} \min \quad & \frac{1}{2} \|A_j w_{ji} + e_{ij}^{(2)} b_{ji}\|^2 + \frac{c_{ji}}{2} e_{ij}^{(2)T} \xi_{ji} \\ \text{s.t.} \quad & (A_j w_{ji} + e_{ij}^{(1)} b_{ji}) + \xi_{ji} \geq e_{ij}^{(2)}, \quad \xi_{ji} \geq 0 \end{aligned} \quad (19)$$

where c_{ij} is a penalty parameter and e_{ij} is a column vector of 1.

For the nonlinear separable phenomenon of training data, OVO TWSVM needs to solve the following optimization problems when training two samples of i and j :

$$\begin{aligned} \min \quad & \frac{1}{2} \|K(A_i, C^T) w_{ji} + e_{ij}^{(1)} b_{ji}\|^2 + \frac{c_{ij}}{2} e_{ij}^T \xi_{ij} \\ \text{s.t.} \quad & (K(A_i, C^T) w_{ji} + e_{ij}^{(2)} b_{ji}) + \xi_{ji} = e_{ij}^{(2)}, \quad \xi_{ij} \geq 0 \end{aligned} \quad (20)$$

$$\begin{aligned} \min \quad & \frac{1}{2} \|K(A_i, C^T) w_{ji} + e_{ij}^{(2)} b_{ji}\|^2 + \frac{c_{ji}}{2} e_{ij}^T \xi_{ji} \\ \text{s.t.} \quad & (K(A_i, C^T) w_{ji} + e_{ij}^{(1)} b_{ji}) + \xi_{ji} = e_{ij}^{(1)}, \quad \xi_{ji} \geq 0 \end{aligned} \quad (21)$$

Taking three-classification problem in two-dimensional space as an example to illustrate the process of OVO TWSVM with Figure 6. Taking i and j in (21) and (22) as 1 and 2 and solving them, we can get a two-class OVO TWSVM that classifies class 1 and class 2, i.e., subclassifier 1 in Figure 6. The subclassifier 2 and the subclassifier 3 can be obtained by a similar method, which constitute the OVO TWSVM for solving the three-classification problem together. Taking the green dot in the figure as an example to illustrate how to

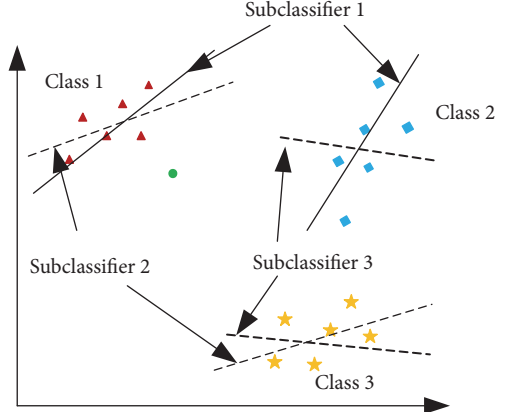


FIGURE 6: The sketch map of OVO TWSVM.

use OVO TWSVM. First, calculate the distance from the dot to the two hyperplanes of subclassifier 1; because the dot is close to the hyperplane of class 1, class 1 gets 1 vote. Second, calculate the distance from the dot to the subclassifier 2 in the same manner; since the dot is close to one hyperplane of subclassifier 2 in class 1, class 1 gets 1 more vote. Third, calculate the distance from the dot to the subclassifier 3; because the dot is close to one hyperplane of subclassifier 3 in class 2, class 2 got 1 vote and class 3 got 0 vote. OVO TWSVM classify the classified sample into class 1.

For the three-classification problem of this article, three OVO TWSVM subclassifiers need to set 6 penalty parameters: $c_{11}, c_{12}, c_{21}, c_{22}, c_{31}$, and c_{32} . This article sets $c_{11}=c_{21}=c_{31}, c_{12}=c_{22}=c_{32}$.

3.5. Multiobjective Genetic Algorithm. The core of the multi-objective genetic algorithm is to coordinate the relationship between the target functions and to make the target functions reach the Pareto optimal set. The quality of a solution in the Pareto optimal set is defined according to the dominance criterion. Any solution λ of the Pareto optimal set can be seen as an acceptable solution. If a solution λ_1 is no worse than λ_2 in all objectives and λ_1 is better than λ_2 in at least one objective, then we define λ_1 dominates λ_2 . The multiobjective optimization problem can be stated as

$$\text{Maximize } F(\omega) = \{f_1(\omega), f_2(\omega), \dots, f_n(\omega)\} \quad (22)$$

where $f_1(\omega), f_2(\omega), \dots, f_n(\omega)$ are the n objective functions and ω represents the parameters of the model.

The NSGA algorithm based on the fitness sharing technique proposed by Goldberg is based on the principle of non-dominated sorting to classify individuals in the population. And it can obtain a uniformly distributed Pareto optimal set or noninferior solution. However, the shortcomings of the algorithm are that the computational complexity is high and the sharing parameters need to be designated by human beings. Therefore, Deb's NSGA-II algorithm, which introduces fast nondominated sorting and elitist strategy to define crowding distance instead of fitness sharing, reduces the complexity of the algorithm and improves the computation

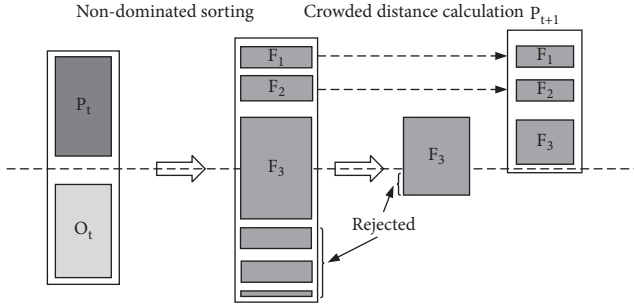


FIGURE 7: The steps of NSGA-II algorithm.

efficiency. NSGA-II overcomes three shortcomings of NSGA: the computational complexity which dropped from $O(MN^3)$ to $O(MN^2)$ (where M is the number of objectives and N is the population size), an elitist-preserving approach, and no sharing parameters which need to be specified. More details can be seen at [26].

Figure 7 describes the application of the dominance criterion in the NSGA-II algorithm. NSGA-II algorithm starts from an initialization population P_t and each individual in a population is no worse than the remaining individuals in the population. The following steps combine the NSGA-II with OVO TWSVM to optimize the classification results of OVO TWSVM. And then generate offspring O_t from P_t through binary tournament selection, crossover, and mutation. Once a foreign source is obtained, the algorithm will combine the current population and the current generation into a group and classify them according to the nondominated sorting and crowding distance. N optimal solutions can be obtained in the final set.

4. Analysis of Experimental Results

4.1. Construction of the Objective Function. Using NSGA-II to optimize the parameters, this paper uses the correct rate to construct the target function. The objective function is given as follows:

$$CRF = \frac{CNF}{TNF} \times 100 \quad (23)$$

$$CRE = \frac{CNE}{TNE} \times 100 \quad (24)$$

$$CRA = \frac{CNA}{TNA} \times 100 \quad (25)$$

$$CR = \frac{(CNF + CNE + CNA)}{(TNF + TNE + TNA)} \times 100 \quad (26)$$

CRF , CRE , and CRA represent the correct rate of flexion, extension and abduction, CNF , CNE , and CNA represent the correct action number of flexion, extension, and abduction, and TNF , TNE , and TNA represent the total number of flexion, extension, and abduction. CR represents the total correct rate.

4.2. Processing Steps. In the training phase, as the search process goes deep, the whole population tends to gather the

TABLE 1: NSGA-II preset parameters.

Parameter	Name	Preset value
P	Population size	100
CR	Crossover rate	0.9
MR	Mutation rate	0.1

global Pareto optimal set until the maximum evolutionary algebra is reached. The process of multiobjective optimization usually has the following steps:

- (1) The dataset can be divided into a training set and a test set (50% for training, 50% for testing) or 5-fold cross validation, and in this article we use 5-folder cross validation in the whole analysis process.
- (2) Change the parameters of the OVO TWSVM and run the target function.
- (3) Set evolution algebra or stop criteria [27].
- (4) Analyze the global optimal set to get the optimal parameters.

Table 1 shows the preset parameters of NSGA-II algorithm. The population size of the article is 100 and the crossover rate and mutation rate are 0.9 and 0.1.

Table 2 shows the range of penalty parameters and kernel function width for OVO TWSVM.

Table 3 shows the partial Pareto optimal set of the subject A and the corresponding OVO TWSVM model parameters using the NSGA-II algorithm.

Figure 8 shows the Pareto optimal fronts constructed by all nondominated solutions when seven subjects reach the optimal recognition rate. The mark points represent the optimum solution.

Figure 9 shows the evolutionary convergence curve of different subjects. It can be seen from the figure that five of the seven subjects achieved the highest recognition rate within 200 generations, they are subjects A, B, C, E, and F, and their accuracies are 91.66%, 95.00%, 90.00%, 85.00%, and 85.00%. All the subjects continued to increase the evolution algebra until the 600 generations. It was found that two subjects D and G had converged in the 200 generation, namely, 85% and 88.33%, respectively. The recognition rate of subjects F increased to 85% in the 400 generations and remained stable within 600 generations.

Figure 10 shows the accuracy of the OVO TWSVM classification using the linear kernel and the RBF kernel, respectively, along with the corresponding penalty parameters c_1 , c_2 and kernel function width λ , and S represent different subject. As can be seen from Figure 10, OVO TWSVM based on RBF kernel achieved the highest recognition rate on six subjects, up to 95% on subject B. Subject D's highest recognition rate appeared in linear kernel based OVO TWSVM, but the recognition result was only 3.33% less than that of RBF kernel based OVO TWSVM. Therefore, this paper chooses RBF kernel based OVO TWSVM as the final recognition model.

4.3. Comparison with Other Methods. Literature [20] uses LS-SVM to classify the motor imagery EEG signals; this paper applies the model to our own dataset for classification. Fivefold cross validation for each person's data, the results,

TABLE 2: OVO TWSVM parameter range.

Parameter	Name	Lower limit	Upper limit
c_1	Penalty parameter 1	2^{-3}	2^3
c_2	Penalty parameter 2	2^{-3}	2^3
λ	RBF kernel function	2^{-20}	2^3

TABLE 3: Pareto optimal set of subject A and the corresponding model parameters.

c_1	c_2	λ	CRF	CRE	CRA	CR
0.2031	0.0100	0.7810	0.95	0.85	0.90	0.9000
5.0102	5.7356	0.1130	0.40	0.20	1.00	0.5333
5.4325	6.6230	0.2384	0.75	1.00	0.65	0.8000
6.7280	7.7008	0.7514	0.95	0.95	0.85	0.9166
4.1136	0.0100	0.6551	0.95	0.85	0.90	0.9000
4.8389	7.3435	0.2332	0.80	1.00	0.60	0.8000
3.6172	4.8072	0.1111	0.45	0.15	1.00	0.5333

TABLE 4: Comparison between AF-CSP and EMD-CSP.

Subjects	A	B	C	D	E	F	G	Mean
AF-CSP	91.66	95.00	90.00	85.00	85.00	85.00	86.67	88.57\%±3.61%
EMD-CSP	88.33	88.33	81.66	76.67	88.33	83.34	73.34	82.85\%±5.61%

and the corresponding parameter settings are shown in Figure 11. Where c is the penalty parameter, g is the kernel function width. As can be seen from Figure 11, LS-SVM with RBF kernel has the highest recognition rate of 92.09% on subject B, five other subjects were over 75%, and the worst recognition rate on subject F is 66.66%. Based on the above results, it can be considered that this method performs well on the data sets of different subjects.

We also use BP with momentum, ELM, PSO-SVM, and grid search OVO TWSVM to classify the datasets. The result of the classification is shown in Figure 12. It can be seen from Figure 12 that the proposed method ($88.57\%±3.61\%$) has the highest average recognition rate among the seven subjects compared to other recognition algorithms. LS-SVM ($79.64\%±7.47\%$), GS OVO TWSVM ($79.99\%±7.76\%$), and PSO-SVM ($75.95\%±7.86\%$) have similar average recognition effect on seven subjects, and the average classification results of BP ($61.70\%±6.62\%$) and ELM ($61.42\%±5.37\%$) in this dataset are lower than that of SVM classifier. This shows that SVM classifier has a great advantage in small sample machine learning.

Since the time domain signal is more similar, especially in the single joint motor imagery EEG signal, in this paper, we combine amplitude-frequency (AF) domain information with CSP, namely, AF-CSP to get feature vectors. Different from the traditional method of combining time domain signal with CSP to construct feature vector, AF information can reveal further the difference between different actions in frequency domain and amplitude range; thus, CSP can get stronger feature extraction ability. In this paper, we compare the classification rate using AF-CSP and CSP directly after EMD, as shown in Table 4. As can be seen from Table 3, the proposed method has achieved a higher recognition rate

among the 5 subjects, and it might be interpreted that AF-CSP is a more effective feature extraction method.

In order to distinguish the significance of the proposed method in this article, the one-way analysis of variance (ANOVA) method was used to compare with the other five algorithms. The p -value values are shown in Table 5, where p_1, p_2, p_3, p_4 , and p_5 represent the p -values between the proposed method and LS-SVM, BP, ELM, PSO-SVM, and grid search OVO TWSVM. When $p \leq 0.05$, there is a significant difference in the recognition effect between the two algorithms. It can be seen from Table 5 that the p -values between the proposed method and the five-other methods are significantly less than 0.01, which proves that the proposed algorithm has significant classification improvement performance compared with other algorithms.

5. Discussion

Common spatial pattern is widely used in motor imagery to extract EEG features [28]. This method uses supervised learning to obtain two types of filter to separate two motor imagery tasks. In recent years, several methods like CSSP [29], RCSP [30], SSCSP [31], FERCSP [32], SBCSP [33], and FBCSP [34] have been used to improve conventional CSP. But the drawback of CSP is that it needs a lot of electrodes. AF-CSP, which taking into account the AF information in the EEG signals, uses only four electrode channels to achieve a better recognition effect than conventional CSP.

And an optimized OVO TWSVM using NSGA-II is used to improve the accuracy of motor imagery; the mean accuracy of the proposed method is $88.57\%±3.61\%$. However, since there are no articles consistent with the contents of this paper, we can only discuss articles that are similar to our research

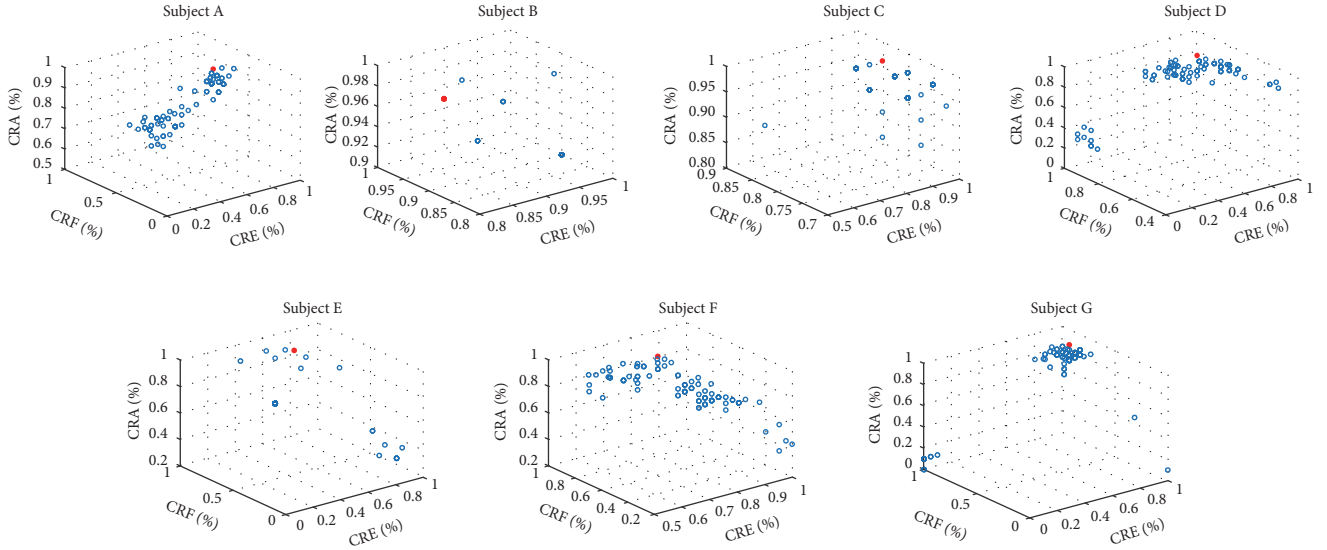


FIGURE 8: The Pareto optimal front of seven subjects based on RBF kernel OVO TWSVM.

TABLE 5: *p*-value score based on RBF kernel OVO TWSVM and five other methods.

Subject	<i>p1</i>	<i>p2</i>	<i>p3</i>	<i>p4</i>	<i>p5</i>
A	1.06e-05	3.90e-07	6.29e-08	2.78e-08	7.22e-05
B	3.80e-02	9.72e-06	6.97e-13	1.00e-03	5.33e-04
C	1.07e-07	6.27e-09	3.60e-11	3.55e-05	2.37e-07
D	2.84e-05	3.99e-07	9.81e-07	6.09e-07	3.00e-04
E	1.00e-04	3.64e-12	3.04e-06	1.84e-06	2.61e-11
F	3.88e-07	8.30e-08	9.84e-08	5.93e-06	3.40e-03
G	3.00e-04	3.82e-09	7.56e-06	4.91e-05	5.94e-07

TABLE 6: Mean confusion matrices of seven subjects for the proposed method.

	Flexion	Extension	Abduction
Flexion	90.71	7.57	3.50
Extension	5.50	82.14	5.79
Abduction	3.93	10.26	90.71

contents. Literature [18] points out that the manual extraction of features in the traditional biological signal pattern recognition model may produce information loss; thus, CNN with deep learning is introduced to identify of changes in the brain topographic map. The results show that three kinds of motor imagery in the hand are 65.51% and the kappa value in this experiment is 0.481. However, there is still a great deal of uncertainty about the intention recognition of single hand. In [19], the wavelet coefficients are calculated from EEG signals as feature and employed including quadratic discriminant analysis, naive Bayes quadratic, decision tree, K nearest neighbors, and SVM classifiers to identify shoulder and elbow joint movement. The highest recognition rate is 84.91%, using the SVM classifier. The weakness of this study is that it only recognizes the shoulder and elbow joint

movements of one hand and there is no further analysis of the complex movement of the single joint.

It should be noted that we use AF-CSP to extract features and enhance the feature extraction ability of CSP. OVO TWSVM is used to identify three types of upper limb movement; the lowest recognition rate is 85.00%. Compared with the current research, we have made a more in-depth analysis of single joint multiclass motor imagery. A more sophisticated analysis can be done using the mean confusion matrices given in Table 6 and the kappa value calculated by Table 6 is 0.82. It appears that the extension action is more difficult to distinguish with flexion and abduction of the shoulder joint using the proposed method. The flexion and extension of the shoulder joint obtain high recognition rate by the proposed method.

In addition, [35] proposes a novel correlation-based time window selection (CTWS) algorithm which considers the variation in the time latency during the MI task for MI-based BCI. CTWS adjusts the starting points of time window for both training and test samples using correlation analysis and shows significantly improvement than feature extraction algorithms without CTWS. As the feature extraction algorithms in the structure of the CTWS algorithm is substitutable, the focus of the next work is to combine CTWS

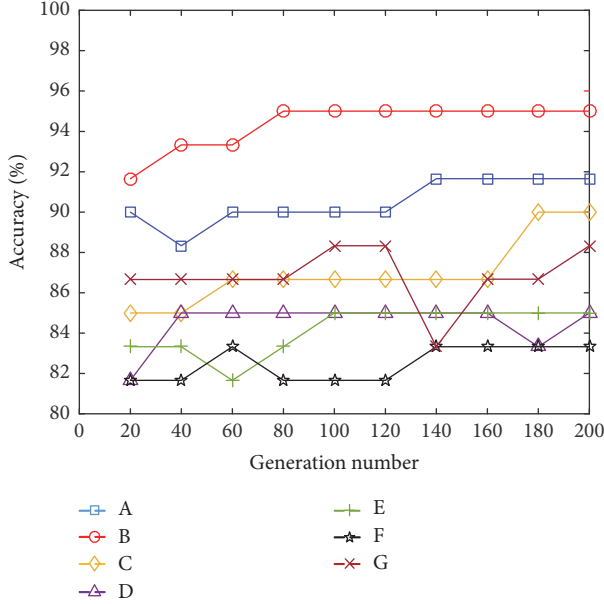


FIGURE 9: Evolutionary convergent fold line chart for different subjects.

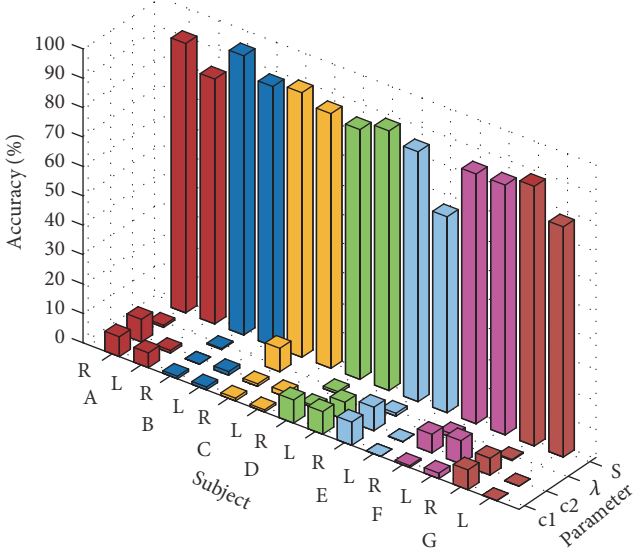


FIGURE 10: OVO TWSVM recognition effect diagram of different kernel function types.

with AF-CSP to increase the recognition rate of the extension and applying this model to the BCI systems.

6. Conclusion

This paper proposes AF-CSP replace the traditional EMD-CSP method. The main idea of this method is to analyze the μ and β rhythm information contained in each IMF component after EMD decomposition and extract corresponding AF information. This preprocessing method not only removes the influence of irrelevant frequency bands, but also strengthens the feature extraction ability of CSP. Secondly, this paper also uses NSGA-II to optimize the OVO TWSVM parameter

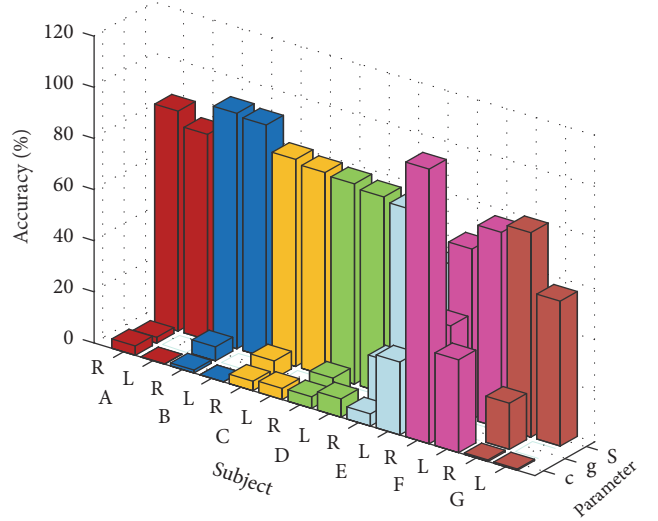


FIGURE 11: LS-SVM recognition rate diagram for different kernel functions.

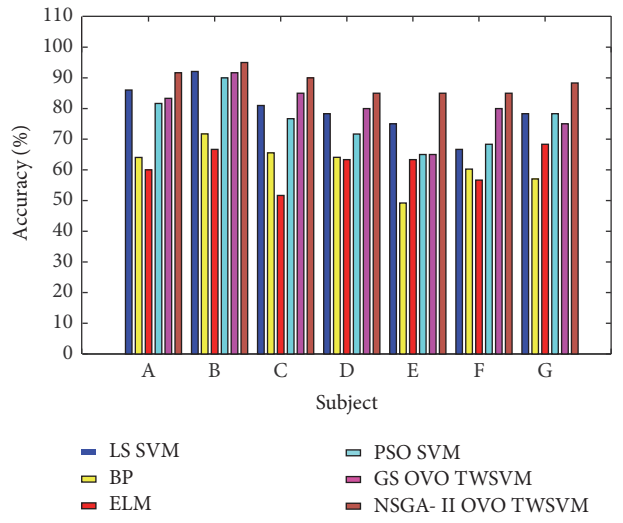


FIGURE 12: Comparison of recognition rates of different methods.

optimization process. Compared with other evolutionary strategies, the Pareto optimal set obtained by NSGA-II can make OVO TWSVM more robust. In the future, we may use this technology to evaluate the classification of real-time BCI and apply this method for reach and grasp tasks of a robotic arm. In order to improve the recognition rate of the method, we may use clustering or dimensionality reduction method to get a more obvious feature vector.

Data Availability

The data used to support the findings of this study are available from the corresponding author upon request.

Conflicts of Interest

The authors declare that they have no conflicts of interest.

References

- [1] J. R. Wolpaw, N. Birbaumer, D. J. McFarland, G. Pfurtscheller, and T. M. Vaughan, "Brain-computer interfaces for communication and control," *Clinical Neurophysiology*, vol. 113, no. 6, pp. 767–791, 2002.
- [2] N. Birbaumer, "Breaking the silence: brain-computer interfaces (BCI) for communication and motor control," *Psychophysiology*, vol. 43, no. 6, pp. 517–532, 2006.
- [3] J. Kalcher, D. Flotzinger, C. Neuper, S. Gößly, and G. Pfurtscheller, "Graz brain-computer interface II: towards communication between humans and computers based on online classification of three different EEG patterns," *Medical & Biological Engineering & Computing*, vol. 34, no. 5, pp. 382–388, 1996.
- [4] J. R. Wolpaw and D. J. McFarland, "Multichannel EEG-based brain-computer communication," *Electroencephalography and Clinical Neurophysiology*, vol. 90, no. 6, pp. 444–449, 1994.
- [5] B. Blankertz, C. Sannelli, S. Halder et al., "Neurophysiological predictor of SMR-based BCI performance," *NeuroImage*, vol. 51, no. 4, pp. 1303–1309, 2010.
- [6] N. Birbaumer, N. Ghanayim, T. Hinterberger et al., "A spelling device for the paralysed," *Nature*, vol. 398, no. 6725, pp. 297–298, 1999.
- [7] J. D. Bayliss, "Use of the evoked potential P3 component for control in a virtual apartment," *IEEE Transactions on Neural Systems and Rehabilitation Engineering*, vol. 11, no. 2, pp. 113–116, 2003.
- [8] U. Hoffmann, J.-M. Vesin, T. Ebrahimi, and K. Diserens, "An efficient P300-based brain-computer interface for disabled subjects," *Journal of Neuroscience Methods*, vol. 167, no. 1, pp. 115–125, 2008.
- [9] G. Pfurtscheller, "EEG Rhythms - Event-Related Desynchronization and Synchronization," in *Rhythms in Physiological Systems*, vol. 55, pp. 289–296, Springer, Berlin, Germany, 1991.
- [10] G. Pfurtscheller and F. H. L. da Silva, "Event-related EEG/MEG synchronization and desynchronization: basic principles," *Clinical Neurophysiology*, vol. 110, no. 11, pp. 1842–1857, 1999.
- [11] L. F. Nicolas-Alonso and J. Gomez-Gil, "Brain computer interfaces, a review," *Sensors*, vol. 12, no. 2, pp. 1211–1279, 2012.
- [12] D. Coyle, G. Prasad, and T. M. McGinnity, "A time-series prediction approach for feature extraction in a brain-computer interface," *IEEE Transactions on Neural Systems and Rehabilitation Engineering*, vol. 13, no. 4, pp. 461–467, 2005.
- [13] T. Kayikcioglu and O. Aydemir, "A polynomial fitting and k-NN based approach for improving classification of motor imagery BCI data," *Pattern Recognition Letters*, vol. 31, no. 11, pp. 1207–1215, 2010.
- [14] K. K. Ang and C. Guan, "EEG-Based Strategies to Detect Motor Imagery for Control and Rehabilitation," *IEEE Transactions on Neural Systems and Rehabilitation Engineering*, vol. 25, no. 4, pp. 392–401, 2017.
- [15] P. Martín-Smith, J. Ortega, J. Asensio-Cubero, J. Q. Gan, and A. Ortiz, "A supervised filter method for multi-objective feature selection in EEG classification based on multi-resolution analysis for BCI," *Neurocomputing*, vol. 250, pp. 45–56, 2017.
- [16] Y. Zhang, G. Zhou, J. Jin, X. Wang, and A. Cichocki, "Optimizing spatial patterns with sparse filter bands for motor-imagery based brain-computer interface," *Journal of Neuroscience Methods*, vol. 255, pp. 85–91, 2015.
- [17] C. Park, C. C. Cheong-Took, and D. P. Mandic, "Augmented complex common spatial patterns for classification of noncircular EEG from motor imagery tasks," *IEEE Transactions on Neural Systems and Rehabilitation Engineering*, vol. 22, no. 1, pp. 1–10, 2014.
- [18] W. Wang, S. Sun, C. Li, and Z. Tang, "Recognition of upper limb motion intention of EEG signal based on convolutional neural network," *Journal of Zhejiang University*, vol. 7, no. 51, pp. 1381–1389, 2017.
- [19] R. Rinku, A. Konar, and N. Tibarewala, "Classification of left-right arm and shoulder joint- elbow joint motor imagery data," in *Proceedings of the National Conference on Telecommunication & Control Engineering*, 2012.
- [20] S. Taran, V. Bajaj, D. Sharma, S. Siuly, and A. Sengur, "Features based on analytic IMF for classifying motor imagery EEG signals in BCI applications," *Measurement*, vol. 116, pp. 68–76, 2018.
- [21] X. Tang, N. Zhang, J. Zhou, and Q. Liu, "Hidden-layer visible deep stacking network optimized by PSO for motor imagery EEG recognition," *Neurocomputing*, vol. 234, pp. 1–10, 2017.
- [22] N. E. Huang, Z. Shen, S. R. Long et al., "The empirical mode decomposition and the Hilbert spectrum for nonlinear and non-stationary time series analysis," *Proceedings of the Royal Society of London A: mathematical, Physical and Engineering Sciences*, vol. 454, no. 1971, pp. 903–995, 1998.
- [23] R. Khemchandani and S. Chandra, "Twin support vector machines for pattern classification," *IEEE Transactions on Pattern Analysis and Machine Intelligence*, vol. 29, no. 5, pp. 905–910, 2007.
- [24] S. Ding, J. Yu, B. Qi, and H. Huang, "An overview on twin support vector machines," *Artificial Intelligence Review*, vol. 42, no. 2, pp. 245–252, 2014.
- [25] D. Tomar and S. Agarwal, "A comparison on multi-class classification methods based on least squares twin support vector machine," *Knowledge-Based Systems*, vol. 81, pp. 131–147, 2015.
- [26] K. Deb, A. Pratap, S. Agarwal, and T. Meyarivan, "A fast and elitist multiobjective genetic algorithm: NSGA-II," *IEEE Transactions on Evolutionary Computation*, vol. 6, no. 2, pp. 182–197, 2002.
- [27] A. R. J. Clark and R. M. Everson, "Multi-objective learning of Relevance Vector Machine classifiers with multi-resolution kernels," *Pattern Recognition*, vol. 45, no. 9, pp. 3535–3543, 2012.
- [28] Z. J. Koles, M. S. Lazar, and S. Z. Zhou, "Spatial patterns underlying population differences in the background EEG," *Brain Topography*, vol. 2, no. 4, pp. 275–284, 1990.
- [29] S. Lemm, B. Blankertz, G. Curio, and K.-R. Müller, "Spatiotemporal filters for improving the classification of single trial EEG," *IEEE Transactions on Biomedical Engineering*, vol. 52, no. 9, pp. 1541–1548, 2005.
- [30] F. Lotte and C. Guan, "Regularizing common spatial patterns to improve BCI designs: unified theory and new algorithms," *IEEE Transactions on Biomedical Engineering*, vol. 58, no. 2, pp. 355–362, 2011.
- [31] Y. Shin, S. Lee, J. Lee, and H.-N. Lee, "Sparse representation-based classification scheme for motor imagery-based brain-computer interface systems," *Journal of Neural Engineering*, vol. 9, no. 5, Article ID 056002, 2012.
- [32] S. Yuxi, L. Yali, and W. Shengjin, "Filter ensemble regularized common spatial pattern for EEG classification," in *Proceedings of the Seventh International Conference on Digital Image Processing (ICDIP '15)*, vol. 9631, International Society for Optics and Photonics, 2015.

- [33] Q. Novi, C. Guan, T. H. Dat, and P. Xue, "Sub-band common spatial pattern (SBCSP) for brain-computer interface," in *Proceedings of the 3rd International IEEE/EMBS Conference on Neural Engineering (CNE '07)*, pp. 204–207, IEEE, Kohala Coast, Hawaii, USA, May 2007.
- [34] K. K. Ang, Z. Y. Chin, C. Wang, C. Guan, and H. Zhang, "Filter bank common spatial pattern algorithm on BCI competition IV datasets 2a and 2b," *Frontiers in Neuroscience*, vol. 6, 9 pages, 2012.
- [35] J. Feng, E. Yin, J. Jin et al., "Towards correlation-based time window selection method for motor imagery BCIs," *Neural Networks*, vol. 102, pp. 87–95, 2018.

Research Article

Using Black Hole Algorithm to Improve EEG-Based Emotion Recognition

Roberto Munoz ,^{1,2} **Rodrigo Olivares** ,^{1,2} **Carla Taramasco** ,¹
Rodolfo Villarroel ,² **Ricardo Soto** ,² **Thiago S. Barcelos** ,³
Erick Merino ,¹ and **María Francisca Alonso-Sánchez** ,⁴

¹*Escuela de Ingeniería Civil Informática, Universidad de Valparaíso, Valparaíso, Chile*

²*Pontificia Universidad Católica de Valparaíso, Valparaíso, Chile*

³*Instituto Federal de Educação, Ciência e Tecnologia de São Paulo, Brazil*

⁴*Centro de Investigación del Desarrollo en Cognición y Lenguaje, Universidad de Valparaíso, Valparaíso, Chile*

Correspondence should be addressed to Roberto Munoz; roberto.munoz@uv.cl

Received 19 February 2018; Revised 18 April 2018; Accepted 8 May 2018; Published 11 June 2018

Academic Editor: Victor H. C. de Albuquerque

Copyright © 2018 Roberto Munoz et al. This is an open access article distributed under the Creative Commons Attribution License, which permits unrestricted use, distribution, and reproduction in any medium, provided the original work is properly cited.

Emotions are a critical aspect of human behavior. One widely used technique for research in emotion measurement is based on the use of EEG signals. In general terms, the first step of signal processing is the elimination of noise, which can be done in manual or automatic terms. The next step is determining the feature vector using, for example, entropy calculation and its variations to generate a classification model. It is possible to use this approach to classify theoretical models such as the Circumplex model. This model proposes that emotions are distributed in a two-dimensional circular space. However, methods to determine the feature vector are highly susceptible to noise that may exist in the signal. In this article, a new method to adjust the classifier is proposed using metaheuristics based on the black hole algorithm. The method is aimed at obtaining results similar to those obtained with manual noise elimination methods. In order to evaluate the proposed method, the MAHNOB HCI Tagging Database was used. Results show that using the black hole algorithm to optimize the feature vector of the Support Vector Machine we obtained an accuracy of 92.56% over 30 executions.

1. Introduction

Emotions play an important role regarding the way in which people think and behave [1]. In physiological terms, emotions are phenomena of short duration that represent efficient modes of adaptation to the constant demands presented by our environment [2]. One of the most accepted models that represent emotions is known as the Circumplex model [3]. This model organizes emotions into points on a bidimensional plane made up of the following dimensions: “Valence” (pleasurable or not pleasurable) and “Arousal” (tension, relaxation); in this way, emotions are organized in a circular manner within this plane [3]. Furthermore, different methods exist for measuring emotions within people; those with the most precision are based on electrophysiological

signals, which can be captured, for example, by an electroencephalogram (EEG) device.

In particular, the increase of the visual component P1 has been studied, with event-related potentials (ERP), by filtering low spatial frequencies, thus evidencing the rapid activation of the magnocellular system against stimuli that trigger emotions of high agitation [4]. The component P1 is of early onset and precedes facial recognition; therefore, it is possible to estimate that emotional processing manages to circumvent the track of regular visual processing when emotions contained in the stimuli are of high agitation [5]. Furthermore, by means of a classifier generated from the combination of wavelet entropy and the averaging of wavelets of EEG signals associated with emotions, a valence of 76.8% and an agitation of 74.3% have been recognized. Furthermore,

the decoding of pleasurable or unpleasant emotions known as valence [6] has been obtained through Linear Discriminant Analysis. In this context and considering both the temporal resolution of EEG signals and the possibility of applying ecological tasks to subjects while registering signals, classification methods are a tool of great potential for the study of emotions.

One of the metrics (features) that is the most representative and which provides the most information is entropy. Entropy is a measurement of information or order; it measures the predictability of data. This is, given a set of N data elements, $X = \langle x_1, x_2, \dots, x_N \rangle$, entropy is the probability of being able to predict an element x_i , i.e., the homogeneity or heterogeneity of the data.

However, this use of entropy can magnify the signal noise, being extremely sensitive to minimal variations. For this reason, different ways of measuring entropy have been proposed, such as approximate entropy, differential entropy, or sample entropy. Among these methods, sample entropy presents a valuable statistical consistency and for this reason was utilized as a basis of comparison [7]. Sample entropy (SampEn) is based on approximate entropy, which by means of elimination of repeated information prevents the evaluation of indeterminate logarithms and self-matching, which can result in inconsistent and erroneous data and thus also achieve a greater statistical consistency.

Although the SampEn method is highly accurate, it is extremely sensitive to its input parameters. In fact, there is no established consensus on the selection of parameters for small data sets, especially for biological data [8]. Another problem in the calculation of SampEn is that if the sampling space is not significant, the built classifiers can produce values with high levels of error.

These situations present the problem of finding or calculating the most suitable value for entropy that allows generating high performance classifiers. This task is complex and can be seen as an optimization problem in itself. A first approximation to a potential solution can be the use of full-search algorithms to explore a tree of extremely large potential solutions. However, these techniques are highly costly and can lead to an unsuitable large amount of attempts to find a solution. With this in mind, it is not possible to propose complete techniques such as Backtracking or hybrid ones such as Forward Checking.

On the other hand, recently, several approaches have emerged, inspired by natural phenomena, that allow solving complex optimization and combinatorial problems in reduced time periods [9–12]. These techniques have been successful when the complexity of the problem is not linear, given that they do not explore the solution tree in their completeness.

In this article, we propose using an approximate optimization approach to find the best values considering the predictability of the classifier. The reason for the proposed approach is the strong impact on the development of classifiers for emotion recognition based on electroencephalography. The main idea is to use the black hole algorithm due to its low cost, similar to the calculation of entropy. This algorithm is inspired by the phenomena of black holes [13]

and will be used to build the classifier iteratively. This method will improve and update the classifier according to its level of performance: lower percentage of error will be associated with better evaluation levels.

The present work is organized as follows: Theoretical background is introduced in Section 2. In Section 3, we detail the required resources to apply our approximation approach. Section 4 illustrates the computational experiments including a comparison with the results obtained using the traditional calculation method. Finally, conclusions and future works are described in Section 5.

2. Background

First, in Section 2.1 we present the theoretical model for the classifications proposed by Russell that supports our work [3]. In Section 2.2, we describe some components associated with electroencephalography and their relationships with emotions detection. Following, in Section 2.3, we present the sample entropy, which is an alternative to entropy. This method is the main component of the feature vector which is classified by a Support Vector Machine (SVM). This model is composed by a set of supervised learning algorithms and they are described in Section 2.4. In Section 2.5 we expose some techniques used for the EEG signals treatment. Finally, in Section 2.6 we will present two relevant works detecting emotions with EEG.

To conclude, our proposal consists of the preprocessing of the signal (through EMD and sample entropy) for the construction of an initial multiclass SVM classifier. Using this classifier as a base, a population (group) of classifiers is created, which are formed by groups of modified characteristics coming from the initial characteristics and a random variation relative to the error of the classifier.

Once this population is created, it is iterated through the black hole metaheuristic, which continuously generates and improves these characteristics in order to obtain distinct classifiers; these classifiers are then evaluated, always, using the original characteristics from the signal. Once all the iterations are completed, the best classifier (historically speaking) is chosen; this classifier is, finally, utilized. Figure 1 shows a scheme of our proposal.

2.1. Theoretical Model for Emotion Classification. Circumplex is one of the most used models for emotion classification [3]. This model is composed by two dimensions. One dimension is known as the valence dimension, which varies from “negative valence” to “positive valence”. The second dimension is called arousal, which varies from “low arousal” to “high arousal”. A graphical representation of the Circumplex model is presented in Figure 2.

There are variants of the Circumplex model in which extra dimensions are added, such as domination or freedom in a given situation [3]. However, it has been proven that this dimension captures the believed consequences by the person regarding emotion and not the emotion itself [14].

In this work, we have used a discrete quadrant division to represent the greatest variation among emotional states. This approach is optimal for classifying and obtaining fewer

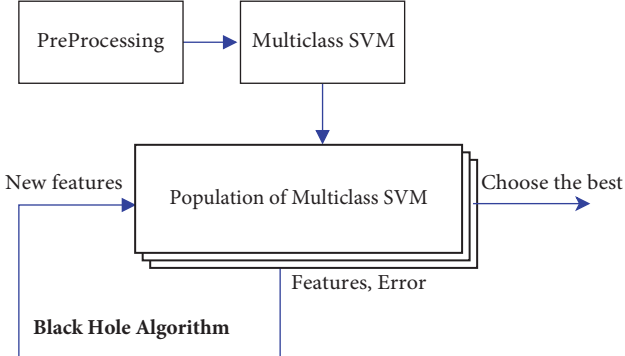


FIGURE 1: Proposed approach.



FIGURE 2: Russell's classification model [3, 14].

error rates. This is because they represent the greatest possible distance between agitation and valence (the digital axes). On the other hand, it would be possible to classify discrete emotions; there would be a greater probability of erroneously classifying nearby emotions in this model because they would represent lower variance values.

2.2. Electroencephalography. Electroencephalography is a method of neurophysiological exploration that is based on the registry of cerebral activity through sensors that translate bioelectric activity into electrical current [15]. It is a noninvasive method that allows the measurement of voltage fluctuations that result from the ionic current of the postsynaptic potentials of neurons.

EEG signals are usually classified by their frequency, amplitude, shape, or electrode position. The EEG bands are δ (lower than 4Hz), θ (between 4Hz and 7Hz), α (8-15Hz), β (16-31Hz), γ (higher than 31Hz), and μ (between 8 and 12 Hz). These bands describe several emotional states [16], although there are alternative definitions for the bands. For example, the Beta Band frequency range may begin at 12, 13, 14, or even 16 Hz as described in [17], where the μ band is not even defined.

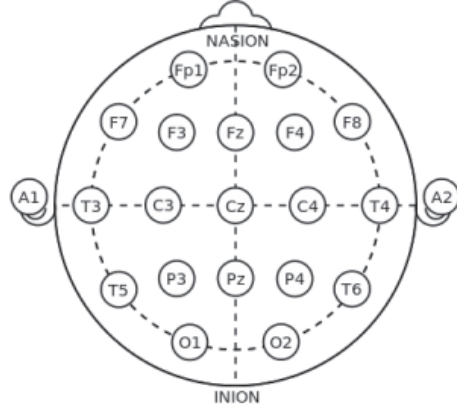


FIGURE 3: EEG 10-20 system.

Even so, the position of sensors is standardized by the 10-20 channel system, by which each position is described by a combination of a letter and a number. The letter indicates the brain region that may be represented as frontal (F), central (C), temporal (T), occipital (O), or parietal (P) [18]. Even numbers indicate positions at the right side of the brain, while odd numbers indicate positions at the left side. The system name refers to the use of 10% and 20% proportions to position the electrodes in relation to four cardinal points: ears, nape and nasion [19] (as shown in Figure 3).

There is also another positioning system named 10-10 system in which only the 10% proportion is used. In this alternative system the same bands mentioned before are used with the addition of other intermediate channels. In the case of the lobes, letter combinations are created for the channels between two regions, for example, FP for frontoparietal [20].

The assembly of the electrodes can be done by referencing the electrodes or with a bipolar method. The reference is made with electrodes that generate a comparison link, generally with an electrode positioned in A2 (the ear electrode) and the bipolar method is performed by recording the potential differences between paired electrodes [21].

The applications of EEG are varied [22-26]. However, its most known use is for clinical diagnosis [27]. In recent years, however, its use has spread in the research of brain functions associated with cognitive processes. One of the most commonly used techniques is event-related potentials (ERP) that allows the repeated measurement of ongoing brain activity segments immediately after the presentation of a stimulus. In this way, by averaging the segments it is possible to measure the cerebral voltage associate with the stimuli presented; i.e., by means of an analysis of time amplitude, it is possible to associate components to the stimuli [28]. It is also possible to analyze the oscillations related to events in the frequency domain. This analysis can be performed in the frequency domain with the analysis of the spectral decomposition represented in power spectral density of each trial through the Fourier transform. However, the time variable with a Fourier transform applied to a series of consecutive time windows or with a discrete Wavelet

Transform Analysis can be included. The so-called rhythms have gained popularity in the research of social neuroscience and frequency bands (i.e., alpha) have been associated with cognitive processes and mental states. Because of this and because of the particular suitability for the investigation of emotions, this study focused on frequency analysis.

2.3. Sample Entropy. Sample entropy is a variation of approximate entropy (ApEn). This entropy reduces the potential bias generated by self-matching that arises during ApEn [29]. The

function of SampEn is the negative of the natural logarithm of the conditional probability that two similar sequences, with a distance of less than r , for m points, continue to be so when increasing the number of points from m to $(m + 1)$. This is to say that the SampEn is calculated by

$$\text{SampEn}(m, r, N) = -\ln \left(\frac{C_{m+1}(r)}{C_m(r)} \right) \quad (1)$$

where C_m is defined as

$$C_m(r) = \frac{\{\text{number of all probable pairs } (i, j) \text{ with } |x_i^m - x_j^m| < r, i \neq j\}}{\{\text{number of all probable pairs, i.e. } (N - m + 1)(N - m)\}} \quad (2)$$

where $|x_i^m - x_j^m|$ denotes the distance between the points x_i^m and x_j^m in the dimension space to be evaluated, m . The variable r represents the tolerable standard deviation of the time series. Furthermore, N represents the length of the time series. Finally, it has been shown that SampEn has a better statistical validity for $m = 1$ or 2 and the range of r in the interval between 0.1 and 0.25.

2.4. Support Vector Machines. Support Vector Machines (SVM) are a set of supervised learning algorithms based on statistics learning theory [30]. SVMs put all features in n-dimensional space (the number of dimensions of the feature vector, 8 in this case) and adjust them to a defined kernel space (Gaussian, polynomial, etc.). To build a multiclass SVM, we use the one-against-all method. This technique consists of constructing $k * (k - 1)/2$ binary classifiers (hyperplanes), separating each class from another, and applying a voting system [31].

The main advantage of using SVMs is that their model can be generalized for nonlinear feature spaces. On the other hand, weighted SVM, which is the method used in this work, has a regularization parameter C that enables accommodation to outliers and allows errors on the training set.

2.5. Signal Processing Algorithms

2.5.1. Technique: Empirical Mode Decomposition. Empirical Mode Decomposition (EMD) is a data-driven signal processing and analysis technique [32]. This technique breaks down the signal into its basic components, similar to the creation of harmonics (fundamental sinusoidal), but with the advantage that each signal has frequencies and variable amplitudes, obtaining more information in each component [33].

The main advantage of using this technique is that it permits softening the signals and decreasing noise, which is especially useful in physiological signals.

Each component fulfills 2 fundamental requirements:

- (i) The number of endpoints and the number of crosses by zero (zero-crossings) is equal or differs at the most in 1.

- (ii) The average between the top and bottom wrapper is always zero at each point.

EMD generates a set of Intrinsic Mode Functions (IMF) that allows obtaining the components of a signal with most significance. The steps to define the set of functions are as follows:

- (1) Identify all of the local endpoints of the signal.
- (2) Connect all local maximums using cubic spline interpolation to create a superior wrapper.
- (3) Repeat the same process for the local minimums.
- (4) Create a $m[x]$ signal, which is the average of both wrappers.
- (5) The first resulting signal is the original signal minus m (average) signal:

$$\text{IMF}[n] = x[n] - m[n] \quad (3)$$

- (6) The remainder of the original signal is obtained minus the IMF; i.e.,

$$r[n] = x[n] - \text{IMF}_1[n] \quad (4)$$

- (7) If IMF satisfies the definition (the 2 basic requirements), it is accepted as a valid IMF; otherwise the process is rejected and repeated using the remainder as the original signal.

This continues until the stopping condition is met, which can be a certain number of iterations or until the residue contains no more than one endpoint.

2.5.2. Technique: Wavelet Transform. The use of wavelet transformation for EEG signal classification was proposed by [34]. To do this, the signal is decomposed in a set of basic signals called wavelets. These signals are obtained from a mother wavelet, which is a signal wavelet prototype that was generated through dilatations, contractions, and signal changes. The wavelet coefficients resulting from this analysis represent similarity between the scaled/shifted wavelets and

the original data. Despite the fact that this method of analysis permits obtaining a higher temporal resolution than the Fourier transform, the frequency resolution is lower in the low frequencies. Also, in the high frequencies, when the frequency resolution increases, the temporal resolution decreases.

In spite of the mentioned limitations, the frequency analysis of wavelet has been used, among other things, to determine the intracortical coupling, unraveling cerebral synchrony through the systems of communication between near and distant neurons associated with cognitive processes [35]. Likewise, the analysis of oscillations has been relevant in the study of mirror neurons, which, according to some authors, is the basis of empathy [36]. The rhythm Mu (μ) (8-12Hz) in the sensorimotor cortex, associated with the system of mirror neurons, is more active when subjects are at rest and it is desynchronized when an action is carried out or an action is observed [37]. In this way, the study of the synchronization of the oscillations has been of great importance for the understanding of aspects such as empathy, emotional reactions, and even social interactions [38].

2.5.3. Comparison: EMD versus Wavelet. EMD is an iterative process that allows a transversal time-frequency analysis by extracting the oscillatory characteristics. On the other hand, the wavelet transform allows performing a longitudinal analysis of the frequency changes over time by convolving a signal based on a mother wavelet. Particularly the EEG signals are characterized by being non-Gaussian and nonstationary; due to this, it has been observed that the wavelet transform has a worst resolution of time and frequency while the EMD provides a more intuitive understanding of the data [39]. In addition, the EMD does not have the need for arbitrary bandpass filter cut-offs and the phase is detected independent of the amplitude.

2.6. Relevant Works

2.6.1. Applications: WEAVE Algorithm. WEAVE is EEG-emotion valence classifier based on five steps:

- (1) Segmentation of EEG signals related to emotions in windows of 6 seconds.
- (2) Extraction of the wavelet metrics to form WEAVE.
- (3) Calculating the complexity of metrics with Normalized Mutual Information (NMI) [40].
- (4) Reduction of channels through NMI.
- (5) Classification with the Support Vector Machine (SVM) algorithm using the Sequential Minimal Optimization (SMO) algorithm to train the SVM.

The advantages of the wavelet transform are due to the regularity in the intersegment estimation and the subbands obtainment through the bandpass filter and the denoiser signal decomposition [41].

2.6.2. EEG-Based Emotion Recognition Using Combined Feature Extraction Method. A state of excitement in the cerebral

cortex can be identified using the detection of a significant Beta Band [42]. This state is recognized as a favorable scenario for emotion recognition [43, 44].

In [42], a method is proposed for the recognition of emotions using Empirical Mode Decomposition (EMD) and the sampled entropy for the generation of a classifier using SVM. The main advantage of this method is that only 2 channels are used (F3 and C4). EMD is used on both signals to calculate the first 4 Intrinsic Mode Functions (IMFs). Each of the 8 resulting IMFs is calculated with SampEn. Later, this entropy is used for the characteristics vectors and to be entered into the SVM for training and testing.

For the reconstruction of the Beta Band they used low pass and high pass Butterworth filters. Signals were filtered using a 3rd-order bandpass Butterworth filter [45] with a cut-off frequency of 12.5 and 30 Hz and the resonant frequency equal to 0.1 Hz [46].

Furthermore, for the experiment, the Database for Emotion Analysis using Physiological Signals (DEAP) was used [47]. In general terms, the experimental results presented by the authors indicate that the proposed method obtains an accuracy of 94.98% for binary-class task and the best accuracy achieves 93.20% for the multiclass task using DEAP database. In this way, the results presented by the authors are highly appropriate in relation to other means of classification. In the Figure 4, we present a working schema of the proposed by [42].

Upon analyzing, in detail, the process, we can see that the entropy values strongly affect the creation of the classifier and are directly related to the configuration of the input parameters. In addition, due to the search process is an iterative procedure, it is not possible to determine the performance of the classifier until the process is finished.

3. Materials and Methods

3.1. Dataset. For our proposal, presented in Section 3.3, we used the MAHNOB HCI Tagging Database [48]. This dataset is formed by 563 sessions realized by 30 participants. Each session contains data from only one person. Participants were presented with movies and images with emotional content. While they were being presented with the emotional content, they were monitored with EEG of 32 channels, 6 cameras, a microphone in the head (head-worn microphone), an eye gaze tracker, and conductivity, among other sensors.

Furthermore, for each session, participants were asked to answer a survey regarding emotions they felt, levels of agitation, valence and domination, among other questions. We used the agitation and valence (high, low) to create the multilabelled classifier, where each of the four classes is one of the quadrants. When using a multiclass model for classification, the answer must be in one of the classes contained in the model. To avoid the creation of a null class, it is advisable to use the full spectrum of emotions. For this, the Russell quadrant model was selected [3], which includes all the possible emotions discretized in points.

For this study, we used the F3 and C4 channels of the EEG sensor, as it was done in [42]. These channels represent part of the Beta Band, which is significant when the brain

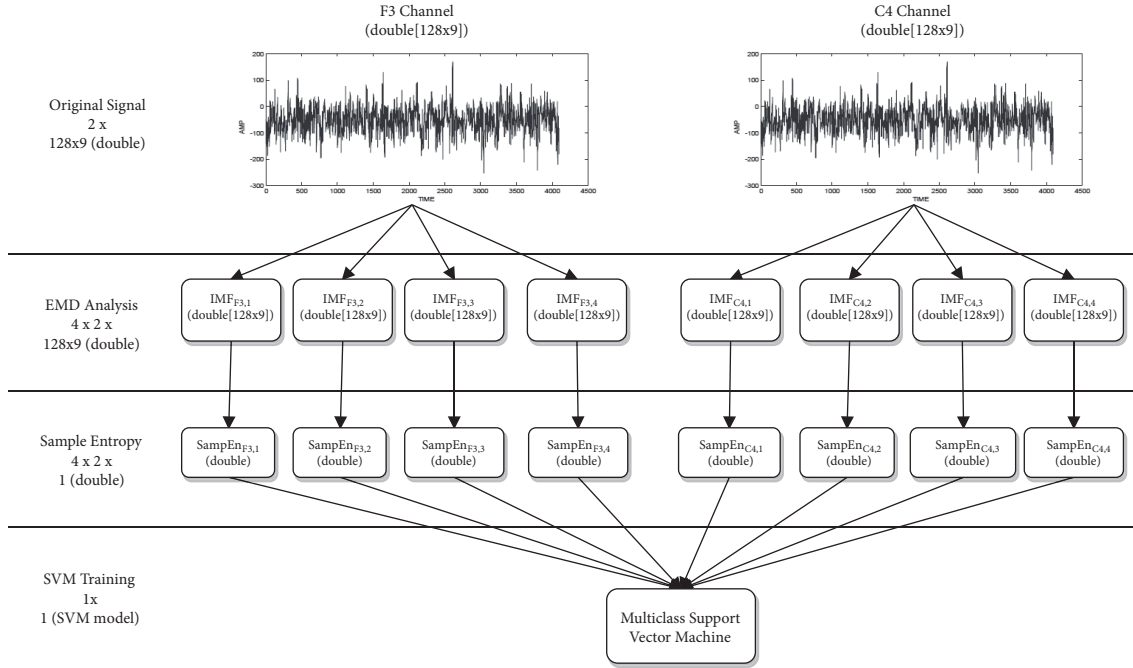


FIGURE 4: EEG-based emotion recognition using combined feature extraction method.

is in excited states [49], an ideal condition for recognizing emotions. The activity of the Beta Band is clearer in the frontal, temporal, and central areas, in regions such as F3, F4, C3, C4, T3, and T4. For the selection of channels, a reconstruction of the Beta Band was performed, and the power spectral density (PSD) was calculated. Since the average of PSD in the F3 and C4 was more significant, these were chosen for the realization of this study.

3.2. Approximate Methods. In optimization new approximate techniques have been proposed in order to improve the search process. Many of these algorithms are inspired in social environments, natural phenomena, and the biological evolution [50]. These methods have widely been used to solve uncountable optimization problems [51]. Swarm intelligence is a particular case of metaheuristics that groups a subset of algorithms and it allows solving optimization problems using collective intelligence. For instance, social situations and human behavior have inspired the imperialist competitive algorithm [52] and the brainstorming algorithm [53], respectively. Techniques based on single-solution such as the intelligence water drop algorithm [54] have been proposed. Moreover, approximate methods such as the ant colony optimization algorithm [55] are population-based using the collective intelligence of individuals. On the other hand, techniques inspired by the collaborative behavior of some animals have been proposed in [56–59], among others. More sophisticated techniques are inspired by spatial phenomena such as the gravitational search algorithm [60], the black hole algorithm [61], the big bang algorithm [62], and the big bang-big crunch algorithm [63] and others. Finally, genetic algorithms [64] and differential evolution [65] are two of

the best-known techniques inspired by the process of natural selection.

3.3. Proposed Approach. To solve this problem, we propose to use an approximate method that permits evaluating previous behavior of the classifier, and if necessary, allowing for improvement. The approximate techniques have been widely used in real world problems [66, 67], being very useful when the search space is extremely large and the use of complete search algorithms is unfeasible. While there are many alternatives to solve this problem, we have decided using the black hole algorithm due to the fact that it is relatively easy to implement, and it is slight free from tuning parameter issues. Moreover, this method uses a technique of exploration/exploitation free of external components reducing the probability of being affected to unexpected changes. Finally, as reported in [68], the black hole algorithm in optimization problem converges to global optimal in each evaluation while its competitors' genetic algorithm, ant colony optimization, and simulated annealing can be caught in local optimum solutions.

The black hole algorithm is based on the phenomenon of the same name, which occurs in outer space and is inspired by the law of attraction/absorption. The algorithm follows three main fundamentals:

- (1) A star in space is considered a solution to the problem. As a population-based algorithm, a certain number of stars are randomly generated.
- (2) The black hole is selected. A black hole represents the star with the best performance of all solutions.

```

Require: number of stars (solutions) and stop criteria (maximum of iterations)
Ensure: the black hole. In our case, the best classifier.
(1) produce the first generation of  $n$  stars in the search space.
(2) select the best solution as black hole.
(3) while a good enough solution has not been reached in a maximum of iterations do
(4)   for all star  $s_i$ , ( $\forall i = 1, \dots, n$ ) do
(5)     evaluate classifier performance using cross-validation of data.
(6)     change the location of  $s_i$  according to Eq.(5).
(7)     if  $s_i$  is better than black hole then
(8)       select the current solution  $s_i$  as black hole.
(9)     endif
(10)     $\{s_i$  cross to the event horizon defined by Eq.(6) $\}$ 
(11)    if  $r > f_{bh} / \sum_{i=1}^n f_i$  then
(12)      replace  $s_i$  with a new star in a random location in the search space.
(13)    endif
(14)   endfor
(15) endwhile
(16) return results and visualization.

```

ALGORITHM 1: Black hole algorithm.

- (3) The movement and generation of new stars are carried out through the absorption formula:

$$x_i^d(t+1) = x_i^d(t) + \alpha [x_{bh}^d - x_i^d(t)], \quad \forall i \in \{1, \dots, n\} \quad (5)$$

where $x_i^d(t)$ corresponds to the d th component of the i th star in the iteration t , x_{bh}^d is the d th component of the black hole in the search space, n represents the number of solutions (number of stars), and α is a random uniform number of distribution between zero and one. Finally, $x_i^d(t+1)$ corresponds to the d th component of the location of the i th star in the next iteration.

The event horizon is a radius originated by the black hole. In case a star crosses the horizon, it will be absorbed and destroyed by the black hole and a new star (solution) is created randomly. This is known as the probability of crossing the event horizon and is calculated as follows:

$$R = \frac{f_{bh}}{\sum_{i=1}^n f_i} \quad (6)$$

where f_{bh} is the performance value that has the best solution, f_i is the value associated with the quality of the i th star, and n is the number of stars (solutions). When the distance between the black hole and the star is less than the radius then the star crosses the event horizon. This star is absorbed and a new is randomly generated. We highlight the variability offered by event horizon that allows resolving the common and complex problem of stagnation in local optimum.

One of the most interesting characteristics of incomplete data processing algorithms is the approximation to good solutions. This concept may be used as stop criteria. However, in situations where the optimal solutions are not known a priori, it is not possible to measure the quality of found solutions. In these cases, possible stop criteria are the number of executed iterations, for the sake of clarity of the proposed

algorithm. In our proposal, the stop criteria are initially set as 100 off-line iterations.

Algorithm 1 displays the optimization procedure. At the beginning, the initial n -star population is randomly generated for each of the intrinsic signals and loop statement begins working.

Randomness allows a degree of variability in the algorithm. Then, in the loop statement, the process of absorption of the algorithm is carried out. The quality of each solution is calculated, determined by the performance exhibited by the classifier. If the rating value is close to 1, the solution is considered to have a high quality (see Line (11) of Algorithm 1). Conversely, if the rating value is close to 0, the solution is considered to exhibit low quality due to the probability of crossing the event horizon is highest. The solutions are generated by the absorption of stars by the black hole that is presented in (5). Performing this process generates a real number of predictability for each intrinsic signal. If a star or solution reaches a value better than the black hole, its locations are swapped. If a star crosses the event horizon of the black hole, calculated by (6), it is absorbed and generates a new one randomly. This comparison is performed according to a random variable with uniform distribution $r \sim [0, 1]$. This whole procedure is done iteratively.

To measure the performance (quality) of the solutions, a proportion given by (6) is used between the fitness of the star and the combined value of all fitness (excluding that star). This value is known as an event horizon. If this percentage value is less than r , randomly generated, the star will be absorbed. This nondeterministic process provides variability to the solutions.

Finally, the loop statement ends when an adequate enough solution is reached for our approach; this condition is determined by updating the solution in a certain amount of iterations. At the end, the best solutions are memorized and visualized.

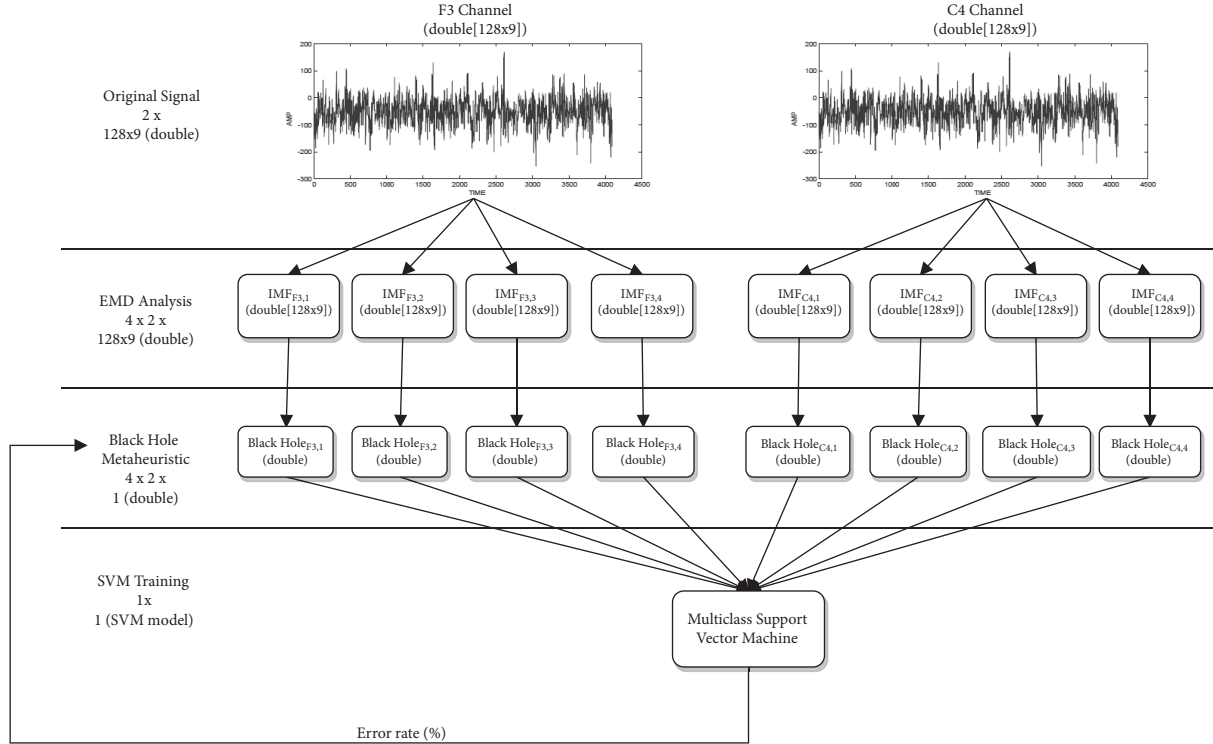


FIGURE 5: Proposed method using black hole algorithm.

Figure 5 illustrates the integration of the black hole algorithm into the process of creation of the classifier and its subsequent evaluation. The process is described in a loop way between the calculation of the predictability value and the performance evaluation of the created classifier. This approach allows improving the quality of the classifier, since it is used during the run of the algorithm itself.

4. Computational Experiments

After applying the approximation approach, we have analyzed the time complexity of the black hole algorithm into the process of creating the classifier and we illustrate that our proposal does not affect its performance. It can be determined that time complexity of the SampEn is given by $O((N^2/2)(1 - (1 - r)^m))$, where N represents the size of the array data and m is the number of matches and is much smaller than N . Finally, r represents the probability of two samples, $y(i)$ and $y(j)$ [69]. Now, by analyzing the approximate algorithm, it can be observed that the time complexity is given by $O(TN)$, where T is a constant and represents the maximum number of iterations, while N is the size of population (stars). Although the incorporation of an optimization algorithm based on swarm intelligence can cause an increase in cyclomatic complexity (19 to 39) [70], this only affects the training phase. The classification phase, being subsequent to the search process of the best configuration of the SVM (gamma and C parameters), is not affected.

The performance of the black hole algorithm was experimentally evaluated by using a set of well-known validated signals using MAHNOB HCI Tagging Database [48].

The approximate approach has been implemented on the programming language C# and the experiments [71–73] have been executed on a 2.6 GHz Intel Core i7 with 16 GB RAM machine running Windows 7. The initial parameter setting used is detailed in Table 1.

Firstly, these parameter settings are adopted after a hard initial training phase, being the one that obtained the best results. Then, we considered previous works to compare the choice of parameter values as reported in [24].

A common method to recognize the emotion based on EEG signals uses the entropy factor to build the classifier. We have implemented this technique and the accuracy obtained was close to 84.77% producing an error of classification outperform to 15%. That can be attributed to the sample entropy that builds the classifier without iterating in order to find the best solution.

Towards the end of iterations, the approximate optimization method reaches an accuracy above to 93% illustrating again that its performance is better than sample entropy approach. All results are available in Appendix B.

Figure 6 illustrates clearly the robustness of our proposed approach. Lower bound is given by the minimum accuracy found. If we only analyze this point only, we can see that immediately after the first iteration, the black hole algorithm always reaches a better value than found by the sample entropy method [42].

TABLE 1: Parameter setting to the entropy and the black hole algorithm.

Section	Component	Description	Value
Data selection	Number of sessions	Emotion elicitation trials	563
	Frequency	Each second has 128 samples or values	128 Hz
	Frame	To classify each frame it lasts 9 seconds, without overlapping	9 sec.
Sample entropy	N	Number of samples	128 samples
	m	Embedded dimension	2
	r	Probability of similarity on two simultaneous datasets	0.15
Empirical Mode Decomposition	Order	Number of IMFs	4
Black Hole Algorithm	n	Number of stars (solutions)	30
	T	Maximum iterations	100
Miscellaneous	–	Runs of the approximate approach	30
	–	Number of used cores (processors)	8

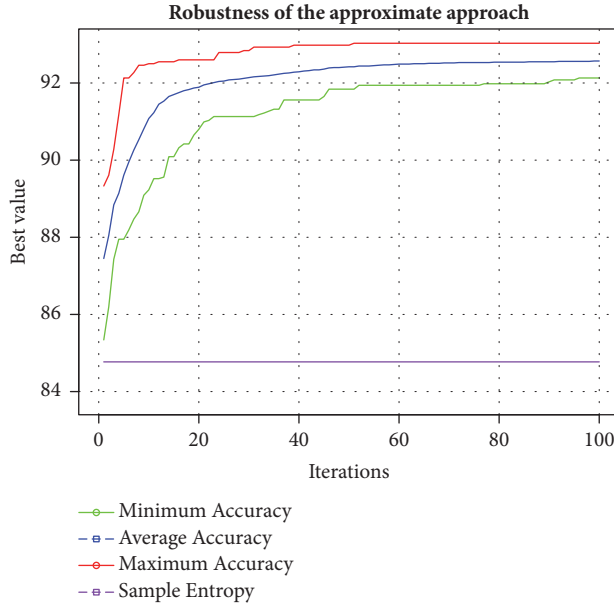


FIGURE 6: Convergence chart of the proposed method.

It is possible to conclude that the results are promising compared to those obtained with other SVM classifiers built by using the entropy factor. The proposed method used the MAHNOB HCI Tagging Database and reached a maximum accuracy level of 93.03%, with an average of 92.57%. Using the same dataset, a standard approach using the entropy factor to build a SVM classifier presents an average accuracy of 84.77%. More details can be seen in Appendix A and Appendix B.

This approach could be useful in emotion classification if the research goal would be to obtain relevant information in real time, for instance, incorporating an EEG in the classroom [74, 75]. This process would involve building a classifier for signal manipulation. The signal could be obtained online.

Also, preprocessing techniques that have a high computational cost were not used, such as signal normalization or eye movement artifact cleaning using blind source separation. Apart from the computational cost, these techniques require a baseline signal previously recorded.

5. Conclusions and Future Works

Emotions have been subject to scientific research for more than a century, as they play many essential roles in people's lives [76]. In this paper, we have presented a new method based on an optimization approach for the building of an SVM classifier for EEG-emotion signals. This approach consists in applying the EMD method to decompose the signal. Then, sampled entropy is applied on the first 4 components. Next, with these initial characteristics, the black hole algorithm was used to optimize them and thus obtain the best combination of the SVM feature vectors to generate a higher accuracy.

EEG-emotion signals allow for the prediction and classification of data with automated noise reduction. The emotion research is especially complex due to the ecological paradigm requirement, specifically the trigger stimuli, and emotional response generates high rate of noise. A common method is detailed in the background section, using entropy as a more relevant element. Nevertheless, results are not what was expected, reaching 85% in accuracy only.

In order to improve these computational results, we conducted an approximate method inspired on the black hole phenomenon. This algorithm is proposed to analyze the performance of an SVM classifier, allowing the extension of emotion ecological paradigms with EEG data.

We have tested our technique using a validated emotion signal, named MAHNOB HCI Tagging Database. Results show that the optimization algorithm allows the SVM classifier to surpass 90% in accuracy in its first iterations, even reaching 93%; furthermore, it is highly competitive with those presented in the related works section.

TABLE 2: Computational results of the approximate approach.

It.	Accuracy			
	Minimum	Average	Standard Deviation	Maximum
1	85.34	87.45	1.18E+04	89.33
2	86.20	88.05	8.89E+03	89.61
3	87.43	88.84	6.67E+03	90.28
4	87.95	89.14	7.32E+03	91.18
5	87.95	89.61	1.10E+04	92.13
6	88.19	89.95	1.15E+04	92.13
7	88.47	90.26	1.13E+04	92.27
8	88.66	90.53	1.15E+04	92.46
9	89.09	90.81	1.05E+04	92.46
10	89.23	91.08	9.90E+03	92.50
11	89.52	91.23	9.35E+03	92.50
12	89.52	91.45	7.81E+03	92.55
13	89.56	91.53	7.74E+03	92.55
14	90.09	91.65	6.72E+03	92.55
15	90.09	91.70	6.37E+03	92.55
16	90.32	91.75	5.98E+03	92.60
17	90.42	91.80	5.61E+03	92.60
18	90.42	91.83	5.58E+03	92.60
19	90.65	91.87	5.43E+03	92.60
20	90.80	91.89	5.28E+03	92.60

Particularly, these results are compatible with those obtained with the EEG-emotion signal with wavelet entropy and Support Vector Machine classifier proposed by Çelikkanat, but with higher accuracy [6].

As future works, we believe that using new approximate optimization algorithms will allow us to find better results to compare the SVM classifier performance. Moreover, we intend to incorporate an autonomous version of these algorithms so that the self-adaptive of its parameters is not complex and suited to the instance of the problem, as described in [9, 11].

On the other hand, we propose an integration of autonomous search in the parameter settings process, in order to find the best values during the run. This research can lead towards new study lines.

Appendix

A. Summary of the Experimental Results

In Tables 2, 3, 4, 5, and 6, we show a summary of the computational results generated by using the approximate approach. All computational results can be seen in Appendix B. Executing the experiments, we can observe that the performance of the optimization algorithm to find the best values for building the SVM classifier was outperforming to entropy approach. If we analyze the resolution process, we can see that in the first ten iterations the black hole algorithm reaches a minimum and average accuracy close to 90%. Finally, the

best value achieved is higher than 92%. In next iterations, the robustness of algorithm is demonstrated, according to the standard deviation values decrease as iterations occur.

B. Details of the Experimental Results

In Tables 7, 8, 9, 10, 11, 12, 13, 14, 15, 16, 17, and 18 we illustrate all computational results that we allow analyzing the performance of the proposed mixed approach. These tables have the same headers, which are described below: column 1 (Iterations) corresponds to the identifier assigned to each iteration. Columns 2-11 (Runs) describe runs each iteration; i.e., for instance, in row 10 (iteration 10) and column six (run #5), of Table 7, we can see that our approach reaches an accuracy of 90.56%. The same description can be used for the other tables.

Data Availability

The software developed and the data generated to support the findings of this study have been deposited in the Figshare repository (10.6084/m9.figshare.5588896, 10.6084/m9.figshare.5588911, and 10.6084/m9.figshare.5590000.v2).

Conflicts of Interest

The authors declare that there are no conflicts of interest regarding the publication of this paper.

TABLE 3: Computational results of the approximate approach (continuation).

It.	Accuracy			
	Minimum	Average	Standard Deviation	Maximum
21	90.99	91.95	4.94E+03	92.60
22	91.03	91.98	4.64E+03	92.60
23	91.13	92.01	4.48E+03	92.60
24	91.13	92.04	4.37E+03	92.79
25	91.13	92.05	4.41E+03	92.79
26	91.13	92.08	4.35E+03	92.79
27	91.13	92.09	4.33E+03	92.79
28	91.13	92.10	4.27E+03	92.79
29	91.13	92.12	4.27E+03	92.84
30	91.13	92.14	4.17E+03	92.84
31	91.13	92.16	4.15E+03	92.93
32	91.18	92.17	4.13E+03	92.93
33	91.22	92.18	4.08E+03	92.93
34	91.27	92.19	4.12E+03	92.93
35	91.32	92.21	3.99E+03	92.93
36	91.32	92.23	3.91E+03	92.93
37	91.56	92.25	3.67E+03	92.93
38	91.56	92.26	3.53E+03	92.93
39	91.56	92.28	3.53E+03	92.98
40	91.56	92.29	3.52E+03	92.98

TABLE 4: Computational results of the approximate approach (continuation).

It.	Accuracy			
	Minimum	Average	Standard Deviation	Maximum
41	91.56	92.31	3.40E+03	92.98
42	91.56	92.32	3.29E+03	92.98
43	91.56	92.34	3.29E+03	92.98
44	91.56	92.34	3.27E+03	92.98
45	91.65	92.36	3.11E+03	92.98
46	91.84	92.39	2.78E+03	92.98
47	91.84	92.40	2.82E+03	92.98
48	91.84	92.40	2.81E+03	92.98
49	91.84	92.41	2.82E+03	92.98
50	91.84	92.42	2.84E+03	92.98
51	91.84	92.42	2.88E+03	93.03
52	91.94	92.44	2.72E+03	93.03
53	91.94	92.44	2.75E+03	93.03
54	91.94	92.44	2.73E+03	93.03
55	91.94	92.45	2.76E+03	93.03
56	91.94	92.46	2.84E+03	93.03
57	91.94	92.47	2.84E+03	93.03
58	91.94	92.47	2.79E+03	93.03
59	91.94	92.48	2.80E+03	93.03
60	91.94	92.49	2.74E+03	93.03

TABLE 5: Computational results of the approximate approach (continuation).

It.	Accuracy			
	Minimum	Average	Standard Deviation	Maximum
61	91.94	92.49	2.74E+03	93.03
62	91.94	92.49	2.70E+03	93.03
63	91.94	92.50	2.68E+03	93.03
64	91.94	92.50	2.70E+03	93.03
65	91.94	92.50	2.70E+03	93.03
66	91.94	92.51	2.65E+03	93.03
67	91.94	92.51	2.60E+03	93.03
68	91.94	92.51	2.61E+03	93.03
69	91.94	92.52	2.60E+03	93.03
70	91.94	92.52	2.59E+03	93.03
71	91.94	92.52	2.59E+03	93.03
72	91.94	92.53	2.59E+03	93.03
73	91.94	92.53	2.59E+03	93.03
74	91.94	92.53	2.61E+03	93.03
75	91.94	92.53	2.62E+03	93.03
76	91.94	92.53	2.62E+03	93.03
77	91.98	92.53	2.59E+03	93.03
78	91.98	92.53	2.61E+03	93.03
79	91.98	92.54	2.58E+03	93.03
80	91.98	92.54	2.58E+03	93.03

TABLE 6: Computational results of the approximate approach (final).

It.	Accuracy			
	Minimum	Average	Standard Deviation	Maximum
81	91.98	92.54	2.59E+03	93.03
82	91.98	92.54	2.59E+03	93.03
83	91.98	92.54	2.59E+03	93.03
84	91.98	92.54	2.58E+03	93.03
85	91.98	92.54	2.55E+03	93.03
86	91.98	92.55	2.57E+03	93.03
87	91.98	92.55	2.55E+03	93.03
88	91.98	92.55	2.55E+03	93.03
89	91.98	92.55	2.55E+03	93.03
90	92.03	92.55	2.51E+03	93.03
91	92.08	92.55	2.48E+03	93.03
92	92.08	92.56	2.49E+03	93.03
93	92.08	92.56	2.49E+03	93.03
94	92.08	92.56	2.49E+03	93.03
95	92.08	92.56	2.49E+03	93.03
96	92.13	92.56	2.43E+03	93.03
97	92.13	92.56	2.43E+03	93.03
98	92.13	92.56	2.41E+03	93.03
99	92.13	92.57	2.41E+03	93.03
100	92.13	92.57	2.41E+03	93.03

TABLE 7: Dataset of experimental results. Twenty-five first iterations of the ten first runs.

Iterations	Runs									
	#1	#2	#3	#4	#5	#6	#7	#8	#9	#10
1	88.24	88.57	87.95	89.04	86.48	88.05	86.15	87.33	88.85	86.95
2	88.76	88.57	88.14	89.04	86.48	88.05	87.43	87.33	89.61	88.24
3	89.28	89.52	88.76	89.04	87.43	88.43	89.18	88.66	90.28	88.47
4	91.18	89.52	89.23	89.04	88.43	88.61	89.47	88.9	90.28	89.23
5	91.18	91.08	90.42	89.47	88.61	89.33	90.04	88.9	92.13	89.8
6	91.46	91.08	91.41	90.32	88.61	89.37	91.32	89.14	92.13	90.23
7	91.46	91.37	91.46	90.32	89.04	89.37	91.46	89.47	92.27	90.37
8	91.75	91.46	92.46	90.61	89.47	89.37	91.98	89.47	92.27	90.56
9	91.84	91.46	92.46	90.94	90.09	89.61	91.98	90.32	92.31	91.51
10	91.89	91.94	92.5	90.94	90.56	90.42	92.13	90.7	92.31	91.51
11	91.94	91.94	92.5	90.94	91.03	90.42	92.13	90.75	92.31	91.51
12	91.98	91.98	92.5	90.94	91.46	90.75	92.22	91.37	92.31	91.51
13	91.98	92.13	92.55	90.94	91.46	90.8	92.22	91.6	92.31	91.6
14	91.98	92.31	92.55	90.94	91.65	91.13	92.22	91.6	92.31	91.6
15	91.98	92.31	92.55	90.99	91.7	91.13	92.22	91.75	92.31	91.6
16	92.03	92.36	92.6	91.03	91.75	91.13	92.22	91.75	92.36	91.6
17	92.03	92.46	92.6	91.08	91.98	91.13	92.22	91.75	92.36	91.6
18	92.13	92.46	92.6	91.08	91.98	91.13	92.22	91.75	92.41	91.7
19	92.13	92.46	92.6	91.08	91.98	91.13	92.22	91.75	92.5	91.7
20	92.17	92.46	92.6	91.22	91.98	91.13	92.22	91.79	92.5	91.89
21	92.17	92.46	92.6	91.37	92.03	91.13	92.22	91.98	92.5	91.89
22	92.17	92.46	92.6	91.37	92.03	91.13	92.22	91.98	92.5	91.89
23	92.17	92.46	92.6	91.37	92.13	91.13	92.31	92.13	92.5	91.89
24	92.17	92.5	92.6	91.51	92.13	91.13	92.31	92.13	92.5	91.89
25	92.27	92.5	92.6	91.51	92.13	91.13	92.36	92.13	92.5	91.89

TABLE 8: Dataset of experimental results. Twenty-five second iterations of the ten first runs.

Iterations	Runs									
	#1	#2	#3	#4	#5	#6	#7	#8	#9	#10
26	92.27	92.5	92.6	91.51	92.31	91.13	92.41	92.13	92.5	91.89
27	92.27	92.5	92.6	91.51	92.31	91.13	92.46	92.13	92.5	91.89
28	92.27	92.5	92.6	91.51	92.31	91.18	92.55	92.13	92.5	91.89
29	92.27	92.5	92.6	91.56	92.46	91.18	92.55	92.13	92.5	91.89
30	92.27	92.5	92.6	91.56	92.46	91.18	92.65	92.13	92.5	91.94
31	92.27	92.5	92.6	91.56	92.46	91.27	92.65	92.17	92.5	91.94
32	92.27	92.5	92.6	91.56	92.5	91.27	92.65	92.22	92.5	91.98
33	92.27	92.5	92.6	91.56	92.5	91.27	92.65	92.27	92.5	91.98
34	92.27	92.5	92.6	91.56	92.65	91.27	92.69	92.41	92.5	92.03
35	92.27	92.5	92.6	91.56	92.79	91.32	92.69	92.41	92.5	92.13
36	92.27	92.5	92.6	91.56	92.88	91.32	92.69	92.41	92.5	92.17
37	92.27	92.5	92.6	91.56	92.88	91.6	92.69	92.41	92.5	92.17
38	92.27	92.5	92.6	91.56	92.88	91.6	92.69	92.41	92.5	92.17
39	92.27	92.5	92.6	91.56	92.98	91.6	92.69	92.41	92.5	92.17
40	92.27	92.5	92.6	91.56	92.98	91.6	92.69	92.41	92.5	92.27
41	92.27	92.5	92.6	91.56	92.98	91.6	92.69	92.41	92.5	92.36
42	92.27	92.5	92.6	91.56	92.98	91.65	92.69	92.41	92.5	92.5
43	92.27	92.5	92.6	91.56	92.98	91.65	92.69	92.41	92.5	92.5
44	92.27	92.5	92.6	91.56	92.98	91.65	92.69	92.41	92.5	92.5
45	92.27	92.5	92.6	91.7	92.98	91.65	92.69	92.41	92.5	92.5
46	92.27	92.5	92.6	91.89	92.98	91.84	92.69	92.41	92.5	92.5
47	92.27	92.5	92.6	91.89	92.98	91.84	92.69	92.41	92.5	92.5
48	92.27	92.5	92.6	91.89	92.98	91.84	92.69	92.41	92.5	92.5
49	92.27	92.5	92.6	91.89	92.98	91.84	92.69	92.41	92.5	92.5
50	92.31	92.5	92.6	91.94	92.98	91.84	92.69	92.41	92.5	92.55

TABLE 9: Dataset of experimental results. Twenty-five third iterations of the ten first runs.

Iterations	Runs									
	#1	#2	#3	#4	#5	#6	#7	#8	#9	#10
51	92.31	92.5	92.6	91.94	93.03	91.84	92.69	92.41	92.5	92.6
52	92.31	92.5	92.6	91.94	93.03	92.17	92.69	92.41	92.5	92.65
53	92.31	92.5	92.6	91.94	93.03	92.17	92.69	92.41	92.5	92.65
54	92.31	92.5	92.6	91.94	93.03	92.17	92.69	92.41	92.5	92.65
55	92.31	92.5	92.6	91.94	93.03	92.17	92.69	92.41	92.5	92.65
56	92.31	92.5	92.6	91.94	93.03	92.22	92.69	92.41	92.5	92.65
57	92.31	92.5	92.6	91.94	93.03	92.22	92.69	92.41	92.5	92.65
58	92.31	92.5	92.6	91.94	93.03	92.22	92.69	92.41	92.5	92.69
59	92.31	92.5	92.6	91.94	93.03	92.22	92.69	92.41	92.5	92.69
60	92.31	92.5	92.6	91.94	93.03	92.27	92.69	92.41	92.55	92.69
61	92.31	92.5	92.6	91.94	93.03	92.27	92.69	92.41	92.55	92.69
62	92.31	92.5	92.6	92.03	93.03	92.27	92.69	92.41	92.55	92.69
63	92.31	92.5	92.6	92.03	93.03	92.31	92.69	92.41	92.55	92.69
64	92.31	92.5	92.6	92.03	93.03	92.31	92.69	92.41	92.55	92.69
65	92.31	92.5	92.6	92.03	93.03	92.31	92.69	92.41	92.55	92.69
66	92.31	92.5	92.6	92.08	93.03	92.31	92.69	92.41	92.55	92.69
67	92.31	92.5	92.6	92.13	93.03	92.31	92.69	92.41	92.55	92.69
68	92.31	92.5	92.6	92.13	93.03	92.31	92.69	92.41	92.55	92.69
69	92.31	92.5	92.6	92.13	93.03	92.31	92.69	92.41	92.55	92.69
70	92.31	92.5	92.6	92.13	93.03	92.36	92.69	92.41	92.55	92.69
71	92.31	92.5	92.6	92.13	93.03	92.36	92.69	92.41	92.55	92.69
72	92.31	92.5	92.6	92.13	93.03	92.36	92.69	92.41	92.55	92.69
73	92.31	92.5	92.6	92.13	93.03	92.36	92.69	92.41	92.55	92.69
74	92.31	92.5	92.6	92.13	93.03	92.36	92.69	92.41	92.55	92.69
75	92.31	92.5	92.6	92.13	93.03	92.36	92.69	92.41	92.55	92.69

TABLE 10: Dataset of experimental results. Twenty-five fourth iterations of the ten first runs.

Iterations	Runs									
	#1	#2	#3	#4	#5	#6	#7	#8	#9	#10
76	92.31	92.5	92.6	92.13	93.03	92.36	92.69	92.41	92.55	92.69
77	92.31	92.5	92.6	92.13	93.03	92.36	92.69	92.41	92.55	92.69
78	92.31	92.5	92.6	92.13	93.03	92.36	92.69	92.41	92.55	92.69
79	92.31	92.5	92.6	92.13	93.03	92.41	92.69	92.41	92.55	92.69
80	92.31	92.5	92.6	92.13	93.03	92.41	92.69	92.41	92.55	92.69
81	92.31	92.5	92.6	92.13	93.03	92.41	92.69	92.41	92.55	92.69
82	92.31	92.5	92.6	92.13	93.03	92.46	92.69	92.41	92.55	92.69
83	92.31	92.5	92.6	92.13	93.03	92.46	92.69	92.41	92.55	92.69
84	92.31	92.5	92.6	92.13	93.03	92.46	92.69	92.46	92.55	92.69
85	92.31	92.5	92.6	92.13	93.03	92.46	92.69	92.46	92.55	92.69
86	92.31	92.5	92.6	92.13	93.03	92.46	92.69	92.46	92.55	92.69
87	92.41	92.5	92.6	92.13	93.03	92.46	92.69	92.46	92.55	92.69
88	92.41	92.5	92.6	92.13	93.03	92.46	92.69	92.46	92.55	92.69
89	92.41	92.5	92.6	92.13	93.03	92.46	92.69	92.46	92.55	92.69
90	92.41	92.5	92.6	92.13	93.03	92.46	92.69	92.46	92.55	92.69
91	92.41	92.5	92.6	92.13	93.03	92.46	92.69	92.46	92.55	92.69
92	92.41	92.5	92.6	92.13	93.03	92.46	92.69	92.46	92.55	92.69
93	92.41	92.5	92.6	92.13	93.03	92.46	92.69	92.46	92.55	92.69
94	92.41	92.5	92.6	92.13	93.03	92.46	92.69	92.46	92.55	92.69
95	92.41	92.5	92.6	92.13	93.03	92.46	92.69	92.46	92.55	92.69
96	92.41	92.5	92.6	92.13	93.03	92.46	92.69	92.46	92.55	92.69
97	92.41	92.5	92.6	92.13	93.03	92.46	92.69	92.46	92.55	92.69
98	92.41	92.5	92.6	92.13	93.03	92.46	92.69	92.46	92.55	92.69
99	92.41	92.5	92.6	92.13	93.03	92.46	92.69	92.46	92.55	92.69
100	92.41	92.5	92.6	92.13	93.03	92.46	92.69	92.46	92.55	92.69

TABLE 11: Dataset of experimental results. Twenty-five first iterations of the ten second runs.

Iterations	Runs									
	#11	#12	#13	#14	#15	#16	#17	#18	#19	#20
1	86.86	87	85.91	87.86	88.52	88.28	88.43	85.39	86.39	86.2
2	87.57	88.28	88.24	87.86	88.52	88.28	88.52	86.48	87.9	86.2
3	88.57	88.95	88.43	89.71	88.52	89.14	88.71	88.9	88.09	87.95
4	88.85	88.95	88.8	89.75	88.66	89.14	88.8	88.9	88.57	87.95
5	89.14	89.71	88.8	90.09	89.28	89.14	88.8	88.9	89.42	87.95
6	89.28	90.51	88.8	90.09	90.51	89.94	88.8	89.33	90.37	88.19
7	89.52	90.51	89.42	91.94	91.37	90.04	89.28	89.33	90.51	88.47
8	89.71	90.8	89.42	91.94	91.37	90.18	89.37	89.33	91.27	90.04
9	89.94	90.84	89.42	92.13	91.37	90.94	89.9	89.33	91.27	90.56
10	90.37	91.08	89.52	92.46	91.79	91.84	89.9	89.42	91.27	90.89
11	90.56	91.18	89.52	92.46	91.79	91.84	90.04	89.52	91.75	90.89
12	91.27	91.51	89.56	92.55	91.79	91.84	91.22	89.52	91.84	90.89
13	91.27	91.56	89.56	92.55	91.79	91.89	91.22	89.66	91.94	90.89
14	91.27	91.7	90.56	92.55	91.84	91.89	91.7	90.09	92.13	90.89
15	91.37	91.75	91.13	92.55	91.84	91.89	91.7	90.09	92.13	90.99
16	91.51	91.75	91.13	92.55	91.84	91.89	91.7	90.42	92.13	90.99
17	91.6	91.79	91.18	92.55	91.84	91.89	91.79	90.42	92.13	90.99
18	91.6	91.79	91.18	92.55	91.89	91.89	91.79	90.42	92.13	90.99
19	91.7	91.79	91.37	92.55	92.08	91.94	91.79	90.65	92.13	90.99
20	91.7	91.79	91.37	92.6	92.08	91.94	91.79	90.8	92.17	90.99
21	91.75	91.79	91.6	92.6	92.08	91.94	91.89	91.03	92.17	90.99
22	91.79	91.84	91.6	92.6	92.08	91.94	91.94	91.56	92.17	91.03
23	91.79	91.84	91.65	92.6	92.22	91.94	91.94	91.56	92.17	91.27
24	91.79	91.94	91.65	92.6	92.22	91.94	91.94	91.6	92.17	91.41
25	91.79	91.94	91.65	92.6	92.22	91.94	91.94	91.6	92.17	91.41

TABLE 12: Dataset of experimental results. Twenty-five second iterations of the ten second runs.

Iterations	Runs									
	#11	#12	#13	#14	#15	#16	#17	#18	#19	#20
26	91.79	91.94	91.65	92.6	92.22	91.94	91.94	91.98	92.17	91.41
27	91.79	91.94	91.65	92.6	92.22	91.94	91.94	91.98	92.17	91.41
28	91.79	91.94	91.75	92.6	92.22	91.98	91.94	92.03	92.17	91.41
29	91.84	91.94	91.79	92.6	92.22	91.98	91.94	92.03	92.17	91.41
30	91.84	91.94	91.89	92.6	92.22	92.03	91.94	92.08	92.17	91.65
31	91.84	91.94	91.89	92.6	92.22	92.03	91.94	92.17	92.17	91.65
32	91.84	91.94	91.89	92.6	92.22	92.03	91.94	92.27	92.17	91.65
33	91.84	91.94	91.94	92.6	92.22	92.03	91.94	92.27	92.17	91.65
34	91.84	91.94	91.94	92.6	92.22	92.08	91.94	92.27	92.17	91.65
35	91.84	91.94	91.94	92.6	92.22	92.08	91.94	92.27	92.17	91.7
36	91.89	91.94	91.94	92.6	92.22	92.13	91.94	92.27	92.17	91.7
37	91.89	91.94	91.94	92.6	92.27	92.17	91.98	92.31	92.17	91.75
38	91.89	91.94	91.94	92.6	92.27	92.22	92.08	92.36	92.17	91.75
39	91.89	91.94	91.94	92.69	92.27	92.22	92.17	92.36	92.17	91.94
40	91.89	91.94	91.94	92.69	92.27	92.27	92.17	92.36	92.17	91.94
41	91.89	91.94	91.94	92.74	92.27	92.36	92.17	92.36	92.17	92.13
42	92.03	91.94	91.98	92.74	92.27	92.36	92.31	92.36	92.17	92.13
43	92.03	91.94	91.98	92.74	92.27	92.36	92.41	92.36	92.17	92.17
44	92.08	91.94	91.98	92.74	92.27	92.36	92.5	92.36	92.17	92.17
45	92.08	91.94	92.03	92.74	92.27	92.36	92.5	92.36	92.17	92.27
46	92.27	91.94	92.03	92.74	92.27	92.36	92.5	92.36	92.22	92.46
47	92.27	91.94	92.03	92.84	92.27	92.36	92.5	92.36	92.22	92.55
48	92.27	91.94	92.03	92.84	92.27	92.41	92.5	92.36	92.31	92.55
49	92.27	91.94	92.03	92.84	92.27	92.41	92.5	92.36	92.31	92.6
50	92.27	91.94	92.03	92.84	92.27	92.46	92.5	92.36	92.36	92.79

TABLE 13: Dataset of experimental results. Twenty-five third iterations of the ten second runs.

Iterations	Runs									
	#11	#12	#13	#14	#15	#16	#17	#18	#19	#20
51	92.27	91.94	92.03	92.84	92.27	92.46	92.5	92.36	92.36	92.79
52	92.27	91.94	92.03	92.84	92.27	92.5	92.5	92.36	92.36	92.79
53	92.27	91.94	92.03	92.84	92.27	92.5	92.5	92.36	92.46	92.84
54	92.27	91.94	92.08	92.84	92.27	92.5	92.5	92.36	92.5	92.84
55	92.31	91.94	92.08	92.84	92.27	92.55	92.5	92.36	92.69	92.84
56	92.31	91.94	92.08	92.88	92.27	92.55	92.5	92.36	92.74	92.93
57	92.31	91.94	92.13	92.93	92.27	92.55	92.5	92.41	92.74	92.93
58	92.36	91.94	92.13	92.93	92.27	92.55	92.5	92.41	92.74	92.93
59	92.36	91.94	92.13	92.93	92.27	92.55	92.5	92.41	92.79	92.93
60	92.36	91.94	92.13	92.93	92.27	92.55	92.5	92.41	92.79	92.93
61	92.36	91.94	92.13	92.93	92.27	92.55	92.5	92.41	92.79	92.93
62	92.36	91.94	92.13	92.93	92.27	92.55	92.5	92.41	92.84	92.93
63	92.41	91.94	92.13	92.93	92.27	92.55	92.5	92.41	92.84	92.93
64	92.41	91.94	92.13	92.93	92.27	92.55	92.5	92.41	92.88	92.93
65	92.41	91.94	92.13	92.93	92.27	92.55	92.5	92.41	92.88	92.93
66	92.41	91.94	92.13	92.93	92.27	92.55	92.5	92.46	92.88	92.93
67	92.41	91.94	92.13	92.93	92.27	92.55	92.5	92.46	92.88	92.93
68	92.41	91.94	92.13	92.93	92.27	92.55	92.5	92.46	92.88	92.93
69	92.41	91.94	92.13	92.93	92.27	92.55	92.5	92.5	92.88	92.93
70	92.41	91.94	92.13	92.93	92.27	92.55	92.5	92.5	92.88	92.93
71	92.41	91.94	92.13	92.93	92.27	92.55	92.5	92.55	92.88	92.93
72	92.41	91.94	92.13	92.93	92.27	92.55	92.5	92.55	92.88	92.93
73	92.41	91.94	92.13	92.93	92.27	92.55	92.5	92.55	92.88	92.93
74	92.41	91.94	92.13	92.93	92.27	92.55	92.5	92.55	92.88	92.93
75	92.41	91.94	92.13	92.93	92.27	92.55	92.5	92.55	92.88	92.93

TABLE 14: Dataset of experimental results. Twenty-five fourth iterations of the ten second runs.

Iterations	Runs									
	#11	#12	#13	#14	#15	#16	#17	#18	#19	#20
76	92.41	91.94	92.13	92.93	92.27	92.55	92.5	92.55	92.88	92.93
77	92.41	91.98	92.13	92.93	92.27	92.55	92.5	92.55	92.88	92.93
78	92.41	91.98	92.13	92.93	92.27	92.55	92.5	92.55	92.88	92.93
79	92.41	91.98	92.13	92.93	92.27	92.55	92.5	92.55	92.88	92.93
80	92.41	91.98	92.13	92.93	92.27	92.55	92.5	92.55	92.88	92.93
81	92.41	91.98	92.13	92.93	92.27	92.55	92.5	92.55	92.88	92.93
82	92.41	91.98	92.13	92.93	92.27	92.55	92.5	92.55	92.88	92.93
83	92.41	91.98	92.13	92.93	92.27	92.55	92.5	92.55	92.88	92.93
84	92.41	91.98	92.13	92.93	92.27	92.55	92.5	92.55	92.88	92.93
85	92.41	91.98	92.17	92.93	92.27	92.55	92.5	92.55	92.88	92.93
86	92.46	91.98	92.17	92.93	92.27	92.55	92.5	92.55	92.93	92.93
87	92.46	91.98	92.17	92.93	92.27	92.55	92.5	92.55	92.93	92.93
88	92.46	91.98	92.17	92.93	92.27	92.55	92.5	92.55	92.93	92.93
89	92.46	91.98	92.17	92.93	92.27	92.55	92.5	92.55	92.93	92.93
90	92.46	92.03	92.17	92.93	92.27	92.55	92.5	92.55	92.93	92.93
91	92.46	92.08	92.17	92.93	92.27	92.55	92.5	92.55	92.93	92.93
92	92.46	92.08	92.17	92.93	92.27	92.55	92.5	92.65	92.93	92.93
93	92.46	92.08	92.17	92.93	92.27	92.55	92.5	92.65	92.93	92.93
94	92.46	92.08	92.17	92.93	92.27	92.55	92.5	92.65	92.93	92.93
95	92.46	92.08	92.17	92.93	92.27	92.55	92.5	92.65	92.93	92.93
96	92.46	92.17	92.17	92.93	92.31	92.55	92.5	92.65	92.93	92.93
97	92.46	92.17	92.17	92.93	92.31	92.55	92.5	92.65	92.93	92.93
98	92.46	92.17	92.17	92.93	92.36	92.55	92.5	92.65	92.93	92.93
99	92.46	92.17	92.17	92.93	92.41	92.55	92.5	92.65	92.93	92.93
100	92.46	92.17	92.17	92.93	92.41	92.55	92.5	92.65	92.93	92.93

TABLE 15: Dataset of experimental results. Twenty-five first iterations of the ten third runs.

Iterations	Runs									
	#21	#22	#23	#24	#25	#26	#27	#28	#29	#30
1	85.34	87.81	89.33	88.14	87.95	87.76	88.85	88.66	86.2	86.39
2	86.67	88.95	89.33	88.14	87.95	87.76	89.61	88.66	87.81	88.33
3	88.14	88.95	89.71	88.61	87.95	89.66	90.28	88.66	88.8	88.61
4	88.47	88.95	90.51	90.04	88.33	89.66	90.28	88.8	88.85	88.66
5	88.61	88.95	91.94	90.04	88.52	89.66	92.13	88.85	89.28	88.8
6	88.66	88.95	91.98	90.04	88.61	90.32	92.13	88.9	89.37	88.99
7	88.66	89.04	92.03	90.56	89.47	90.32	92.27	89.47	90.23	88.99
8	88.66	89.33	92.17	91.18	89.75	90.56	92.27	89.47	90.84	88.99
9	89.47	89.66	92.17	91.89	90.04	91.46	92.31	89.75	91.13	89.09
10	89.47	90.04	92.17	91.89	91.03	91.46	92.31	90.32	91.13	89.23
11	89.61	91.6	92.17	92.13	91.08	91.46	92.31	90.42	91.7	89.56
12	90.89	91.6	92.17	92.17	91.13	91.46	92.31	90.89	91.84	90.09
13	90.89	91.84	92.17	92.31	91.32	91.6	92.31	91.79	91.84	90.09
14	90.89	92.08	92.22	92.31	91.32	91.6	92.31	91.98	91.84	90.09
15	90.99	92.08	92.22	92.36	91.37	91.79	92.31	91.98	91.89	90.09
16	90.99	92.08	92.22	92.36	91.46	91.98	92.36	92.17	91.94	90.32
17	91.13	92.27	92.22	92.36	91.46	91.98	92.36	92.17	91.94	90.8
18	91.13	92.27	92.22	92.36	91.46	92.27	92.41	92.17	91.94	91.03
19	91.13	92.46	92.22	92.36	91.46	92.27	92.5	92.22	91.94	91.08
20	91.13	92.46	92.22	92.36	91.56	92.27	92.5	92.27	91.94	91.08
21	91.13	92.5	92.22	92.36	92.03	92.27	92.5	92.27	91.94	91.08
22	91.13	92.55	92.22	92.36	92.03	92.27	92.5	92.31	91.94	91.13
23	91.13	92.6	92.22	92.41	92.08	92.27	92.5	92.31	91.94	91.27
24	91.13	92.79	92.27	92.46	92.08	92.27	92.5	92.31	91.94	91.41
25	91.13	92.79	92.27	92.46	92.17	92.27	92.5	92.36	91.94	91.41

TABLE 16: Dataset of experimental results. Twenty-five second iterations of the ten third runs.

Iterations	Runs									
	#21	#22	#23	#24	#25	#26	#27	#28	#29	#30
26	91.13	92.79	92.31	92.5	92.17	92.27	92.5	92.36	91.94	91.51
27	91.13	92.79	92.31	92.5	92.17	92.27	92.5	92.46	91.94	91.65
28	91.13	92.79	92.31	92.5	92.17	92.27	92.5	92.46	91.94	91.7
29	91.13	92.84	92.31	92.5	92.17	92.27	92.5	92.5	91.94	91.79
30	91.13	92.84	92.31	92.5	92.31	92.31	92.5	92.5	91.98	91.79
31	91.13	92.93	92.36	92.5	92.36	92.36	92.5	92.5	91.98	91.84
32	91.18	92.93	92.36	92.5	92.36	92.36	92.5	92.5	91.98	91.84
33	91.22	92.93	92.36	92.5	92.41	92.36	92.5	92.5	91.98	91.84
34	91.27	92.93	92.36	92.5	92.46	92.36	92.5	92.5	91.98	91.89
35	91.41	92.93	92.36	92.5	92.46	92.36	92.5	92.5	91.98	91.98
36	91.56	92.93	92.36	92.5	92.5	92.36	92.5	92.5	91.98	92.08
37	91.56	92.93	92.36	92.5	92.5	92.36	92.5	92.5	91.98	92.13
38	91.75	92.93	92.36	92.5	92.5	92.36	92.5	92.5	91.98	92.13
39	91.75	92.93	92.36	92.5	92.5	92.36	92.5	92.55	92.08	92.13
40	91.75	92.93	92.36	92.5	92.5	92.36	92.5	92.55	92.08	92.17
41	91.89	92.93	92.36	92.5	92.5	92.36	92.5	92.55	92.13	92.17
42	91.89	92.93	92.36	92.5	92.5	92.36	92.5	92.55	92.13	92.17
43	91.89	92.93	92.36	92.5	92.5	92.36	92.5	92.55	92.17	92.17
44	91.89	92.93	92.36	92.5	92.5	92.36	92.5	92.55	92.27	92.17
45	91.94	92.93	92.36	92.5	92.5	92.41	92.5	92.55	92.36	92.17
46	91.94	92.93	92.36	92.5	92.5	92.41	92.5	92.55	92.41	92.17
47	91.98	92.93	92.36	92.5	92.5	92.41	92.5	92.55	92.41	92.17
48	91.98	92.93	92.36	92.5	92.5	92.41	92.5	92.55	92.5	92.17
49	91.98	92.93	92.36	92.5	92.5	92.41	92.5	92.55	92.5	92.17
50	91.98	92.93	92.36	92.5	92.5	92.41	92.5	92.55	92.5	92.17

TABLE 17: Dataset of experimental results. Twenty-five third iterations of the ten third runs.

Iterations	Runs									
	#21	#22	#23	#24	#25	#26	#27	#28	#29	#30
51	91.98	92.93	92.36	92.5	92.5	92.41	92.5	92.55	92.5	92.17
52	91.98	92.93	92.36	92.5	92.5	92.41	92.5	92.55	92.5	92.17
53	91.98	92.93	92.36	92.5	92.5	92.41	92.5	92.55	92.5	92.17
54	91.98	92.93	92.36	92.5	92.5	92.41	92.5	92.55	92.5	92.17
55	91.98	92.93	92.36	92.5	92.5	92.41	92.5	92.55	92.5	92.17
56	91.98	92.93	92.36	92.5	92.5	92.41	92.5	92.55	92.5	92.17
57	91.98	92.93	92.36	92.5	92.5	92.41	92.5	92.55	92.5	92.17
58	92.03	92.93	92.36	92.5	92.5	92.41	92.5	92.55	92.5	92.22
59	92.03	92.93	92.36	92.5	92.5	92.41	92.5	92.55	92.5	92.27
60	92.08	92.93	92.36	92.5	92.5	92.41	92.55	92.55	92.5	92.41
61	92.08	92.93	92.36	92.5	92.5	92.41	92.55	92.55	92.5	92.41
62	92.08	92.93	92.36	92.5	92.5	92.41	92.55	92.55	92.5	92.41
63	92.08	92.93	92.36	92.5	92.5	92.41	92.55	92.55	92.5	92.41
64	92.08	92.93	92.36	92.5	92.5	92.41	92.55	92.55	92.5	92.41
65	92.08	92.93	92.36	92.5	92.5	92.41	92.55	92.55	92.5	92.41
66	92.13	92.93	92.36	92.5	92.5	92.41	92.55	92.55	92.5	92.6
67	92.17	92.93	92.36	92.5	92.55	92.41	92.55	92.55	92.5	92.6
68	92.17	92.93	92.36	92.5	92.55	92.41	92.55	92.55	92.5	92.65
69	92.22	92.93	92.36	92.5	92.6	92.41	92.55	92.55	92.5	92.69
70	92.22	92.93	92.36	92.5	92.6	92.41	92.55	92.55	92.5	92.69
71	92.22	92.93	92.36	92.5	92.6	92.41	92.55	92.55	92.5	92.69
72	92.22	92.93	92.36	92.5	92.65	92.41	92.55	92.55	92.5	92.69
73	92.22	92.93	92.36	92.5	92.65	92.41	92.55	92.55	92.5	92.69
74	92.22	92.93	92.36	92.5	92.65	92.41	92.55	92.55	92.5	92.74
75	92.22	92.93	92.36	92.5	92.65	92.41	92.55	92.55	92.5	92.79

TABLE 18: Dataset of experimental results. Twenty-five fourth iterations of the ten third runs.

Iterations	Runs									
	#21	#22	#23	#24	#25	#26	#27	#28	#29	#30
76	92.22	92.93	92.36	92.5	92.65	92.41	92.55	92.55	92.5	92.79
77	92.22	92.93	92.36	92.5	92.65	92.41	92.55	92.55	92.5	92.79
78	92.22	92.93	92.36	92.5	92.74	92.41	92.55	92.55	92.5	92.79
79	92.27	92.93	92.36	92.5	92.74	92.41	92.55	92.55	92.5	92.79
80	92.27	92.93	92.36	92.5	92.74	92.41	92.55	92.55	92.5	92.79
81	92.27	92.93	92.36	92.5	92.79	92.41	92.55	92.55	92.5	92.79
82	92.27	92.93	92.36	92.5	92.79	92.41	92.55	92.55	92.5	92.79
83	92.27	92.93	92.36	92.5	92.79	92.41	92.55	92.55	92.5	92.79
84	92.27	92.93	92.36	92.5	92.79	92.41	92.55	92.55	92.5	92.79
85	92.27	92.93	92.36	92.5	92.79	92.41	92.55	92.55	92.5	92.79
86	92.27	92.93	92.36	92.5	92.79	92.41	92.55	92.55	92.5	92.79
87	92.27	92.93	92.36	92.5	92.79	92.41	92.55	92.55	92.5	92.79
88	92.27	92.93	92.36	92.5	92.79	92.41	92.55	92.55	92.5	92.79
89	92.27	92.93	92.36	92.5	92.79	92.41	92.55	92.55	92.5	92.79
90	92.27	92.93	92.36	92.5	92.79	92.41	92.55	92.55	92.5	92.79
91	92.27	92.93	92.36	92.5	92.79	92.41	92.55	92.55	92.5	92.79
92	92.27	92.93	92.36	92.5	92.79	92.41	92.55	92.55	92.5	92.79
93	92.27	92.93	92.36	92.5	92.79	92.41	92.55	92.55	92.5	92.79
94	92.27	92.93	92.36	92.5	92.79	92.41	92.55	92.55	92.5	92.79
95	92.27	92.93	92.36	92.5	92.79	92.41	92.55	92.55	92.5	92.79
96	92.27	92.93	92.36	92.5	92.84	92.41	92.55	92.55	92.5	92.79
97	92.27	92.93	92.36	92.5	92.84	92.41	92.55	92.55	92.5	92.79
98	92.27	92.93	92.36	92.5	92.84	92.41	92.55	92.55	92.5	92.79
99	92.27	92.93	92.36	92.55	92.84	92.41	92.55	92.55	92.5	92.84
100	92.27	92.93	92.36	92.55	92.84	92.41	92.55	92.55	92.5	92.84

Acknowledgments

Roberto Munoz and Rodrigo Olivares are supported by Postgraduate Grant of Pontificia Universidad Católica de Valparaíso (INF-PUCV 2015). Carla Taramasco and Rodrigo Olivares are supported by CONICYT/FONDEF/IDeA/ID16I10449, CONICYT/STIC-AMSUD/I7STIC-03, and CONICYT/MEC/MEC80170097 and CENS (National Center for Health Information Systems). Rodolfo Villarroel is funded by the VRIEA-PUCV 2017 039.440/2017 Grant. Ricardo Soto is supported by Grant CONICYT/FONDECYT/REGULAR/I160455. María Francisca Alonso-Sánchez is supported by CONICYT, FONDECYT INICIACION I1160212. Roberto Munoz and Carla Taramasco also acknowledge the Center for Research and Development in Health Engineering of the Universidad de Valparaíso. Finally, the authors would like to thank Travis Jones for his valuable contributions to the elaboration of this paper.

References

- [1] S. Spence, "Descartes' Error: Emotion, Reason and the Human Brain," *BMJ*, vol. 310, no. 6988, p. 1213, 1995.
- [2] R. W. Levenson, "Human emotion: A functional view," *The Nature of Emotion: Fundamental Questions*, vol. 1, pp. 123–126, 1994.
- [3] J. A. Russell, "A circumplex model of affect," *Journal of Personality and Social Psychology*, vol. 39, no. 6, pp. 1161–1178, 1980.
- [4] P. H. J. M. Vlaming, V. Goffaux, and C. Kemner, "Is the early modulation of brain activity by fearful facial expressions primarily mediated by coarse low spatial frequency information?" *Journal of Vision*, vol. 9, no. 5, 2009.
- [5] S. Jessen and T. Grossmann, "Exploring the role of spatial frequency information during neural emotion processing in human infants," *Frontiers in Human Neuroscience*, vol. 11, 2017.
- [6] H. Celikkanat, H. Moriya, T. Ogawa et al., "Decoding emotional valence from electroencephalographic rhythmic activity," in *Proceedings of the 2017 39th Annual International Conference of the IEEE Engineering in Medicine and Biology Society (EMBC)*, pp. 4143–4146, Jeju Island, South Korea, July 2017.
- [7] J. S. Richman and J. R. Moorman, "Physiological time-series analysis using approximate entropy and sample entropy," *American Journal of Physiology - Heart and Circulatory Physiology*, vol. 278, no. 6, pp. H2039–H2049, 2000.
- [8] J. M. Yentes, N. Hunt, K. K. Schmid, J. P. Kaipust, D. McGrath, and N. Stergiou, "The appropriate use of approximate entropy and sample entropy with short data sets," *Annals of Biomedical Engineering*, vol. 41, no. 2, pp. 349–365, 2013.
- [9] R. Soto, B. Crawford, R. Olivares et al., "Solving the non-unicost set covering problem by using cuckoo search and black hole optimization," *Natural Computing*, vol. 16, no. 2, pp. 213–229, 2017.
- [10] P. Shunmugapriya and S. Kanmani, "A hybrid algorithm using ant and bee colony optimization for feature selection and classification (AC-ABC Hybrid)," *Swarm and Evolutionary Computation*, vol. 36, pp. 27–36, 2017.
- [11] R. Soto, B. Crawford, R. Olivares et al., "Using autonomous search for solving constraint satisfaction problems via new modern approaches," *Swarm and Evolutionary Computation*, vol. 30, pp. 64–77, 2016.
- [12] R. Soto, B. Crawford, R. Olivares et al., "Online control of enumeration strategies via bat algorithm and black hole optimization," *Natural Computing*, vol. 16, no. 2, pp. 241–257, 2017.
- [13] A. Hatamlou, "Black hole: a new heuristic optimization approach for data clustering," *Information Sciences*, vol. 222, Supplement C, pp. 175–184, 2013.
- [14] X.-W. Wang, D. Nie, and B.-L. Lu, "Emotional state classification from EEG data using machine learning approach," *Neurocomputing*, vol. 129, pp. 94–106, 2014.
- [15] M. H. Libenson, *Practical Approach to Electroencephalography*, Elsevier Health Sciences, 1st edition, 2009.
- [16] F. Meyjes and R. Arts, "Recommendations for the practice of clinical neurophysiology," *Journal of the Neurological Sciences*, vol. 66, no. 2-3, p. 349, 1984.
- [17] W. O. Tatum and R. Ellen, "Grass Lecture: Extraordinary EEG," *The Neurodiagnostic Journal*, vol. 54, no. 1, pp. 3–21, 2014.
- [18] G. H. Klem, H. O. LuÈders, H. Jasper, C. Elger et al., "The ten-twenty electrode system of the international federation," *Electroencephalography and Clinical Neurophysiology*, vol. 52, no. 3, pp. 3–6, 1999.
- [19] "The ten twenty electrode system: international federation of societies for electroencephalography and clinical neurophysiology," *American Journal of EEG Technology*, vol. 1, no. 1, pp. 13–19, 1961.
- [20] E. P. N. Committee et al., "Guideline thirteen: guidelines for standard electrode position nomenclature," *Journal of Clinical Neurophysiology*, vol. 11, pp. 111–113, 1994.
- [21] S. C. Ng and P. Raveendran, "Comparison of different montages on to EEG classification," in *Proceedings of the 3rd Kuala Lumpur International Conference on Biomedical Engineering 2006*, vol. 15 of *IFMBE Proceedings*, pp. 365–368, Springer Berlin Heidelberg, 2007.
- [22] M. Yadava, P. Kumar, R. Saini, P. P. Roy, and D. Prosad Dogra, "Analysis of EEG signals and its application to neuromarketing," *Multimedia Tools and Applications*, vol. 76, no. 18, pp. 19087–19111, 2017.
- [23] B. Kerous, F. Skola, and F. Liarokapis, "EEG-based BCI and video games: a progress report," *Virtual Reality*, pp. 1–17, 2017.
- [24] M. Mohammadpour, S. M. R. Hashemi, and N. Houshmand, "Classification of EEG-based emotion for bci applications," in *Proceedings of the 7th Conference on Artificial Intelligence and Robotics, (IRANOPEN '17)*, pp. 127–131, IEEE, Qazvin, Iran, 2017.
- [25] J. Falkowska, J. Sobecki, and M. Pietrzak, "Eye tracking usability testing enhanced with EEG analysis," *Lecture Notes in Computer Science (including subseries Lecture Notes in Artificial Intelligence and Lecture Notes in Bioinformatics): Preface*, vol. 9746, pp. 399–411, 2016.
- [26] J. M. De Oliveira, R. C. G. Fernandes, C. S. Pinto, P. R. Pinheiro, S. Ribeiro, and V. H. C. De Albuquerque, "Novel virtual environment for alternative treatment of children with cerebral palsy," *Computational Intelligence and Neuroscience*, vol. 2016, Article ID 8984379, 2016.
- [27] G. Williams, R. Lesser, J. Silvers et al., "Clinical diagnoses and EEG interpretation," *Cleveland Clinic Journal of Medicine*, vol. 57, no. 5, pp. 437–440, 1990.
- [28] E. S. Kappenan and S. J. Luck, "Best Practices for Event-Related Potential Research in Clinical Populations," *Biological Psychiatry: Cognitive Neuroscience and Neuroimaging*, vol. 1, no. 2, pp. 110–115, 2016.

- [29] J. S. Richman and J. R. Moorman, "Physiological time-series analysis using approximate entropy and sample entropy," *American Journal of Physiology-Heart and Circulatory Physiology*, vol. 278, no. 6, pp. H2039–H2049, 2000.
- [30] C. Cortes and V. Vapnik, "Support-vector networks," *Machine Learning*, vol. 20, no. 3, pp. 273–297, 1995.
- [31] J. Weston and C. Watkins, "Multi-class support vector machines," Technical Report, Citeseer, 1998.
- [32] N. E. Huang, Z. Shen, S. R. Long et al., "The empirical mode decomposition and the Hilbert spectrum for nonlinear and non-stationary time series analysis," *Proceedings of the Royal Society A: Mathematical, Physical and Engineering Science*, vol. 454, no. 1971, pp. 903–995, 1998.
- [33] N. E. Huang, Z. Shen, S. R. Long et al., "The empirical mode decomposition and the Hilbert spectrum for nonlinear and non-stationary time series analysis," *Proceedings of the Royal Society of London A: Mathematical, Physical and Engineering Sciences*, vol. 454, pp. 903–995, 1998.
- [34] N. Hazarika, J. Z. Chen, A. C. Tsoi, and A. Sergejew, "Classification of EEG signals using the wavelet transform," *Signal Processing*, vol. 59, no. 1, pp. 61–72, 1997.
- [35] J.-P. Lachaux, E. Rodriguez, J. Martinerie, and F. J. Varela, "Measuring phase synchrony in brain signals," *Human Brain Mapping*, vol. 8, no. 4, pp. 194–208, 1999.
- [36] F. B. M. De Waal and S. D. Preston, "Mammalian empathy: behavioural manifestations and neural basis," *Nature Reviews Neuroscience*, vol. 18, no. 8, pp. 498–509, 2017.
- [37] J. A. Pineda, "The functional significance of mu rhythms: translating "seeing" and "hearing" into "doing"," *Brain Research Reviews*, vol. 50, no. 1, pp. 57–68, 2005.
- [38] A. Moore, I. Gorodnitsky, and J. Pineda, "EEG mu component responses to viewing emotional faces," *Behavioural Brain Research*, vol. 226, no. 1, pp. 309–316, 2012.
- [39] N. Kannathal, U. R. Acharya, C. M. Lim, and P. K. Sadasivan, "Characterization of EEG—a comparative study," *Computer Methods and Programs in Biomedicine*, vol. 80, no. 1, pp. 17–23, 2005.
- [40] P. A. Estévez, M. Tesmer, C. A. Perez, and J. M. Zurada, "Normalized mutual information feature selection," *IEEE Transactions on Neural Networks and Learning Systems*, vol. 20, no. 2, pp. 189–201, 2009.
- [41] H. Candra, M. Yuwono, R. Chai, H. T. Nguyen, and S. Su, "EEG emotion recognition using reduced channel wavelet entropy and average wavelet coefficient features with normal mutual information method," in *Proceedings of the 39th Annual International Conference of the IEEE Engineering in Medicine and Biology Society, EMBC 2017*, pp. 463–466, IEEE, Seogwipo, South Korea, July 2017.
- [42] Y. Zhang, X. Ji, and S. Zhang, "An approach to EEG-based emotion recognition using combined feature extraction method," *Neuroscience Letters*, vol. 633, pp. 152–157, 2016.
- [43] Z. Mohammadi, J. Frounchi, and M. Amiri, "Wavelet-based emotion recognition system using EEG signal," *Neural Computing and Applications*, pp. 1–6, 2016.
- [44] B. Gntekin and E. Baar, "Event-related beta oscillations are affected by emotional eliciting stimuli," *Neuroscience Letters*, vol. 483, no. 3, pp. 173–178, 2010.
- [45] S. Butterworth, "On the theory of filter amplifiers," *Wireless Engineer*, vol. 7, no. 6, pp. 536–541, 1930.
- [46] A. Garcés, L. Orosco, and E. Laciár, "Automatic detection of drowsiness in EEG records based on multimodal analysis," *Medical Engineering & Physics*, vol. 36, no. 2, pp. 244–249, 2013, <https://doi.org/10.1016/j.medengphy.07.011.doi>.
- [47] S. Koelstra, C. Mühl, M. Soleymani et al., "DEAP: a database for emotion analysis; using physiological signals," *IEEE Transactions on Affective Computing*, vol. 3, no. 1, pp. 18–31, 2012.
- [48] M. Soleymani, J. Lichtenauer, T. Pun, and M. Pantic, "A multimodal database for affect recognition and implicit tagging," *IEEE Transactions on Affective Computing*, vol. 3, no. 1, pp. 42–55, 2012.
- [49] O. Jensen, P. Goel, N. Kopell, M. Pohja, R. Hari, and B. Ermentrout, "On the human sensorimotor-cortex beta rhythm: sources and modeling," *NeuroImage*, vol. 26, no. 2, pp. 347–355, 2005.
- [50] A. Gogna and A. Tayal, "Metaheuristics: review and application," *Journal of Experimental & Theoretical Artificial Intelligence*, vol. 25, no. 4, Article ID 0952813, pp. 503–526, 2013, <https://doi.org/10.1080/0952813x.2013.782347>.
- [51] X.-S. Yang, *Nature-Inspired Metaheuristic Algorithms*, Luniver Press, 2008.
- [52] S. Hosseini and A. A. Al Khaled, "A survey on the imperialist competitive algorithm metaheuristic: Implementation in engineering domain and directions for future research," *Applied Soft Computing*, vol. 24, pp. 1078–1094, 2014.
- [53] A. R. Jordehi, "Brainstorm optimisation algorithm (BSOA): An efficient algorithm for finding optimal location and setting of FACTS devices in electric power systems," in *Proceedings of the International Journal of Electrical Power Energy Systems* 69, 2015, <https://doi.org/10.1016/j.ijepes.2014.12.083>.
- [54] H. Shah-Hosseini, "Intelligent water drops algorithm: a new optimization method for solving the multiple knapsack problem," *International Journal of Intelligent Computing and Cybernetics*, vol. 1, no. 2, pp. 193–212, 2008.
- [55] M. Dorigo and C. Blum, "Ant colony optimization theory: a survey," *Theoretical Computer Science*, vol. 344, no. 2-3, pp. 243–278, 2005.
- [56] X.-S. Yang and A. H. Gandomi, "Bat algorithm: A novel approach for global engineering optimization," *Engineering Computations*, vol. 29, no. 5, pp. 464–483, 2012.
- [57] I. Fister, I. Fister Jr., X.-S. Yang, and J. Brest, "A comprehensive review of firefly algorithms," *Swarm and Evolutionary Computation*, vol. 13, no. 1, pp. 34–46, 2013.
- [58] D. Karaboga and B. Basturk, "On the performance of artificial bee colony (ABC) algorithm," *Applied Soft Computing*, vol. 8, no. 1, pp. 687–697, 2008.
- [59] R. Rajabioun, "Cuckoo optimization algorithm," *Applied Soft Computing*, vol. 11, no. 8, pp. 5508–5518, 2011.
- [60] E. Rashedi, H. Nezamabadi-pour, and S. Saryazdi, "GSA: a gravitational search algorithm," *Information Sciences*, vol. 213, pp. 267–289, 2010.
- [61] A. Hatamlou, "Black hole: a new heuristic optimization approach for data clustering," *Information Sciences*, vol. 222, pp. 175–184, 2013.
- [62] E. Hosseini, "Big bang algorithm: A new meta-heuristic approach for solving optimization problems," *Asian Journal of Applied Sciences*, vol. 10, no. 3, pp. 134–144, 2017.
- [63] B. Xing and W.-J. Gao, "Big bang-big crunch algorithm," in *Innovative Computational Intelligence: A Rough Guide to 134 Clever Algorithms*, vol. 62, pp. 321–331, Springer International Publishing, Cham, Switzerland, 2013.
- [64] M. Mitchell, *An Introduction to Genetic Algorithms*, MIT Press, Cambridge, MA, USA, 1998.

- [65] R. Storn and K. Price, "Differential evolution—a simple and efficient heuristic for global optimization over continuous spaces," *Journal of Global Optimization*, vol. 11, no. 4, pp. 341–359, 1997.
- [66] S.-J. Huang, "Enhancement of hydroelectric generation scheduling using ant colony system based optimization approaches," *IEEE Transactions on Energy Conversion*, vol. 16, no. 3, pp. 296–301, 2001.
- [67] D. Karaboga, B. Gorkemli, C. Ozturk, and N. Karaboga, "A comprehensive survey: artificial bee colony (ABC) algorithm and applications," *Artificial Intelligence Review*, vol. 42, pp. 21–57, 2014.
- [68] S. Kumar, D. Datta, and S. K. Singh, "Black hole algorithm and its applications," in *Studies in Computational Intelligence*, vol. 575, pp. 147–170, Springer International Publishing, Cham, Switzerland, 2014.
- [69] Y. Jiang, D. Mao, and Y. Xu, "A Fast Algorithm for Computing Sample Entropy," *Advances in Adaptive Data Analysis (AADA)*, vol. 03, no. 01n02, pp. 167–186, 2011.
- [70] T. J. McCabe, "A complexity measure," *IEEE Transactions on Software Engineering*, vol. SE-2, no. 4, pp. 308–320, 1976.
- [71] R. Munoz, R. Olivares, and E. Merino, "Black hole EEG results (summary)," https://figshare.com/articles/BH_EEG_Results/5588896, 2017.
- [72] R. Munoz, R. Olivares, and E. Merino, "Black hole EEG results (all data)," https://figshare.com/articles/BH_EEG_Results_All_data./5588911, 2017.
- [73] R. Munoz and R. Olivares, "EEG-black-hole (application)," <https://figshare.com/articles/EEG-Black-Hole/5590000/2>, 2017.
- [74] L.-W. Ko, O. Komarov, W. D. Hairston, T.-P. Jung, and C.-T. Lin, "Sustained Attention in Real Classroom Settings: An EEG Study," *Frontiers in Human Neuroscience*, vol. 11, p. 388, 2017.
- [75] A. T. Poulsen, S. Kamronn, J. Dmochowski, L. C. Parra, and L. K. Hansen, "EEG in the classroom: Synchronised neural recordings during video presentation," *Scientific Reports*, vol. 7, p. 43916, 2017.
- [76] W. B. Cannon, "The James-lange theory of emotions: a critical examination and an alternative theory," *The American Journal of Psychology*, vol. 39, no. 1, pp. 106–124, 1927.

Research Article

Spatial and Time Domain Feature of ERP Speller System Extracted via Convolutional Neural Network

Jaehong Yoon ,¹ Jungnyun Lee ,² and Mincheol Whang ,²

¹Department of Biomedical Engineering, Duke University, Durham, NC 27708, USA

²Department of Digital Media Engineering, Sangmyung University, Seoul 03016, Republic of Korea

Correspondence should be addressed to Jaehong Yoon; jaehong.ryan.yoon@gmail.com

Received 6 January 2018; Revised 5 March 2018; Accepted 1 April 2018; Published 15 May 2018

Academic Editor: Victor H. C. de Albuquerque

Copyright © 2018 Jaehong Yoon et al. This is an open access article distributed under the Creative Commons Attribution License, which permits unrestricted use, distribution, and reproduction in any medium, provided the original work is properly cited.

Feature of event-related potential (ERP) has not been completely understood and illiteracy problem remains unsolved. To this end, P300 peak has been used as the feature of ERP in most brain-computer interface applications, but subjects who do not show such peak are common. Recent development of convolutional neural network provides a way to analyze spatial and temporal features of ERP. Here, we train the convolutional neural network with 2 convolutional layers whose feature maps represented spatial and temporal features of event-related potential. We have found that nonilliterate subjects' ERP show high correlation between occipital lobe and parietal lobe, whereas illiterate subjects only show correlation between neural activities from frontal lobe and central lobe. The nonilliterates showed peaks in P300, P500, and P700, whereas illiterates mostly showed peaks in around P700. P700 was strong in both subjects. We found that P700 peak may be the key feature of ERP as it appears in both illiterate and nonilliterate subjects.

1. Introduction

A brain-computer interface (BCI) is a system which provides a communication method by utilizing biophysiological signals [1]. BCI system enables the users to communicate with external world through measurements of biological signals and mostly do not require voluntary muscle movement. The system has been utilized to support severe locked-in syndrome (LIS) patients who lack motor ability, such as amyotrophic lateral sclerosis (ALS) and Guillain-Barre syndrome patients, as a means of communication [2–7]. Of many biophysiological signals, electroencephalography (EEG) has been most widely used in BCI field for its easiness in and low cost of measurement [8, 9].

Among different applications of BCI, event-related potential (ERP) based speller system has been one of the most widely used paradigms. The system was pioneered by Farwell and Donchin [10] in 1988 which utilized oddball paradigm in order to induce visual evoked potential (VEP), especially the P300 response. However, there are still illiteracy problems associated with ERP speller system [11, 12]. There has been reports of ERP features other than P300 [13, 14] which may be a key feature of distinguishing identifying illiterates.

One of the most prominent classification methods for ERP system is support vector machine (SVM) [15–18]. SVM is mathematically simple and, with sufficient knowledge of feature matrix, the experimenter can modulate the kernel for the target problem. Unfortunately, the kernel of SVM is sensitive to overfitting [19]. As EEG are measured from multiple electrodes [20–23], feature matrix can have high dimension with possible duplicates, which increase possibility of overfitting. As most of ERP system paradigms are dependent on P300 peak, the information (peak magnitude and latency) from each electrode should be similar. Moreover, it is hard to extract temporal and spatial information of EEG of a single kernel. Although multiple kernel learning (MKL) problem has been suggested [24], it is hard to extract intuition of the given problem through the method.

Recent development of deep learning provides an alternative approach. The convolutional neural network (CNN) can extract the feature from a given feature vector by using convolution. When an optimal filter is applied, the convolution will magnify the feature of interest and reduce the others [25]. CNN has been used in pattern recognition, especially in image recognition and speech recognition, as it provides topological information within the extracted feature [26–30].

Therefore, data with sequence or topological information can be recognized more efficiently as CNN enables extracting both temporal and spatial information within the raw data. As the ERP shows sequence of rise and fall as a response to visual stimuli, pattern recognition technique as CNN can be applied. Moreover, the convolution kernel of CNN can be used as tool for interpreting the spatial correlation among EEG electrodes.

In this paper, we explore the performance of CNN on ERP data to identify the key features that distinguish illiterates of ERP speller system. The convolution kernels of trained model will be explored to analyze the spatial correlation between cortices and pattern within ERP of each electrode. The subjects were grouped as either strong (nonilliterate) or weak (illiterate) depending on clarity of ERP signals. Results of two groups were compared to analyze difference in features.

2. Methods

2.1. ERP Speller Design. 6 icons shown in Figure 2 were used as visual stimuli for the speller system of this paper. Rapid serial visual presentation (RSVP) panel design was adopted for the speller system to avoid gaze effect. During the experiment, screen size icons appeared on the center of the monitor in a random sequence [31]. The oddball paradigm was implemented by presenting target icon with distractors in a random sequence [10]. Each icon appeared 20 times per trial. The interstimulus interval (ISI) between icon appearances was set to 300 ms.

2.2. Data Acquisition. For this paper, 33 subjects (13 female, 20 male) participated in the experiment. The subjects' age ranged from 24 to 30 (mean = 27.25, std = ± 1.92). During the experiment, subjects were asked to sit upright on a chair and instructed to keep still. No straps or ties were attached. Subjects were asked to self-report any inconvenience that might bother the concentration.

Each trial was initiated with an acoustic cue instructing the target of the given trial in subjects' mother tongue (Korean). 10 seconds after the acoustic cue was given, the icons appeared on the monitor according to RSVP design in random sequence. The subjects were instructed to mentally count the target occurrence during each trial (Figure 2(b)). Each session consisted of 12 trials. Each icon was selected as a target during the session twice in random sequence.

All subjects were naive; 10–20-minute preexperiment session was given to get subjects used to the procedure. The subjects were asked to self-report if they felt confident of the procedure. After the preexperiment session ended, the measurements of EEG were made. During the experiment, one training session and online session were conducted as a pair. To minimize subject's stress level and fatigue, 10-minute break was given in between training and online session. Each subject conducted minimum of 2 pairs of training and online session. No subjects had participated in more than 4 pairs of sessions.

EEG was collected by B-Alert X10 headset from Advanced Brain Monitoring (ABM) with sampling rate of 256 Hz. The EEG electrodes recorded followed international 10/20 system [32] as shown in Figure 2(a). All experiments were held in

accordance with the Declaration of Helsinki, and the protocol was approved by the Ethics Committee of Sangmyung University.

2.3. Convolutional Neural Network. The architecture of CNN for this paper was as shown in Figure 2(c). The CNN consisted of 2 convolutional layers, 2 max-pooling layers, and 2 fully connected layers. Rectified linear unit (ReLU) function was applied as activation function for each convolutional layer since its performance was proven by another [33]. A softmax function was applied to output the last layer to regularize the final output to be between 0 and 1. The output of CNN was vector of 2 elements where each element represented the score of target and nontarget.

The CNN was designed to perform both spatial and temporal filtering. The feature maps of each layer were used to access correlation between adjacent electrodes and temporal feature of target ERP. In the 1st convolutional layer (L_1), a filter of size 6×20 was applied to extract correlation of EEG recorded in adjacent electrodes. The row number of the filter was set to 6 as 3 electrodes were placed on each lobe (except for occipital lobe where two electrodes were placed). The size of filter enables analyzing the correlation of all 6 electrodes from adjacent lobes. For analysis of temporal feature of feature map from L_1 among different lobes, a filter with size of 1×12 was applied for 2nd convolutional layer (L_2) whose window size was approximately 100 ms in time scale.

To reduce the receptive field size for ease of calculation and prevent overfitting, max-pooling layers (M_1 and M_2) were inserted after each convolutional layer [27, 34]. The max-pooling layers downsample the feature map by applying a sliding window without overlap. As the name implies, the maximum value within the window is extracted. As the max-pooling introduces downsampling effect, a generalization of feature map was achieved which prevented overfitting of the model. Sliding window sizes of M_1 and M_2 were 2×2 and 1×10 , respectively.

To further reduce the possibility of overfitting while training the model, drop-out technique was applied on the first fully connected layer (F_1). The drop-out technique padded zeros to randomly selected rows in the given feature map. By intentionally losing the data within the feature map, generalization was achieved for the feature map which prevented the model from being overfitted by the training data [35, 36].

The size of input matrix fed into the CNN was 14×300 where each row corresponded to EEG collected from each electrode in Figure 2.

The CNN architecture was implemented in Python via TensorFlow on Python [37, 38]. The Adam optimizer was used to train the CNN which controls the learning rate to use larger step size. 10,000 iterations were conducted for training the model for each subject's data.

2.4. Tie Breaking. Ideally, if the model is perfect, only one icon will be identified as the target for a given trial. However, the system identified multiple icons as the targets in several trials. On the other extreme, the system failed to identify any target icon for some trials. For each case, the tie breaking rule was applied as follows.

- (i) Multiple icons cases: When multiple icons were thought to be the target of a given trial by the CNN, the tie breaking rule was applied to select the target among these candidates. Since the first element of output vector represents the icons affiliation to target ERP property, the icon with the greatest value of the element was selected as the target of the trial.
- (ii) No target case: When the system failed to find the association of the ERP from any icons to property of target ERP, that is, no icons were identified as the target, same rules as those in multiple icons case were applied to select the target for the given trial. In this case, the first element of output vector from all icons was compared. The icon whose first element of output vector was the greatest was selected as the target of the trial.

2.5. Analysis. Both qualitative and quantitative analysis were performed to analyze the characteristics of filters of each convolutional layer. The subjects were divided into two groups according to their relative strength of ERP as follows:

- (i) ERP detection: if the target icon was detected as positive in a given trial, the ERP is considered detected. The subjects were divided accordingly into either H or L group (H and L for high and low) ERP detection group. The threshold between H and L group was 50%.
- (ii) Feature map: feature maps from L_1 and L_2 were drawn in color map. As higher weights of feature map denote high discriminant power, the colormap can qualitatively give insight of how each electrode is correlated and at which time the main peak is formed.
- (iii) Statistical analysis: for quantitative analysis of performance, accuracy, sensitivity, precision, F1 measure, and ROC were calculated for each subject and ANOVA test was held to compare mean difference. The accuracy is defined as the ratio of number of correctly identified trial to total trial numbers. The classical statistic measurements for quantitative evaluation are as follows:

$$TP \equiv \text{true positive},$$

$$FP \equiv \text{false positive}$$

$$TN \equiv \text{true negative},$$

$$FN \equiv \text{false negative}$$

$$\begin{aligned} \text{Sensitivity} &= \frac{TP}{TP + FN} \\ \text{Precision} &= \frac{TP}{TP + FP} \\ \text{F1 measure} &= \frac{2 \times \text{Sensitivity} \times \text{Precision}}{\text{Sensitivity} + \text{Precision}}. \end{aligned} \quad (1)$$

- (iv) Receiver operating characteristic: receiver operating characteristic (ROC), which plots the sensitivity

against specificity, widely used statistical measurement for its diagnostic ability of binary classifier. As the CNN of the paper is a binary classifier, the ROC information is provided to compare the performance of CNN between H and L group.

- (v) Peak signal to noise ratio: peak signal to noise ratio (PSNR) is used as measurement of qualitative reconstruction method of compression codes [39]. As the performance of filter will depend on how many core features are extracted from raw ERP, the PSNR of L_1 's feature map was calculated as a mean of measurement of performance. The greater PSNR shows the presence of significantly high weight inside feature map whereas lower PSNR represents only low weights that are present in the given feature map and the discriminant power of the filter is low.

3. Results

3.1. ERP Detection. Of 33 subjects, 19 were identified as H group. In Figure 3, time course of learning curve and other statistical measurements over the training iteration from H and L subject are presented. The learning curve of L subject shown in Figure 3(a) indicates that although the false negative rate (FN) drops according to the training iteration, reaching 0 eventually, the false positive rate (FP) becomes 1. Although the learning curve shows sharp increase at 1st and 13th iteration, mostly it remains around .2. This indicates that the CNN becomes overtrained to positives (target). Moreover, as the CNN identifies most of the ERP to be positive (high FP and low FN), the result indicates that discriminant feature of target ERP was not found. On the other hand, both FN and FP of H subject drop to around 0 and .2. The learning curve saturates around .85 indicating nonoverfitting of the CNN (Figure 3(b)).

The errors shown in Figures 3(c) and 3(d) are defined as follows for training and online data:

$$\text{error} = \frac{TP + TN}{TP + TN + FP + FN}. \quad (2)$$

Although both H and L group show drop in both training and validation error as training iteration continues, the validation error of L subject is higher than that of H subject.

The ROCs of H and L subject shown in Figure 3(e) indicate the performance of CNN of H group to be greater than that of L group subject.

3.2. Spatial and Temporal Features. The feature map of each convolutional layer did not contain negative weights associated with negative peaks, such as N1 [40] as the activation function was set to ReLU [33].

The target ERP and feature map of L_1 of sampler H and L subject are shown in Figures 4 and 6. The target ERP shown in both figures is target ERP averaged over all trials. To analyze the correlation of frontal and occipital lobe electrodes, the first 3 electrodes (first 3 rows of averaged target ERP matrix) were copied and pasted at the end of ERP matrix. As shown in Figure 4(a), the target ERP of L group subject shows

TABLE 1: Results of the CNN classification. Data are sorted according to the ERP group. Accuracy (Acc.), sensitivity (Sens.), precision (Prec.), F1 measure, ROC, PSNR, and peak time of 2nd layer (PeT.) are given for comparison.

Subject number	Type	Acc.	Sens.	Prec.	F1 measure	ROC	PSNR	PeT.
1	H	.917	.250	.028	.050	.695	-42.285	.372
2	H	1.000	.647	.131	.218	.863	-34.468	.485
3	H	.917	.750	.188	.300	.997	-35.677	.594
4	H	.833	.750	.255	.344	.766	-32.909	.437
5	H	.833	.744	.242	.366	.660	-37.448	.354
6	H	.750	.782	.276	.408	.562	-39.263	.449
7	H	.833	.803	.292	.428	.814	-25.565	.595
8	H	1.000	.826	.317	.458	.873	-25.902	.411
9	H	.667	.844	.333	.478	.696	-22.070	.527
10	H	.750	.838	.346	.490	.873	-39.588	.367
11	H	.917	.869	.327	.475	.922	-25.750	.448
12	H	.917	.878	.342	.493	.940	-24.519	.664
13	H	.667	.747	.294	.422	.638	-23.987	.497
14	H	.833	.713	.279	.401	.778	-40.687	.543
15	H	.917	.721	.290	.414	.935	-39.207	.489
16	H	.750	.733	.302	.428	.998	-35.497	.362
17	H	.917	.733	.289	.415	.799	-38.910	.284
18	H	.917	.740	.295	.421	.861	-27.944	.452
19	H	1.000	.746	.298	.426	.780	-29.202	.458
20	L	.583	.846	.344	.489	.843	-25.722	.445
21	L	.583	.854	.343	.490	.573	-18.743	.575
22	L	.667	.849	.338	.483	.249	-21.219	.341
23	L	.833	.849	.341	.486	.427	-46.836	.638
24	L	.750	.853	.337	.483	.582	-20.236	.282
25	L	1.000	.860	.343	.488	.888	-20.511	.558
26	L	.917	.866	.343	.492	.535	-22.905	.627
27	L	.833	.868	.337	.485	.580	-22.883	.451
28	L	.750	.881	.362	.513	.898	-23.225	.381
29	L	.583	.808	.321	.460	.709	-31.783	.350
30	L	.833	.814	.324	.464	.874	-36.084	.396
31	L	.583	.755	.298	.428	.742	-27.483	.422
32	L	.667	.752	.303	.432	.931	-19.580	.533
33	L	.583	.745	.294	.432	.377	-32.561	.454

broad peak around P700 range on F3 and CZ. ERP of other lobes did not show any significant positive weight indicating nonsignificant features associated with target being observed and being flat. Feature maps shown in Figures 4(b) through (i) have shown high correlation between ERP from central and parietal lobe electrodes.

On the other hand, the correlation of ERP among adjacent electrodes for H group subject shown in Figure 6 indicates the correlation is restricted to specific time range. Most of the high weights of feature maps shown in Figures 6(b), 6(d), 6(f), and 6(e) show significant positive value around P500 and P700 range for frontal and central lobe electrodes. The correlation between central and parietal lobe is shown in Figure 6(c) around P500 range. Some features around P500 region were found to show high correlation among all electrodes. Unlike that of L group subjects, feature map of L₁ for H group subject showed high correlation among all electrodes, where each case shows specific temporal characteristics.

The temporal features shown in feature map in Figure 5 indicate that temporal features associated with P700 peak are present for L group subjects as expected. In Figures 5(a), 5(b), and 5(c), high positive weights were found around P700 range (row 4 and 6). However, most of the feature maps did not show significant weights or were either flat as in Figure 5(i).

The temporal features of H group subjects showed more variety. Some feature maps showed high positive weights in their feature maps around P300 and P500 range as shown in Figures 7(a), 7(b), 7(c), and 7(d), whereas the others indicated significant positive weight around P700 range as in Figures 7(a)–7(i). However, the weight associated with P700 range is more widely defined than those associated with P300 and P500.

3.3. Statistical Analysis. Comparison of classical statistical measurements and other measurements is shown in Table 1. The accuracy, sensitivity, and precision showed significant mean difference between H and L group (p values were

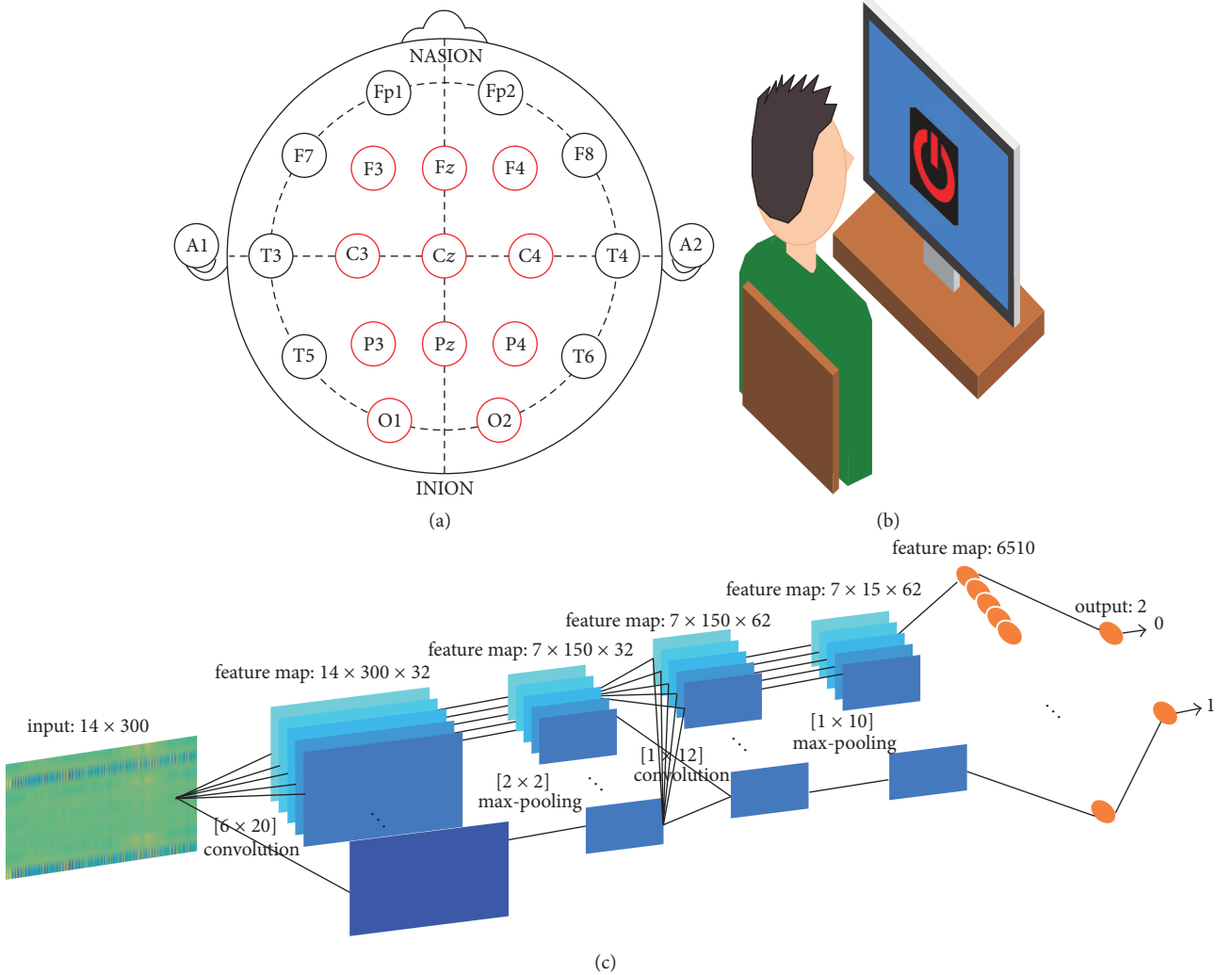


FIGURE 1: Experimental paradigm. (a) The position of EEG channels in 10/20 system. The EEG were collected from F3, Fz, F4, C3, Cz, C4, P3, Pz, P4, O1, and O2 positions as indicated by red circle. (b) Experimental setting schematics. Subjects were sat on a chair and were asked to mentally count the occurrence of target icon. The ERP speller system for this paper was implemented with RSVP. The icon appeared on the center of the monitor. (c) Schematics of CNN architecture. The architecture consisted of 2 convolutional layers, 2 max-pool layers, and 2 fully connected layers. The number on top of each layer indicates size of feature map.

0.0135, $0.8.88e - 05$, and 0.0072, resp.). A significant mean difference in F1 measure did not exist between H and L group. The accuracy of H and L group was 0.889 and 0.687, respectively. The sensitivity of H group was higher than that of L group, but the precision of H group was significantly lower than that of L group. The area under ROC of H group was significantly higher than that of L group (p value = 0.0137).

The PSNR for L_1 of H group was significantly lower than that of L group. As all PSNR measured were negative, the absolute value of PSNR of H group was greater than that of L group. On the other hand, no mean difference of the peak time (PeT.) between H and L group was found (p value = 0.965).

4. Discussion

In this study, CNN has been used to investigate the spatial and temporal characteristics of ERP that distinguish the

performance difference between illiterates and nonilliterates (L and H group). As a comparison of performance, classical statistic measurements as well as filter comparison measurement had been collected to compare the correlation of ERP taken from different EEG electrodes and identify characteristic temporal features associated with each group.

The statistical measurement shows that the mean performance of CNN with H and L group data had significant difference. The accuracy of H group data was higher than that of L group data. Interestingly, although the sensitivity of H group was higher than that of L group, the precision of H group was significantly lower than that of L group. This reflects the fact that the ERP of L group was not identified as target in most of the cases, and the CNN identified ERP from all 6 icons to be nontarget in more than half of the trials.

The learning curve and errors in Figure 3 demonstrate how the statistical measurement affects the performance of CNN. Although the false negative rate remains mostly near

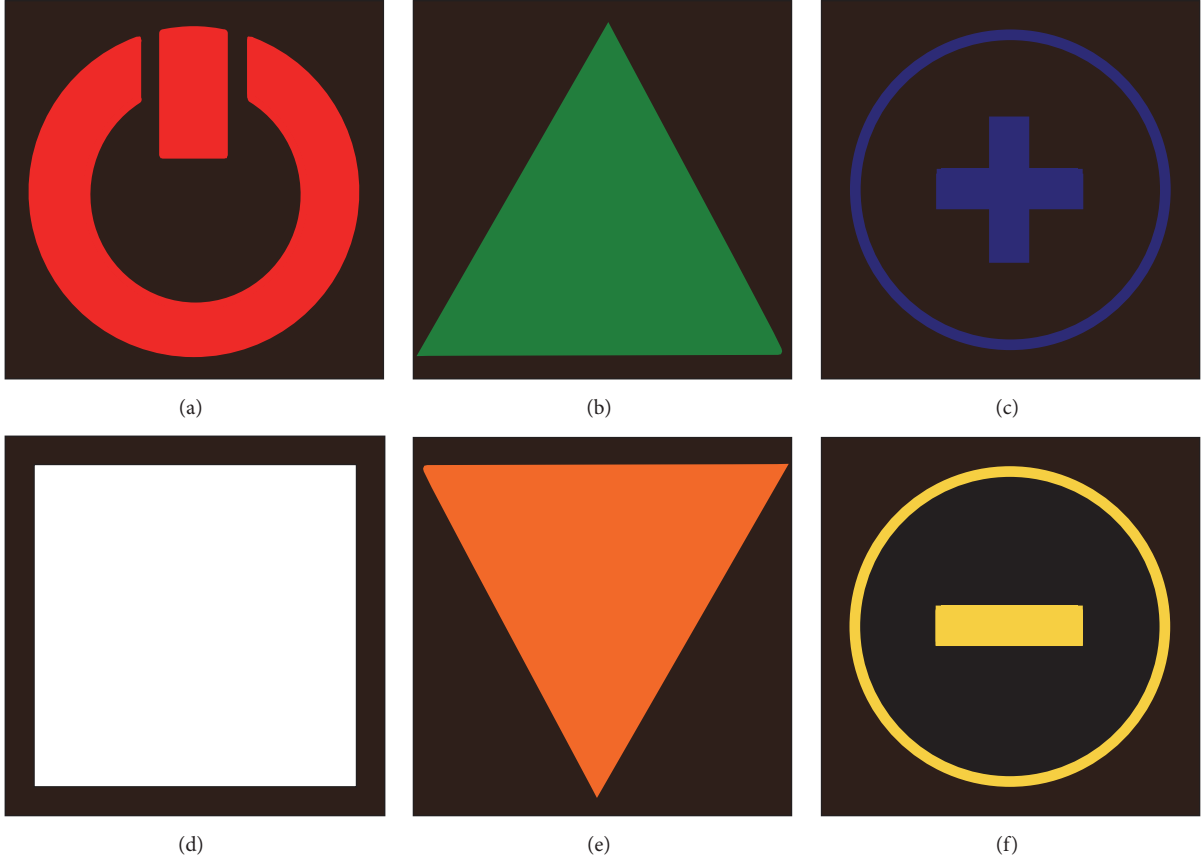


FIGURE 2: Schematics of icons used for rapid serial visual presentation (RSVP) panel. The design of icons was taken from television remote controller. (a) Turn on. (b) Volume up. (c) Channel up. (d) Turn off. (e) Volume down. (f) Channel down.

0, as the false positive rate remains close to 0, the learning curve remains stable around .2 for the L group subject. This again reflects the characteristics of L group ERP who were mostly identified as nontarget. Some of the ERP that were identified as target ERP were mostly from nontarget icons, indicating lack of distinctive feature associated with target ERP. However, both false negative and false positive rate drop as training iteration continues for H group subject's data, leading to increase of learning accordingly to the iteration. As the ERP of L group does not have sufficient distinctive features, the model becomes slightly overtrained compared to the model of H group subject as shown in validation error plot in Figures 3(c) and 3(d). The comparison of ROC validates the analysis as ROC of H group was significantly higher than that of L group (p value = 0.0137).

As shown in Figure 4, most of the ERP collected from L group were flat in most of the channels. Most of the positive weights in target ERP were observed in frontal and central lobe electrodes (1st and 5th row of Figure 4(a)) which was contrary to the expectation as previous research indicated positive peaks associated with target event were mostly observed in parietal or occipital lobe [41, 42]. The correlation of ERP collected from adjacent electrodes did not show existence of significant correlation between occipital and parietal lobe data in L group subjects. On the other hand, ERP of H group were more invigorated, showing stronger activity

in P300 area as shown in Figure 6(a). The ERP correlation indicated in feature map also indicated stronger correlation of ERP data collected from occipital and parietal lobe with other lobes. The spatial correlation shown in feature map of H group also indicated that the correlation was restricted in specific time range corresponding to either P300, P500, or P700.

The feature map of 2nd convolutional layer demonstrated the difference in temporal features between H and L group subjects. In most of L group subjects, the feature map did not show strong positive weights and was flat. Some indication of positive weights was mostly restricted in P700 region. On the other hand, the positive weights of H group were distributed around P300, P500, and P700 and the positive weights found near P300 and P500 range was sharper compared to those found around P700 range. Previous researches have indicated the possibility of existence of different features other than P300 [41, 43, 44]. The result of the paper also supports the idea that P300 may not be the only key feature of ERP speller system. Rather, the P700, which were identified among both L and H group subjects, may represent more universal ERP feature. However, the ERP from central lobe area observed in L group indicates the possibility of effect of stimulus probability [32] (Figure 1(a)).

The PSNR indicated that lack of activities in occipital/parietal lobe and broad peak found in P700 affect the

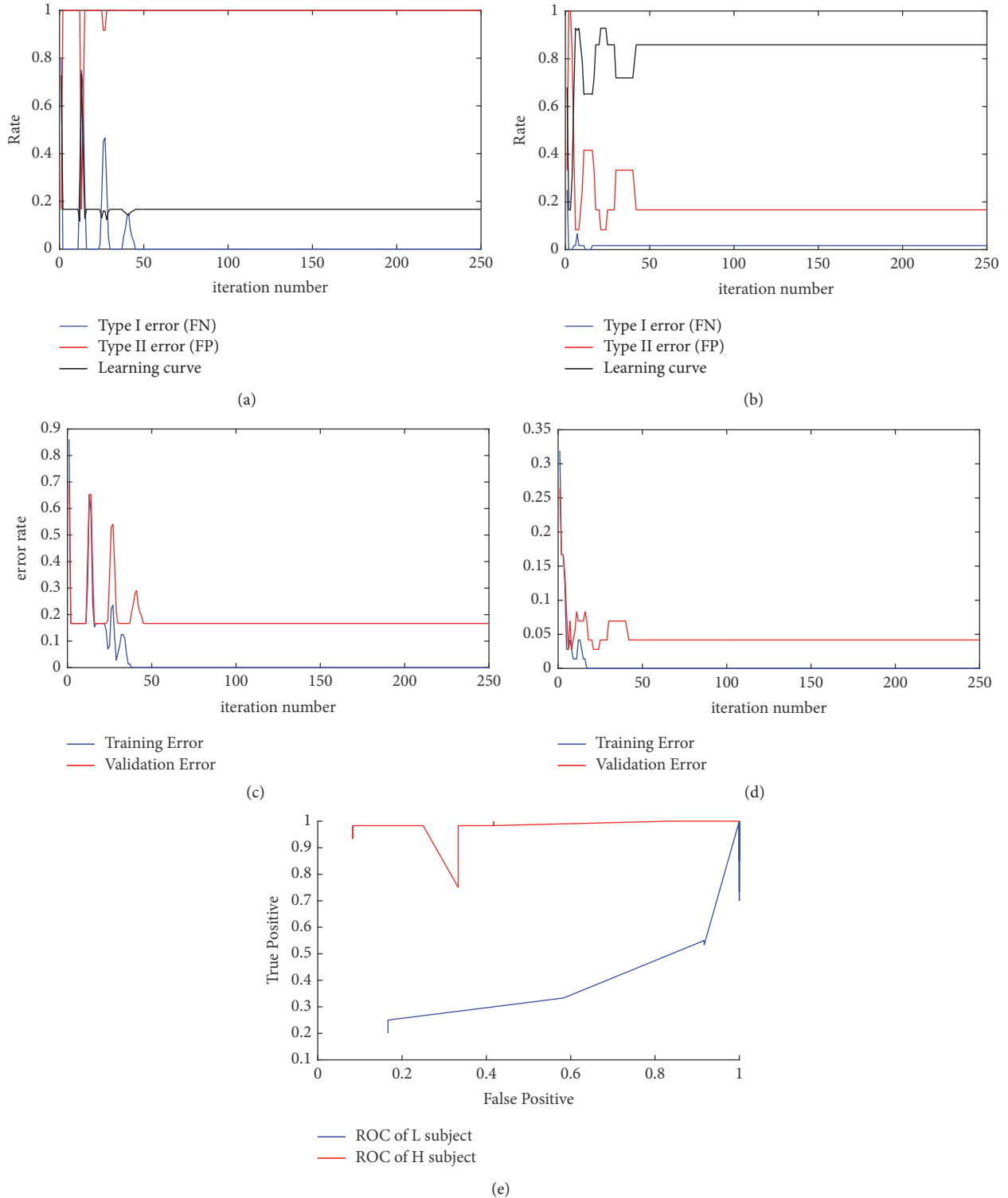


FIGURE 3: Learning curve and receiver operating characteristic curve (ROC) of L and H subject. (a) False negative rate (FN) and learning curve of L subject saturates near 0 and .2, respectively, whereas false positive rate (FP) increase to 1. (b) Both FP and FN drop over the time course for H subject and learning curve saturates near .8. (c) Training and validation error of drops over the time course for both L subject and (d) H subject. Both validation and training error are lower for H subject. (e) ROC curve of H and L subjects.

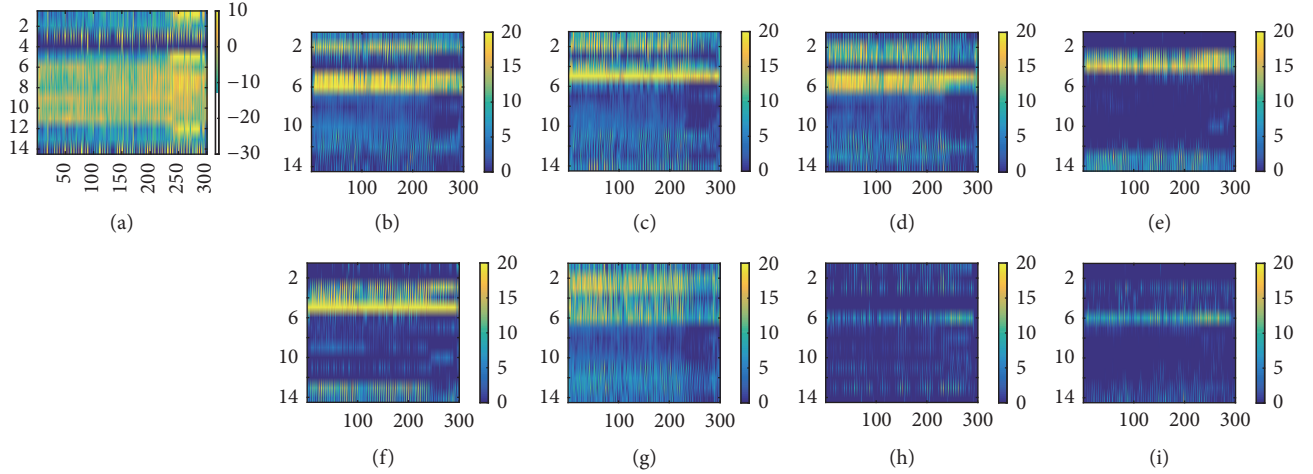


FIGURE 4: ERP averaged over all trials and feature map of L_1 of L subject. The ERP from frontal lobe was copied and pasted on last three rows. (a) Grand average ERP over all trials. Feature maps from L_1 shown in (b), (c), (d), (e), (f), (g), (h), and (i). Strong correlation between frontal and central lobe and between central and parietal lobe was found. Spatial correlation among other electrodes is not well defined.

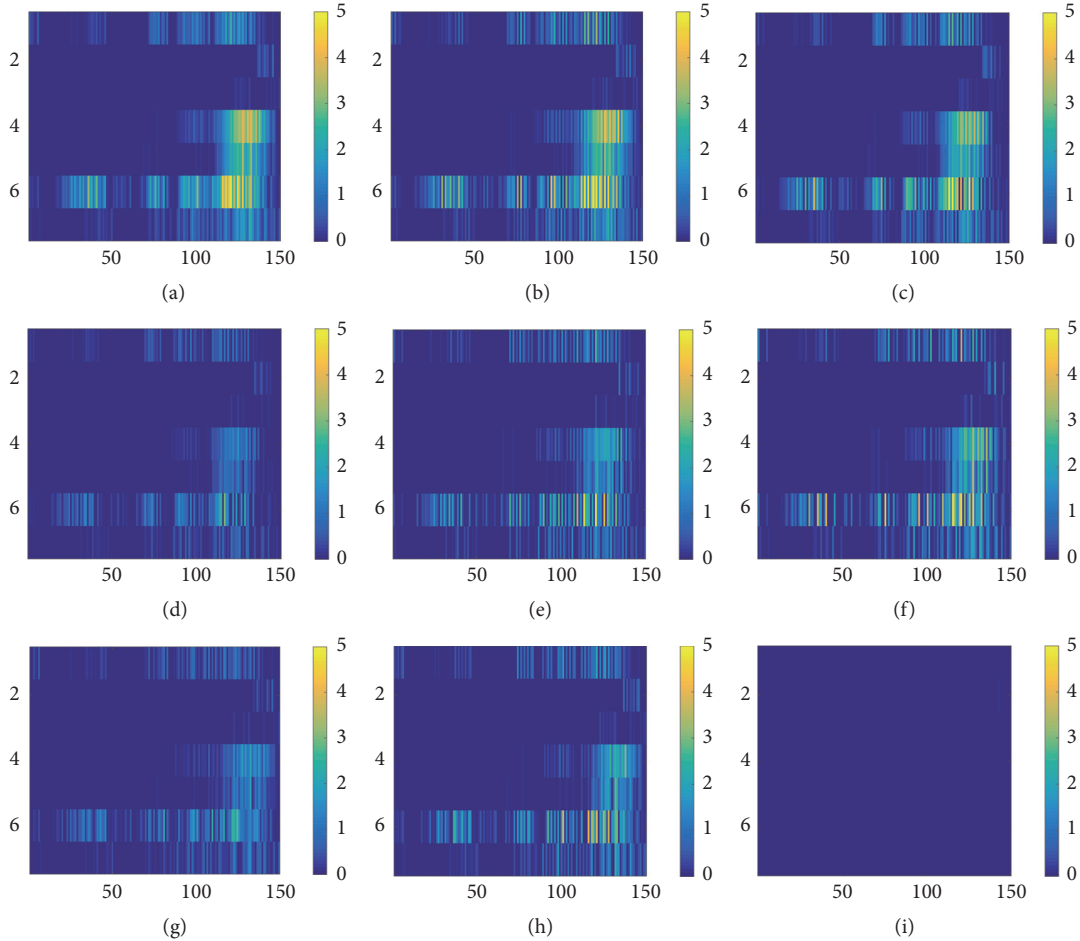


FIGURE 5: Feature map of L_2 of L subject data. Temporal feature associated with P700 peak is found as shown in (a), (b), and (c).

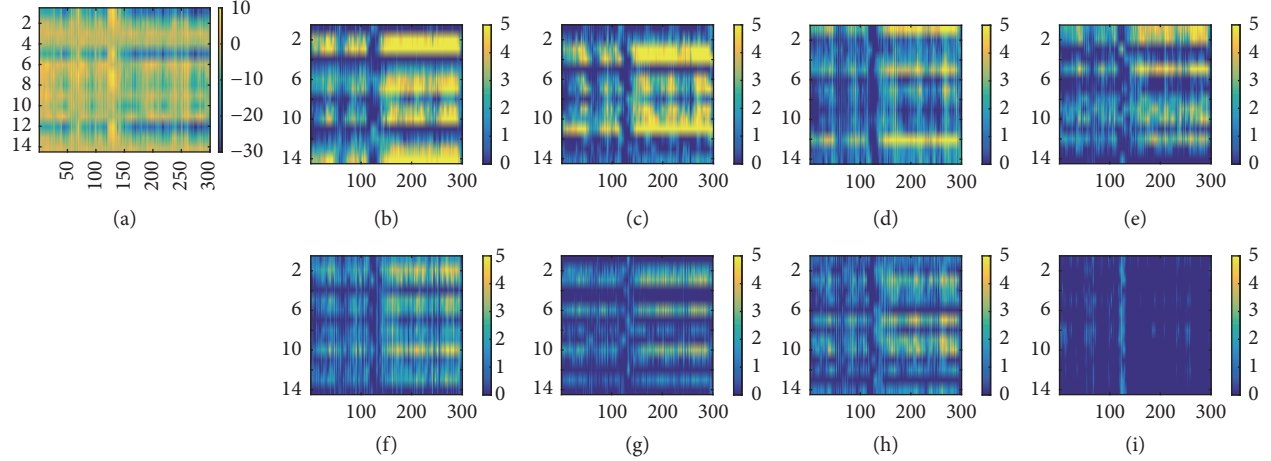


FIGURE 6: ERP averaged over all trials and feature map of L_1 of H group. The format is the same as shown in Figure 4. (a) The grand averaged ERP of H group shows significant peak around P300 and P500 (rows 1, 5, 7, and 8). Correlation between ERP from adjacent electrodes shows high correlation related to specific time rage (P300 and P700) in (b), (d), (f), and (e).

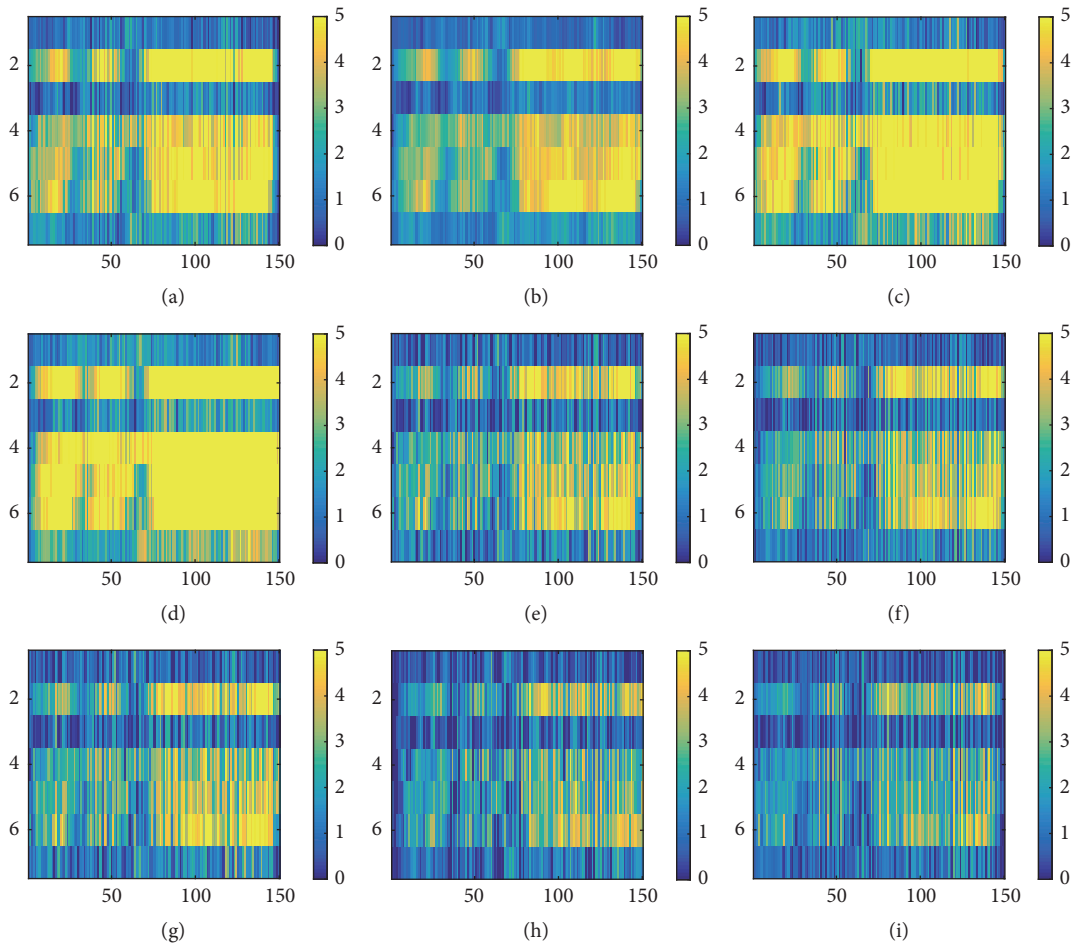


FIGURE 7: Feature map of L_2 of H subject. Format is the same as Figure 5. High positive weight around P300 and P500 range were found in (a), (b), (c), and (d). (e)-(i) Moderate positive weight around P700 were also found.

performance of spatial filter in L1 as well. As the PSNR measures the maximum power of a signal and the power of corrupting noise [45], the result indicates that the filter was not able to extract distinctive signal of target ERP from background noise for L group subjects' data. This may be since peaks near P700 were broad and fluctuating. On the other hand, P300 and P500 peaks found in H group subjects were sharper, which made the filter extract relevant features more precisely without being affected by background noise. Interestingly, the major peak of L₂ of H and L group subjects did not differ significantly (p value = 0.965). As the major peak was found by averaging the feature maps from L₂, the difference in each feature map may have been overshadowed. Further statistical analysis to access temporal feature within each feature map must be applied to validate the results found in this study.

5. Conclusions

This study has investigated the difference in spatial and temporal features of ERP between high performance group (H group) and low performance group (L group). The result indicated that the major difference arises from spatial correlation of ERP among other lobes rather than temporal features. Although the temporal feature difference was not found to be quantitative in this study, the qualitative analysis indicated lack of P300 in low performance group. Interestingly, both low and high performance group showed activity near P700 which may be the key activity of ERP speller system instead of traditional P300 peak. Further analysis of individual feature map will be needed to investigate the key temporal feature of ERP speller system.

Conflicts of Interest

The authors declare that they have no conflicts of interest.

Acknowledgments

This work was partly supported by Institute for Information & Communications Technology Promotion (IITP) grant funded by the Korea government (MSIT) (no. 2015-0-00312, the development of technology for social life logging based on analyzing social emotion and intelligence of convergence contents) and National Research Foundation of Korea (NRF) grant funded by the Korea government (MSIT) (no. 2011-0030079).

References

- [1] J. R. Wolpaw, N. Birbaumer, D. J. McFarland, G. Pfurtscheller, and T. M. Vaughan, "Brain-computer interfaces for communication and control," *Clinical Neurophysiology*, vol. 113, no. 6, pp. 767–791, 2002.
- [2] T. Fomina, G. Lohmann, M. Erb, T. Ethofer, B. Schölkopf, and M. Grosse-Wentrup, "Self-regulation of brain rhythms in the precuneus: A novel BCI paradigm for patients with ALS," *Journal of Neural Engineering*, vol. 13, no. 6, Article ID 066021, 2016.
- [3] W. Speier, N. Chandravadia, D. Roberts, S. Pendekanti, and N. Pouratian, "Online BCI typing using language model classifiers by ALS patients in their homes," *Brain-Computer Interfaces*, vol. 4, no. 1-2, pp. 114–121, 2017.
- [4] L. Botrel, E. M. Holz, and A. Kübler, "Using brain painting at home for 5 years: Stability of the P300 during prolonged BCI usage by two end-users with ALS," *Lecture Notes in Computer Science (including subseries Lecture Notes in Artificial Intelligence and Lecture Notes in Bioinformatics): Preface*, vol. 10285, pp. 282–292, 2017.
- [5] S. Saeedi, R. Chavarriaga, R. Leeb, and J. d. Millan, "Adaptive Assistance for Brain-Computer Interfaces by Online Prediction of Command Reliability," *IEEE Computational Intelligence Magazine*, vol. 11, no. 1, pp. 32–39, 2016.
- [6] S. Saeedi, R. Chavarriaga, and J. D. R. Millan, "Long-Term Stable Control of Motor-Imagery BCI by a Locked-In User Through Adaptive Assistance," *IEEE Transactions on Neural Systems and Rehabilitation Engineering*, vol. 25, no. 4, pp. 380–391, 2017.
- [7] R. Swaminathan and S. Prasad, "Brain computer interface used in health care technologies," *SpringerBriefs in Applied Sciences and Technology*, vol. 7, pp. 49–58, 2016.
- [8] C. Reichert, S. Dürschmid, H.-J. Heinze, and H. Hinrichs, "A comparative study on the detection of covert attention in event-related EEG and MEG signals to control a BCI," *Frontiers in Neuroscience*, vol. 11, article no. 575, 2017.
- [9] D. McFarland and J. Wolpaw, "EEG-based brain-computer interfaces," *Current Opinion in Biomedical Engineering*, vol. 4, pp. 194–200, 2017.
- [10] L. A. Farwell and E. Donchin, "Talking off the top of your head: Toward a mental prosthesis utilizing event-related brain potentials," *Electroencephalography and Clinical Neurophysiology*, vol. 70, no. 6, pp. 510–523, 1988.
- [11] J. Yoon, M. Whang, and J. Lee, "Methodology of improving illiteracy in P3 speller system with ICA blind detection," *Proceedings of HCI Korea*, pp. 87–93, 2016.
- [12] R. Carabalona, "The role of the interplay between stimulus type and timing in explaining BCI-illiteracy for visual P300-based Brain-Computer Interfaces," *Frontiers in Neuroscience*, vol. 11, article no. 363, 2017.
- [13] S. L. Shishkin, I. P. Ganin, I. A. Basyul, A. Y. Zhigalov, and A. Y. Kaplan, "N1 wave in the P300 BCI is not sensitive to the physical characteristics of stimuli," *Journal of integrative neuroscience*, vol. 8, no. 4, pp. 471–485, 2009.
- [14] L. Bianchi, S. Sami, A. Hillebrand, I. P. Fawcett, L. R. Quitadamo, and S. Seri, "Which physiological components are more suitable for visual ERP based brain-computer interface? A preliminary MEG/EEG study," *Brain Topography*, vol. 23, no. 2, pp. 180–185, 2010.
- [15] K. Yoon and K. Kim, "Multiple kernel learning based on three discriminant features for a P300 speller BCI," *Neurocomputing*, vol. 237, pp. 133–144, 2017.
- [16] D. B. Ryan, G. Townsend, N. A. Gates, K. Colwell, and E. W. Sellers, "Evaluating brain-computer interface performance using color in the P300 checkerboard speller," *Clinical Neurophysiology*, vol. 128, no. 10, pp. 2050–2057, 2017.
- [17] V. Guy, M.-H. Soriani, M. Bruno, T. Papadopoulos, C. Desnuelle, and M. Clerc, "Brain computer interface with the P300 speller: Usability for disabled people with amyotrophic lateral sclerosis," *Annals of Physical and Rehabilitation Medicine*, 2017.
- [18] Q. Li, K. Shi, S. Ma, and N. Gao, "Improving classification accuracy of SVM ensemble using random training set for BCI P300-speller," in *Proceedings of the 13th IEEE International Conference on Mechatronics and Automation, IEEE ICMA 2016*, pp. 2611–2616, China, August 2016.

- [19] G. C. Cawley and N. L. Talbot, "On over-fitting in model selection and subsequent selection bias in performance evaluation," *Journal of Machine Learning Research*, vol. 11, pp. 2079–2107, 2010.
- [20] D. J. Krusienski, E. W. Sellers, F. Cabestaing et al., "A comparison of classification techniques for the P300 Speller," *Journal of Neural Engineering*, vol. 3, no. 4, article 007, pp. 299–305, 2006.
- [21] A. Rakotomamonjy and V. Guigue, "BCI competition III: dataset II-ensemble of SVMs for BCI P300 speller," *IEEE Transactions on Biomedical Engineering*, vol. 55, no. 3, pp. 1147–1154, 2008.
- [22] Y. Yu, Z. Zhou, J. Jiang et al., "Toward a Hybrid BCI: Self-Paced Operation of a P300-based Speller by Merging a Motor Imagery-Based "Brain Switch" into a P300 Spelling Approach," *International Journal of Human-Computer Interaction*, vol. 33, no. 8, pp. 623–632, 2017.
- [23] Y. Yu, J. Jiang, Z. Zhou et al., "A self-paced brain-computer interface speller by combining motor imagery and P300 potential," in *Proceedings of the 8th International Conference on Intelligent Human-Machine Systems and Cybernetics, IHMSC 2016*, pp. 160–163, China, September 2016.
- [24] S. Sonnenburg, G. Rätsch, C. Schäfer, and B. Schölkopf, "Large scale multiple kernel learning," *Journal of Machine Learning Research*, vol. 7, pp. 1531–1565, 2006.
- [25] Q. V. Le, J. Ngiam, A. Coates, A. Lahiri, B. Prochnow, and A. Y. Ng, "On optimization methods for deep learning," in *Proceedings of the 28th International Conference on Machine Learning (ICML '11)*, pp. 265–272, Bellevue, Wash, USA, July 2011.
- [26] S. Lawrence, C. L. Giles, A. C. Tsoi, and A. D. Back, "Face recognition: a convolutional neural-network approach," *IEEE Transactions on Neural Networks and Learning Systems*, vol. 8, no. 1, pp. 98–113, 1997.
- [27] A. Krizhevsky, I. Sutskever, and G. E. Hinton, "Imagenet classification with deep convolutional neural networks," in *Proceedings of the 26th Annual Conference on Neural Information Processing Systems (NIPS '12)*, pp. 1097–1105, Lake Tahoe, Nev, USA, December 2012.
- [28] P. Y. Simard, D. Steinkraus, and J. C. Platt, "Best practices for convolutional neural networks applied to visual document analysis," in *Proceedings of the 7th International Conference on Document Analysis and Recognition*, vol. 2, pp. 958–963, IEEE Computer Society, Edinburgh, UK, August 2003.
- [29] O. Abdel-Hamid, A.-R. Mohamed, H. Jiang, L. Deng, G. Penn, and D. Yu, "Convolutional neural networks for speech recognition," *IEEE Transactions on Audio, Speech and Language Processing*, vol. 22, no. 10, pp. 1533–1545, 2014.
- [30] Y. LeCun and Y. Bengio, "Convolutional networks for images, speech, and time series," *The Handbook of Brain Theory and Neural Networks*, vol. 3361, no. 10, p. 1995, 1995.
- [31] M. S. Treder, N. M. Schmidt, and B. Blankertz, "Gaze-independent brain-computer interfaces based on covert attention and feature attention," *Journal of Neural Engineering*, vol. 8, no. 6, Article ID 066003, 2011.
- [32] R. W. Homan, J. Herman, and P. Purdy, "Cerebral location of international 10–20 system electrode placement," *Electroencephalography and Clinical Neurophysiology*, vol. 66, no. 4, pp. 376–382, 1987.
- [33] V. Nair and G. E. Hinton, "Rectified linear units improve Restricted Boltzmann machines," in *Proceedings of the 27th International Conference on Machine Learning (ICML '10)*, pp. 807–814, Haifa, Israel, June 2010.
- [34] G. Benjamin, "Fractional max-pooling, 2014," <https://arxiv.org/abs/1412.6071>.
- [35] G. E. Dahl, T. N. Sainath, and G. E. Hinton, "Improving deep neural networks for LVCSR using rectified linear units and dropout," in *Proceedings of the 38th IEEE International Conference on Acoustics, Speech, and Signal Processing (ICASSP '13)*, pp. 8609–8613, May 2013.
- [36] N. Srivastava, "Improving neural networks with dropout," *University of Toronto*, vol. 182, 2013.
- [37] M. Abadi, P. Barham, C. Jianmin et al., "Tensorflow: A system for large-scale machine learning," *12th USENIX Symposium on Operating Systems Design and Implementation*, vol. 16, pp. 265–283, 2016.
- [38] G. Aurélien, "Hands-on machine learning with scikit-learn and tensorflow: concepts, tools, and techniques to build intelligent systems, 2017."
- [39] Q. Huynh-Thu and M. Ghanbari, "Scope of validity of PSNR in image/video quality assessment," *IEEE Electronics Letters*, vol. 44, no. 13, pp. 800–801, 2008.
- [40] R. Näätänen, *Attention and Brain Function*, Psychology Press, 1992.
- [41] K. Takano, H. Ora, K. Sekihara, S. Iwaki, and K. Kansaku, "Coherent activity in bilateral parieto-occipital cortices during P300-BCI operation," *Frontiers in Neurology*, vol. 5, Article ID Article 74, 2014.
- [42] F. A. Capati, R. P. Bechelli, and M. C. F. Castro, "Hybrid SSVEP/P300 BCI keyboard: Controlled by Visual Evoked Potential," in *Proceedings of the 9th International Conference on Bio-Inspired Systems and Signal Processing, BIOSIGNALS 2016 - Part of 9th International Joint Conference on Biomedical Engineering Systems and Technologies, BIOSTEC 2016*, pp. 214–218, ita, February 2016.
- [43] S. Ikegami, K. Takano, M. Wada, N. Saeki, and K. Kansaku, "Effect of the green/blue flicker matrix for P300-based brain-computer interface: An EEG-fMRI study," *Frontiers in Neurology*, 2012.
- [44] W. Speier, A. Deshpande, and N. Pouratian, "A method for optimizing EEG electrode number and configuration for signal acquisition in P300 speller systems," *Clinical Neurophysiology*, vol. 126, no. 6, pp. 1171–1177, 2015.
- [45] C.-Y. Chen, C.-H. Chen, C.-H. Chen, and K.-P. Lin, "An automatic filtering convergence method for iterative impulse noise filters based on PSNR checking and filtered pixels detection," *Expert Systems with Applications*, vol. 63, pp. 198–207, 2016.

Research Article

A New Approach to Diagnose Parkinson's Disease Using a Structural Cooccurrence Matrix for a Similarity Analysis

João W. M. de Souza, Shara S. A. Alves, Elizângela de S. Rebouças, Jefferson S. Almeida, and Pedro P. Rebouças Filho 

Laboratório de Processamento de Imagens, Sinais e Computação Aplicada (LAPISCO), Instituto Federal de Educação, Ciência e Tecnologia do Ceará, Fortaleza, CE, Brazil

Correspondence should be addressed to Pedro P. Rebouças Filho; pedrosarf@ifce.edu.br

Received 1 January 2018; Accepted 14 March 2018; Published 24 April 2018

Academic Editor: Roshan J. Martis

Copyright © 2018 João W. M. de Souza et al. This is an open access article distributed under the Creative Commons Attribution License, which permits unrestricted use, distribution, and reproduction in any medium, provided the original work is properly cited.

Parkinson's disease affects millions of people around the world and consequently various approaches have emerged to help diagnose this disease, among which we can highlight handwriting exams. Extracting features from handwriting exams is an important contribution of the computational field for the diagnosis of this disease. In this paper, we propose an approach that measures the similarity between the exam template and the handwritten trace of the patient following the exam template. This similarity was measured using the Structural Cooccurrence Matrix to calculate how close the handwritten trace of the patient is to the exam template. The proposed approach was evaluated using various exam templates and the handwritten traces of the patient. Each of these variations was used together with the Naïve Bayes, OPF, and SVM classifiers. In conclusion the proposed approach was proven to be better than the existing methods found in the literature and is therefore a promising tool for the diagnosis of Parkinson's disease.

1. Introduction

According to the World Health Organization, neurological disorders such as Parkinson's disease, multiple sclerosis, Alzheimer's disease, epilepsy, shingles, and stroke are nervous system diseases that affect the brain, the spine, and the nerves that connect them. Approximately 16 in 60 people suffer from some neurological disease [1]. Parkinson's disease (PD), first described by Parkinson [2], is a degenerative disease of the central nervous system associated with a chronic and progressive movement disorder [1]. Parkinson's Disease Foundation claims that this disease affects about 7–10 million people worldwide and 4% of people with PD are diagnosed before the age of 50. The cause is unknown and there is no cure for PD, but an early diagnosis helps in the treatment that continues throughout the patient's life.

PD studies, in the computational field, are mainly focused on diagnosing the disease. The literature shows that some works aim to recognize the presence or absence of PD and identify the patients degree of severity [3, 4], and another extracts features from handwriting exams [5], among

others [6–12]. Most of the studies use signals from exams to make a diagnosis. However, studies related to a diagnosis through handwriting exams (handwriting exams based on the quality of the patient's tracing results can be used for PD diagnosis) are quite scarce [5].

Handwriting exams may be conducted on paper [13] or by using more sophisticated methods such as digitizers [5] or even a smartphone [14]. This type of exam has advantages as it is easily obtainable and can also provide diversity, such as spirals, ellipses, connected syllables, connected words, and many other ways to test a patient's ability to trace such forms [15–19]. However, the extraction of the features is complicated since the paper exams have some printing error and the information in this type of exam is not so clear.

This paper compares handwriting templates and patients handwriting using a novel Structural Cooccurrence Matrix-based approach which relies on similarity metrics as attributes. This approach was used because feature extraction through cooccurrence between similar images appeared as a promising method for this application. The proposal was

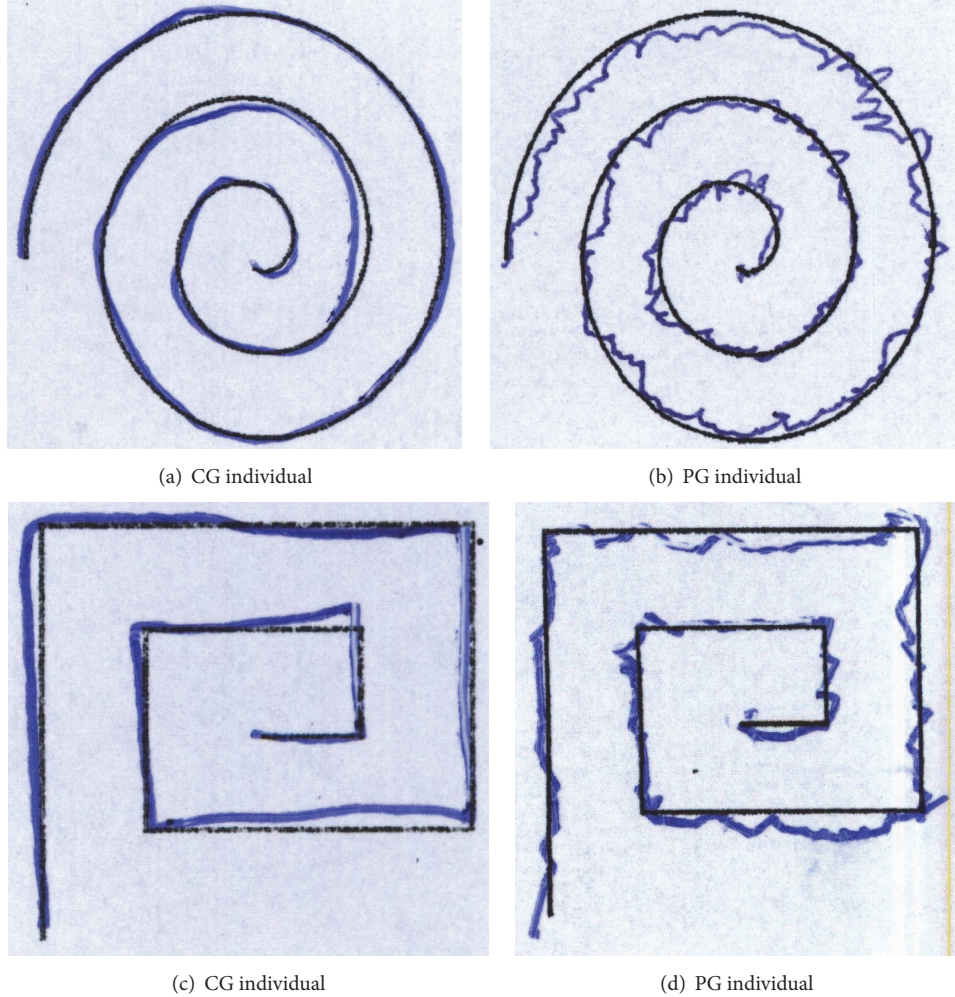


FIGURE 1: (a-b) Handwriting exams in a spiral format; (c-d) handwriting exams in a meander format [13].

evaluated using three classifiers and the results were compared against those in [13].

The rest of this paper is organized as follows. The essentials of handwriting exams and some machine learning methods are explained in Sections 2 and 3, respectively. Section 4 describes the Structural Cooccurrence Matrix features. Our proposal is presented in Section 5. The experimental setup is presented in Section 6. Then, the results and discussion are given in Section 7 and finally the conclusions are given in Section 8.

2. Diagnosis of Parkinson's Disease through Handwriting Exams

There are several examples in the literature that apply handwriting exams to diagnose PD. Drotár et al. recorded the examination time as a parameter for PD diagnosis [5] while Surangsirat used a polar coordinates interpretation to define the features [20]. There are also works based on the difference between the patient's trace and the template [13].

Pereira et al. [13] introduced a new method to obtain the exam which is performed on paper and relies on underlining the template correctly. Pereira et al. also proposed a set of

images composed of handwriting exams known as HandPD dataset.

The HandPD dataset [13] consists of 736 images from handwriting exams divided into two groups: the Control Group (CG) containing 144 images and the Patient Group (PG) containing 592 images. The exams were obtained from 92 individuals, in which 18 were healthy individuals (CG) and 74 were patients (PG) diagnosed with PD. These exams were performed at the Botucatu Medical School of the State University of São Paulo, Brazil, and include spiral and meander handwriting exam templates. Figure 1 shows some samples from this dataset [13].

Pereira et al. [13] used an approach to define the dataset attributes based on the differences between the exam template (ET) and the handwritten trace (HT). Pereira et al. [13] described the HandPD dataset exams using the 9 attributes listed below:

- (1) Root mean square (RMS) of the difference between HT and ET radius:

$$\text{RMS} = \sqrt{\frac{1}{n} \sum_{i=0}^n (r_{\text{HT}}^i - r_{\text{ET}}^i)^2}, \quad (1)$$

where n is the number of sample points drawn for each HT and ET skeleton and r_{HT}^i and r_{ET}^i denote the HT and ET radius, which is basically the length of the straight line that connects the i th sampled point, respectively, to the center of the spiral or meander.

(2) Maximum difference between HT and ET radius:

$$\Delta_{\max} = \operatorname{argmax}_i \left\{ |r_{\text{HT}}^i - r_{\text{ET}}^i| \right\}. \quad (2)$$

(3) Minimum difference between HT and ET radius:

$$\Delta_{\min} = \operatorname{argmin}_i \left\{ |r_{\text{HT}}^i - r_{\text{ET}}^i| \right\}. \quad (3)$$

(4) Another attribute is standard deviation of the difference between HT and ET radius.

(5) Mean relative tremor (MRT) [13] is a quantitative evaluation to measure the “amount of tremor” of a given individual’s HT:

$$\text{MRT} = \frac{1}{n-d} \sum_{i=d}^n \left\{ |r_{\text{ET}}^i - r_{\text{ET}}^{i-d+1}| \right\}, \quad (4)$$

where d is the displacement of the sample points used to compute the radius difference.

(6) There is maximum ET radius.

(7) Another attribute is minimum ET radius.

(8) There is also standard deviation of HT radius.

(9) The last one is the number of times the difference between HT and ET radius changes from negative to positive or the opposite.

3. Overview of Machine Learning Methods

Pereira et al. [13] evaluated their approach using experiments which involved the Naïve Bayes, Optimum-Path Forest (OPF), and Support Vector Machines (SVM) classifiers. Therefore, we conducted our experiments with the same aforementioned classifiers in order to compare our proposal with Pereira et al.’s.

All three classifiers deal with recognition problems in different ways. Based on Bayes’ Theorem, the Naïve Bayes classifier is a probabilistic approach that makes a strong independence assumption among the predictors [21]. The common terms in such a theorem, a priori and a posteriori, are related to an indication of known probabilities and the probability in future indications, respectively.

On the other hand, the OPF classifier designs the recognition problem based on the Graph Theory in a particular feature space [22]. A competition process is established among some patterns, called prototypes that are determined during the training step, and each connected pattern carries its cost. After that, the optimal-path forest is computed using the Image Forest Transform (ITF) algorithm. The LibOPF library [23] was used to implement the OPF classifier used in this work.

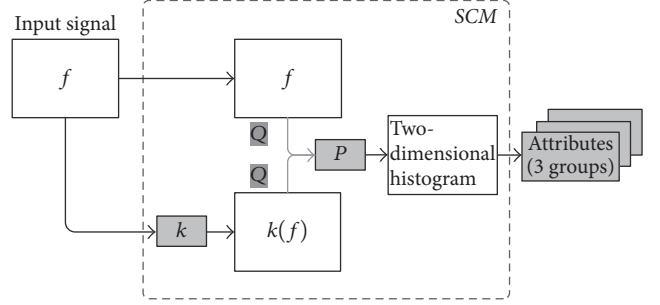


FIGURE 2: An example of an SCM [25].

The SVM classifier is based on the Vapnik statistical learning theory [24]. The main goal of this classifier is to find an optimal hyperplane able to separate the patterns of each label. This optimal hyperplane is obtained through the linear separation of the patterns in space, and after the feature space is defined the SVM determines the optimal hyperplane.

4. Structural Cooccurrence Matrix (SCM)

In this section, we present a brief description of the SCM, which is the basis for the approach of this article, as proposed by Bezerra Ramalho et al. [25].

Bezerra Ramalho et al. [25] introduced a general purpose structural image analytical method based on cooccurrence statistics saved in a matrix, namely, Structural Cooccurrence Matrix (SCM). This method analyzes, in an n -dimensional space, the relation between low-level structures of two discrete signals. Figure 2 shows an example of this method.

This method has a variable k which is any invariant image filter that exposes saliences of the image f . Here, k is configurable for each application. Thus, depending on the a priori knowledge of the characteristics of the image being analyzed, k can be either a high-pass filter or a low-pass filter [25].

5. Proposed Approach

In this section, we present our SCM-based approach to diagnose PD. This new approach extracts features from the spiral and meander handwriting exams of the HandPD dataset [13]. Figure 3 shows the proposed flowchart. This flowchart presents one of the combinations which uses handwritten trace (c) and exam template (b).

The first step is the exam segmentation which returns two new images: the exam template (ET) and the handwritten trace (HT). This step is presented in detail in Figure 4. The images are obtained by applying digital image processing techniques on the handwriting exams.

In order to obtain the ET segmentation the image is smoothed through a Median filter (5×5) to eliminate the noise picked up during the acquisition of the exam. Then, an erosion (9×9 ellipse structure) is applied to ensure that there is no discontinuity in the ET segmentation. After that, an empirically defined threshold is used. Finally, an erosion

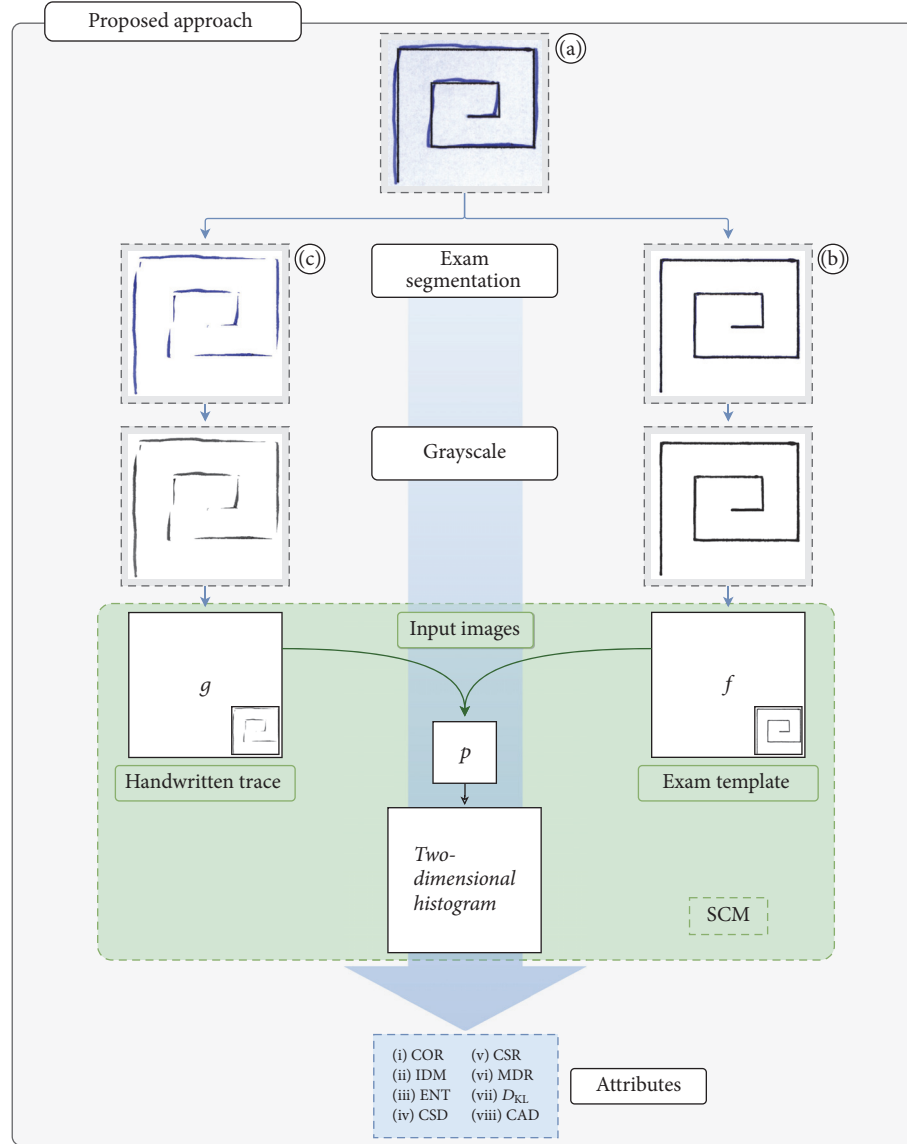


FIGURE 3: Flowchart of the proposed approach.

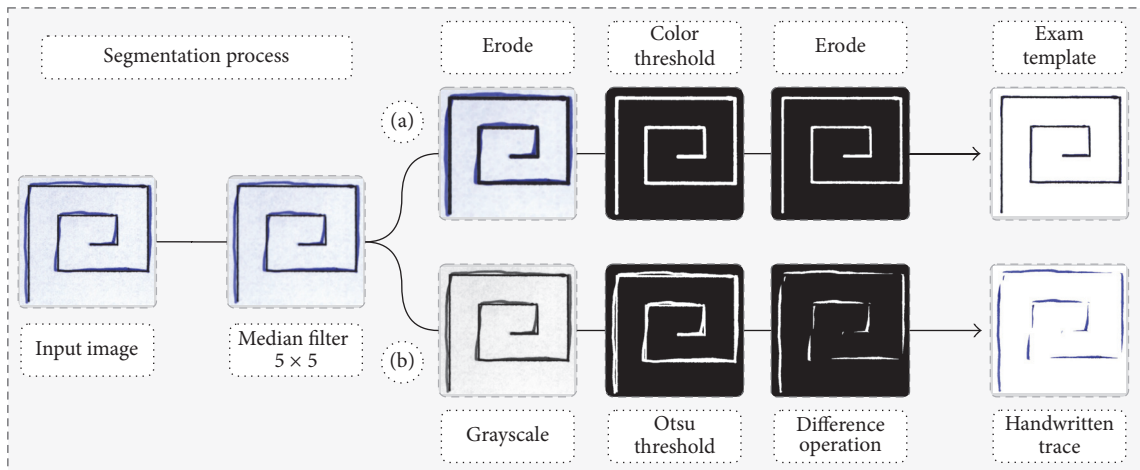


FIGURE 4: An example of the segmentation process: (a) segmentation of exam template; (b) segmentation of handwritten trace.

is applied again with the same structuring element to obtain the real size of the ET as shown in Figure 4.

In order to obtain the HT segmentation the image is also smoothed through the Median filter (5×5) to eliminate the noise picked up during the exams. Then, the handwriting exam is converted to the grayscale, after which the Otsu threshold is applied. Finally, we apply a difference operation between the grayscale image and the ET. These steps are shown in Figure 4.

The second step in our proposal converts the segmented exams to the grayscale for the next step. The third step is feature extraction from the images obtained after the segmentation and conversion to the grayscale. These images are used as the input to SCM as showed in Figure 2. The feature extraction through the SCM is a method to analyze the relationship between signals, in this case, in a two-dimensional space.

A slight modification was made to the original SCM method. The SCM has two input parameters, an image and a filter. We replaced the filter with another image. The new configuration of the input parameters is presented as an example in Figure 3. This proposal is intended to enhance the differences between the two input images by computing the similarity approximation between the patient's trace and the exam template. There is no need to configure a filter as in this SCM method the filter was replaced for another image.

Three combinations of three images were proposed as the SCM inputs, which were then used for a complete analysis: (i) handwriting exam and handwritten trace; (ii) handwriting exam and exam template; and (iii) handwritten trace and exam template.

The scalar attributes, obtained through the SCM method, are computed by the SCM generated between the input images. These attributes are divided into three groups: statistical group, information group, and divergent group [25]. All these attributes are computed based on the SCM matrix represented by $\mathbf{M} = \mathbf{m}_{ij}$, and some are related to the marginal distribution \mathbf{P} of the SCM. A brief description of each attribute is given below:

- (i) Correlation (COR) measures how the information is correlated. The COR is given by

$$\text{COR} = \sum_{ij=0}^{N-1} \mathbf{m}_{ij} \frac{(i - \mu_i)(j - \mu_j)}{\sqrt{\sigma_i^2 \sigma_j^2}} \in [-1, 1], \quad (5)$$

where μ_i and μ_j are the average value of rows and columns of \mathbf{M} . σ_i and σ_j are the standard deviation of rows and columns of \mathbf{M} .

- (ii) Inverse difference moment (IDM) measures the homogeneity and it is given by

$$\text{IDM} = \sum_{ij=0}^{N-1} \frac{\mathbf{m}_{ij}}{1 + (|i - j|)} \in [0, 1]. \quad (6)$$

- (iii) Entropy (ENT): the randomness of the information is measured and it is given by

$$\text{ENT} = - \sum_{ij=0}^{N-1} \mathbf{m}_{ij} \log(\mathbf{m}_{ij}). \quad (7)$$

- (iv) Chi-square distance (CSD): since the $\mathbf{P}_i^0 = \mathbf{m}_{ij} = j$ and $\mathbf{P}_i^e = \sum_{j=0}^{N-1} \mathbf{m}_{ij} \geq i$,

$$\text{CSD} = \sum_{i=0}^{N-1} \frac{(\mathbf{P}_i^0 - \mathbf{P}_i^e)^2}{\mathbf{P}_i^e}. \quad (8)$$

- (v) Chi-square distance ratio (CSR): with the distributions of the quadrants I, $\mathbf{P}_i^I = \sum_{i=0}^{N/2-1} \sum_{j=0}^{N/2-1} \mathbf{m}_{ij}$, and III, $\mathbf{P}_i^{III} = \sum_{i=N/2}^{N-1} \sum_{j=N/2}^{N-1} \mathbf{m}_{ij}$, the CSR is given by

$$\text{CSR} = \sum_{i=0}^{N-1} \frac{(\mathbf{P}_i^I - \mathbf{P}_i^m)^2}{\mathbf{P}_i^m}, \quad (9)$$

$$\text{where } \mathbf{P}_i^m = (\mathbf{P}_i^I + \mathbf{P}_i^{III})/2.$$

- (vi) Mean absolute difference ratio (MDR) calculates the statistical dispersion, where $\text{MD}_{\min} = \min(\text{MD}_{p^c}, \text{MD}_{p^r})$, $\text{MD}_{\max} = \max(\text{MD}_{p^c}, \text{MD}_{p^r})$, and $\text{MD}_p = \sum_{i=0}^{N-1} \sum_{j=0}^{N-1} \mathbf{P}(S_i) \mathbf{P}(S_j) |S_i - S_j|$. The MDR is given by

$$\text{MDR} = \frac{\text{MD}_{\min}}{\text{MD}_{\max}}, \quad (10)$$

where $S_i, S_j, i = 0, \dots, N - 1$ are the indexes of the nonzero values of the marginal distribution \mathbf{P} .

- (vii) Divergence of Kullback Leibler (D_{KL}) measures the information gain between bordering distributions and it is given by

$$D_{KL} = \sum_{i=0}^{N-1} \log\left(\frac{\mathbf{P}_i^c}{\mathbf{P}_i^r}\right) \mathbf{P}_i^c, \quad (11)$$

$$\text{where } \mathbf{P}_i^c / \mathbf{P}_i^r = 0, \text{ where } \mathbf{P}_i^r = 0.$$

- (viii) Complementary absolute difference (CAD) compares the two probability distributions \mathbf{P}_i^c and \mathbf{P}_i^r . The CAD is given by

$$\text{CAD} = 1 - \sum_{i=0}^{N-1} |\mathbf{P}_i^c - \mathbf{P}_i^r|. \quad (12)$$

At the end of the SCM process we have the attributes to be applied as pattern recognition inputs to any machine learning method.

TABLE 1: Results from the best classifiers and combinations.

	Meander Acc (%)	Spiral Acc (%)	M/S Acc (%)
Bayes			
a ↔ c	72.77 ± 9.91	69.57 ± 11.07	65.95 ± 2.05
a ↔ b	75.11 ± 3.99	76.36 ± 4.26	68.38 ± 2.18
c ↔ b	77.72 ± 4.27	82.01 ± 5.53	71.39 ± 2.39
OPF			
a ↔ c	75.54 ± 3.76	69.73 ± 3.63	64.28 ± 2.05
a ↔ b	68.59 ± 3.76	70.49 ± 3.63	61.13 ± 2.57
c ↔ b	77.50 ± 2.75	75.71 ± 4.39	67.21 ± 1.98
SVM			
a ↔ c	80.05 ± 1.80	78.04 ± 2.74	67.63 ± 2.73
a ↔ b	75.00 ± 2.90	78.04 ± 2.85	65.30 ± 2.92
c ↔ b	82.23 ± 3.02	85.54 ± 3.62	74.13 ± 2.27

6. Experimental Setup

We conducted some experiments with the handwriting exams used by Pereira et al. [13]. These exams concern the patient's ability to underline the two exam templates: spiral and meander. First, the spiral and meander exam attributes were extracted by the proposed approach presented in Section 5. Then, we applied three machine learning methods: Naive Bayes, OPF, and SVM in 3 different experiments: (i) considering only the spiral exam attributes; (ii) considering only the meander exam attributes; and (iii) considering spiral and meander exam attributes together. That is, we evaluate the proposed approach using the two handwriting formats separately and also together. After that, we compared the results with those of Pereira et al. [13].

The number of HandPD dataset samples, used in all of the experiments, are divided into 368 spiral exam samples and 368 meander exam samples, resulting in 736 samples. We emphasize that each subset is divided into 296 samples from the CG and 72 samples from the PG.

All the three experiments were conducted with 75% for the training set, 25% for testing set, and the remaining 25% for the validation set. We applied a cross-validation with 20 runs for the reliability of the results. The setup of the OPF classifier was configured with the Euclidean distance and the SVM with the radial basis function. The SVM and OPF classifiers were automatically optimised by choosing the optimal parameters from each method. Parameters are considered optimal when the cross-validation estimates the minimal error [26–32].

Accuracy was used to classify the machine learning methods. This metric is defined using the terms obtained in the confusion matrix generated after applying the machine learning methods and refers to the closeness of a measured value to a standard or known value.

7. Results and Discussion

In this section, we provide an analysis of the results using the handwriting exams from Pereira et al. [13]. These exams

present the patient's ability to underline the exam template. The results were obtained by applying machine learning methods to the features extracted from cooccurrence matrix obtained over the SCM extractor used in this work.

Table 1 presents the classification results of the combinations between the images obtained in the segmentation (ET and HT) and the handwritten exam using SCM, where the meander and spiral formats were evaluated separately and together. The handwritten exam, exam template, and handwritten trace are represented in Table 1 as **a**, **b**, and **c**, respectively.

Table 1 also shows that the combination of the meander and spiral exam obtained the lowest accuracy rates. The very significant difference between the spiral and meander formats justifies these low rates.

Another important factor, observed in the best results obtained with the classifiers in Table 1, was the predominance of the best results using the combination of the handwritten trace and the exam template which proves that these two are the most similar.

The results of this work were compared with the results obtained by Pereira et al. approach [13] in Table 2 which shows each classifier with subdivisions for the experiments using handwriting exams in the formats of meanders, spirals, and the combination of the meanders and spirals. Immediately after that, there is a new subdivision between the results obtained with our proposal and those of Pereira et al. [13]. In Table 2 the highest accuracy results are in underline font and the lowest ones in italic font, for each of the classifiers. Also, highlight in bold are the highest and the lowest accuracy results of both approaches and experiments.

The results obtained in this paper proved to be superior in all of the experiments in comparison to those of Pereira proposal [13]. The highest accuracy was 85.54% using the approach proposed. This highest result was provided with the SVM classifier, using the handwriting in a spiral format with the combination of the handwritten trace and the exam template. The lowest accuracy among the best results presented in Table 2 was 45.79%.

TABLE 2: Comparison between the best results of this paper and the best results of the Pereira et al. approach [13].

Classif.	Database	Feature extractor	Accuracy (%)
Bayes	<i>Meander</i>	Pereira et al. approach [13]	59.20 ± 4.78
		<i>Proposed approach</i>	$\underline{77.72 \pm 4.27}$
	<i>Spiral</i>	Pereira et al. approach [13]	64.23 ± 7.11
		<i>Proposed approach</i>	$\underline{82.01 \pm 5.53}$
OPF	<i>M/S</i>	Pereira et al. approach [13]	45.79 ± 4.15
		<i>Proposed approach</i>	$\underline{71.39 \pm 2.39}$
	<i>Meander</i>	Pereira et al. approach [13]	57.54 ± 6.35
		<i>Proposed approach</i>	$\underline{77.50 \pm 2.75}$
SVM	<i>Spiral</i>	Pereira et al. approach [13]	52.48 ± 5.32
		<i>Proposed approach</i>	$\underline{75.71 \pm 4.39}$
	<i>M/S</i>	Pereira et al. approach [13]	55.86 ± 3.63
		<i>Proposed approach</i>	$\underline{67.21 \pm 1.98}$
SVM	<i>Meander</i>	Pereira et al. approach [13]	66.72 ± 5.33
		<i>Proposed approach</i>	$\underline{82.23 \pm 3.02}$
	<i>Spiral</i>	Pereira et al. approach [13]	50.16 ± 1.71
		<i>Proposed approach</i>	$\underline{85.54 \pm 3.62}$
	<i>M/S</i>	Pereira et al. approach [13]	58.61 ± 2.84
		<i>Proposed approach</i>	$\underline{74.13 \pm 2.27}$

8. Conclusion

The proposal of this paper is based on the patient's trace and the exam template using the SCM method for a similarity approximation. The SVM classifier with the RBF kernel and handwriting in the spiral format proved being the most promising for this application. This configuration had an accuracy of 85.54% for the combination of the handwritten trace and the exam template in the feature extraction. The results obtained in this paper were 21.31% superior to the best result achieved by Pereira et al. approach [13].

We conclude that this is promising approach to help in the diagnosis of PD. Another advantage of this proposal is that there is no need to configure a filter to obtain the structured cooccurrence matrix, facilitating its application.

These results encourage us to propose future works for handwriting feature extraction.

Conflicts of Interest

The authors declare that there are no conflicts of interest regarding the publication of this paper.

Acknowledgments

Pedro P. Rebouças Filho acknowledges the sponsorship from the IFCE via Grant PROINFRA PPG/2017. João W. M. de Souza acknowledges the CNPq for financial support. Jefferson S. Almeida acknowledges the FUNCAP for financial support.

References

- [1] WHO, *Neurological Disorders: Public Health Challenges*, World Health Organization, 2006.
- [2] J. Parkinson, "An essay on the shaking palsy. 1817," *The Journal of Neuropsychiatry and Clinical Neurosciences*, vol. 14, no. 2, pp. 223–236, 2002.
- [3] J. Chen, Z. Lei, L. Liu, G. Zhao, and M. Pietikäinen, "RoLoD: Robust local descriptors for computer vision," *Neurocomputing*, vol. 184, pp. 1-2, 2016.
- [4] N. Bouadjenek, H. Nemmour, and Y. Chibani, "Robust soft-biometrics prediction from off-line handwriting analysis," *Applied Soft Computing*, vol. 46, pp. 980–990, 2016.
- [5] P. Drotár, J. Mekyska, I. Rektorová, L. Masarová, Z. Smékal, and M. Faundez-Zanuy, "Evaluation of handwriting kinematics and pressure for differential diagnosis of Parkinson's disease," *Artificial Intelligence in Medicine*, vol. 67, pp. 39–46, 2016.
- [6] M. S. Baby, A. J. Saji, and C. S. Kumar, "Parkinsons disease classification using wavelet transform based feature extraction of gait data," in *Proceedings of the 2017 IEEE International Conference on Circuit, Power and Computing Technologies, ICCPCT 2017*, India, April 2017.
- [7] A. Brahim, L. Khedher, J. M. Gorriz et al., "A proposed computer-aided diagnosis system for Parkinson's disease classification using 123I-FP-CIT imaging," in *Proceedings of the 3rd International Conference on Advanced Technologies for Signal and Image Processing, AT SIP 2017*, Morocco, May 2017.
- [8] C. R. Pereira, S. A. T. Weber, C. Hook, G. H. Rosa, and J. P. Papa, "Deep learning-aided Parkinson's disease diagnosis from handwritten dynamics," in *Proceedings of the 29th SIBGRAPI Conference on Graphics, Patterns and Images, SIBGRAPI 2016*, pp. 340–346, Brazil, October 2016.
- [9] V. V. Shah, S. Goyal, and H. J. Palanthandlam-Madapusi, "A perspective on the use of high-frequency stimulation in deep brain stimulation for Parkinson's disease," in *Proceedings of the 2nd Indian Control Conference, ICC 2016*, pp. 19–24, India, January 2016.
- [10] N. Zhi, B. K. Jaeger, A. Gouldstone, R. Sipahi, and S. Frank, "Toward Monitoring Parkinson's Through Analysis of Static Handwriting Samples: A Quantitative Analytical Framework,"

- IEEE Journal of Biomedical and Health Informatics*, vol. 21, no. 2, pp. 488–495, 2017.
- [11] A.-M. Schiffer, A. J. Nevado-Holgado, A. Johnen, A. R. Schönberger, G. R. Fink, and R. I. Schubotz, “Intact action segmentation in Parkinson’s disease: Hypothesis testing using a novel computational approach,” *Neuropsychologia*, vol. 78, pp. 29–40, 2015.
- [12] R. Guzman-Cabrera, M. Gomez-Sarabia, M. Torres-Cisneros, M. A. Escobar-Acevedo, and J. R. Guzman-Sepulveda, “Parkinson’s disease: Improved diagnosis using image processing,” in *Proceedings of the 2017 Photonics North (PN)*, pp. 1–1, Ottawa, ON, Canada, June 2017.
- [13] C. R. Pereira, D. R. Pereira, F. A. Silva et al., “A new computer vision-based approach to aid the diagnosis of Parkinson’s disease,” *Computer Methods and Programs in Biomedicine*, vol. 136, pp. 79–88, 2016.
- [14] R. Graça, R. S. E. Castro, and J. Cevada, “Parkdetect: Early diagnosing parkinson’s disease,” in *Proceedings of the 9th IEEE International Symposium on Medical Measurements and Applications, IEEE MeMeA 2014*, Portugal, June 2014.
- [15] C. R. Pereira, D. R. Pereira, F. A. D. Silva et al., “A step towards the automated diagnosis of parkinson’s disease: Analyzing handwriting movements,” in *Proceedings of the 28th IEEE International Symposium on Computer-Based Medical Systems, CBMS 2015*, pp. 171–176, Brazil, June 2015.
- [16] P. Drotár, J. Mekyska, I. Rektorová, L. Masarová, Z. Smékal, and M. Faundez-Zanuy, “Analysis of in-air movement in handwriting: A novel marker for Parkinson’s disease,” *Computer Methods and Programs in Biomedicine*, vol. 117, no. 3, pp. 405–411, 2014.
- [17] P. Drotar, J. Mekyska, Z. Smekal, I. Rektorova, L. Masarova, and M. Faundez-Zanuy, “Contribution of different handwriting modalities to differential diagnosis of Parkinson’s Disease,” in *Proceedings of the 2015 IEEE International Symposium on Medical Measurements and Applications, MeMeA 2015*, pp. 344–348, Italy, May 2015.
- [18] C. Taleb, M. Khachab, C. Mokbel, and L. Likforman-Sulem, “Feature selection for an improved Parkinson’s disease identification based on handwriting,” in *Proceedings of the 2017 1st International Workshop on Arabic Script Analysis and Recognition (ASAR)*, pp. 52–56, Nancy, France, April 2017.
- [19] Z. Smekal, J. Mekyska, I. Rektorova, and M. Faundez-Zanuy, “Analysis of neurological disorders based on digital processing of speech and handwritten text,” in *Proceedings of the 2013 International Symposium on Signals, Circuits and Systems, ISSCS 2013*, Romania, July 2013.
- [20] D. Surangsirat, A. Intarapanich, C. Thanawattano, R. Bhidayasiri, S. Petchratchatachart, and C. Anan, “Tremor assessment using spiral analysis in time-frequency domain,” in *Proceedings of the IEEE SoutheastCon 2013: Moving America into the Future*, USA, April 2013.
- [21] S. Theodoridis and K. Koutroumbas, *Pattern Recognition, fourth edition Edition*, Academic Press, fourth edition Edition, 2009.
- [22] J. P. Papa, A. X. Falcão, and C. T. N. Suzuki, “Supervised pattern classification based on optimum-path forest,” *International Journal of Imaging Systems and Technology*, vol. 19, no. 2, pp. 120–131, 2009.
- [23] J. P. Papa, C. T. N. Suzuki, and A. X. Falcão, *A library for the design of optimum-path forest classifiers*, 2014, <http://www.ic.unicamp.br/afalcao/libopf/index.htmlLibopf>.
- [24] V. N. Vapnik, *Statistical Learning Theory*, John Wiley Sons, Inc, 2009.
- [25] G. L. Bezerra Ramalho, D. S. Ferreira, P. P. Rebouças Filho, and F. N. S. de Medeiros, “Rotation-invariant feature extraction using a structural co-occurrence matrix,” *Measurement*, vol. 94, pp. 406–415, 2016.
- [26] S. L. Gomes, E. D. S. Rebouças, E. C. Neto et al., “Embedded real-time speed limit sign recognition using image processing and machine learning techniques,” *Neural Computing and Applications*, vol. 28, pp. 573–584, 2017.
- [27] P. P. R. Filho, A. C. D. S. Barros, G. L. B. Ramalho et al., “Automated recognition of lung diseases in CT images based on the optimum-path forest classifier,” *Neural Computing and Applications*, pp. 1–14, 2017.
- [28] P. P. Rebouças Filho, E. D. S. Rebouças, L. B. Marinho, R. M. Sarmento, J. M. R. S. Tavares, and V. H. C. de Albuquerque, “Analysis of human tissue densities: A new approach to extract features from medical images,” *Pattern Recognition Letters*, vol. 94, pp. 211–218, 2017.
- [29] P. P. Rebouças Filho, R. M. Sarmento, G. B. Holanda, and D. de Alencar Lima, “New approach to detect and classify stroke in skull CT images via analysis of brain tissue densities,” *Computer Methods and Programs in Biomedicine*, vol. 148, pp. 27–43, 2017.
- [30] E. C. Neto, S. L. Gomes, P. P. Rebouças Filho, and V. H. C. De Albuquerque, “Brazilian vehicle identification using a new embedded plate recognition system,” *Measurement*, vol. 70, pp. 36–46, 2015.
- [31] L. B. Marinho, J. S. Almeida, J. W. M. Souza, V. H. C. Albuquerque, and P. P. Rebouças Filho, “A novel mobile robot localization approach based on topological maps using classification with reject option in omnidirectional images,” *Expert Systems with Applications*, vol. 72, pp. 1–17, 2017.
- [32] P. P. Rebouças Filho, J. C. D. Santos, F. N. C. Freitas et al., “New approach to evaluate a non-grain oriented electrical steel electromagnetic performance using photomicrographic analysis via digital image processing,” *Journal of Materials Research and Technology*, 2017.

Research Article

Brain State Decoding Based on fMRI Using Semisupervised Sparse Representation Classifications

Jing Zhang ,¹ Chuncheng Zhang ,² Li Yao ,^{1,2} Xiaojie Zhao,² and Zhiying Long ¹

¹State Key Laboratory of Cognitive Neuroscience and Learning & IDG/McGovern Institute for Brain Research, Beijing Normal University, Beijing 100875, China

²School of Information Science & Technology, Beijing Normal University, Beijing 100875, China

Correspondence should be addressed to Zhiying Long; friskying@163.com

Received 30 October 2017; Revised 5 February 2018; Accepted 27 February 2018; Published 19 April 2018

Academic Editor: João Manuel R. S. Tavares

Copyright © 2018 Jing Zhang et al. This is an open access article distributed under the Creative Commons Attribution License, which permits unrestricted use, distribution, and reproduction in any medium, provided the original work is properly cited.

Multivariate classification techniques have been widely applied to decode brain states using functional magnetic resonance imaging (fMRI). Due to variabilities in fMRI data and the limitation of the collection of human fMRI data, it is not easy to train an efficient and robust supervised-learning classifier for fMRI data. Among various classification techniques, sparse representation classifier (SRC) exhibits a state-of-the-art classification performance in image classification. However, SRC has rarely been applied to fMRI-based decoding. This study aimed to improve SRC using unlabeled testing samples to allow it to be effectively applied to fMRI-based decoding. We proposed a semisupervised-learning SRC with an average coefficient (semiSRC-AVE) method that performed the classification using the average coefficient of each class instead of the reconstruction error and selectively updated the training dataset using new testing data with high confidence to improve the performance of SRC. Simulated and real fMRI experiments were performed to investigate the feasibility and robustness of semiSRC-AVE. The results of the simulated and real fMRI experiments showed that semiSRC-AVE significantly outperformed supervised learning SRC with an average coefficient (SRC-AVE) method and showed better performance than the other three semisupervised learning methods.

1. Introduction

Functional magnetic resonance imaging (fMRI), which measures brain activity by detecting changes in blood oxygenation level-dependent signals, is a powerful technique for indirectly investigating the neural activity in the brain. Recently, multivariate classification techniques have been widely applied to fMRI data to decode brain states from observed brain activities [1]. Compared with the traditional univariate analysis methods, multivariate supervised-learning techniques are able to reveal the neural mechanism that is discriminative to different brain states [2].

Among the various multivariate supervised-learning classification techniques, sparse representation-based classification (SRC) exhibits a state-of-the-art classification performance and is robust against noise. SRC has attracted increasing attention and achieved promising results in many areas, for example, image [3], digit, and texture classifications [4, 5]. SRC represents the test sample using an overcomplete

dictionary whose base elements are the training samples. If sufficient training samples are available from each class, SRC will be possible to represent the test samples as a linear combination of the training samples from the same class. Although various supervised-learning classification techniques that included support vector machine (SVM), logistic regression, naïve Bayesian, and deep neural networks were applied to brain state decoding of fMRI data [6–9], SRC has seldom been applied to fMRI-based brain state decoding due to the various variabilities in fMRI data, such as complex and high noises and the delay of hemodynamic response. Given the promising outcomes of SRC in other research fields, it is necessary to explore the effective use of SRC in fMRI analysis.

SRC is a type of supervised-learning method that must be trained using labeled samples. If the labeled training data are insufficient, the performance of the trained classifier cannot be guaranteed. Because the collection of human fMRI data is restricted by the high cost of experiments and is highly

constrained by the limited amount of time during which a participant can safely remain in the scanner, it is challenging to collect a large amount of labeled training data for a participant. To solve the insufficiency of labeled training data, semisupervised learning was developed to train the classifier using both labeled training data and unlabeled data. Many machine learning studies have found that unlabeled data, in conjunction with a small amount of labeled data, can produce a considerable improvement in the learning accuracy [10, 11].

Various semisupervised-learning algorithms have already been developed over the past decade, including self-training [10, 12], cotraining [13], transductive support vector machine [14], graph-based algorithms [11], and generative models [15]. Among these methods, self-training is a simple and effective model and is less time-consuming than the other models [16]. Self-training gradually updates the labeled training data by using test samples with the most confident predictions step by step to improve the performance of the traditional supervised learning algorithm. In contrast to most conventional classifications that are usually divided into two independent steps, that is, training and testing, SRC does not have a training process, and all test data are adaptively represented by all the training samples in the dictionary. Therefore, SRC has an adaptive characteristic [17] and does not need to be retrained as the training data are gradually enlarged. Therefore, self-training can be easily combined with SRC. Thus far, one study proposed a type of semisupervised SRC method for EEG in brain-computer interface application by combining self-training learning and SRC [17]. This method simply updates all tested data without estimating the confidence of the predictions, which may result in performance degeneration due to many false predictions.

In addition, a few semisupervised machine learning methods have recently been proposed for fMRI data analysis. Plumpton et al. proposed a naïve random subspace ensemble strategy using linear classifiers [18]. This method is time-consuming and can easily be affected by testing samples with inaccurate predictions. Plumpton (2014) further proposed random subspace ensemble of online linear discriminant classifier (RSE-OLDC) that updates only the predicted labels with a high confidence rather than all predicted labels [19]. However, two parameters, that is, the subspace scale and the number of individual classifiers in RSE-OLDC, may vary with different datasets, and the random selection of feature subsets may induce some fluctuations in the classification results. Due to the low signal-to-noise ratio (SNR) and low sample-to-feature ratio of fMRI data, the introduction of a few incorrect sample labels may heavily affect the classification performance. Therefore, a robust and effective semisupervised learning method is essential for brain state decoding based on fMRI data.

This study aimed to investigate how to improve SRC and effectively applied SRC to fMRI-based decoding. Zou et al. (2015) proposed a local sparse representation-based nearest neighbor (LSRNN) classifier that averaged the k largest sparse coefficients in each class and assigned the label of the class with the maximum average sparse coefficient to the testing sample [20]. It was demonstrated that class-specific sparse coefficients could be utilized to improve the performance

of classification. Based on the previous study, this study proposed the semisupervised SRC with an average coefficient (semiSRC-AVE) method that performed the classification using the average coefficient of each class instead of the reconstruction error and selectively updated the training dataset using new testing data with high confidence to improve the performance of SRC. The results of the simulated and real fMRI data both demonstrated that semiSRC-AVE exhibited a more stable and better performance than the supervised SRC with an average coefficient (SRC-AVE) method. Compared to the other three semisupervised methods, including naïve semiSRC-AVE, RSE-OLDC [19], and random subspace ensemble of online SRC-AVE (RSE-OSRC-AVE), semiSRC-AVE showed better performance in the multiclass classification and comparable performance in the two-class classification.

2. Related Works

For self-training, the confidence of prediction is calculated after a test sample is classified. If the confidence is higher than a threshold, the test sample and its predicted label are added to the training set and the classifier is retrained for the next test sample. The confidence of predication is critical to the self-training algorithm. An appropriate confidence measure can prevent test samples with wrong predicted label from entering into the training set. Different self-learning classifiers may use different confidence measures.

For the well-known decision tree algorithm C4.5 [21], the confidence of a prediction can be obtained from the accuracy of the leaf, that is, the percentage of correctly classified training samples from all training samples [16]. For the self-training naïve Bayesian classifier (NB), the confidence is determined by the probability of predicted class for a given test sample [16]. The self-training SVM algorithm can determine the confidence of a prediction using Platt scaling [22] that returns posterior probability of predicted class for a test sample [23].

Recently, a few self-training update strategies have been applied to fMRI-based classification. Naïve strategy does not judge the predicted labels' reliabilities and updates the classifier using the predicted naïve labels directly. Plumpton et al. (2012) applied the naïve strategy to a random subspace ensemble classifier that used the vote result of the ensemble linear discriminant classifiers as the true label and updated the classifier by adding the test data to the training set [18].

Plumpton (2014) further improved their ensemble method and proposed the new random subspace ensemble of online linear discriminant classifier (RSE-OLDC) by updating the training data using the predicted labels with a high confidence [19]. Because RSE-OLDC was used in this study, we presented a detail review on RSE-OLDC.

RSE-OLDC has two parameters that are the number of individual classifiers (L) and the subspace scale (M). Suppose that each sample has n features. For each training sample, L feature subsets are drawn independently. Each subset contains $M < n$ features that are randomly selected from the total feature set without replacement. Therefore, L training datasets are generated and L diverse linear discriminant

classifiers (LDC) [18] are generated by training each ensemble member on a different training dataset. Suppose that the training data for class i come from a multivariate normal distribution with the class-specific mean μ^i and the common covariance matrix Σ . The optimal discriminant function $g_i(x)$ of LDC for a test sample x is calculated by

$$g_i(x) = \ln P^i - \frac{1}{2} \mu^{iT} \Sigma^{-1} \mu^i + \mu^{iT} \Sigma^{-1} x. \quad (1)$$

The test sample x is assigned to the class with the largest $g_i(x)$.

For each test sample, L feature subsets are generated in the same way as the training datasets. Each feature subset of a testing sample has the same features as the training datasets. The L classifiers are applied to the corresponding L feature subsets of a testing sample separately. The final prediction of a test sample is determined by majority vote of the L ensemble classifiers. Suppose that y is the final prediction and y_i is the predicted label of the i th classifier. Confidence of the prediction is calculated by

$$\text{confidence} = \frac{\sum_{i=1}^L \{y_i = y\}}{L}. \quad (2)$$

For the next test sample, the classifiers were updated by adding the test sample with the confidence higher than a threshold to the training dataset. Plumpton chose 75% as the threshold in their study [19].

3. Proposed Methods

In this section, the theoretical frameworks underlying the SRC and semiSRC-AVE methods are described.

3.1. Sparse Representation-Based Classification. SRC aims to seek a suitable sparse solution to represent test data y from the whole training set [3]. Suppose that the matrix $A = [A_1, A_2, \dots, A_k] \in R^{N \times M}$ concatenates the M training samples of all k classes, N represents the feature dimension of the sample, and A_i represents the subset of training samples of class i . Let y be a test sample. If the training samples in the dictionary are sufficient, test sample y can be represented by solving the following problem:

$$\begin{aligned} \min & \quad \|x\|_0 \\ \text{s.t.} & \quad y = Ax, \end{aligned} \quad (3)$$

where x is a coefficient vector. The above l_0 -norm minimization problem is nonconvex and NP-hard. If the solution x is sufficiently sparse, the l_0 minimization problem in (3) is equivalent to the l_1 minimization problem in [24]

$$\begin{aligned} \hat{x} = \arg \min & \quad \|x\|_1 \\ \text{s.t.} & \quad y = Ax. \end{aligned} \quad (4)$$

The l_1 minimization problem has been broadly investigated, and various algorithms can be used to solve it [25]. In this study, the gradient projection for sparse reconstruction

(GPSR) is applied due to its relatively rapid computation speed.

After the sparse coefficient vector \hat{x} is estimated, the classification can be performed by

$$I(y) = \arg \min_i r_i(y) = \arg \min_i \|y - A\delta_i(\hat{x})\|_2. \quad (5)$$

Here, $r_i(y)$ is the representation residual error corresponding to class i . $\delta_i(\hat{x})$ is a vector whose nonzero elements are those that are associated with class i .

In the context of fMRI-based brain state decoding, $y \in R^N$ is the fMRI volume at a time point of the testing data and N is the number of the spatial voxels. Each column in the matrix A represents the fMRI volume of the training data from one of the tasks (classes). The goal of classifier model is to determine which class the test data y belongs to.

3.2. Semisupervised SRC with an Average Coefficient (semiSRC-AVE). For fMRI data, the hemodynamic responses have a delay of approximately 6 seconds to reach the maximum value after a short-duration stimulus. In contrast to the static face image, the fMRI volumes that respond to the same task vary greatly across different time points. Those variations may largely affect the performance of SRC in fMRI data analyses.

If a test sample belongs to a specific class, it is generally positively correlated with the training samples in the same class and should be better represented by the training samples from the class with larger positive coefficients and smaller negative coefficients compared to those from the other classes. Therefore, the average of all coefficients associated with a specific class may be a useful index for the classification. Moreover, the average sparse coefficient was used as classification index in LSRNN classifier and was demonstrated to be able to improve the performance of classification in the previous study [20]. Based on the previous study [20], this study also used the average of all coefficients related to a class as the classification criterion of SRC. For the SRC with an average coefficient (SRC-AVE) method, test sample y is assigned to an object class that has the maximal average value of the corresponding coefficients.

$$I(y) = \arg \max_i S_i(y) = \arg \max_i \text{ave}(\delta_i(\hat{x})), \quad (6)$$

where $S_i(y)$ is the mean of all coefficients from class i .

To solve the insufficiency of the training data, the unlabeled testing data can be used to update the training data. However, it is challenging for self-training learning to choose reliable unlabeled samples and guarantee the accuracy of the updated labels [26]. For SRC-AVE, the predication is usually more reliable if the average coefficient of the predicated class is much larger than that of the other classes. Based on this criterion, we investigated a method to measure the predication reliability of the testing sample. First, a distance d_m for the m th test sample y_m is defined in

$$d_m = S_I(y_m) - \frac{\sum_{j=1, j \neq I}^K S_j(y_m)}{K-1}, \quad (7)$$

```

Input: training matrix  $A \in R^{N \times M}$ , training label  $L \in R^M$ , test set  $Y = [y_1, \dots, y_P] \in R^{N \times P}$  ( $P$  is the number of test samples).
Output: identities of  $Y$ 
Method:
for  $m = 1$  to  $P$ 
    (1) Normalize the columns of  $A$  to have unit  $l^2$ -norm.
    (2) Solve the  $l^1$ -minimization problem:
        
$$\hat{x} = \arg \min \|x\|_1$$

        s.t.  $y_m = Ax$ 
    (3) Compute and output the identity of  $y_m$ :
        
$$I(y_m) = \arg \max_i S_i(y_m) = \arg \max_i \text{ave}(\delta_i(\hat{x}))$$

    (4) Compute the distance of  $y_m$ :
        
$$d_m = S_I(y_m) - \frac{\sum_{j=1, j \neq I}^K S_j(y_m)}{K - 1}$$

    (5) Compute the threshold of  $y_m$ :
        
$$\text{threshold}_m = \alpha \frac{\sum_{i=1}^{m-1} d_i}{m - 1}, \quad m > 1$$

    (6) if  $d_m > \text{threshold}_m$ 
        
$$A = [A, y_m],$$

        
$$L = [L, I]$$

    end
end

```

ALGORITHM 1: semiSRC-AVE.

where $S_I(y_m)$ is the mean of the coefficients from predicted class I and $S_j(y_m)$ is the mean of the coefficients from the other classes. K is the total number of classes. The distance d_m measures how far the average coefficient $S_I(y_m)$ of class I is from the mean of $S_j(y_m)$ of the other $k - 1$ classes. If d_m is large enough, the predicated class label should be true with a high confidence. Thus, it is necessary to set a threshold to determine d_m . Given the variability across the testing samples, the threshold is set as the mean of distances d_i ($i = 1 \dots m - 1$) of all the previous testing samples as follows:

$$\text{threshold}_m = \alpha \frac{\sum_{i=1}^{m-1} d_i}{m - 1}, \quad \text{s.t. } m > 1, \quad (8)$$

where m corresponds to m th testing data. The threshold_m is fully determined by the previous $m - 1$ testing samples and reflects the average difference between the predicted class and the other unpredicted classes in the testing data. The coefficient α can be used to adjust the threshold level. In general, coefficient α can be set to 1 when the training data and testing data are from the same classes. When the training and testing data are not from the same classes, coefficient α can be set to less than 1 so that more testing data can be used to update the training data. For the first testing data, the training data cannot be updated by default. If the distance d_m of the m th testing sample is larger than threshold_m , the predicated class label is considered reliable and the m th testing sample y_m is added to dictionary A as a new column. Dictionary A and training label L are replaced with $A = [A, y_m]$ and $L = [L, I]$, respectively. Based on the updating criterion, we propose the semisupervised SRC-AVE (semiSRC-AVE) algorithm that combines self-training

and SRC-AVE. Algorithm 1 illustrates the semiSRC-AVE procedure.

4. Experiments and Results

In this section, we evaluated the effectiveness and robustness of semiSRC-AVE using simulated and real fMRI data. Moreover, the performance of semiSRC-AVE was compared to that of SRC-AVE and the other three self-training classifiers. The three classifiers were naïve semiSRC-AVE that updates the training data using naïve strategy, RSE-OLDC, and RSE-OSRC-AVE that used the SRC-AVE to replace the LDC of RSE-OLDC. The code of the GPSR algorithm was downloaded from <http://www.lx.it.pt/~mtf/GPSR/>, and the codes of SRC, SRC-AVE, semiSRC-AVE, and RSE-OSRC-AVE algorithms were written based on the core GPSR algorithm. In this paper, all the computations were performed on a computer with AMD Phenom(tm) II X4 B97 processor, CPU 3.20 GHz, and RAM 8 GB.

4.1. Simulated Experiments

4.1.1. Generation of Simulated Data. Two groups of datasets were generated to investigate the performance of semiSRC-AVE in this section. It was assumed that each group of datasets included two runs and each run contained three tasks.

The first group was generated by expressing the observations as the product of the time courses and super-Gaussian sources using the MATLAB toolbox SimTB [27]. For each run, we assumed that the simulated data from each subject contained 27 spatial sources. Each source that had 50×50 voxels with a baseline intensity of 800 was independently

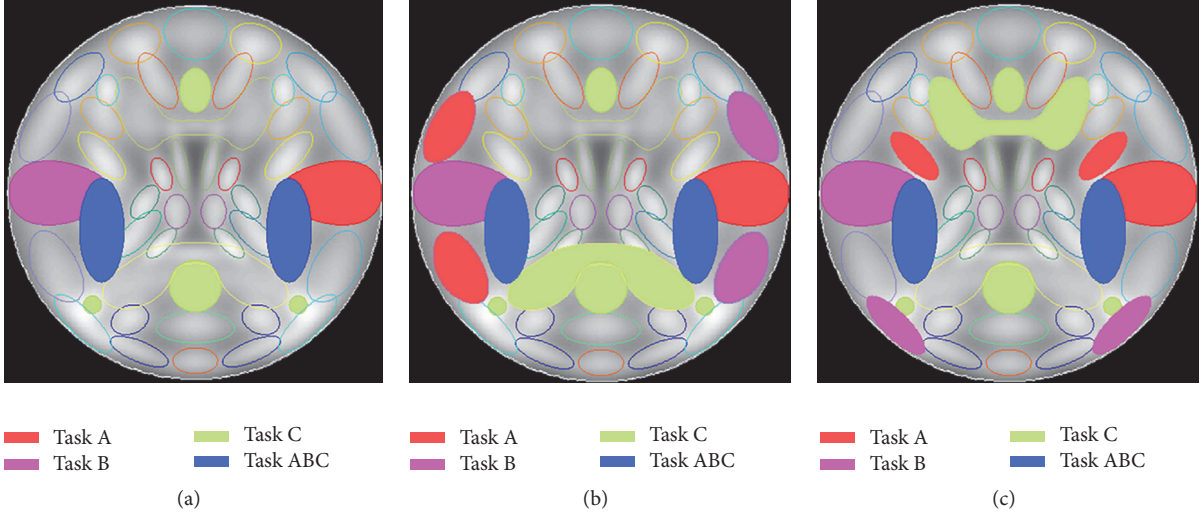


FIGURE 1: Regions of interest that are engaged in the three tasks for the first group of simulated datasets (a), the first run of the second group of datasets (b), and the second run of the second group of datasets (c).

translated, rotated, and contracted or expanded to simulate the intersubject differences. Figure 1(a) presents the regions of interest (ROI) that were activated by each task. The red/purple/green regions were assumed to be activated by tasks A/B/C, and the amplitude of each task block was set to 1.5 relative to the unique events whose amplitudes were 1. The blue regions were assumed to be engaged in the three tasks jointly with the amplitude of 2. There were twelve 40 s task blocks that alternated with twelve 20 s rest blocks with a TR of 2 s in each run, four blocks per task. The simulated fMRI response of each task that was derived from the convolution of the stimulus paradigm and the hemodynamic response function (HRF) was added to the corresponding ROIs. The simulated fMRI responses of the other task-unrelated sources were derived from the convolution of the unique events and HRF. Head motion was added with a translation of less than 2% of the entire image and a rotation less than 5 degrees. Each of the 12 subjects had nine levels of contrast-to-noise ratios (CNR) that varied from 0.08 to 0.16 with an increment of 0.01. Thus, the first group of simulated datasets contained 108 (12×9) datasets. The order of the task blocks was randomized across the nine noise levels. At each noise level, the simulated datasets of 12 subjects had the same order of task blocks.

The second group of datasets was used to investigate the performance of semiSRC-AVE for cross-decoding that tested generalization to novel stimuli or tasks. In cross-decoding, a decoder is trained with one set of stimuli and then tested with another, or the task eliciting the response patterns is changed [28]. For the second group, it was assumed that the tasks in the training runs were different from the tasks in the testing runs and the regions activated by the tasks in the training runs were not the same as those in the testing runs. The second group of simulated datasets was generated in the same way as the first group, except that the activated ROIs were different. Figures 1(b) and 1(c) present the ROIs that were activated by the three tasks in the first run and second run, respectively.

4.1.2. Feature Selection. Each subject's first run was used as the training samples, and the second run was used as the testing samples for all the simulated datasets. The correlation between the time course of each voxel and the reference function was calculated. The reference function was derived from the convolution of the paradigm of the three tasks and HRF. The top 1000 voxels with the highest correlations were selected as features. The testing data in the second run used the same features as the training data. As a pragmatic approach, we fixed the number of voxels rather than the level of the correlations that may fluctuate across different datasets. The time course of each voxel and the spatial pattern of each time point were then normalized to a zero mean and unit variance.

4.1.3. Comparison of SRC and SRC-AVE. The first group of datasets was used to compare the performances of SRC and SRC-AVE. Three-class classifiers of SRC and SRC-AVE were trained from the training data (the first run) and applied to the testing data (the second run). For each subject in each group, the accuracy was calculated at each noise level using the ratio between the number of testing samples that were correctly classified and the total number of testing samples. The mean accuracy of each classifier across the 12 subjects was obtained at each noise level for each group of datasets.

4.1.4. Comparison of the Semisupervised Learning Methods. Both the first and second groups of datasets were used to investigate the performances of semiSRC-AVE in the case of different noise levels and cross-decoding. Because the advantage of SRC-AVE over SRC in fMRI-based decoding was demonstrated in the above section, only SRC-AVE was used to be compared with the semisupervised learning method in the following simulated and real fMRI experiments. Two-class (tasks A and B) and three-class SRC-AVE, semiSRC-AVE, naïve semiSRC-AVE, RSE-OLDC, and RSE-OSRC-AVE

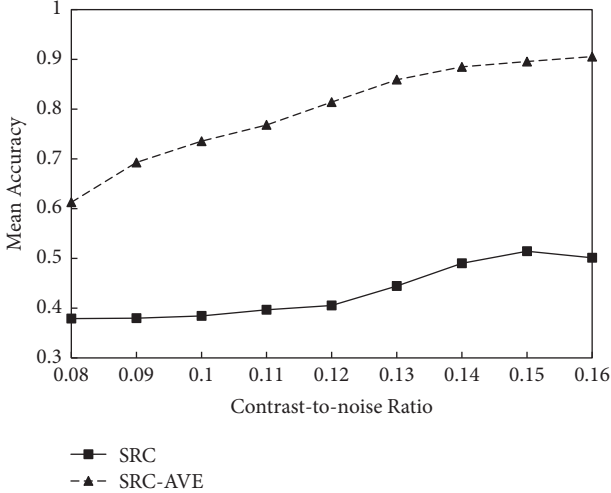


FIGURE 2: The mean classification accuracies of SRC and SRC-AVE at various CNR levels.

classifiers were trained from the training data (the first run) and applied to the testing data (the second run). The mean accuracy of each classifier across the 12 subjects was obtained at each noise level for each group of datasets. To examine the difference of the classification accuracies between the proposed semiSRC-AVE and the other four methods, the nonparametric Wilcoxon signed rank tests for paired samples were performed. Moreover, the computation time of each three-class classification for the first group of dataset was recorded to compare the time efficiency of all the five methods. The mean time across 12 subjects of all noise levels was calculated.

4.1.5. Determination of Parameter α in SemiSRC-AVE. Parameter α was set to 1 in the first group of datasets because the training and testing data were from the same tasks. For the second group of datasets that used different tasks in the training and testing data, the optimal value of parameter α was determined using the simulated datasets. The three-class semiSRC-AVE classifiers with different α values were trained using each subject's training data in the second group. Parameter α was varied from 0.5 to 1 with an increment of 0.1. For each α , the mean accuracy across all subjects was obtained for each noise level, and then the mean accuracy across all noise levels was obtained. The α value with the highest accuracy was selected as the optimal value for the datasets with different training and testing tasks.

4.2. Results of Simulated Experiments

4.2.1. Comparison of SRC and SRC-AVE. Figure 2 shows the mean accuracies of SRC-AVE method compared with those of the conventional SRC at all the CNR levels. The mean accuracies of the two methods increased as the CNR levels increased (see Figure 2). The classification accuracies of SRC are much lower than those of SRC-AVE at all the noise levels.

4.2.2. Comparison of the Semisupervised Learning Methods. Figures 3(a)-3(b) show the mean accuracy of SRC-AVE and

the four semisupervised methods at different CNR levels for the first group of simulated datasets. For the three-class classification, RSE-OLDC showed the worst performance, and semiSRC-AVE showed the best performance at all noise levels (see Figure 3(a)). SemiSRC-AVE showed significantly higher accuracy than SRC-AVE, RSE-OSRC-AVE, and RSE-OLDC at most noise levels and significantly higher accuracy than naïve semiSRC-AVE at the middle noise levels. For the two-class classification, the accuracy of RSE-OLDC was the lowest, while the performances of semiSRC-AVE, RSE-OSRC-AVE, and naïve semiSRC-AVE showed slight differences. The accuracies of SRC-AVE were lower than those of semiSRC-AVE, RSE-OSRC-AVE, and naïve semiSRC-AVE at most noise levels (see Figure 3(b)).

Figures 3(c)-3(d) show the performances of the five classifiers for cross-decoding the second group of simulated datasets with different training and testing tasks. For the three-class classification, semiSRC-AVE produced the highest accuracy while RSE-OLDC produced the lowest accuracy among the five methods (see Figure 3(c)). SemiSRC-AVE showed significantly higher accuracy than SRC-AVE, RSE-OSRC-AVE, and RSE-OLDC at most noise levels and significantly higher accuracy than naïve semiSRC-AVE at the middle noise levels. For the two-class classification, the performance of RSE-OLDC remained the worst, while the performances of semiSRC-AVE, RSE-OSRC-AVE, and naïve semiSRC-AVE only showed slight differences (see Figure 3(d)). The semiSRC-AVE significantly outperformed supervised-learning SRC-AVE at most noise levels. In contrast to the datasets with the same training and testing tasks, the accuracy of SRC-AVE was reduced to a larger extent than that of semiSRC-AVE for cross-decoding the datasets with different training and testing tasks (see Figure 3).

4.2.3. Determination of Parameter α in SemiSRC-AVE. For cross-decoding the dataset with different training and testing tasks, the mean accuracies of semiSRC-AVE using six different α values are presented in Figure 3(e). It can be seen that the mean accuracy was the highest when parameter α was set to 0.7. Therefore, 0.7 was used as the optimal value of parameter α in cross-decoding the simulated and real fMRI datasets with different training and testing tasks.

4.2.4. Time Efficiency Analysis. Table 1 lists the computation time of the five three-class classifiers for the first group of simulated datasets. The computation time of semiSRC-AVE was close to that of supervised-learning classifier SRC-AVE. RSE-OSRC-AVE, and RSE-OLDC took much more computation time than SRC-AVE, semiSRC-AVE, and naïve semiSRC-AVE.

4.3. Real fMRI Experiment. The real fMRI data used in this study were the same as those used in our previous study [29]. For readability, the main points are repeated here.

4.3.1. Datasets. Fourteen right-handed college students (age: 22.2 ± 1.9 years, eight females) participated in this study. The fMRI data were acquired using a 3-T Siemens scanner

TABLE 1: Mean computation time of the five three-class classifiers for the simulated datasets.

	SRC-AVE	SemiSRC-AVE	RSE-OSRC-AVE	Naïve semiSRC-AVE	RSE-OLDC
Time (second)	3.55	5.83	46.70	5.88	30.87

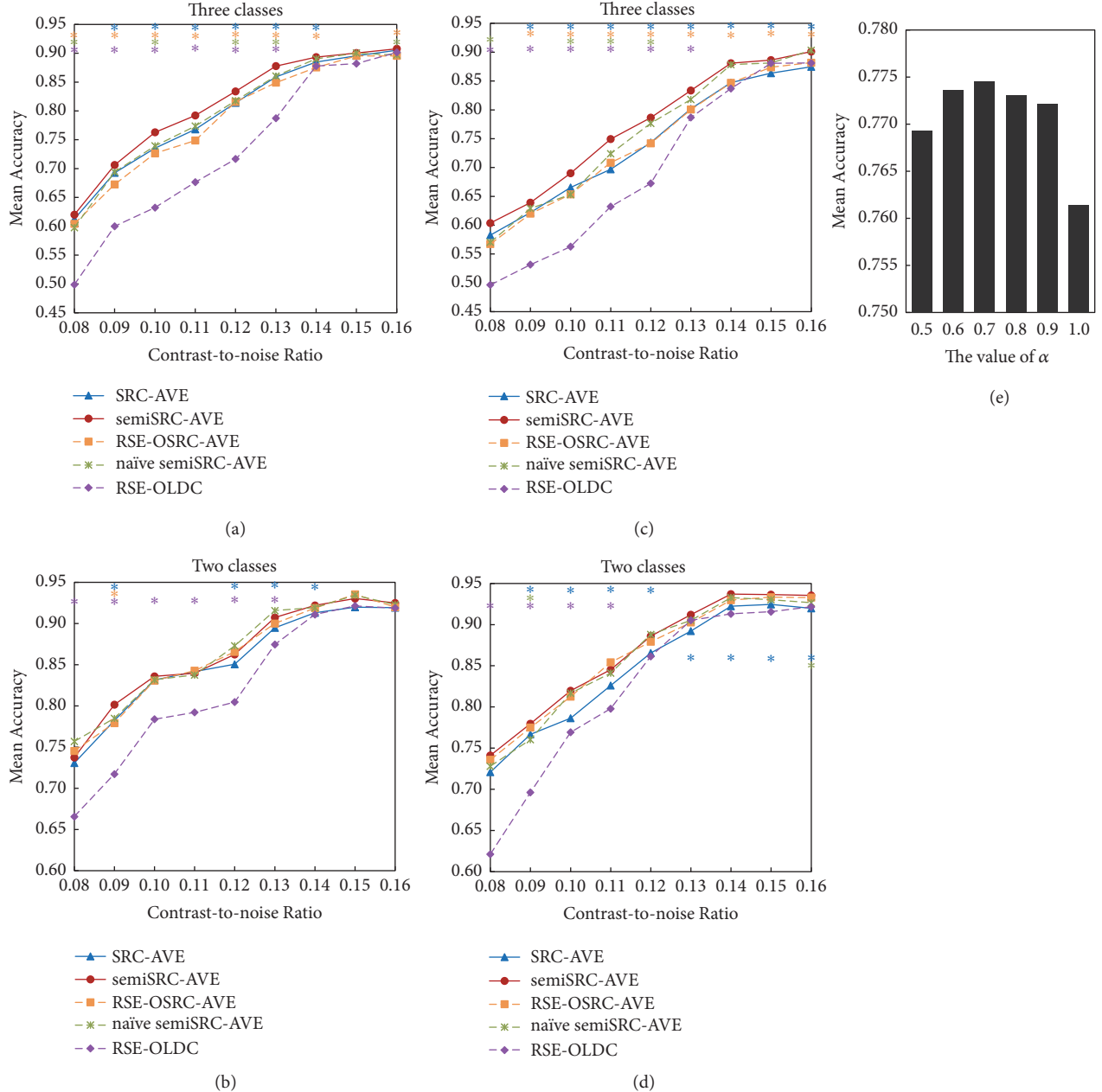


FIGURE 3: Mean accuracies of SRC-AVE, semiSRC-AVE, naïve semiSRC-AVE, RSE-OLDC, and RSE-OSRC-AVE classifiers. (a) Three-class performances of the simulated datasets with the same training and testing tasks. (b) Two-class performances of the simulated datasets with the same training and testing tasks. (c) Three-class performances of the simulated datasets with different training and testing tasks. (d) Two-class performances of the simulated datasets with different training and testing tasks. (e) Determination of parameter α in semiSRC-AVE. The asterisk * represents $p < 0.05$. The color of asterisk indicates the comparison between semiSRC-AVE and the method having the same color as the asterisk in each panel.

equipped for echo planar imaging (EPI) at the Brain Imaging Center of Beijing Normal University (TR = 2000 ms; TE = 30 ms; 32 slices; voxel size = $3.125 \times 3.125 \times 3.84$ mm; flip angle (FA) = 90°; FOV = 190×200 cm). In addition, a high-resolution, three-dimensional T1-weighted structural image was acquired (TR = 2530 ms; TE = 3.39 ms; 128 slices; FA = 7°; resolution = $1 \times 1 \times 1.33$ mm).

The experiment was conducted in a block design and consisted of eight runs. Each run included four 24 s task blocks that were alternated with five 12 s resting blocks. Visual stimuli belonging to four categories (i.e., house, face, car, and cat) corresponded to the four tasks in each run and were separately displayed for 500 ms, followed by a 1500 ms blank screen.

The data preprocessing was performed using Statistical Parametric Mapping (SPM8) (<http://www.fil.ion.ucl.ac.uk/spm/software/spm8/>). For each subject, the first three volumes of each run were removed due to the instability of the initial scanning of each run. The functional images of each subject were realigned to correct for head motion, spatially normalized into the standard Montreal Neurological Institute (MNI) template space, resliced into $3 \times 3 \times 4$ mm³ voxels, and spatially smoothed using an 8 mm full-width-at-half-maximum (FWHM) Gaussian kernel.

4.3.2. Comparison of Classifiers

(a) *Datasets with the Same Training and Testing Tasks.* A generalized linear model (GLM) was applied to each subject's training data to estimate the brain regions that were activated by each task using SPM8. The significance level was set as $p < 0.001$ and was uncorrected. A brain mask that included the fusiform gyrus, inferior temporal gyrus, inferior occipital gyrus, and middle occipital gyrus was generated using the WFU Pickatlas toolbox (<http://www.fmri.wfubmc.edu>). The union of the voxels that were activated by each task within the mask was selected as features. The testing data used the same features as the training data. For each dataset, the linear drift was removed using the `spm_detrend` function in SPM8. The time series of each feature and the spatial pattern of each scan were normalized to a zero mean and unit variance.

For each subject, a twofold cross validation was performed. In the first fold, the first four runs were used as the training runs, and the last four runs were used as the testing runs, and vice versa in the second fold. Four-class, three-class, and two-class classifiers of SRC-AVE, semiSRC-AVE, naïve semiSRC-AVE, RSE-OLDC, and RSE-OSRC-AVE were trained from each subject's training data separately. Each classifier was applied to each test volume to determine the task state. The mean accuracy across the 14 participants in the twofold was obtained for each classifier. To examine the difference in the classification accuracies between any two methods, the nonparametric Wilcoxon signed rank tests for paired samples were performed. For each method, the computation time of the four-class classification was recorded and the mean time across the 14 subjects was calculated.

(b) *Cross-Decoding Datasets with Different Training and Testing Tasks.* To further explore the performance of

semiSRC-AVE for cross-decoding, we regenerated the training and testing datasets. It should be noted that cat and human face are animate objects with sense organs while house and car are inanimate objects. Therefore, the volumes of the house and cat tasks in eight runs consisted of the training datasets, and the volumes of the car and face tasks in eight runs consisted of the testing datasets for each subject. The GLM was applied to the training data, and any voxels that were activated by at least one of the two tasks (i.e., house and cat) within the mask were selected as features. After SRC-AVE, semiSRC-AVE, naïve semiSRC-AVE, RSE-OLDC, and RSE-OSRC-AVE classifiers were trained from the training samples, they were applied to the testing volumes to predict their task states (car versus face). The mean accuracy of each classifier across the 14 subjects was obtained. Moreover, we also performed classification by using the volumes of the car and face tasks as the training data and the volumes of the house and cat tasks as the testing data. The feature selection and classifications were performed in the same way as described above. The nonparametric Wilcoxon signed rank tests for paired samples were performed to examine the differences between any two methods.

4.4. Results of Real fMRI Experiment

4.4.1. Comparison of Classifiers

(a) *Datasets with the Same Training and Testing Tasks.* Figures 4(a)–4(c) display the mean accuracies of the one four-class, four three-class, and six two-class classifications of SRC-AVE and the four semisupervised learning methods. SemiSRC-AVE showed the highest accuracy in most cases, and RSE-OLDC showed the lowest accuracy in all cases among the five methods. In contrast to SRC-AVE, semiSRC-AVE produced a significantly higher accuracy for the four-class classification, three three-class classifications, and one two-class classification. No significant differences were found between the performances of naïve semiSRC-AVE/RSE-OSRC-AVE and SRC-AVE for all classifications. Moreover, the accuracy of semiSRC-AVE was significantly higher than that of RSE-OSRC-AVE for house versus car versus cat, face versus cat versus car, and house versus face and significantly higher than that of naïve semiSRC-AVE for house versus car versus cat and face versus cat versus car.

(b) *Cross-Decoding Datasets with Different Training and Testing Tasks.* Figures 4(d)–4(e) show the results of the two-class classifications of SRC-AVE and the four semisupervised learning methods for cross-decoding datasets with different training and testing tasks. When the volumes of the house and cat tasks were used as the training data, the three semisupervised learning methods, including semiSRC-AVE, naïve semiSRC-AVE, and RSE-OSRC-AVE, produced significantly higher accuracies compared to that of SRC-AVE (see Figure 4(d)). The accuracy of RSE-OLDC was significantly lower than those of the other four methods. When the volumes of the car and face tasks were used as the training data, semiSRC-AVE and RSE-OSRC-AVE showed a significantly higher performance than that of SRC-AVE, and

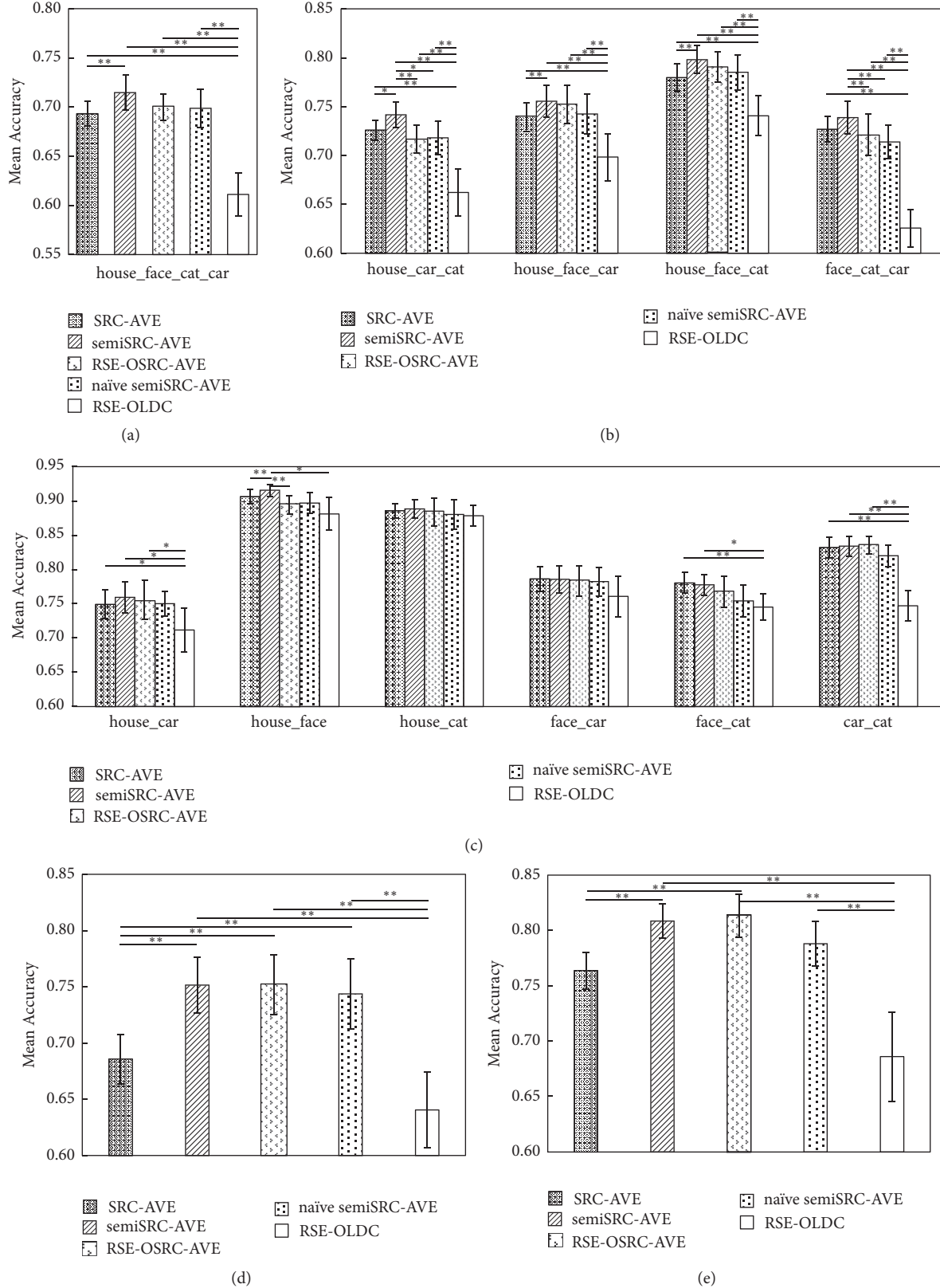


FIGURE 4: Mean accuracies of real fMRI data with same (a–c) and different (d–e) training and testing tasks using the SRC-AVE, semiSRC-AVE, naïve semiSRC-AVE, RSE-OLDC, and RSE-OSRC-AVE classifiers. (a) Two-class classifications. (b) Three-class classifications. (c) Four-class classifications. (d) Training data consisting of house and cat tasks. (e) Training data consisting of face and car tasks. The symbols “**” represent $p < 0.05$ and the symbol “*” represents $p < 0.1$.

TABLE 2: Computation time of five classifiers for real fMRI datasets.

	SRC-AVE	SemiSRC-AVE	RSE-OSRC-AVE	Naïve semiSRC-AVE	RSE-OLDC
Time (second)	2.30	2.71	17.57	3.26	7.90

RSE-OLDC showed a significantly worse performance than those of the other four methods (see Figure 4(e)).

4.4.2. Time Efficiency Analysis. Table 2 presents the mean computation time of the five four-class classifiers for the real fMRI datasets. The computation time of semiSRC-AVE was close to that of SRC-AVE and was less than that of RSE-OSRC-AVE and RSE-OLDC.

5. Discussion

The present study proposed the semisupervised learning semiSRC-AVE method to improve the decoding performance of SRC. Our major findings are as follows: (1) the semiSRC-AVE method can significantly improve the performance of SRC-AVE, particularly for cross-decoding; and (2) in contrast to RSE-OSRC-AVE, naïve semiSRC-AVE, and RSE-OLDC, semiSRC-AVE method shows better performance for multiclass classification and comparable performance for two-class classification.

SRC exhibited state-of-the-art classification performances in previous studies of image classification and recognition [3]. However, in this study, SRC produced a very low classification accuracy when it was applied to the fMRI data. There are two possibilities that may result in the low performance of SRC for fMRI-based decoding. One possibility is the complicated and high noises in the fMRI data. Generally, fMRI data contain various noises, such as thermal noise, system noise, motion and physiological noise, non-task-related neural variability, and behavioral and cognitive variability [29]. Signals in fMRI data are much weaker than noises. Moreover, behavioral and cognitive variability may lead to changes in arousal and attention over time. Evoked brain activity may change in each trial, even in the same types of trials. Another possibility may be attributed to the hemodynamic response. After the stimulus onset, the hemodynamic response exhibits an initial dip, rises to a peak value after approximately 6 seconds, and then falls to the baseline level [29]. There is a delay between the peak and the stimulus onset, indicating that the initial volumes of each task block may show very different brain activity patterns than the volumes in the middle of the blocks, although the volumes in the same task blocks respond to the same type of stimulus. Both the noises and hemodynamic responses can result in large variabilities in the brain activity that is evoked by each trial. For the sparse representation model, testing sample y is assumed to be linearly represented by the training samples of the same class. Because of the high variability in the training and testing samples of the same class in fMRI data, the testing samples cannot be well represented by the training samples and coefficient vector x may not be very sparse. Accordingly, SRC does not perform well in decoding brain states from fMRI data.

The results of the simulated data showed that SRC-AVE had a much better performance than SRC. It should be noted that the test samples are generally represented by the training samples from the same class with larger positive coefficients and smaller negative coefficients than the training samples from the other classes. Thus, the average of all positive and negative coefficients can be used as a criterion to determine the testing samples, which is consistent with the previous study that demonstrated that class-specific average sparse coefficients were useful to improve the performance of classification [20]. Moreover, our results further indicated that the average coefficient worked better than the reconstruction error for SRC in fMRI-based decoding.

Both the simulated and real fMRI datasets indicated that the proposed semiSRC-AVE effectively improved the performance of SRC-AVE, particularly for the multiclass classifications. SRC-AVE method used fixed training dataset while semiSRC-AVE gradually updated training dataset using the new testing samples with high confidence. The performance of SRC-AVE was easily affected by the insufficient labeled training samples because limited training dataset tended to increase the generalization error of classifiers. In contrast, the performance of semiSRC-AVE was improved due to gradually enlarged training dataset. Meanwhile, the distance between the predicted class and the other classes was calculated to measure the confidence of the predicated label of each test sample for semiSRC-AVE. The threshold of the confidence was determined by the previous testing samples rather than a fixed value. Because the threshold was adaptive to the changes of the testing samples, it was helpful to the selection of the testing samples with high confidence. The results indicated that the selected testing samples using the proposed strategy were reliable and contributed to the improvement of semiSRC-AVE.

For cross-decoding, compared to SRC-AVE, the advantages of semiSRC-AVE were more prominent. Because the training and testing samples were not entirely from the same distribution, the testing samples cannot be well represented by the training data, which may greatly affect the performance of SRC-AVE. For semiSRC-AVE, the training dataset was updated by the testing data. The dictionary that was adaptive to the testing data represented the testing samples better than the fixed dictionary. Accordingly, semiSRC-AVE worked much better than SRC-AVE when the training and testing tasks were different. In contrast to SRC-AVE, semiSRC-AVE showed better generalization to novel stimuli or tasks.

Among the four semisupervised learning methods, RSE-OLDC showed the worst performance and semiSRC-AVE showed the best performance in both the simulated and real fMRI experiment. The worst performance of RSE-OLDC may be attributed to the worse performance of LDC than SRC-AVE. In contrast to the naïve semiSRC-AVE and RSE-OSRC-AVE, the semiSRC-AVE showed better performance

for multiclass classification and comparable performance for the two-class classification. In contrast to multiclass classification, two-class classification generally has higher prediction accuracy and produces more reliable predicated labels of the testing samples. Therefore, the confidence determination for the testing samples may have a minor effect on the two-class classification of the semisupervised learning methods, which possibly resulted in the comparable performance of the naive semiSRC-AVE and semiSRC-AVE in the two-class classification. In contrast, the confidence determination of semiSRC-AVE played an important role in selecting reliable testing samples to update the dictionary in the multiclass classification. Thus, semiSRC-AVE outperformed naïve SRC in the three-class classification. Moreover, the results also indicated that the confidence determination strategy of semiSRC-AVE was simpler, more time-saving, and more efficient compared to the random subspace ensemble strategy of RSE-OSRC-AVE.

It should be noted that there is a balance between the update accuracy and the number of updated samples. If the threshold of the confidence determination is increased to improve the update accuracy, the number of updated samples will be reduced and vice versa. The small number of updated samples may only have a slight impact on the classifiers. It is critical to maintain a balance between the accuracy and the proportion of updates for semisupervised learning. We set parameter α to adjust the threshold for different types of datasets. Our simulated and real fMRI datasets indicated that a threshold with $\alpha = 1$ worked well for datasets with the same training and testing classes. For certain specific datasets, properly adjusting parameter α may achieve better results. For cross-decoding, the amount of updated samples becomes more important due to the lack of test-like samples in training dataset. Therefore, parameter α was set to 0.7, which was demonstrated to be the optimal value by cross-decoding the simulated data with different training and testing tasks in the study. The lowered parameter α allowed more testing data to update the training data. Both our simulated and real fMRI experiments indicated that the optimal value 0.7 was good for data with different training and testing classes.

6. Conclusion

In this study, we demonstrated the robustness and feasibility of the semisupervised learning semiSRC-AVE using both simulated and real fMRI data. The results indicated that semiSRC-AVE showed significantly better performance than SRC-AVE. In addition, semiSRC-AVE performed better than naïve semiSRC-AVE, RSE-OSRC-AVE, and RSE-OLDC for multiclass classifications. For the two-class classification, semiSRC-AVE did not show prominent advantages over the other three semisupervised learning methods. Therefore, it is essential to further investigate the optimal update strategy that is suitable to the two-class classification in the future studies. Moreover, the proposed update strategy in this study can be easily extended to the other supervised-learning classifiers.

Data Availability

The datasets used and analysed during the current study are available from the corresponding author on reasonable request.

Consent

All participants gave written consent according to the guidelines set by the MRI center of Beijing Normal University.

Ethical Approval

The experiment in this study was approved by the Institutional Review Board (IRB) of the State Key Laboratory of Cognitive Neuroscience and Learning in Beijing Normal University (IRB00005903). All experimental procedures were carried out in accordance with the approved guidelines and regulations.

Conflicts of Interest

The authors declare that there are no conflicts of interest regarding the publication of this article.

Acknowledgments

The authors wish to thank Dr. Hui Wu and Dr. Litao Zhu for technical assistance with real fMRI data acquisition. This work is supported by Key Program of National Natural Science Foundation of China [Grant no. 61731003], the National Natural Science Foundation of China [Grant nos. 61671067, 61473044], the Interdisciplinary Research Funds of Beijing Normal University, the Fundamental Research Funds for the Central Universities [Grant no. 2017XTCX04], and the Funds for International Cooperation and Exchange of the National Natural Science Foundation of China [Grant no. 61210001].

References

- [1] J. V. Haxby, A. C. Connolly, and J. S. Guntupalli, "Decoding neural representational spaces using multivariate pattern analysis," *Annual Review of Neuroscience*, vol. 37, pp. 435–456, 2014.
- [2] K. A. Norman, S. M. Polyn, G. J. Detre, and J. V. Haxby, "Beyond mind-reading: multi-voxel pattern analysis of fMRI data," *Trends in Cognitive Sciences*, vol. 10, no. 9, pp. 424–430, 2006.
- [3] J. Wright, A. Y. Yang, A. Ganesh, S. S. Sastry, and Y. Ma, "Robust face recognition via sparse representation," *IEEE Transactions on Pattern Analysis and Machine Intelligence*, vol. 31, no. 2, pp. 210–227, 2009.
- [4] K. Huang and S. Aviyente, "Sparse representation for signal classification," in *Proceedings of the NIPS*, pp. 609–616, Vancouver, Canada, December 2006.
- [5] J. Mairal, F. Bach, J. Ponce, G. Sapiro, and A. Zisserman, "Supervised dictionary learning," in *Proceedings of the 23rd Annual Conference on Neural Information Processing Systems (NIPS '09)*, pp. 1033–1040, Vancouver, Canada, December 2009.
- [6] S. Song, Z. Zhan, Z. Long, J. Zhang, and L. Yao, "Comparative study of SVM methods combined with voxel selection for object

- category classification on fMRI data," *PLoS ONE*, vol. 6, no. 2, Article ID e17191, 2011.
- [7] D. D. Cox and R. L. Savoy, "Functional magnetic resonance imaging (fMRI) "brain reading": detecting and classifying distributed patterns of fMRI activity in human visual cortex," *NeuroImage*, vol. 19, no. 2, pp. 261–270, 2003.
- [8] K. Friston, C. Chu, J. Mourão-Miranda et al., "Bayesian decoding of brain images," *NeuroImage*, vol. 39, no. 1, pp. 181–205, 2008.
- [9] H. Jang, S. M. Plis, V. D. Calhoun, and J. H. Lee, "Task-specific feature extraction and classification of fMRI volumes using a deep neural network initialized with a deep belief network: Evaluation using sensorimotor tasks," *Neuroimage*, p. 145, 2016.
- [10] C. Rosenberg, M. Hebert, and H. Schneiderman, "Semi-supervised self-training of object detection models," in *Proceedings of the Application of Computer Vision*, vol. 1, IEEE, Breckenridge, CO, USA, 2005.
- [11] M. Belkin, P. Niyogi, and V. Sindhwani, "Manifold regularization: A geometric framework for learning from labeled and unlabeled examples," *Journal of Machine Learning Research*, vol. 7, pp. 2399–2434, 2006.
- [12] X. Zhu and A. B. Goldberg, "Introduction to semi-supervised learning," in *Synthesis Lectures on Artificial Intelligence and Machine Learning*, vol. 3, pp. 1–130, Morgan & Claypool, 2009.
- [13] A. Blum and T. Mitchell, "Combining labeled and unlabeled data with co-training," in *Proceedings of the eleventh annual conference on Computational learning theory*, pp. 92–100, ACM, 1998.
- [14] T. Joachims, "Transductive inference for text classification using support vector machines," in *ICML*, vol. 668, pp. 200–209, Springer, 1999.
- [15] A. Fujino, N. Ueda, and K. Saito, "Semisupervised learning for a hybrid generative/discriminative classifier based on the maximum entropy principle," *IEEE Transactions on Pattern Analysis and Machine Intelligence*, vol. 30, no. 3, pp. 424–437, 2008.
- [16] I. Triguero, S. García, and F. Herrera, "Self-labeled techniques for semi-supervised learning: taxonomy, software and empirical study," *Knowledge and Information Systems*, vol. 42, no. 2, pp. 245–284, 2015.
- [17] Y. Shin, S. Lee, M. Ahn, H. Cho, S. C. Jun, and H.-N. Lee, "Simple adaptive sparse representation based classification schemes for EEG based brain-computer interface applications," *Computers in Biology and Medicine*, vol. 66, pp. 29–38, 2015.
- [18] C. O. Plumpton, L. I. Kuncheva, N. N. Oosterhof, and S. J. Johnston, "Naive random subspace ensemble with linear classifiers for real-time classification of fMRI data," *Pattern Recognition*, vol. 45, no. 6, pp. 2101–2108, 2012.
- [19] C. O. Plumpton, "Semi-supervised ensemble update strategies for on-line classification of fMRI data," *Pattern Recognition Letters*, vol. 37, no. 1, pp. 172–177, 2014.
- [20] J. Zou, W. Li, and Q. Du, "Sparse Representation-Based Nearest Neighbor Classifiers for Hyperspectral Imagery," *IEEE Geoscience and Remote Sensing Letters*, vol. 12, no. 12, pp. 2418–2422, 2015.
- [21] J. R. Quinlan, *C4.5 programs for machine learning*, Morgan Kaufmann Publishers, San Francisco, CA, USA, 1993.
- [22] J. C. Platt, "Probabilistic outputs for support vector machines and comparisons to regularized likelihood methods," *Advances in Large Margin Classifiers*, vol. 10, no. 4, pp. 61–74, 2000.
- [23] T. Iju, S. Endo, K. Yamada, N. Toma, and Y. Akamine, "Estimating age on twitter using self-training semi-supervised svm," *Journal of Robotics, Networking and Artificial Life*, vol. 3, no. 1, p. 24, 2016.
- [24] E. J. Candes, J. K. Romberg, and T. Tao, "Stable signal recovery from incomplete and inaccurate measurements," *Communications on Pure and Applied Mathematics*, vol. 59, no. 8, pp. 1207–1223, 2006.
- [25] M. A. T. Figueiredo, R. D. Nowak, and S. J. Wright, "Gradient projection for sparse reconstruction: application to compressed sensing and other inverse problems," *IEEE Journal of Selected Topics in Signal Processing*, vol. 1, no. 4, pp. 586–597, 2007.
- [26] Z.-H. Zhou and M. Li, "Semi-supervised learning by disagreement," *Knowledge and Information Systems*, vol. 24, no. 3, pp. 415–439, 2010.
- [27] E. B. Erhardt, E. A. Allen, Y. Wei, T. Eichele, and V. D. Calhoun, "SimTB, a simulation toolbox for fMRI data under a model of spatiotemporal separability," *NeuroImage*, vol. 59, no. 4, pp. 4160–4167, 2012.
- [28] N. Kriegeskorte, "Pattern-information analysis: From stimulus decoding to computational-model testing," *NeuroImage*, vol. 56, no. 2, pp. 411–421, 2011.
- [29] C. Zhang, S. Song, X. Wen, L. Yao, and Z. Long, "Improved sparse decomposition based on a smoothed L0 norm using a Laplacian kernel to select features from fMRI data," *Journal of Neuroscience Methods*, vol. 245, pp. 15–24, 2015.

Research Article

Assessment of Multivariate Neural Time Series by Phase Synchrony Clustering in a Time-Frequency-Topography Representation

M. A. Porta-Garcia , R. Valdes-Cristerna , and O. Yanez-Suarez 

Neuroimaging Research Laboratory, Electrical Engineering Department, Edificio T-227, Universidad Autónoma Metropolitana Iztapalapa, Av. San Rafael Atlixco 186, Col. Vicentina, Del. Iztapalapa, 09340 Ciudad de México, Mexico

Correspondence should be addressed to M. A. Porta-Garcia; maporta@gmail.com

Received 25 December 2017; Accepted 30 January 2018; Published 21 March 2018

Academic Editor: Victor H. C. de Albuquerque

Copyright © 2018 M. A. Porta-Garcia et al. This is an open access article distributed under the Creative Commons Attribution License, which permits unrestricted use, distribution, and reproduction in any medium, provided the original work is properly cited.

Most EEG phase synchrony measures are of bivariate nature. Those that are multivariate focus on producing global indices of the synchronization state of the system. Thus, better descriptions of spatial and temporal local interactions are still in demand. A framework for characterization of phase synchrony relationships between multivariate neural time series is presented, applied either in a single epoch or over an intertrial assessment, relying on a proposed clustering algorithm, termed Multivariate Time Series Clustering by Phase Synchrony, which generates fuzzy clusters for each multivalued time sample and thereupon obtains hard clusters according to a circular variance threshold; such cluster modes are then depicted in Time-Frequency-Topography representations of synchrony state beyond mere global indices. EEG signals from P300 Speller sessions of four subjects were analyzed, obtaining useful insights of synchrony patterns related to the ERP and even revealing steady-state artifacts at 7.6 Hz. Further, contrast maps of Levenshtein Distance highlight synchrony differences between ERP and no-ERP epochs, mainly at delta and theta bands. The framework, which is not limited to one synchrony measure, allows observing dynamics of phase changes and interactions among channels and can be applied to analyze other cognitive states rather than ERP versus no ERP.

1. Introduction

There is a growing interest among the neuroscientific community to unravel the intricate neural mechanisms involved in the broad integration of different brain structures, which enable the emergence of cognitive processes. Several studies conducted with electroencephalography (EEG) and magnetoencephalography (MEG) have provided evidence that supports the idea of neural synchronization intrinsic to mental tasks, with the fluctuating disposition of communication channels in the nervous system, especially between active regions in the brain [1–5].

In this regard, phase locking analysis of neural oscillations and other different measures of synchronization has gained attention, as several methods have been developed to provide a quantitative view of synchronism in brain sources and their behavior, estimating phase synchrony (PS) from different

perspectives, depending on the purpose of the study in question [6]. This same variety of methods and proposals causes lack of agreement in the terminology used to refer to all these measures. Roach and Mathalon have provided a wide review attempting to clarify this situation [7]. Thus, for the sake of following a standard of terms, descriptions of any PS measure will follow the referred publication.

In order to perform PS analysis, instantaneous phase information of EEG signals must be extracted. Most methods are based on wavelet analysis [6–10]. Another common technique besides wavelets for extracting instantaneous phase values from the analytical signal is the Hilbert transform. Analytic phase from wavelets or Hilbert transform has been shown to give almost same results as Short Time Fourier Transform adjusting the filter settings adequately [11, 12]. There are also other Time-Frequency (TF) decompositions used for obtaining phase information, such as Rihaczek

distribution, Empirical Mode Decomposition, sinusoidal quadrature filters, and Matching Pursuit [13–16].

In general, for the study of PS, it can be said that there are two main approaches: phase locking and phase coherence. The former refers to the event-related phase locking across trials regarding an event's onset over one electrode, that is, the Phase Locking Factor (PLF). If instantaneous phase angles between trials are closer to a uniform distribution over the unit circle, the PLF is close to zero; otherwise, it is close to one if instantaneous phase angles between trials are highly synchronized in the same direction over the unit circle. The latter approach, phase coherence, also called Phase Locking Value (PLV), or within the context, the *event-related phase coherence across trials*, evaluates consistency of phase differences between 2 electrodes across trials, also with values between 0 and 1. As the reader already noticed, each measure determines different types of PS; therefore, both measures can be complementary to each other [7].

Other types of measures, such as linear coherence or magnitude squared coherence, are not suitable to analyze PS; unlike PLF and PLV, both measures yield results weighted by magnitude, and the interpretation of these becomes unclear, since phase synchronization patterns and amplitude changes are not necessarily related to the same neural process [6–8]; Rosenblum demonstrated that PS of chaotic oscillators is possible, where bounded phase differences exist and variations of amplitude are chaotic and uncorrelated [17]. The Phase Cross-Coherence (PCC) eliminates amplitude information and produces a function of phase differences averaged across trials [6].

All PS measures mentioned above focus on the evaluation of intertrial phase consistency over an individual EEG channel or phase differences between signals from two recording sites, that is, providing only univariate or bivariate approaches. Nevertheless, the complete scenario involves a multichannel recording; thus a bivariate approach may not capture relevant information of all the dynamics and interactions of the full system [18, 19]. Thereupon, existing methods of multivariate synchronization analysis comprise even other metrics besides PS, based on different types of correlation measures. Correlation between probabilities of recurrence is used to measure PS, clearly distinguishing preseizure and seizure states of epileptic EEG [20, 21]. Based on Random-Matrix Theory (RMT), Osorio and Lai compute the average phase synchronization times (APSTs) among pairs of channels in order to construct a matrix, from which they use both the determinant and the eigenvalue spectra for assessing synchronization [22]. Li et al. presented another method based on RMT, using equal-time correlation instead of PS, and then the eigenvalue decomposition is used to calculate a global synchronization index that increases during epileptic seizures [23]. Mutlu et al. extend the concept of phase differences between two signals, mapping these differences onto an N -dimensional hyperspherical coordinate system; however, the authors later reported that Hyper-spherical Phase Synchrony (HPS) is dependent on how the phase differences are sorted, which is corrected with another hyperdimensional coordinate system [19, 24]. Alba et al. proposed a visualization system with multitoposcopic graphs

and Time-Frequency-Topography (TFT) maps for synchrony patterns, indicating increase, decrease, or an equal level of synchronization between pairs of electrodes with respect to a previous state, using different PS bivariate measures [15].

Some other approaches aim to improve the resolution of the TF decomposition used for extracting phase information. Aviyente and colleagues used a reduced interference distribution-Rihaczek (RID-Rihaczek) for computing PLV [25]. Subsequently, the authors extend their method to quantify all possible pairwise comparisons and analyze those interactions between electrodes through a graph clustering algorithm, which allows overlapping clusters, and each electrode has a “participation score” that reflects their significance in the formation of a cluster [26]. Previous works also conceive the idea of clustering with degrees of membership. Allefeld and Kurths addressed the multivariate synchronization as a mean-field cluster of oscillators that participate in different degrees, that is, how close an oscillator phase is close to a reference phase, which is determined by the circular mean of all oscillator phases [27]. Nevertheless, the single cluster assumption dismisses other possible cluster formations. Later, the authors made a generalization of the cluster analysis to correct this issue based on eigenvalue decomposition of a matrix containing indices of bivariate synchronization strength, associating each eigenvalue greater than one to a cluster [28]; however, the one-to-one correspondence between dominant eigenvectors and clusters is not always fulfilled [29].

Summarizing, multivariate methods help in perceiving overall synchronization patterns, providing a global index instead of matrices of bivariate comparisons [19]. Since many of these investigations focus on epilepsy studies, it makes sense to provide a general assessment of the synchronization state of the system with a crisp numerical value in order to distinguish seizure and preseizure conditions. Rather than a global index and aiming to characterize a broader variety of cognitive states, such as mental tasks for Brain-Computer Interface (BCI), the framework proposed in this article points to observing the dynamics of phase changes along multivariate neural time series over the TF plane and projecting their interactions in TFT maps.

The proposed clustering algorithm, Multivariate Time Series Clustering by Phase Synchrony (mCPS), establishes local relations by means of clusters of highly synchronized signals in each sample time, allowing exploring these phase associations through all samples searching for patterns of cluster formations. Additionally, our proposal also addresses an across-trials perspective. Thus, it can be said that the PS measure used in this work is more related to PLF (circular variance) rather than to phase coherence (consistency of phase differences), applied channel-wise. Haig et al. proposed a similar conception of PS, which lacks an automatized selection of synchronized signals via clustering [30].

Beyond yielding a PS measurement and a TFT portrayal, the framework also provides contrast maps of Levenshtein Distance (LD) as a metric for visual analysis and comparison of differences in PS patterns between different conditions (in this case, ERP and no-ERP epochs), as well as TF images of channels, highlighting which clusters of PS can be related

to the changes of power due to the ERP. While some of the methods mentioned before use clustering analysis, like [26], most of them are fuzzy clusters in short time windows and without topographic representation. The way mCPS is conceived requires hard clustering, as it will be further detailed.

2. Materials and Methods

2.1. Simulated EEG and Experimental Data. Several experiments were carried out with both synthetic and real EEG signals (sEEG and rEEG, resp.) in order to determine the extent to which our framework is capable of retrieving reliable and useful information (presented as clusters of electrodes) that allows establishing relationships between highly synchronized EEG channels and the brain activity of interest through time samples and over different bandwidths. The sEEG was built based on a linear mixing model of N_s independent sources $S = (s_1, s_2, \dots, s_{N_s})^T$, with a sampling frequency of 256 Hz, resulting in N_{ch} observed signals $C = (c_1, c_2, \dots, c_{N_{\text{ch}}})^T$. Contributions of every s_i ($i = 1, 2, \dots, N_s$) through the N discrete-time samples ($n = 1, 2, 3, \dots, N$) are weighted by the $N_{\text{ch}} \times N_s$ matrix W , which is determined by the inverse-square law of distances between C and S locations:

$$C = WS;$$

$$\begin{bmatrix} c_{1,n} \\ \vdots \\ c_{N_{\text{ch}},n} \end{bmatrix} = \begin{bmatrix} w_{1,1} & \cdots & w_{1,N_s} \\ \vdots & \ddots & \vdots \\ w_{N_{\text{ch}},1} & \cdots & w_{N_{\text{ch}},N_s} \end{bmatrix} \begin{bmatrix} s_{1,n} \\ \vdots \\ s_{N_s,n} \end{bmatrix}. \quad (1)$$

Spatial location of each electrode c_j ($j = 1, 2, \dots, N_{\text{ch}}$) corresponds to the basic 10–20 international system [32] over a unit sphere. The volume conduction of the EEG model was assumed to be homogeneous and isotropic. The complete sEEG record is constructed with 30 epochs of 3 seconds, each of them containing a simulated Visual Evoked Potential (VEP) centered at 1.5 s from the epoch onset (peak amplitude at 1500 ms and constant across trials). Equation (2) describes the construction of the VEP:

$$\text{VEP} = \frac{1}{\sqrt{2\pi}} e^{-((n-\mu)/\sigma^2)^2} \sin\left(\frac{2\pi f n}{N}\gamma\right), \quad (2)$$

where $f = 10 \text{ Hz}$, $\mu = 0.5N$, $\sigma^2 = 0.125N$, $\gamma = (N - 0.5n)/N$, and $n = 1, 2, 3, \dots, N$. Besides the VEP, sources S comprise three different types of noise components: (a) harmonics, which vary in amplitude, frequency of the sinusoidal oscillations, and initial phase and (b) white Gaussian and (c) colored Gaussian cgn noise. Localization (x, y, z) of S within the brain area of the model can be either a fixed position or a linear displacement or with rotational motion.

In order to assess the framework with rEEG, four subjects (S2, S5, S6, and S7) were selected from a record of P300 evoked potentials [33] using the P300 Speller proposed by Farwell and Donchin [34] (available at <http://bnci-horizon-2020.eu/database/data-sets>). The subjects were patients with

amyotrophic lateral sclerosis and were naive to BCI training. The authors recorded eight EEG signals according to 10-10 standard (Fz, Cz, Pz, Oz, P3, P4, PO7, and PO8) using active electrodes, referenced to the right earlobe and grounded to the left mastoid. EEG signal was digitized at 256 Hz and band-pass-filtered between 0.1 and 30 Hz. Subjects were required to spell seven predefined words of five characters each by controlling the P300 matrix speller. It should be mentioned that no extra preprocessing was performed over the data. The first three runs (15 trials in total) are described as “calibration runs” and runs 4–7 are the “testing runs” where participants were provided with feedback.

2.2. Clustering EEG Channels according to Circular Variance

2.2.1. Extraction of Phase Information. Given N_{ch} (for sEEG, $N_{\text{ch}} = 19$ and, for rEEG, $N_{\text{ch}} = 8$) signals, a TF decomposition is performed over the continuous EEG with predefined bandwidths at center frequencies:

$$f_k = e^{\ln(f_{\min}) + ((\ln(f_{\max}) - \ln(f_{\min}))/K)k}; \quad k = 1, 2, 3, \dots, K, \quad (3)$$

where $f_{\min} = 1$, $f_{\max} = 12 \text{ Hz}$, and $K = 12$ for both sEEG and rEEG. Such decomposition is carried out with a Continuous Wavelet Transform (CWT) at peak frequencies f_k from (3) with complex Morlet wavelets:

$$\Psi(n, f_k) = e^{i2\pi f_k t} e^{-n^2/2\varsigma^2}; \quad n = 1, 2, 3, \dots, N, \quad (4)$$

where $\varsigma = \varrho/2\pi f_k$ is the standard deviation of the Gaussian function used to make each Ψ and ϱ is the number of wavelet cycles (in this case, $\varrho = 4$). Then, the instantaneous phase is obtained from (5), using implementation of the four-quadrant inverse tangent:

$$\theta_j(n, f_k) = \arctan\left(\frac{\text{imag}(\Psi)}{\text{real}(\Psi)}\right); \quad j = 1, 2, \dots, N_{\text{ch}}. \quad (5)$$

2.2.2. Multivariate Time Series Clustering by Phase Synchrony (mCPS). Algorithm 1 explains how mCPS works, which is based on directional statistics to measure the degree of phase locking and formation of clusters. The circular spread in angular data can be computed with the magnitude of the so-called *mean resultant vector* \bar{R} [35]. Directional data (in this case, $\theta_j(n, f_k)$ of the N_{ch} signals) can be observed as points $x_j = (\cos \theta_j, \sin \theta_j)$ over the unit circle. Then, the Cartesian coordinates of the center of mass can be expressed as (A, B) , where

$$A = \frac{1}{N_{\text{ch}}} \sum_{j=1}^{N_{\text{ch}}} \cos \theta_j; \quad (6)$$

$$B = \frac{1}{N_{\text{ch}}} \sum_{j=1}^{N_{\text{ch}}} \sin \theta_j.$$

Therefore, $\bar{R} = \sqrt{A^2 + B^2}$. Magnitude of \bar{R} is close to 1 when EEG channels are highly phase-locked; it is close to zero otherwise. Porta-Garcia et al. presented an example using

```

    ▷  $K$ : total peak frequencies  $f_k$ 
    ▷  $N$ : number of discrete time EEG samples
    ▷  $N_{\text{ch}}$ : number of EEG channels
    ▷  $R$ : magnitude of mean resultant vector  $\bar{R}$ 
    ▷  $r$ : threshold value of  $R$ 

(1) for  $k \leftarrow 1$  to  $K$  do
(2)   for  $n \leftarrow 1$  to  $N$  do
(3)      $fC \leftarrow \text{CreateFuzzyClusters}(\theta_{1:N_{\text{ch}}}(n, f_k), r)$ 
(4)      $hC \leftarrow \text{ConvertToHardClusters}(fC)$ 
(5)   end for
(6) end for
(7) procedure CREATEFUZZYCLUSTERS ( $\theta, r$ )
(8)   for  $i \leftarrow 1$  to  $N_{\text{ch}} - 1$  do
(9)     Initialize new empty cluster  $C(i)$ 
(10)    Add electrode  $c(\theta_i)$  to  $C(i)$ 
(11)    for  $j \leftarrow i + 1$  to  $N_{\text{ch}}$  do
(12)      Compute  $R$  between  $c(\theta_i)$  and  $c(\theta_j)$ 
(13)      if  $R(i, j) > r$  then
(14)        Add electrode  $c(\theta_j)$  to  $C(i)$ 
(15)      end if
(16)    end for
(17)  end for
(18) return  $C$ 
(19) end procedure
(20) procedure CONVERTTOHARDCLUSTERS ( $C$ )
(21)    $C_{\text{intersect}} \leftarrow \text{Find clusters } C \text{ with intersections}$ 
(22)   for all  $C_{\text{intersect}}$  do
(23)     Compute  $R$ 
(24)      $C_{R_{\max}} \leftarrow C_{\text{intersect}}$  with maximum value of  $R$ 
(25)     Eliminate intersected elements from all clusters  $C_{\text{intersect}} \neq C_{R_{\max}}$ 
(26)   end for
(27) end procedure

```

ALGORITHM 1: Multivariate Time Series Clustering by Phase Synchrony (mCPS).

magnitude changes of vector \bar{R} over time in a determined group of EEG channels comparing two different conditions [36]. The functioning of mCPS over EEG channels according to circular variance is as follows.

Once $\theta_j(n, f_k)$ is retrieved for the entire EEG, the procedure `CreateFuzzyClusters` generates fC fuzzy clusters of electrodes for each time sample n and for each center frequency f_k . The threshold r ($0 < r < 1$) defines whether or not an electrode is assigned to a determined fC , and as fuzzy clusters consider intersections of cluster elements, the main task of the procedure `ConvertToHardClusters` is to obtain hard clusters hC by preserving clusters with higher value of r and proceed to eliminate intersections iteratively of the remaining fC in such a way that $hC_1 \cap hC_2 \cap \dots \cap hC_i = \emptyset$; $i | 1 \leq i \leq N_{\text{ch}}$. Therefore, the result of mCPS is a new $N_{\text{ch}} \times N$ matrix cEEG, containing the cluster labels to which each EEG channel belongs in each time sample n .

2.2.3. Cluster Labeling. Every run of mCPS is bounded for each time sample n , and an arbitrary numeric label is assigned to each cluster. Then, an example of generated clusters could be $hC_1 = \{\text{P3}, \text{P4}, \text{Oz}\}$ for $n = 1$ and $hC_2 = \{\text{P3}, \text{P4}, \text{Oz}\}$ for $n = 2$. In this case, numeric labels 1 and 2 do not provide

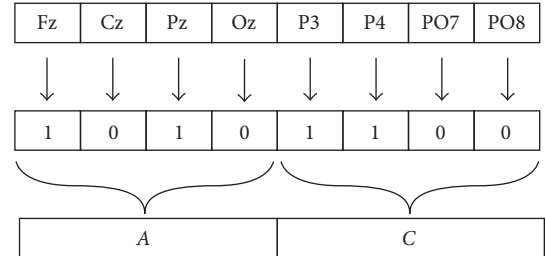


FIGURE 1: Example of hexadecimal cluster labeling for an 8-channel EEG array, where AC represents the cluster containing Fz, Pz, P3, and P4.

any useful information of cluster content. In order to establish a meaningful relationship that reflects that hC_1 and hC_2 are actually the same cluster, a labeling system was developed based on hexadecimal words that encode which electrode belongs to the cluster and then assign a specific color in a one-to-one relationship to represent clusters in a TFT map, which will be described further. In Figure 1, it can be observed that each hexadecimal digit corresponds to binary bits of electrode quartets, where digit 1 means that the electrode is

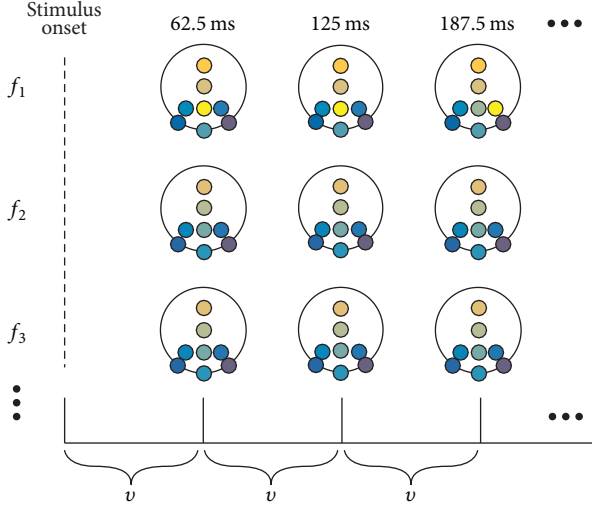


FIGURE 2: Depiction of how a TFT map is generated. Using the settings for the assessment of cEEG (sampling rate of 256 Hz), the size of each window is $v = 16$. Hence, each scalp map in the TFT map represents the cluster modes within the cEEG window of size v for each electrode.

assigned to a determined cluster if magnitude of \bar{R} is greater than threshold r . Therefore, a hexadecimal word of two digits encodes the cluster membership for eight EEG channels. As a consequence of this encoding system, a slightly different hue of color label should depict similarity between clusters, for example, a blue cluster containing electrodes P3, Pz, and P4 and a lighter blue cluster that only contains P3 and Pz. Hence, the matrix cEEG now has as elements the cluster labels of hexadecimal words.

2.2.4. Construction of Time-Frequency-Topography (TFT) Maps. To be able to condense the large amount of information obtained from mCPS and make it suitable for visual analysis, we used TFT maps for topographic representation of all hC yielded in previous steps. Some previous schemes of Time-Frequency-Topographic visualization can be found in literature [15, 37]. Then, the cEEG section that corresponds to the rEEG segment to be analyzed is windowed, displaying scalp maps with cluster modes of the cEEG windows of size v , which is specified in number of samples (Figure 2). The cluster modes for each channel are assigned only if the mode frequency is greater than threshold ρ . For both rEEG and sEEG, $\rho = 50\%$; this way, bimodal or multimodal results are avoided.

With regard to the rEEG, it should be mentioned that as the selected runs for analysis with our method were clustered separately, the color labels in a TFT map of ERP condition are the same as a TFT map of no ERP only if it is the same subject and same run; otherwise, this condition may not be satisfied, except for two cases: the color map is bounded between specific RGB values between dark blue and bright yellow, which corresponds with cluster with hexadecimal label “01” (only channel P8 is assigned) and cluster “FF” (all channels are assigned), respectively. Intermediate variations of label color depend on the amount of generated clusters along time.

2.2.5. Intertrial TFT (iTFT) Maps. An iTFT depicts hC modes across epochs. It can be seen as a TFT map containing intertrial cluster modes (ITCM) instead of computing cluster modes over a cEEG segment directly (Figure 3). Regarding the rEEG, for each run of the experimental protocol, the instantaneous phase is computed over the complete run and the clustering is performed before epoch segmentation. After these steps, ERP and no-ERP epochs are taken separately and their ITCM is computed in such a way that the most representative cluster formations over the ERP and no-ERP epochs are retrieved. For the rEEG case, the resultant iTFT map illustrates the most prevalent phase clustering patterns over 1000 ms (duration of trials) with a time window of size $v = 16$ (62.5 ms).

2.2.6. Levenshtein Distance (LD) and Complementary TF Maps. LD is included to sense relevant differences between ERP and no-ERP epochs. This measure can be defined as the minimum cost of transforming one string into another through a sequence of operations [38]:

$$\begin{aligned} \text{LD}(\Phi_1, \Phi_2) &= \min \{ \psi(T_{\Phi_1, \Phi_2}) \}; \\ \psi(T_{\Phi_1, \Phi_2}) &= \sum_{i=1}^l \psi(T_i), \end{aligned} \quad (7)$$

where Φ_1 and Φ_2 are strings constructed with characters $\phi_1, \phi_2, \dots, \phi_z$ of the same alphabet Γ and $T_{\Phi_1, \Phi_2} = \{T_1, T_2, \dots, T_l\}$ represents the set of edit operations to make $\Phi_1 = \Phi_2$, weighted by function $\psi \in \Re^+$. With $p \rightarrow q$ being a simple edit operation and λ being the null string, there are three types of transformations: insertions ($\lambda \rightarrow p$), substitutions ($p \rightarrow q$), and deletions ($q \rightarrow \lambda$). Adapted to our case, $\Gamma = \{"0", "1"\}$, $\psi = 1$, and Φ_1 and Φ_2 are binary cluster labels of same length; thus the only operation to perform is substitutions of characters. Since clusters labels encipher the membership of electrodes, the maximum LD should be equal to 8 for the extreme case of $\Phi_1 = "00000000"$ (which means that no cluster mode was assigned to any channel due to threshold ρ) and a cluster mode with all 8 electrodes within ($\Phi_2 = "11111111"$).

Furthermore, additional TF maps are generated from the CWT of each channel, which coupled with LD measures, and they help to observe findings in the mCPS information that could be associated with the changes of power due to the ERP over the time series. The LD distances are depicted in Time-Frequency-Levenshtein (TFL) maps.

2.2.7. Framework Pipeline. The complete framework pipeline is shown in Figure 4. Once the extraction of phase information of EEG in block a and mCPS is performed in block b , EEG clusters (cEEG) are labeled in block c and then segmented according to the acquisition protocol. For this particular case, condition 1 and condition 2 in Figure 4 correspond to ERP and no-ERP epochs, respectively. Important to notice, segmentation of cEEG occurs after the hexadecimal labeling (block c) in order to allow direct comparison between conditions in the iTFT maps, ensuring a one-to-one correspondence among color labels in the topographic scalp layouts of clusters and hexadecimal labels. Finally,

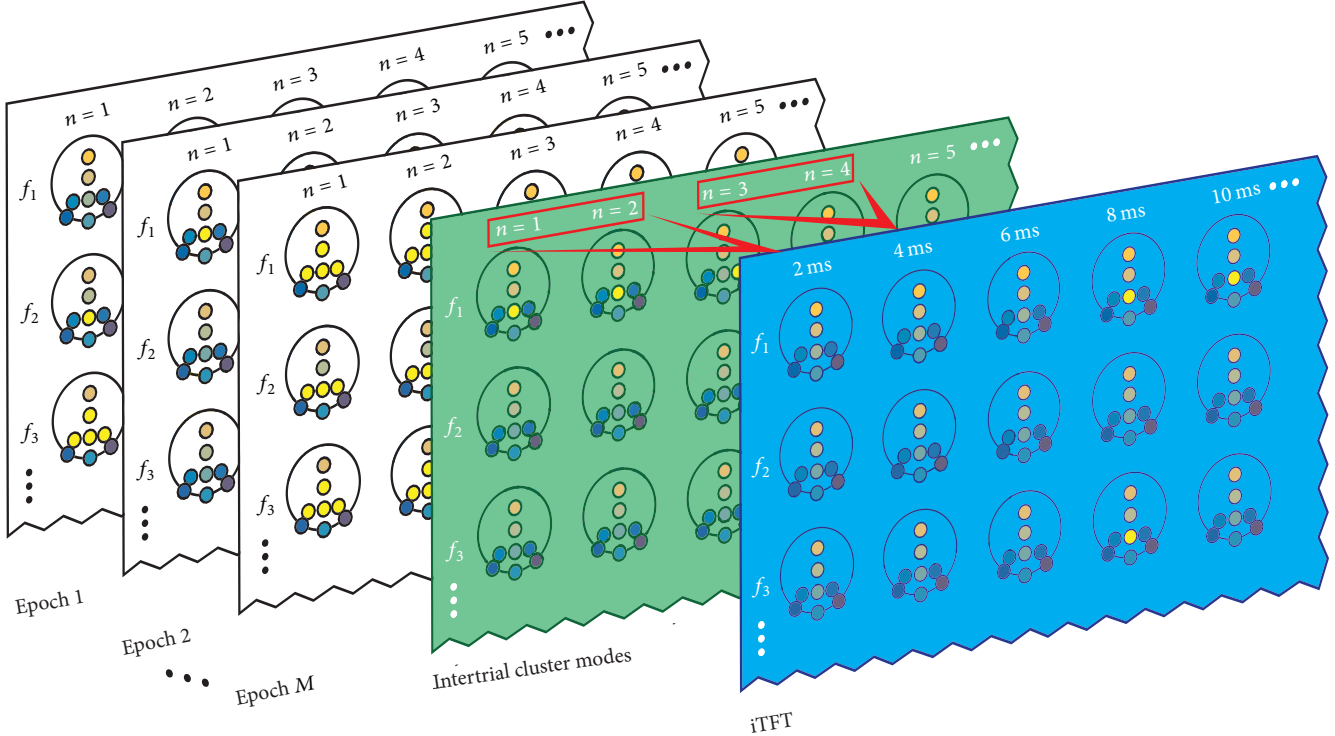


FIGURE 3: Depiction of how an iTFT map (blue background) is constructed. Following the same principle of a grand average for ERP (computing modes instead), the scalp maps in the green TFT map contain the ITCM of epochs $1, 2, \dots, M$. For illustration purposes only, let us consider the final step, that is, computing the modes of every window over the discrete time axis, setting $v = 2$ samples (indicated with the red rectangles and arrows) with a sampling rate of 1 kHz. Thereby, each topographic map in the iTFT map represents the cluster modes of all samples of the array containing the ITCM within the window of size v for each electrode.

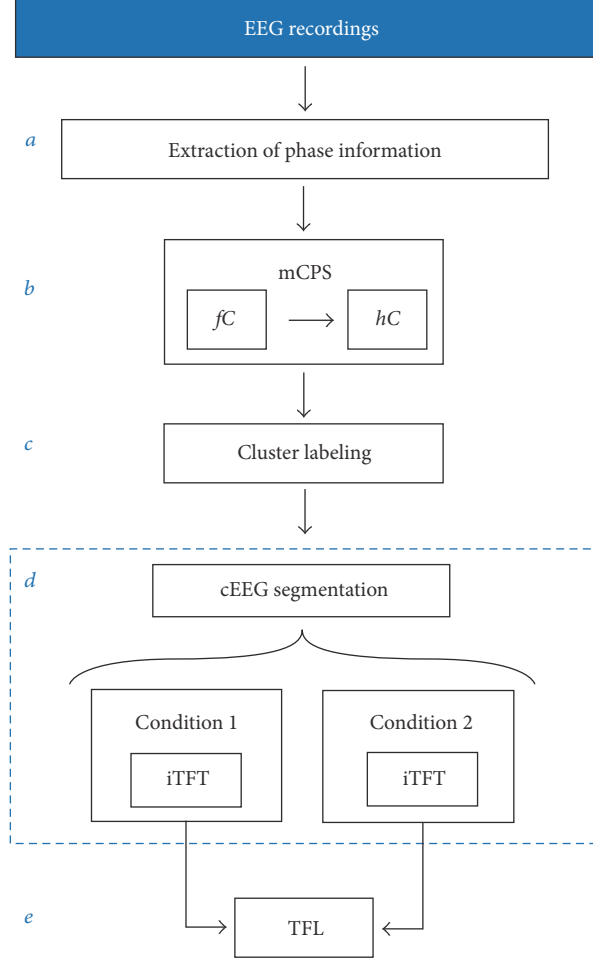
TFL maps (block e) highlight dissimilarities over time and frequency of the mCPS outputs for ERP and no-ERP.

3. Results

Figure 5 summarizes the most remarkable outcome of the experiments with sEEG. Figure 5(a) shows the grand average of each channel, and Figure 5(b) displays the corresponding spectra of all channels as well as the scalp distribution of power at center frequency $f = 1.6$ Hz. Figure 5(c) shows a single scalp map extracted from the correspondent TFT maps after applying mCPS over a single trial of sEEG, positioned at 1500 ms (which is where the peak amplitude of the VEP is found) and centered at f , with a signal-to-noise ratio (SNR) of 0.328 dB. Figure 5(d) also shows a single scalp map, at same latency and center frequency f , coming from a TFT map generated after applying mCPS over the grand average of the 30 epochs, with SNR = 3.16 dB. By visual inspection, it can be observed in Figure 5(d) that electrodes in blue cluster correspond to those in Figure 5(a), where the VEP is more evident (marked with red circles); it also largely coincides with the scalp areas with highest power at f (Figure 5(b)). Remarkable to say, despite the lower SNR in a single trial compared to scalp map of Figure 5(d), mCPS is able to retrieve some of the electrodes within the blue cluster (Figure 5(c)).

With respect to rEEG, the main attention was on the intertrial analysis searching for differences between ERP and no-ERP conditions, using iTFT maps. Different values of threshold r were tested between 0.90 and 0.99 for cluster mode assignments, while ρ was fixed at 50% and $v = 16$ samples. In relation to the data, from the seven runs of each subject, only the testing runs (4–7) were processed with our framework, each of them individually. For reasons of space, only some relevant portions of maps per subject are presented in figures: run 4 for S2 and for S5 ($r = 0.90$ and 0.975, resp.), run 7 for S6, and run 6 for S7 (both with $r = 0.96$). Figure 6 shows grand averages of all channels for these runs for each subject, contrasting ERP condition (blue) versus no-ERP condition (red). Respecting the TFL and TF maps, only the most illustrating channel is depicted. For the full maps of the runs mentioned before, please refer to <http://itzamna.uam.mx/lini/mcps.html>.

Results of run 4 for S2 are displayed in Figure 7. In the ERP iTFT map (Figure 7(a)), formations of cluster modes with label “FF” (bright yellow) containing P3-P4-PO7-Oz-PO8 can be observed from 312.5 ms to 750 ms at 2 Hz. The same situation occurs at 2.5 Hz with P3-PO7-P4. No characteristic cluster formation is shown in the no-ERP iTFT map (Figure 7(b)). Noteworthy, run 5 portrayed similar conditions compared to run 4, except that relevant cluster formations were found in bins centered at 1.3, 1.6, and 2 Hz.



iTFT: intertrial Time-Frequency-Topography
TFL: Time-Frequency-Levenshtein

FIGURE 4: Block diagram of the framework pipeline. Blocks *a*, *b*, and *c* are described in Sections 2.2.1, 2.2.2, and 2.2.3, respectively. This is a general pipeline, and as such another phase extraction technique might be used in block *a* (we opted for CWT). In block *b*, other PS criteria can be introduced (we opted for circular variance) to perform mCPS. The blocks contained in *d* are described in Section 2.2.5, where condition 1 and condition 2 refer to ERP and no-ERP epochs, obtained after segmentation of the time series of cluster labels cEEG. Additionally, TF maps of each channel for both conditions (not depicted in this block diagram) can be used together with the TFL maps of block *e* for visual analysis.

As for runs 6 and 7, neither ERP nor no-ERP iTFT maps of S2 revealed any characteristic cluster formation. In Figure 7(d), the TFL map for P4 is displayed. Important to highlight, this map depicts yellow areas that coincide (at least visually) with the concentration of power of the P300 wave (Figure 7(e)), particularly for P3, P4, PO7, and Oz (TFL maps for P3, PO7, and Oz can be observed in the complete study). It is also coincidental with the cluster formations described previously in the ERP iTFT map and with the P300 power time course, around 312 ms and 750 ms approximately (Figure 7(e)), which is not the case if such cluster arrangements are compared with no-ERP TF maps (Figure 7(f)).

3.1. Steady-State Visual Evoked Potential (SSVEP) Artifact. As depicted in Figure 7(c), it can be observed that cluster “FF”

contains all EEG channels at 7.6 Hz over the entire row. This is highly likely to be related to an SSVEP artifact derived from a fixed value of the interstimulus duration (125 ms). This pattern appears in all subjects, with some minor variations of f_k . For example, for S2, this fact can be related to the concentration of power around 7.6 Hz in the entire epoch in all TF maps of each channel (Figures 7(e) and 7(f)). This can be verified with almost all TF maps presented for both ERP and no ERP for all subjects.

Regarding S5, observations within runs are very similar ($r = 0.975$). For ERP condition (Figure 8(a)), cluster formations of “FF” with parietal channels and Cz clearly coincide with yellow areas of TFL map of P3 (Figure 8(c)) and power concentration of P300 in the TF map (Figure 8(d)). This can be observed over the ERP iTFT cluster formations in bins

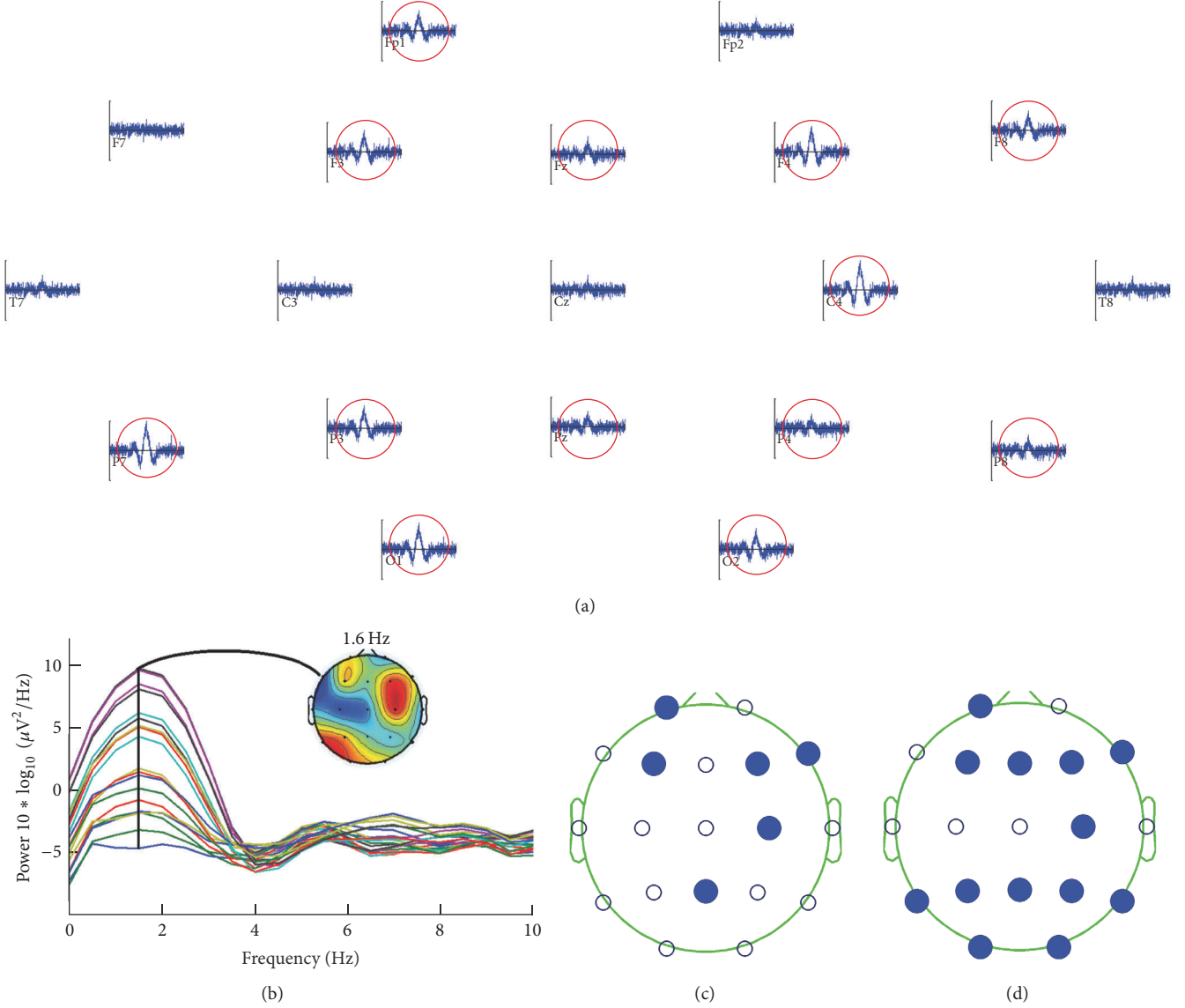


FIGURE 5: (a) Grand average of each channel; (b) corresponding spectra and scalp distribution of power at 1.6 Hz. Both images were generated with EEGLAB [31]. (c) TFT map at 1500 ms, 1.6 Hz, and SNR = 0.328 dB. (d) TFT map at same time and frequency of grand average, with SNR = 3.16 dB.

centered at 1.6, 2, 2.5, and 3.1 Hz (Figure 8(a)). iTFT maps of no ERP (Figure 8(b)) did not show any relevant cluster formation.

For S6 ($r = 0.96$), Figures 9(a) and 9(b) illustrate a section of the correspondent iTFT map of ERP and no-ERP conditions, respectively. The “FF” cluster formations can be observed in the 3.1 Hz bin, which takes place at different time windows. There are no relevant cluster formations over no-ERP map at the same times. The TFL map confirms these differences with the yellow areas for Pz (Figure 9(c)). In this case, the relationship with the power in TF map of P300 wave (Figures 9(d) and 9(e)) is not so evident.

Concerning S7, in run 6 with a threshold of $r = 0.96$, parietal electrodes stand out again portraying diverse “FF” cluster arrangements over the scalp, mainly at 2, 2.5, and

3.1 Hz (Figure 10(a)), concurring with yellow areas in corresponding TFL map of P3 (Figure 10(c)) and with the power of P300 wave in the TF map (Figure 10(d)). In run 7, the appearance of other cluster formations besides “FF” (perceived in other runs and subjects) was noticeable, with parietal electrodes between 375 and 625 ms.

4. Discussion

The findings over the TFT maps of sEEG served as a starting point for leading the research to the analysis with real data, as coincidences of the generated cluster in the single trial and the one over the grand average reflected the ability of mCPS to retrieve the PS information of interest. For rEEG, the iTFT maps exposed several differences between ERP and

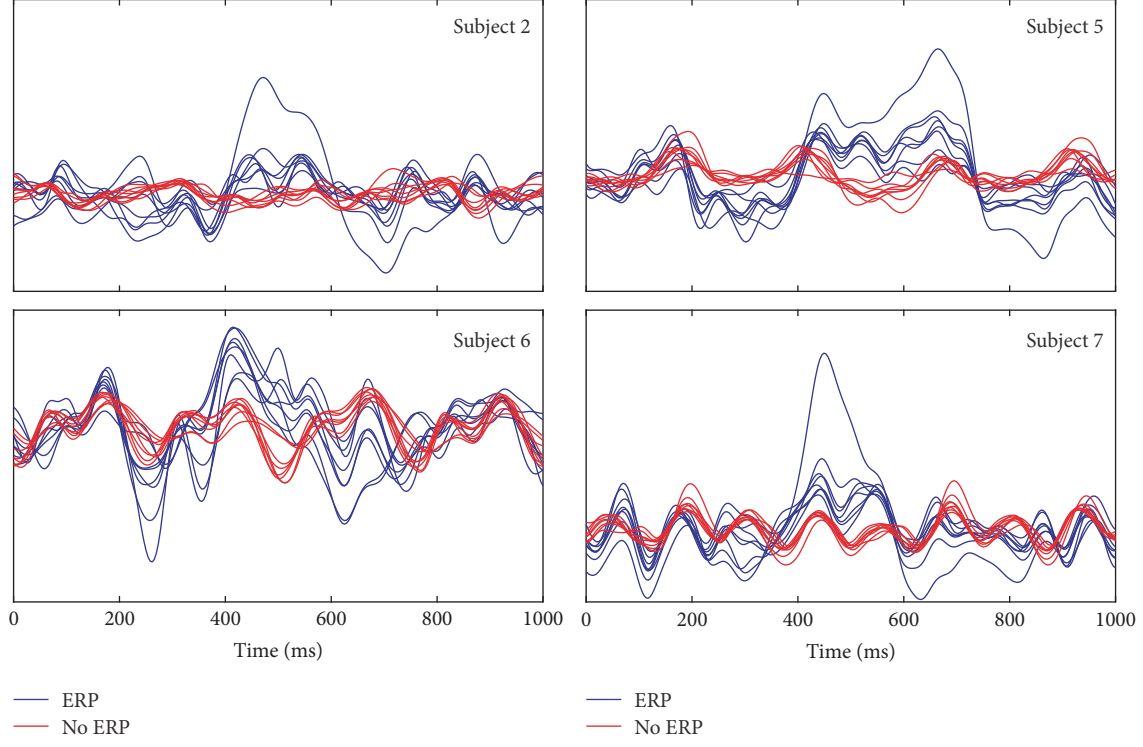


FIGURE 6: Grand averages of ERP (blue) versus no-ERP (red) condition for each subject (run 4 for S2 and S5, run 7 for S6, and run 6 for S7).

no ERP, and maybe the most notable and consistent feature was the arrangements of clusters labeled “FF” systematically appearing in ERP maps (Figures 7(a), 8(a), 9(a), and 10(a)) derived from the ITCM computation, contrasting with the absence of such patterns in the no-ERP maps (Figures 7(b), 8(b), 9(b), and 10(b)). This fact is evidenced with the TFL maps (Figures 7(d), 8(c), 9(c), and 10(c)), highlighting the areas of the TF plane with perceptible differences among ERP and no ERP. Such differences can be noted by contrasting Figures 7(e), 7(f), 8(d), 8(e), 9(d), 9(e), 10(d), and 10(e), respectively. Moreover, most of the “FF” appearances can be related (at least by visual inspection) to the P300 wave, given the times and bandwidths where these clusters appear, as most of them were localized within delta and theta ranges, which is consistent with frequency content of a P300 ERP [39–41]. The frequency content of no-ERP epochs observed in Figures 7(f), 8(e), 9(e), and 10(e) could hardly be explained by any neurophysiological event of relevance, but rather it could be due to subharmonics of the SSVEP artifact, as the power concentration can be perceived as extended “lines” throughout the time series.

There were cases (like S6) where analysis with TFL and TF maps did not yield any clear distinction between ERP and no ERP, like run 6, where cluster formations were sporadic and intermittent, making it difficult to establish a relationship with the P300 wave. Noteworthy, samples of ERP and no-ERP epochs are highly unbalanced (each run per subject contains 100 ERP epochs and 500 no-ERP epochs), which reinforces our results distinguishing these conditions, considering the fact that we are using mode as statistical measure, and despite

a greater amount of samples of no-ERP epochs, no relevant cluster modes formations were detected.

Another important aspect is related to frequency locking and tracking of frequency flows [42, 43]. A limitation in some methods relying on a narrow band TF decomposition, such as the frequency bins generated with wavelets, is the assumption of frequency stationarity of PS, hiding or masking periods of continuous PS with transient variability of synchronization frequency through time. However, the TFT maps can capture this frequency flow of PS, as it can be observed how the “FF” cluster patterns appear over different low frequency narrow bands, such as $f_k = 1.6, 2, 2.5$, and 3.1 Hz for S5 (Figure 8(a)) and $f_k = 2, 2.5$, and 3.1 Hz for S7 (Figure 10(a)).

With respect to hyperparameters, further analysis should be made varying threshold values (r and v) in order to evaluate the produced effect in cluster generation and visualization. As mentioned before, several tests were made with different values of r , yet the results shown in this work are only for one r per subject, which was heuristically selected by identifying the TFL maps that yield a better differentiation of ERP and no-ERP conditions. The method is highly sensitive to r variations, and future work can be directed to automate selection of optimal values for r .

Even though in these results our framework serves in identifying PS dynamics related to the neural activity of interest organized and structured in clusters of EEG channels, there is still a lot of room for improvement. At this point, our method describes near-zero phase lag relationships between EEG channels ($r > 0.90$ in most of the cases). By definition, volume conduction requires zero phase lag, but a phase

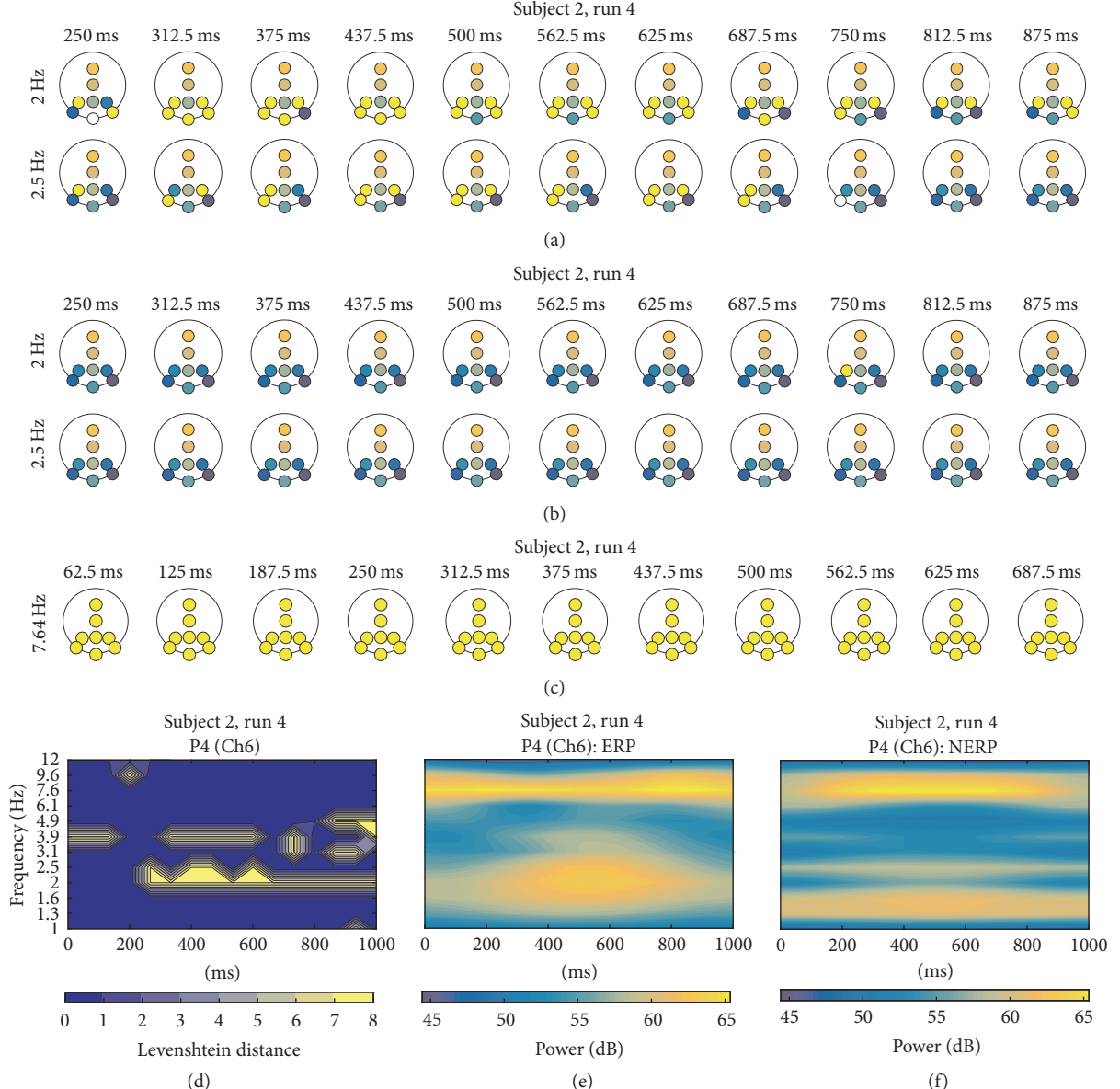


FIGURE 7: (a) A portion of iTFT maps for S2, showing only the row of bins centered at 2 Hz and 2.5 Hz, from 250 ms to 875 ms of ERP epochs; (b) same f_k depicted for no-ERP epochs. (c) An example of the cluster related with the steady-state artifact. (d) TFL map for P4. (e) TF map for P4 for ERP and (f) TF map for P4 for no ERP.

difference close to zero is not necessarily due to volume conduction, as this kind of phase associations can be found widespread over the cerebral cortex because of corticothalamic projections [44]. There are some measures such as Phase Lag Index (PLI) [45] or imaginary coherence [46] which deal with volume conduction by discarding zero phase lags, but at the same time these approaches are insensitive to true near-zero phase lag interactions [47].

On the other hand, volume conduction can be addressed by measuring phase reset, which can be detected when a phase shift takes place between two phase-locked signals [48]. This idea can be extended in our framework, trying to find phase resets between EEG channels. Adding other

phase differences or phase-locking measures could retrieve different clustering patterns, which along with our already implemented mCPS measure and detection of phase resets could deliver complementary and relevant information.

5. Conclusions

Our framework provides a feasible way to address both single and intertrial PS analysis of multivariate neural time series, characterizing the PS variability through time. The majority of PS measures so far suggested in literature such as PLV or PCC are calculated between two signals [6–8] or provide only a global index of synchronization in the case of multivariate

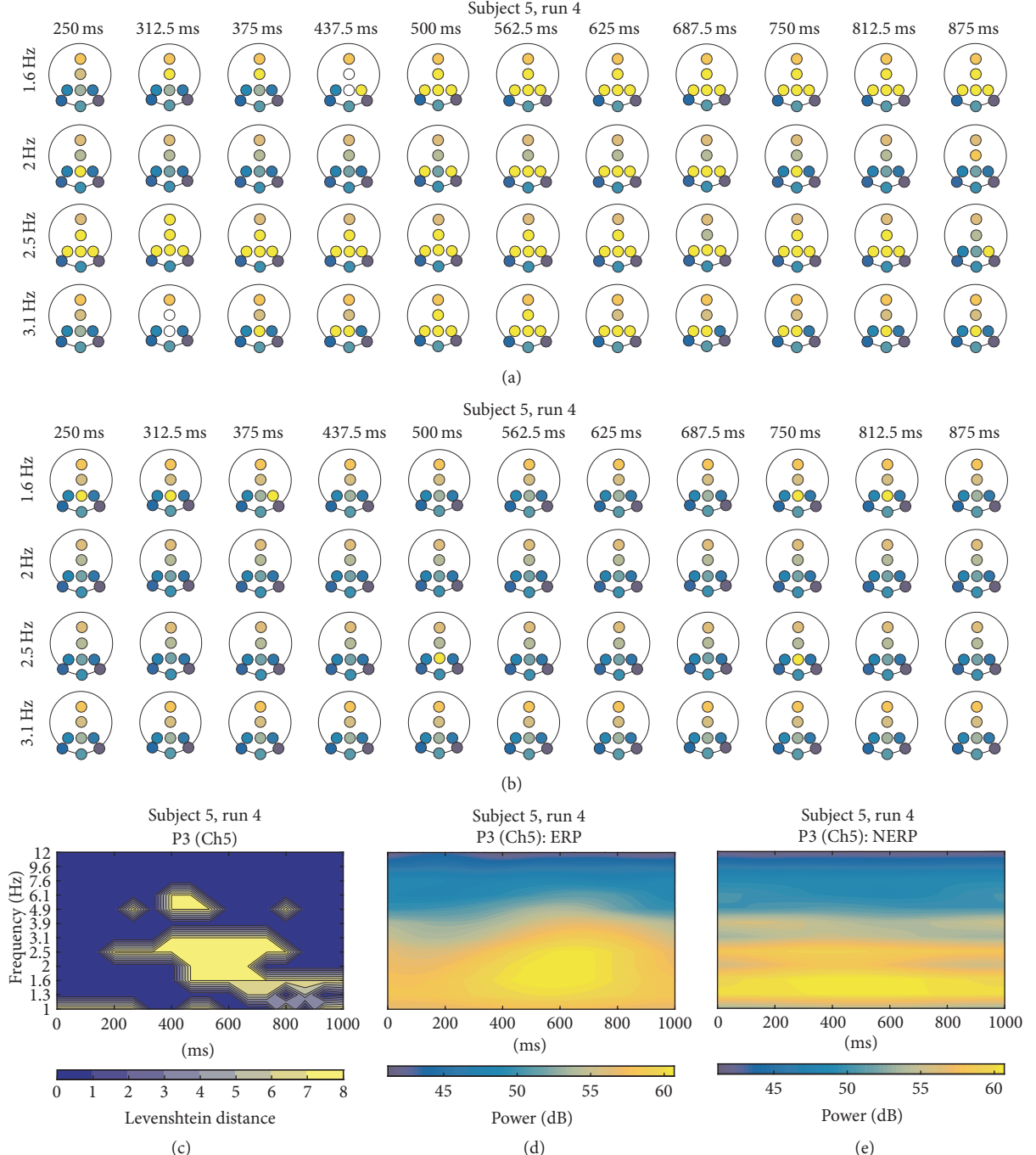


FIGURE 8: (a) A portion of iTFT maps for S5, showing only the row of bins centered at 1.6, 2, 2.5, and 3.1 Hz, from 250 ms to 875 ms of ERP epochs; (b) same f_k depicted for no-ERP epochs. (c) TFL map for P3. (d) TF map for P3 for ERP, and (e) TF map for P3 for no ERP.

measures [19, 20, 23, 27]. Our framework is an alternative for studying the behavior of phase synchronization between all EEG channels at once in a given time window within different bandwidths of interest. Noticeable to say, the framework is not limited to any particular phase extraction technique (further discussion about the selection of these techniques is beyond the scope of this article) and can also easily be adapted to other PS measures like phase coherence, obtaining clusters

of phase differences consistency from mCPS. It remains to assess and compare the proposed algorithm to other clustering algorithms in terms of efficiency and computational complexity.

The insight given by the iTFT maps provides a qualitative measure of intertrial cluster consistency, which when combined with the TFL and TF maps becomes helpful to assess which clusters patterns are related to a specific mental task. It

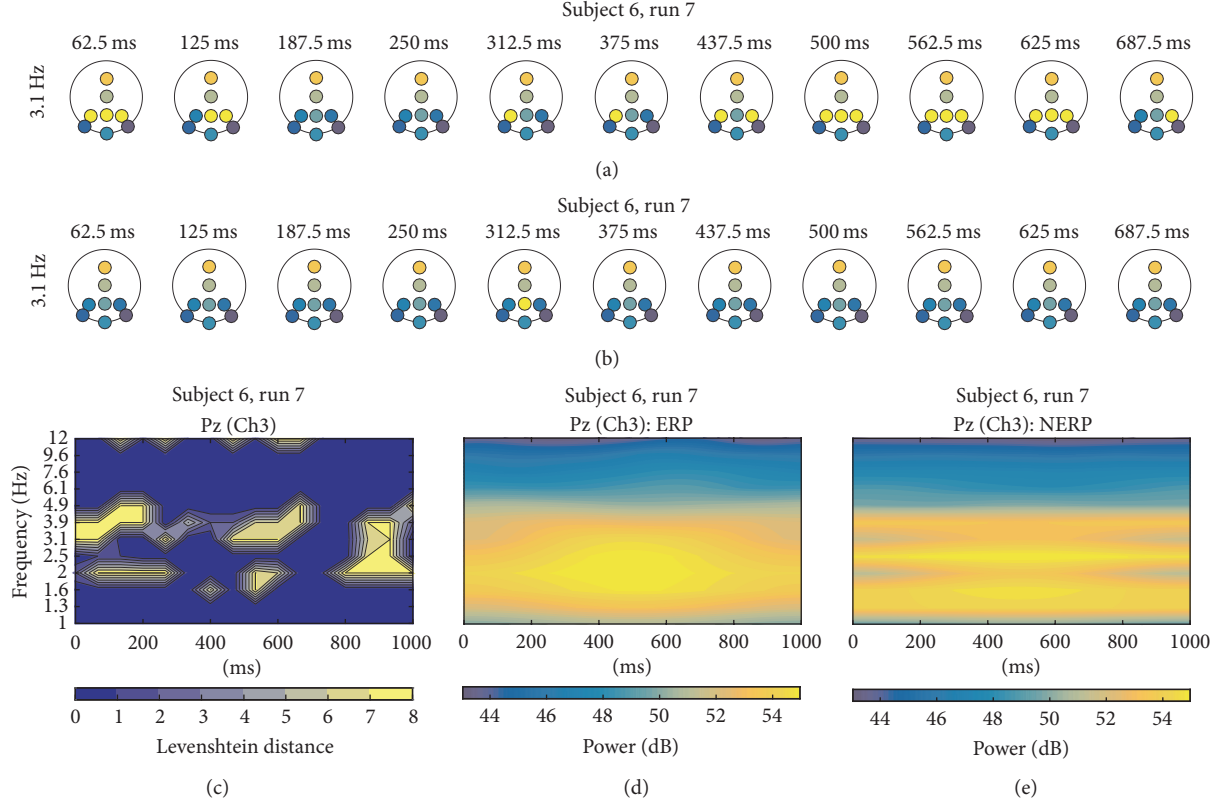


FIGURE 9: (a) A portion of iTFT maps for S6, showing only the row of bin centered at 3.1 Hz, from 62.5 ms to 687.5 ms of ERP epochs; (b) same f_k depicted for no-ERP epochs. (c) TFL map for Pz. (d) TF map for Pz for ERP and (e) TF map for Pz for no ERP.

should be mentioned that some yellow areas depicted in TFL maps that do not match with the power increase of the P300 wave shown in TF maps could be due to artifacts artificially derived from LD computation or due to other relevant neural information not related to ERP. Further analysis should be made regarding this issue.

Although in this first approach mCPS was applied over synthetic signals and P300 wave data with relatively few electrodes, the aim of this work was merely to illustrate the framework pipeline and how it describes PS patterns. As mentioned before, our work attempts to encompass a broader variety of cognitive states. For example, in the context of BCI, our framework might be useful for the characterization of mental tasks suitable for endogenous BCI paradigms with no external stimuli in the system. Then, feature extraction could be performed from mCPS outcome for asynchronous (self-paced) BCI classification, distinguishing idle state from a specific mental task. Additionally, when exploring higher density EEG (64 channels or more), this framework could be used as a channel optimization tool finding the clusters of electrodes that contribute the most to characterization of a mental state.

Electrical signals from brain sources are volume conducted through nervous tissue, cerebrospinal fluid, skull, and scalp. Hence, an underlying issue in EEG recordings regards the single source contamination of multiple sensors via volume conduction. The EEG recorded over the scalp does

not necessarily capture the direct activity underneath the electrode but a weighted mixture of different sources (neural or artifact). Then, distinction between volume conduction and true synchrony remains an open issue. Some authors have reported that methods for improving spatial resolution of EEG, such as scalp current density profiles (SCD), seem convenient as preprocessing steps before the estimation of PS [7, 8]. For future work, it should be interesting to study the effects of rereferencing. Again, in the BCI field, it could be assessed if rereferencing enhances performance using phase clusters as features for classification, bearing in mind the fact that the original phase delays may be distorted. It should be pointed out that no additional preprocessing was made, preserving the data as raw as possible. Further approaches for addressing volume conduction should be considered in forthcoming research.

Finally, to summarize the contributions, the proposed framework incorporates several features useful for PS analysis, such as iTFT and TFL maps, taking into account some aspects like frequency nonstationarity and flexibility of use of other synchronization measures besides PLF. The LD is applied as a metric for better distinction of differences between conditions, highlighting synchrony differences between ERP and no-ERP epochs, mainly at delta and theta bands. Additional information like the steady-state artifacts at 7.6 Hz is also retrieved and depicted in iTFT maps. Taking EEG as the view port of cortical activity, our

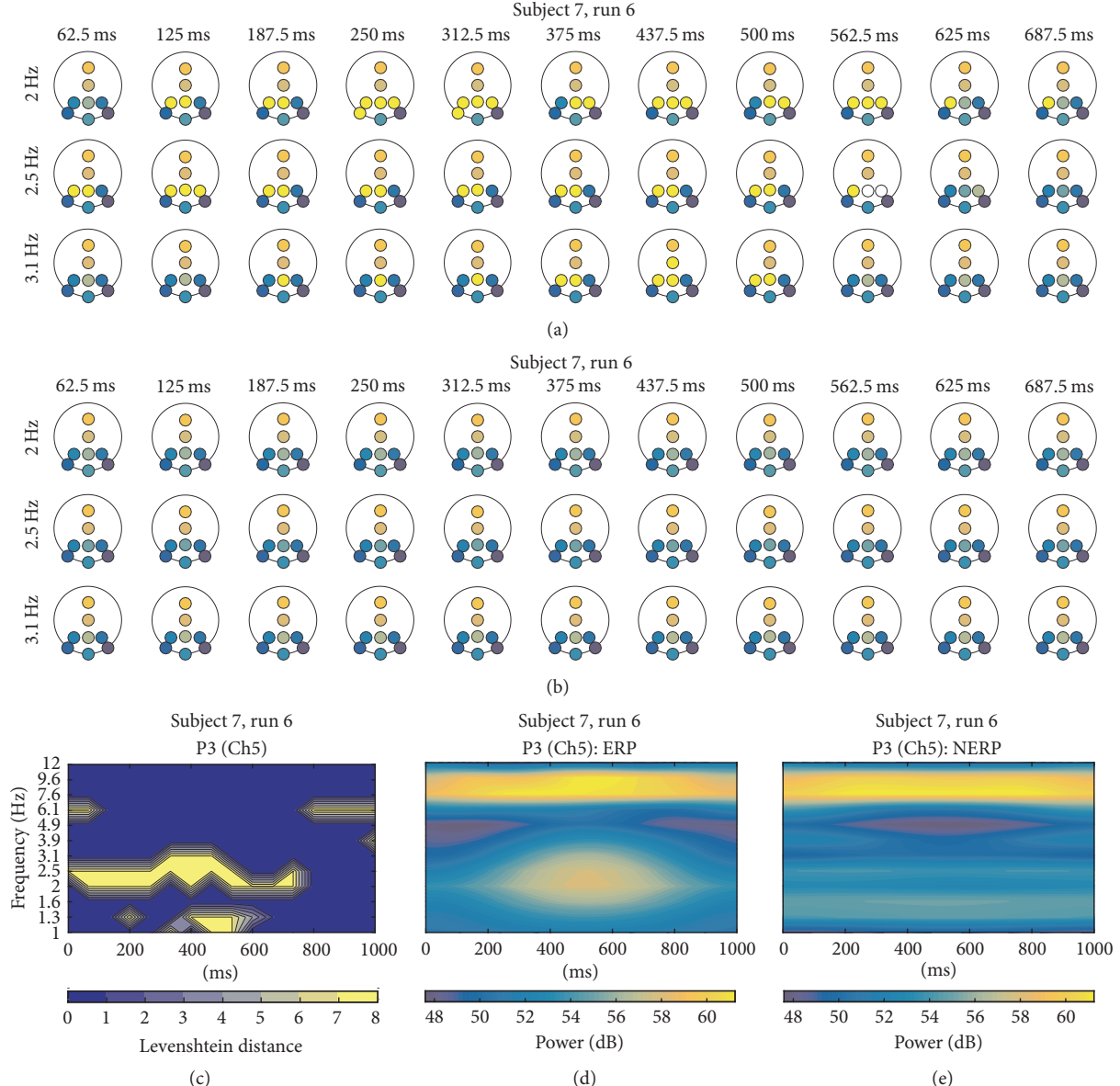


FIGURE 10: (a) A portion of iTFT maps for S7, showing only the row of bin centered at 2, 2.5, and 3.1 Hz, from 62.5 ms to 687.5 ms of ERP epochs; (b) same f_k depicted for no-ERP epochs. (c) TFL map for P3. (d) TF map for P3 for ERP and (e) TF map for P3 for no ERP.

framework provides a new insight into terms of large-scale integration of emerging synchrony patterns of instantaneous phase during cognitive tasks, depicted in phase-related cluster arrangements over the time series of EEG signals.

Conflicts of Interest

The authors declare that they have no conflicts of interest.

Acknowledgments

M. A. Porta-Garcia, M.S., gratefully acknowledges Consejo Nacional de Ciencia y Tecnología (CONACYT) for Ph.D. scholarship 271659.

References

- [1] W. H. Miltner, C. Braun, M. Arnold, H. Witte, and E. Taub, “Coherence of gamma-band EEG activity as a basis for associative learning,” *Nature*, vol. 397, no. 6718, pp. 434–436, 1999.
- [2] J. Bhattacharya, H. Petsche, and E. Pereda, “Interdependencies in the spontaneous EEG while listening to music,” *International Journal of Psychophysiology*, vol. 42, no. 3, pp. 287–301, 2001.
- [3] M. Popescu, A. Otsuka, and A. A. Ioannides, “Dynamics of brain activity in motor and frontal cortical areas during music listening: A magnetoencephalographic study,” *NeuroImage*, vol. 21, no. 4, pp. 1622–1638, 2004.
- [4] J. Bhattacharya and H. Petsche, “Phase synchrony analysis of EEG during music perception reveals changes in functional

- connectivity due to musical expertise,” *Signal Processing*, vol. 85, no. 11, pp. 2161–2177, 2005.
- [5] J. F. Cavanagh, M. X. Cohen, and J. J. B. Allen, “Prelude to and resolution of an error: EEG phase synchrony reveals cognitive control dynamics during action monitoring,” *The Journal of Neuroscience*, vol. 29, no. 1, pp. 98–105, 2009.
- [6] M. S. Doesburg and M. L. Ward, “Synchronization between sources: emerging methods for understanding large-scale functional networks in the human brain,” in *In Coordinated Activity in the Brain*, pp. 25–42, Springer, 2009.
- [7] B. J. Roach and D. H. Mathalon, “Event-Related EEG Time-Frequency Analysis: An Overview of Measures and An Analysis of Early Gamma Band Phase Locking in Schizophrenia,” *Schizophrenia Bulletin*, vol. 34, no. 5, pp. 907–926, 2008.
- [8] J.-P. Lachaux, E. Rodriguez, J. Martinerie, and F. J. Varela, “Measuring phase synchrony in brain signals,” *Human Brain Mapping*, vol. 8, no. 4, pp. 194–208, 1999.
- [9] J.-P. Lachaux, E. Rodriguez, M. Le Van Quyen, A. Lutz, J. Martinerie, and F. J. Varela, “Studying single-trials of phase synchronous activity in the brain,” *International Journal of Bifurcation and Chaos*, vol. 10, no. 10, pp. 2429–2439, 2000.
- [10] S. G. Roux, T. Cenier, S. Garcia, P. Litaudon, and N. Buonviso, “A wavelet-based method for local phase extraction from a multi-frequency oscillatory signal,” *Journal of Neuroscience Methods*, vol. 160, no. 1, pp. 135–143, 2007.
- [11] M. le van Quyen, J. Foucher, J.-P. Lachaux et al., “Comparison of Hilbert transform and wavelet methods for the analysis of neuronal synchrony,” *Journal of Neuroscience Methods*, vol. 111, no. 2, pp. 83–98, 2001.
- [12] A. Bruns, “Fourier-, Hilbert- and wavelet-based signal analysis: are they really different approaches?” *Journal of Neuroscience Methods*, vol. 137, no. 2, pp. 321–332, 2004.
- [13] A. W. Rihaczek, “Signal Energy Distribution in Time and Frequency,” *IEEE Transactions on Information Theory*, vol. 14, no. 3, pp. 369–374, 1968.
- [14] N. E. Huang, Z. Shen, S. R. Long et al., “The empirical mode decomposition and the Hilbert spectrum for nonlinear and non-stationary time series analysis,” *Proceedings A*, vol. 454, no. 1971, pp. 903–995, 1998.
- [15] A. Alba, J. L. Marroquin, J. Peña, T. Harmony, and B. Gonzalez-Frankenberger, “Exploration of event-induced EEG phase synchronization patterns in cognitive tasks using a time-frequency-topography visualization system,” *Journal of Neuroscience Methods*, vol. 161, no. 1, pp. 166–182, 2007.
- [16] S. G. Mallat and Z. Zhang, “Matching Pursuits With Time-Frequency Dictionaries,” *IEEE Transactions on Signal Processing*, vol. 41, no. 12, pp. 3397–3415, 1993.
- [17] M. G. Rosenblum, A. S. Pikovsky, and J. Kurths, “Phase synchronization of chaotic oscillators,” *Physical Review Letters*, vol. 76, no. 11, pp. 1804–1807, 1996.
- [18] S. Bialonski and K. Lehnertz, “Identifying phase synchronization clusters in spatially extended dynamical systems,” *Physical Review E: Statistical, Nonlinear, and Soft Matter Physics*, vol. 74, no. 5, Article ID 051909, 2006.
- [19] M. Al-Khassawneh, M. Villafane-Delgado, A. Y. Mutlu, and S. Aviyente, “A measure of multivariate phase synchrony using hyperdimensional geometry,” *IEEE Transactions on Signal Processing*, vol. 64, no. 11, pp. 2774–2787, 2016.
- [20] D. Rangaprakash, “Connectivity analysis of multichannel EEG signals using recurrence based phase synchronization technique,” *Computers in Biology and Medicine*, vol. 46, no. 1, pp. 11–21, 2014.
- [21] D. Rangaprakash and N. Pradhan, “Study of phase synchronization in multichannel seizure EEG using nonlinear recurrence measure,” *Biomedical Signal Processing and Control*, vol. 11, no. 1, pp. 114–122, 2014.
- [22] I. Osorio and Y.-C. Lai, “A phase-synchronization and random-matrix based approach to multichannel time-series analysis with application to epilepsy,” *Chaos: An Interdisciplinary Journal of Nonlinear Science*, vol. 21, no. 3, 033108, 11 pages, 2011.
- [23] X. Li, D. Cui, P. Jiruska, J. E. Fox, X. Yao, and J. G. R. Jefferys, “Synchronization measurement of multiple neuronal populations,” *Journal of Neurophysiology*, vol. 98, no. 6, pp. 3341–3348, 2007.
- [24] A. Y. Mutlu and S. Aviyente, “Hyperspherical phase synchrony for quantifying multivariate phase synchronization,” in *Proceedings of the 2012 IEEE Statistical Signal Processing Workshop, SSP 2012*, pp. 888–891, USA, August 2012.
- [25] S. Aviyente, E. M. Bernat, W. S. Evans, and S. R. Sponheim, “A phase synchrony measure for quantifying dynamic functional integration in the brain,” *Human Brain Mapping*, vol. 32, no. 1, pp. 80–93, 2010.
- [26] M. E. Bolanos, S. Aviyente, and E. M. Bernat, “Identifying functional clusters in the brain using phase synchrony,” in *Proceedings of the 2010 IEEE International Conference on Acoustics, Speech, and Signal Processing, ICASSP 2010*, pp. 5446–5449, March 2010.
- [27] C. Allefeld and J. Kurths, “An approach to multivariate phase synchronization analysis and its application to event-related potentials,” *International Journal of Bifurcation and Chaos*, vol. 14, no. 2, pp. 417–426, 2004.
- [28] C. Allefeld, M. Müller, and J. Kurths, “Eigenvalue decomposition as a generalized synchronization cluster analysis,” *International Journal of Bifurcation and Chaos*, vol. 17, no. 10, pp. 3493–3497, 2007.
- [29] C. Allefeld and S. Bialonski, “Detecting synchronization clusters in multivariate time series via coarse-graining of Markov chains,” *Physical Review E: Statistical, Nonlinear, and Soft Matter Physics*, vol. 76, no. 6, Article ID 066207, 2007.
- [30] A. R. Haig, E. Gordon, J. J. Wright, R. A. Meares, and H. Bahramali, “Synchronous cortical gamma-band activity in task-relevant cognition,” *NeuroReport*, vol. 11, no. 4, pp. 669–675, 2000.
- [31] A. Delorme and S. Makeig, “EEGLAB: an open source toolbox for analysis of single-trial EEG dynamics including independent component analysis,” *Journal of Neuroscience Methods*, vol. 134, no. 1, pp. 9–21, 2004.
- [32] Trans Cranial Technologies, “Trans Cranial Technologies, 2410 Fortis Tower,” in *10/20 System Positioning Manual*, pp. 77–79, Hong Kong, China, 2012.
- [33] A. Riccio, L. Simione, F. Schettini et al., “Attention and P300-based BCI performance in people with amyotrophic lateral sclerosis,” *Frontiers in Human Neuroscience*, vol. 7, article 732, 2013.
- [34] L. A. Farwell and E. Donchin, “Talking off the top of your head: Toward a mental prosthesis utilizing event-related brain potentials,” *Electroencephalography and Clinical Neurophysiology*, vol. 70, no. 6, pp. 510–523, 1988.
- [35] K. V. Mardia and P. E. Jupp, *Directional Statistics*, John Wiley & Sons, New York, NY, USA, 1999.
- [36] M. A. Porta-Garcia, F. J. Garciduenas-Vargas, O. Yanez-Suarez, and R. Valdes-Cristerna, “EEG clustering based on phase synchrony for self-paced BCI development,” in *Proceedings*

of the In Proceedings of the 6th International Brain-Computer Interface Meeting, 2016.

- [37] T. Koenig, F. Marti-Lopez, and P. Valdes-Sosa, "Topographic time-frequency decomposition of the EEG," *NeuroImage*, vol. 14, no. 2, pp. 383–390, 2001.
- [38] L. Yujian and L. Bo, "A normalized Levenshtein distance metric," *IEEE Transactions on Pattern Analysis and Machine Intelligence*, vol. 29, no. 6, pp. 1091–1095, 2007.
- [39] C. Basar-Eroglu, E. Basar, T. Demiralp, and M. Schürmann, "P300-response: possible psychophysiological correlates in delta and theta frequency channels. A review," *International Journal of Psychophysiology*, vol. 13, no. 2, pp. 161–179, 1992.
- [40] V. Kolev, T. Demiralp, J. Yordanova, A. Ademoglu, and Ü. Isoglu-Alkaç, "Time-frequency analysis reveals multiple functional components during oddball P300," *NeuroReport*, vol. 8, no. 8, pp. 2061–2065, 1997.
- [41] T. Demiralp, A. Ademoglu, M. Schürmann, C. Basar-Eroglu, and E. Basar, "Detection of P300 waves in single trials by the wavelet transform (WT)," *Brain and Language*, vol. 66, no. 1, pp. 108–128, 1999.
- [42] P. Tass, M. G. Rosenblum, J. Weule et al., "Detection of n:m phase locking from noisy data: application to magnetoencephalography," *Physical Review Letters*, vol. 81, no. 15, pp. 3291–3294, 1998.
- [43] D. Rudrauf, A. Douiri, C. Kovach et al., "Frequency flows and the time-frequency dynamics of multivariate phase synchronization in brain signals," *NeuroImage*, vol. 31, no. 1, pp. 209–227, 2006.
- [44] M. Steriade, "Grouping of brain rhythms in corticothalamic systems," *Neuroscience*, vol. 137, no. 4, pp. 1087–1106, 2006.
- [45] C. J. Stam, G. Nolte, and A. Daffertshofer, "Phase lag index: assessment of functional connectivity from multi channel EEG and MEG with diminished bias from common sources," *Human Brain Mapping*, vol. 28, no. 11, pp. 1178–1193, 2007.
- [46] G. Nolte, O. Bai, L. Wheaton, Z. Mari, S. Vorbach, and M. Hallett, "Identifying true brain interaction from EEG data using the imaginary part of coherency," *Clinical Neurophysiology*, vol. 115, no. 10, pp. 2292–2307, 2004.
- [47] J. M. Palva, "Phase-locking methods," *Encyclopedia of Computational Neuroscience*, pp. 2356–2359, 2015.
- [48] R. W. Thatcher, "Coherence, phase differences, phase shift, and phase lock in EEG/ERP analyses," *Developmental Neuropsychology*, vol. 37, no. 6, pp. 476–496, 2012.

Research Article

Liraglutide Activates the Nrf2/HO-1 Antioxidant Pathway and Protects Brain Nerve Cells against Cerebral Ischemia in Diabetic Rats

Caihong Deng ,¹ Jun Cao,² Jiangquan Han ,¹ Jianguo Li,³ Zhaojun Li,⁴ Ninghua Shi,¹ and Jing He¹

¹Department of Neurology, The Fifth Affiliated Hospital of Zunyi Medical College, Zhuhai 519100, China

²Department of Pharmacy, Xindu District People's Hospital of Chengdu, Chengdu 610500, China

³Department of Emergency, The Fifth Affiliated Hospital of Zunyi Medical College, Zhuhai 519100, China

⁴Department of Neurology, Zhuhai People's Hospital, Zhuhai 519100, China

Correspondence should be addressed to Jiangquan Han; gdshanjq@163.com

Received 21 September 2017; Revised 15 December 2017; Accepted 27 December 2017; Published 12 February 2018

Academic Editor: João Manuel R. S. Tavares

Copyright © 2018 Caihong Deng et al. This is an open access article distributed under the Creative Commons Attribution License, which permits unrestricted use, distribution, and reproduction in any medium, provided the original work is properly cited.

This study aimed to determine the effect of liraglutide pretreatment and to elucidate the mechanism of nuclear factor erythroid 2-related factor (Nrf2)/heme oxygenase-1 (HO-1) signaling after focal cerebral ischemia injury in diabetic rats model. Adult male Sprague-Dawley rats were randomly divided into the sham-operated (S) group, diabetes mellitus ischemia (DM + MCAO) group, liraglutide pretreatment normal blood glucose ischemia (NDM+MCAO+L) group, and liraglutide pretreatment diabetes ischemia (DM + MCAO + L) group. At 48 h after middle cerebral artery occlusion (MCAO), neurological deficits and infarct volume of brain were measured. Oxidative stress brain tissue was determined by superoxide dismutase (SOD) and myeloperoxidase (MPO) activities. The expression levels of Nrf2 and HO-1 of brain tissue were analyzed by western blotting. In the DM + MCAO + L group, neurological deficits scores and cerebral infarct volume seemed to decrease at 48 h after MCAO cerebral ischemia compared with those in DM + MCAO group ($P < 0.05$). In addition, the expression of Nrf2 and HO-1 increased in 48 h at liraglutide pretreatment groups after MCAO cerebral ischemia if compared with those in the DM + MCAO group ($P < 0.05$). Furthermore, the DM + MCAO + L group has no significant difference compared with the NDM + MCAO + L group ($P > 0.05$). To sum up, alleviating effects of liraglutide on diabetes complicated with cerebral ischemia injury rats would be related to Nrf2/HO-1 signaling pathway.

1. Introduction

Ischemic stroke is characterized by high rates of morbidity, mortality, disability, and relapse [1, 2]. At present, intravascular thrombolysis and embolectomy are achieved via the blood vessels, while other therapeutic means remain unsatisfactory. Diabetes mellitus (DM) is an important risk factor for cerebral infarction. Compared with nondiabetic patients, the incidence of cerebral infarction in patients with diabetes is 1.8–6.0 times higher [3]. Liraglutide is a long-acting synthetic analog of glucagon-like peptide-1 (GLP-1) in the treatment of type 2 diabetes drugs and has been sold in the United States, Europe, and China. It is chemically similar to natural

GLP-1, with 97% homology [4], and also has some biological effects of GLP-1. In 2013, Sato et al. suggested that liraglutide reduced neuronal damage caused by cerebral ischemia in diabetic and nondiabetic rats through antioxidative stress and antiapoptosis pathways [5]. Previous studies have confirmed that the Nrf2/HO-1 signaling pathway plays an important role in antioxidative stress. In view of liraglutide's antioxidative stress activity, we speculated that it could activate the nuclear factor erythroid 2-related factor (Nrf2)/heme oxygenase-1 (HO-1) pathway in the treatment of diabetes complicated with cerebral infarction. We recommend explaining the relationship between Nrf2/HO-1 signaling pathway and neuronal damage caused by cerebral ischemia. This could make your

investigation more convincing. Generally speaking, introduction is too simple and therefore needs more information inserted into this part.

2. Materials and Methods

2.1. Animals. Adult male Sprague-Dawley rats (280–320 g) were purchased from Guangdong Provincial Medical Laboratory Animal Center. Animals were housed in cages at constant temperature (22°C) and relative humidity (55%) with a 12-h light–12-h dark cycle (light 06.00–18.00 h). The experimental protocol was approved by the Animal Ethics Committee of Guangdong Medical Laboratory Animal Center and performed in accordance with the National Institutes of Health Guide for the Care and Use of Laboratory Animals. Precautions were taken to minimize suffering and the number of animals used in each experiment. Rats were randomly divided into four groups with 12 rats per group: sham-operated (S) group, liraglutide pretreatment normal blood glucose cerebral ischemia (NDM + MCAO + L) group, liraglutide pretreatment diabetes mellitus cerebral ischemia (DM + MCAO + L) group, and diabetes mellitus cerebral ischemia (DM + MCAO) group.

2.2. Type 1 Diabetes Mellitus Model. A rat model of type 1 DM was established by intraperitoneal (i.p.) injection of streptozotocin (STZ; Sigma, USA) at 20 mg/kg in the first 24 h and at 35 mg/kg on the next day following 8 h of fasting [6]. The animals were allowed normal drinking water and feeding for 7 days, and there was no blood glucose intervention until on the diabetes diet control on 7 consecutive days. The changes in symptoms and signs in rats were observed. A blood glucose meter (Roche, Germany) was used to determine blood glucose in a tail vein sample. The diabetes model was deemed successful when random blood glucose was more than 13.9 mm/L and accompanied by polydipsia, polyuria, and weight loss. Rats were excluded for not up to 13.9 mm/L of blood glucose or because of death before the start of the experiment.

2.3. Middle Cerebral Artery Occlusion Model. After DM induction, middle cerebral artery occlusion (MCAO) models were established once blood glucose levels remained stable for 7–14 days. Rats were anesthetized with chloral hydrate (300 mg/kg, i.p.) and subjected to MCAO as previously described with slight modifications [7]. Briefly, the left common carotid artery, internal carotid artery (ICA), and external carotid artery (ECA) were exposed, and the ECA was dissected distally. A special nylon suture with a rounded tip (line diameter of 0.28 mm, head diameter of 0.36 ± 0.02 mm) was inserted into the ICA through the ECA stump and was gently advanced to occlude the middle cerebral artery (MCA). The animals that died after ischemia induction or that had evidence of subarachnoid hemorrhage on extraction of brain tissue were excluded. Skin and subcutaneous tissue were sutured immediately after the MCAO. Body temperature was monitored with a rectal probe and maintained at 37°C during the entire procedure. Rats in the sham group were manipulated in the same way but without MCAO.

2.4. Liraglutide Administration. Liraglutide (Novo Nordisk Denmark) was dissolved in saline and administered at a dose of 100 µg/kg (for the two groups of liraglutide pretreatment). The studies were only performed in the 100 µg/kg liraglutide group, because this dose given twice daily in rats can be converted to the human equivalent dose of 1.92 mg/day, assuming a 60-kg human, according to FDA^S guidance [8] (i.p.) for 7 days prior to MCAO [9]. The remaining drug was stored in a refrigerator at 4°C. The rats in the sham group with normal blood glucose and ischemia group with normal blood glucose were injected with sterile sodium citrate buffer. The diabetic cerebral ischemia liraglutide group and normal blood glucose cerebral ischemia liraglutide group were given a lower left abdominal cavity injection of liraglutide at 100 µg/kg, every 12 h for 7 days after MCAO. The rats in the sham group with normal blood glucose and diabetic cerebral ischemia group were injected with an equal volume of normal saline.

2.5. Neurological Deficit Scores and Determination of Cerebral Infarct Volume. Neurological functions were evaluated according to 5-point scoring criterion of Longa et al. [7]: 0 points, no neurological deficit; 1 point, failure to extend left forepaw fully; 2 points, circling to the left; 3 points, falling to the left; and 4 points, no walking spontaneously and having a depressed level of consciousness. The first evaluation was performed 3 h after the operation, and animals that were given a score of 0 or 4 were excluded (except the sham operation group). Neurological function was reappraised at 24 and 48 h after the MCAO.

Infarct volume was examined 48 h after MCAO; the rats were anesthetized with chloral hydrate (10%, stored in 4°C refrigerator) and decapitated. The brains were quickly removed and placed in cold saline for 5 min. The tissues were cut at 2-mm intervals from the frontal pole to obtain five coronal sections that were stained with 2% 2,3,5-triphenyltetrazolium chloride (TTC; Sigma, USA) for 30 min followed by overnight immersion in 10% formalin. The infarcted regions were quantified by assessing each section with Image J software (National Institutes of Health, Bethesda, Maryland, USA). The infarct size as a percentage of the whole brain was calculated [10].

2.6. Measurement of Superoxide Dismutase (SOD) and Myeloperoxidase (MPO) Activity in Brain Tissue Homogenate. The rats were sacrificed at 48 h after MCAO and brains were rapidly removed. Brain tissue samples (about 100 mg) were obtained, and a homogenate (10%) was prepared by homogenizing the sample in normal saline at 1:9 ratio, and the supernatant was obtained by refrigerated centrifugation (10 min, 3000 rpm) to measure superoxide dismutase (SOD) and myeloperoxidase (MPO) activity. SOD activity in the brain tissue was determined according to the method described by Kakkar et al. [11]. A xanthine and xanthine oxidase system was used to generate superoxide radicals, which reacted with *p*-iodonitrotetrazolium violet (INT), converting it into a red formazan product. Spectrometry was used to measure absorbance of the sample at 550 nm. MPO activity in the brain tissue was determined according to the

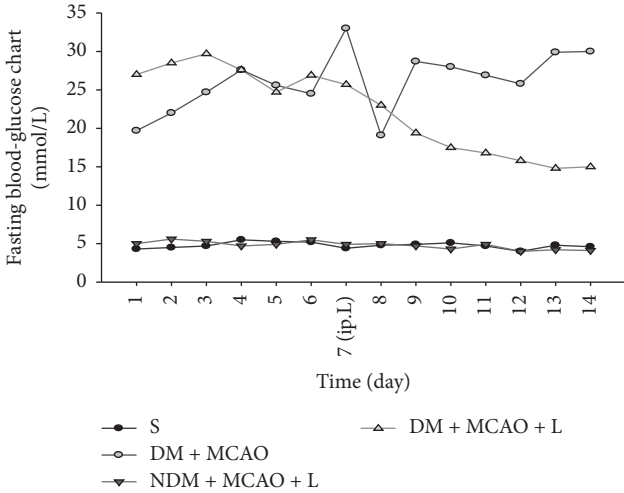


FIGURE 1: Fasting blood glucose concentrations. There was no change in blood glucose in the sham group and blood glucose in the NDM + MCAO + L, DM + MCAO and DM + MCAO + L groups increased significantly ($P < 0.05$); after liraglutide administration, the blood glucose level in the DM + MCAO + L group decreased significantly when compared with that in DM + MCAO group ($P < 0.05$). Values are mean \pm SD, $n = 12$, all $P < 0.05$.

method previously described [12]. Briefly, MPO activity was measured by the hydrogen peroxide reduction method.

SOD and MPO activities were expressed as U/mg protein. The SOD kit (A001-1) and MPO kit were obtained from Nanjing Jiancheng Bioengineering Institute (Nanjing Jiancheng, China).

2.7. Measurement of Nrf2 and HO-1 Protein Expression in Brain Tissue. At 48 h after MCAO, the rats ($n = 6$ per group) were anesthetized with chloral hydrate (10%, stored in 4°C refrigerator) and decapitated. The brains were quickly removed and stored in a -80°C freezer. Total proteins in the cerebral cortex samples were extracted as previously described. Nuclear proteins in the cortical tissues were isolated using RIPA lysis buffer and Cytoplasmic Extraction Reagents (Boster Company, Wuhan, China) according to the manufacturer's instructions. Protein concentrations were determined by using the bicinchoninic acid protein assay with bovine serum albumin as the standard [13] (McConkey, 1984). Protein expression was detected as follows. In brief, the protein samples (20 mg) were separated on 10% sodium dodecyl sulfate-polyacrylamide gels and then transferred to a nitrocellulose membrane. The membrane was blocked with 5% nonfat dry milk in Tris-buffered saline with Tween-20 (TBST) and incubated overnight at 4°C with rabbit anti-rat Nrf2 monoclonal antibody (1:1000; Abcam Company, USA) and rabbit anti-rat HO-1 monoclonal antibody (1:2000; Abcam Company). Rabbit anti-rat β -actin monoclonal antibody (1:5000; Boster Company, Wuhan, China) was used for the internal control. After extensive rinsing with TBST, the membranes were incubated with goat anti-rabbit IgG conjugated with horseradish peroxidase (1:8000; Boster Company, Wuhan, China) for 1 h at 37°C. Bound antibody was detected by using an enhanced chemiluminescence detection system

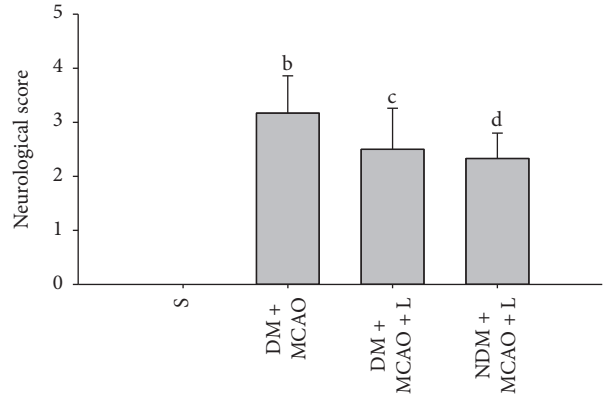


FIGURE 2: Neurological deficit score in each group. In the sham operation group, the neurological deficit score was 0. The neurological deficit score in the DM + MCAO + L group was significantly lower than in the DM + MCAO group (bc $P < 0.05$); DM + MCAO + L and NDM + MCAO + L groups did not differ significantly in neurological deficit score (cd $P > 0.05$). Values are mean \pm SD, $n = 12$, all $P < 0.05$.

(ECL, Boster Company, Wuhan, China) and exposure of membranes to X-ray films. The ratio of optical density value as protein expression in each sample was analyzed with Image J software.

2.8. Statistical Analysis. SPSS 13.0 software was used for statistical analysis. The results were expressed as mean \pm SEM for normally distributed data. One-way analysis of variance (ANOVA) was used to analyze the difference between multiple means. The LSD *t*-test was used to analyze the difference between two groups. $P < 0.05$ was considered statistically significant.

3. Results

3.1. Blood Glucose Measurement. In 24 h after the diabetes model was established, tail vein blood glucose of each rat was monitored regularly for 14 days. Blood glucose in the DM + MCAO and DM + MCAO + L groups increased significantly compared with the S group ($P < 0.05$). In addition, rats treated with liraglutide reduced blood glucose levels in DM + MCAO + L groups ($P < 0.05$) (Figure 1). These results indicated the diabetes model was deemed successful and the liraglutide reduced blood glucose levels.

3.2. Neurological Deficit Evaluation. The neurological deficit score showed that there was no neurological deficit in the sham operation group (score 0). Liraglutide decreased the neurological deficit score in the DM + MCAO + L and NDM + MCAO + L groups ($P < 0.05$) (Figure 2). The DM + MCAO + L and NDM + MCAO + L groups have no significant difference in neurological deficit score ($P > 0.05$) (Figure 2). The result indicated that the liraglutide improved neurological deficit score in rats after MCAO.

3.3. Cerebral Infarction Volume. TTC staining showed that no infarct was observed in sham operation group. Liraglutide

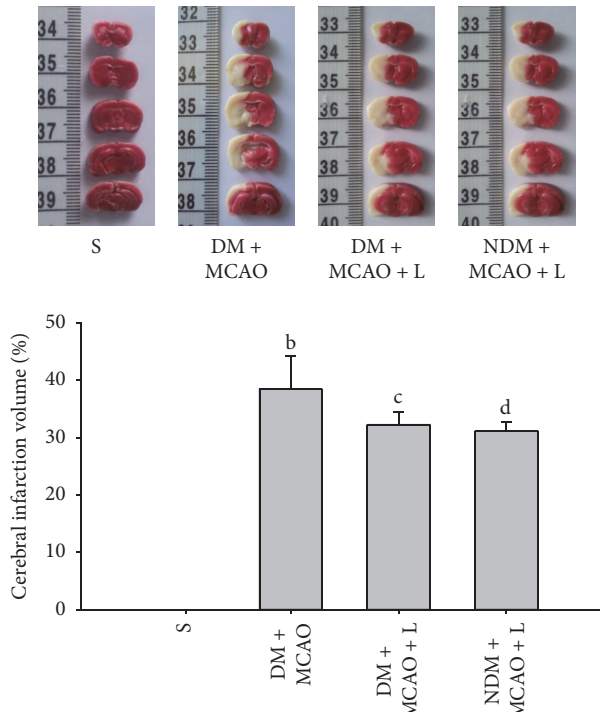


FIGURE 3: Cerebral infarction volume in each group. There was no cerebral infarction in the S group; the infarction volume in the S group was significantly lower than in the other cerebral ischemia group ($P < 0.05$). The infarction volume in the DM + MCAO + L group was significantly lower than in the DM + MCAO group ($cb P < 0.05$). The DM + MCAO + L and NDM + MCAO + L groups did not differ significantly in infarction volume ($cd P > 0.05$). Values are mean \pm SD, $n = 6$, all $P < 0.05$.

decreased infarct volume in the DM + MCAO + L and NDM + MCAO + L groups ($P < 0.05$) (Figure 3). But comparing the DM + MCAO + L group and NDM + MCAO + L group, there was no significant difference ($P > 0.05$) (Figure 3). The result indicated that the liraglutide attenuated cerebral infarction volume in diabetic rats after MCAO.

3.4. Determination of SOD and MPO Activity. After the injection of liraglutide the results showed differences in experimental groups respectively ($P < 0.01$). Liraglutide increased SOD and decreased MPO activity levels in the DM + MCAO + L and NDM + MCAO + L groups ($P < 0.05$) (Figures 4 and 5). But the NDM + MCAO + L and DM + MCAO + L groups have no significant difference in SOD and MPO activity ($P > 0.05$) (Figures 4 and 5). The result indicated that liraglutide increases antioxidant SOD and decreases inflammatory substance MPO in diabetic rats after MCAO.

3.5. Western Blot. Western blot results show that there are significant differences in the expression levels of Nrf2 and HO-1 in experimental groups respectively ($P < 0.01$) (Figure 6). Liraglutide decreased the expression levels of Nrf2 and HO-1 in the NDM + MCAO + L and DM + MCAO + L groups ($P < 0.05$) (Figure 6). But the NDM + MCAO + L and DM + MCAO + L groups have no significant difference

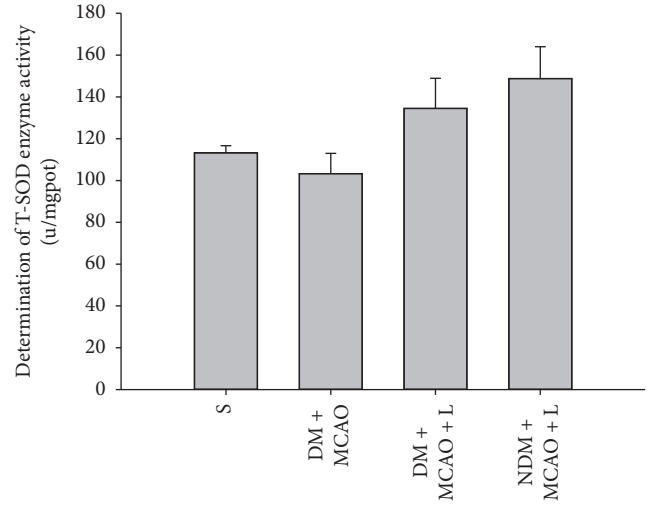


FIGURE 4: SOD activity in each group. There are significant differences in SOD activity levels between the S, DM + MCAO, NDM + MCAO + L, and DM + MCAO + L groups ($P < 0.01$); SOD activity in the NDM + MCAO + L and DM + MCAO + L groups is significantly higher than in the DM + MCAO group ($P < 0.05$). SOD activity levels in the NDM + MCAO + L and DM + MCAO + L groups did not differ significantly ($P > 0.05$). Values are mean \pm SD, $n = 6$, all $P < 0.05$.

in expression levels of Nrf2 and HO-1 ($P > 0.05$) (Figure 6). The result indicated that Nrf2 and HO-1 expression were upregulated in diabetic rats after MCAO and the liraglutide injection augmented expression of Nrf2 and HO-1 in the cerebral ischemia tissue.

4. Discussion

Diabetes is a chronic disease and a serious threat to human health. It is often complicated with cardiac and cerebral vascular diseases. Previous studies have shown that DM is an independent risk factor for cerebral infarction and/or poor prognosis [14]. This study demonstrates that, in the diabetic rats with cerebral ischemia, neurological symptoms are more serious than in other groups. Data in current investigation indicated that neurological deficit scores in diabetic rats with cerebral ischemia were higher compared with those in other groups. We also found that the infarction area in rats with DM and ischemia was significantly greater than in normal blood glucose rats with ischemia. These findings suggest that DM is one of the important factors leading to cerebral ischemia exacerbation.

In recent years, more and more studies have proved that oxidative stress is one of the important factors in diabetes that aggravate the damage in ischemic brain tissue [15, 16]. It has been shown that, in diabetes, the systemic and local inflammatory reaction is enhanced and the levels of serum inflammatory markers are increased. Regardless of the duration of DM, oxidative stress and the expression of antioxidative stress factors are observed in various tissues of patients. Therefore, it is suggested that diabetes is associated with cerebral ischemia and oxidative stress [17].

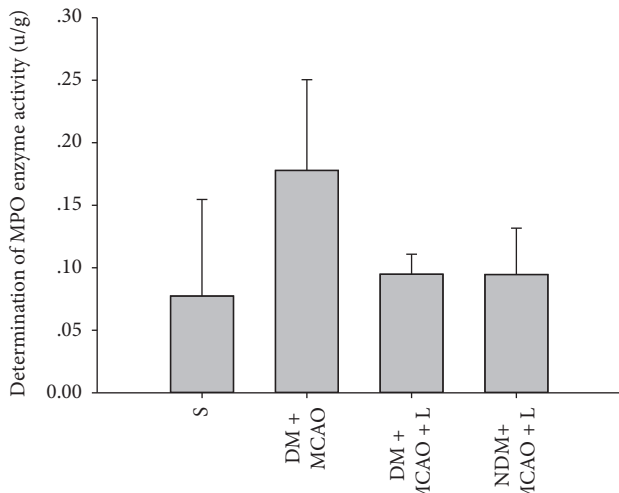


FIGURE 5: MPO activity in each group. There were significant differences in MPO activity levels in the S, DM + MCAO, NDM + MCAO + L, and DM + MCAO + L groups ($P < 0.01$). MPO activity in the NDM + MCAO + L and DM + MCAO + L groups is significantly higher than in the DM + MCAO group ($cdb P < 0.05$). MPO activity levels in the NDM + MCAO + L and DM + MCAO + L groups have no significant difference ($cd P > 0.05$). Values are mean \pm SD, $n = 6$, all $P < 0.05$.

Nrf2 is one of the most important nuclear transcription factors in eukaryotic cells. When the occurrence of diabetes complicated with cerebral infarction, the Nrf2/HO-1 signaling pathway is activated and regulates other antioxidant enzymes and phase II detoxifying enzymes. These enzymes can be against the damage of nerve cells.

Previous studies have shown that overexpression of Nrf2 can significantly reduce ischemic brain injury [17]. It has been confirmed that there is oxidative stress injury in ischemic neuronal cells immediately after the cerebral ischemia occurs and that the mechanism of antioxidative stress is activated. The expression of nuclear transcription factor Nrf2 and downstream HO-1 was significantly increased. Many studies have shown that when cerebral ischemia occurs, Nrf2 is activated in neuronal cells, vascular endothelial cells, and glial cells [18]. Meanwhile, it prompts the expression of the downstream of antioxidant proteasome, phase II detoxifying enzymes, and HO-1 protein. Thus, Nrf2 is considered to be one of the initiating mechanisms of cerebral ischemia and oxidative stress. Tu et al. found that, in a permanent cerebral ischemia mouse model, exposure to 20 mmol/L tBHQ for 6 hours after ischemia significantly decreased infarct size [19], and at the same time, Nrf2 and HO-1 expression increased. However, this phenomenon cannot be found in Nrf2 knockout mice. Jiang et al. showed that oxymatrine protected neurons after cerebral ischemia/reperfusion injury by activating the Nrf2/HO-1 signaling pathway [20]. Oxymatrine increased Nrf2 and HO-1 expression in the cerebral cortex, after 6 h in the cerebral ischemia/reperfusion model, which peaked at 48 h, while ischemic infarction and edema were significantly reduced. It had a clear protective effect in ischemic nerve cells.

Our study shows that the DM with cerebral ischemia group has significantly increased expression of Nrf2 and HO-1 compared to the sham operation group. The expressions of Nrf2 and HO-1 are involved in the process of occurrence and development of diabetes complicated with cerebral ischemia. In addition, the expression of Nrf2 and HO-1 is significantly lower in DM with cerebral ischemia group than in the normal blood glucose with cerebral ischemia group, which suggests that diabetes can aggravate the injury to ischemic cells. It is also one of the important mechanisms of diabetic cerebral ischemia injury.

4.1. Nrf2 Can Regulate the Expression of HO-1 Protein. The oxidative/antioxidant system is activated when diabetes complicated with cerebral ischemia occurs. The oxidation of substances increases substantially in cells, producing large amounts of oxygen free radicals, and increased SOD activity may be a direct response to the extent of oxygen free radical scavenging [21]. After the occurrence of diabetes complicated with cerebral ischemia, the inflammatory reaction is considered another important factor in aggravating brain cell injury. MPO is an important factor in the inflammatory response, the determination of the increase of MPO can be confirmed to be one of the mechanisms of cerebral ischemia aggravated diabetes [22].

The results show that SOD and MPO are significantly higher in the diabetes complicated with cerebral ischemia group than in the sham operation group, and it is confirmed that DM is one of the most important factors in cerebral ischemia injury. The liraglutide pretreatment diabetes ischemia group of SOD and MPO enzyme increases significantly compared to the diabetes complicated with cerebral ischemia group. It can explain that the liraglutide has anti-inflammatory and protective effect of ischemic brain cells.

Many past studies have demonstrated that liraglutide has an antioxidative effect [23]. It can protect nerve cells from cerebral ischemic injury. It has a clear protective effect on injured myocardial cells, islet cells, nerve cells, and so on.

There had been no earlier studies showing a neuroprotective effect of liraglutide in diabetic rats with cerebral ischemia injury. This study demonstrates that liraglutide has a protective effect on brain nerve cells in rats with diabetes mellitus combined with cerebral ischemic neuronal injury. The western blot findings for Nrf2 and HO-1 expression levels have showed that the protective effect of liraglutide on brain nerve cells in diabetes complicated with cerebral ischemia injury may be through the activation of the Nrf2/HO-1 signaling pathway.

Further *in vitro* studies are needed to elucidate the molecular mechanism of liraglutide against diabetic cerebral ischemia.

5. Conclusion

Liraglutide's alleviating effects on diabetes complicated with cerebral ischemia injury rats may be related to upregulation of Nrf2/HO-1 protein expression. Our findings have shed light on the effects of liraglutide, and further study is necessary to determine its mechanism *in vitro*.

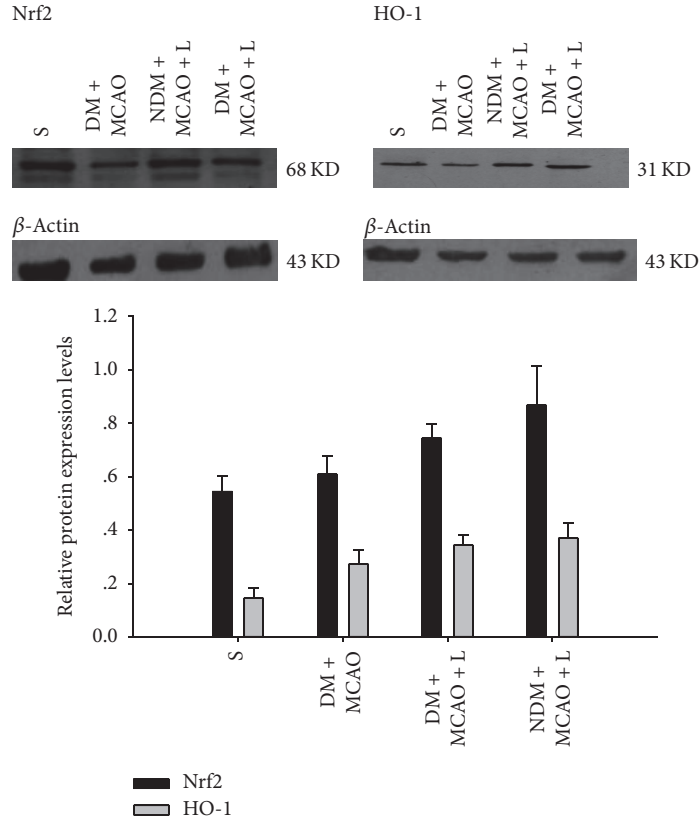


FIGURE 6: Western blot measurement of Nrf2 and HO-1 protein expression. There are significant differences in the expression levels of Nrf2 and HO-1 between the sham, DM + MCAO, NDM + MCAO + L, and DM + MCAO + L groups ($P < 0.01$). Nrf2 and HO-1 expression in the NDM + MCAO + L and DM + MCAO + L groups is significantly higher than in the DM + MCAO group ($P < 0.05$), but the NDM + MCAO + L and DM + MCAO + L groups have no significant difference in Nrf2 and HO expression levels ($P > 0.05$). Values are mean \pm SD, $n = 6$, all $P < 0.05$.

Disclosure

Caihong Deng and Jun Cao are co-authors.

Conflicts of Interest

The authors declare that there are no conflicts of interest regarding the publication of this paper.

Authors' Contributions

Jiangquan Han has conceived and designed this study. Caihong Deng and Jun Cao have performed experiments and wrote this paper. Caihong Deng is responsible for data collection, analysis, and interpretation and participated in the writing of this paper. The final version of this paper has been approved by all authors. Caihong Deng and Jun Cao contributed equally to this work.

Acknowledgments

This study was supported by a grant from the Zhuhai Key Discipline Project, no. 200880.

References

- [1] D. Mozaffarian, E. J. Benjamin, and A. S. Go, "Executive summary: heart disease and stroke statistics—2016 update: a report from the American Heart Association," *Circulation*, vol. 133, pp. 447–454, 2016.
- [2] A. G. Thrift, D. A. Cadilhac, T. Thayabaranathan et al., "Global stroke statistics," *International Journal of Stroke*, vol. 9, no. 1, pp. 6–18, 2014.
- [3] R. Meierhans, M. Béchir, S. Ludwig et al., "Brain metabolism is significantly impaired at blood glucose below 6 mM and brain glucose below 1 mM in patients with severe traumatic brain injury," *Critical Care*, vol. 14, no. 1, article no. R13, 2010.
- [4] T. Vilsbøll, "Liraglutide: A new treatment for type 2 Diabetes," *Drugs of Today*, vol. 45, no. 2, pp. 101–113, 2009.
- [5] K. Sato, M. Kameda, T. Yasuhara et al., "Neuroprotective effects of liraglutide for stroke model of rats," *International Journal of Molecular Sciences*, vol. 14, no. 11, pp. 21513–21524, 2013.
- [6] N. Sun, G. Yang, H. Zhao, H. F. J. Savelkoul, and L. An, "Multidose streptozotocin induction of diabetes in BALB/c mice induces a dominant oxidative macrophage and a conversion of TH1 to TH2 phenotypes during disease progression," *Mediators of Inflammation*, vol. 2005, no. 4, pp. 202–209, 2005.

- [7] E. Z. Longa, P. R. Weinstein, S. Carlson, and R. Cummins, "Reversible middle cerebral artery occlusion without craniectomy in rats," *Stroke*, vol. 20, no. 1, pp. 84–91, 1989.
- [8] F. D. Administration, "Guidance for industry: estimating the maximum safe starting dose in initial clinical trials for therapeutics in adult healthy volunteers," 2005.
- [9] V. Darsalia, S. Mansouri, H. Ortsäter et al., "Glucagon-like peptide-1 receptor activation reduces ischaemic brain damage following stroke in type 2 diabetic rats," *Clinical Science*, vol. 122, no. 10, pp. 473–483, 2012.
- [10] R. A. Frieler, H. Meng, S. Z. Duan et al., "Myeloid-specific deletion of the mineralocorticoid receptor reduces infarct volume and alters inflammation during cerebral ischemia," *Stroke*, vol. 42, no. 1, pp. 179–185, 2011.
- [11] P. Kakkar, B. Das, and P. N. Viswanathan, "A modified spectrophotometric assay of superoxide dismutase," *Indian Journal of Biochemistry and Biophysics*, vol. 21, no. 2, pp. 130–132, 1984.
- [12] L. M. Hillefass, D. E. Griswold, B. Brickson, and C. Albrightson-Winslow, "Assessment of myeloperoxidase activity in whole rat kidney," *Journal of Pharmacological Methods*, vol. 24, no. 4, pp. 285–295, 1990.
- [13] J. F. Meschia, C. Bushnell, B. Boden-Albala et al., "Guidelines for the primary prevention of stroke: a statement for healthcare professionals from the American Heart Association/American Stroke Association," *Stroke*, vol. 45, no. 12, pp. 3754–3832, 2014.
- [14] N. Kostulas, I. Markaki, H. Cansu, T. Masterman, and V. Kostulas, "Hyperglycaemia in acute ischaemic stroke is associated with an increased 5-year mortality," *Age and Ageing*, vol. 38, no. 5, pp. 590–594, 2009.
- [15] M. Vijayan and P. H. Reddy, "Peripheral biomarkers of stroke: focus on circulatory microRNAs," *Biochimica et Biophysica Acta*, vol. 1862, no. 10, pp. 1984–1993, 2016.
- [16] F. Santilli, D. Lapenna, S. La Barba, and G. Davi, "Oxidative stress-related mechanisms affecting response to aspirin in diabetes mellitus," *Free Radical Biology & Medicine*, vol. 80, pp. 101–110, 2015.
- [17] E. Forsberg, C. Xu, J. Grünler et al., "Coenzyme Q10 and oxidative stress, the association with peripheral sensory neuropathy and cardiovascular disease in type 2 diabetes mellitus," *Journal of Diabetes and its Complications*, vol. 29, no. 8, pp. 1152–1158, 2015.
- [18] D. Zagoura, D. Canovas-Jorda, F. Pistollato, S. Bremer-Hoffmann, and A. Bal-Price, "Evaluation of the rotenone-induced activation of the Nrf2 pathway in a neuronal model derived from human induced pluripotent stem cells," *Neurochemistry International*, vol. 106, pp. 62–73, 2017.
- [19] J. Tu, X. Zhang, Y. Zhu et al., "Cell-permeable peptide targeting the Nrf2-keap1 interaction: A potential novel therapy for global cerebral ischemia," *The Journal of Neuroscience*, vol. 35, no. 44, pp. 14727–14739, 2015.
- [20] G. Jiang, X. Liu, M. Wang, H. Chen, Z. Chen, and T. Qiu, "Oxy-matrine ameliorates renal ischemia-reperfusion injury from oxidative stress through Nrf2/HO-1 pathway," *Acta Cirurgica Brasileira*, vol. 30, no. 6, pp. 422–429, 2015.
- [21] Z. Yang, C. Weian, H. Susu, and W. Hanmin, "Protective effects of mangiferin on cerebral ischemia-reperfusion injury and its mechanisms," *European Journal of Pharmacology*, vol. 771, pp. 145–151, 2016.
- [22] S.-S. Shi, W.-Z. Yang, Y. Chen, J.-P. Chen, and X.-K. Tu, "Propofol reduces inflammatory reaction and ischemic brain damage in cerebral ischemia in rats," *Neurochemical Research*, vol. 39, no. 5, pp. 793–799, 2014.
- [23] H. Fujita, T. Morii, H. Fujishima et al., "The protective roles of GLP-1R signaling in diabetic nephropathy: possible mechanism and therapeutic potential," *Kidney International*, vol. 85, no. 3, pp. 579–589, 2014.

Research Article

Selection of the Optimal Algorithm for Real-Time Estimation of Beta Band Power during DBS Surgeries in Patients with Parkinson's Disease

Ángeles Tepper,¹ Mauricio Carlos Henrich,¹ Luciano Schiaffino,¹ Alfredo Rosado Muñoz,² Antonio Gutiérrez,³ and Juan Guerrero Martínez²

¹*Laboratory of Rehabilitation Engineering, National University of Entre Ríos, Oro Verde, Argentina*

²*Group for Digital Design and Processing (GDDP), ETSE, Department of Electronic Engineering, University of Valencia, Valencia, Spain*

³*Functional Neurosurgery Unit, La Fe Hospital, Valencia, Spain*

Correspondence should be addressed to Alfredo Rosado Muñoz; alfredo.rosado@uv.es

Received 31 August 2017; Accepted 29 November 2017; Published 24 December 2017

Academic Editor: Plácido R. Pinheiro

Copyright © 2017 Ángeles Tepper et al. This is an open access article distributed under the Creative Commons Attribution License, which permits unrestricted use, distribution, and reproduction in any medium, provided the original work is properly cited.

Deep Brain Stimulation (DBS) is a surgical procedure for the treatment of motor disorders in patients with Parkinson's Disease (PD). DBS involves the application of controlled electrical stimuli to a given brain structure. The implantation of the electrodes for DBS is performed by a minimally invasive stereotactic surgery where neuroimaging and microelectrode recordings (MER) are used to locate the target brain structure. The Subthalamic Nucleus (STN) is often chosen for the implantation of stimulation electrodes in DBS therapy. During the surgery, an intraoperative validation is performed to locate the dorsolateral region of STN. Patients with PD reveal a high power in the β band (frequencies between 13 Hz and 35 Hz) in MER signal, mainly in the dorsolateral region of STN. In this work, different power spectrum density methods were analyzed with the aim of selecting one that minimizes the calculation time to be used in real time during DBS surgery. In particular, the results of three nonparametric and one parametric methods were compared, each with different sets of parameters. It was concluded that the optimum method to perform the real-time spectral estimation of beta band from MER signal is Welch with Hamming windows of 1.5 seconds and 50% overlap.

1. Introduction

Parkinson's Disease (PD) is a common neurodegenerative disorder. Many successful pharmacological therapies and strategies have been developed to treat both the motor and nonmotor manifestations of PD. However, as PD progresses, it often becomes difficult to treat, typically because of motor complications. In these cases, Deep Brain Stimulation (DBS) is a therapy used to treat PD. Most recently, DBS is also being used in early stages of PD [1].

DBS involves the application of controlled electrical stimuli to a given brain structure by implanted stimulation electrodes. The implantation of the electrodes for DBS is performed by a minimally invasive stereotactic surgery where neuroimaging and microelectrode recordings (MER) are used to locate the target brain structure (Figure 1).

Neuroimaging studies, both Computerized Tomography (CT) and Magnetic Resonance Images (MRI), are used for surgery planning and validation of the implantation site. MER are obtained by recording the neuronal electrical activity using micro EEG technique during implantation surgery and they are used to perform an intraoperative validation of the electrode position. MER signals recorded during surgery are the sum of a variety of signals generated by several neural processes and elements. The extracellular activity captured by MER can be divided into three categories: Local Field Potential (LFP) < 300 Hz, Multi-Unit Activity (MUA) > 300 Hz, and single-unit activity.

For PD, the Subthalamic Nucleus (STN) is often chosen as the target brain structure (Figure 1) [2]. During implantation surgery, an intraoperative validation is performed to locate the dorsolateral region of STN (Figure 1). For these

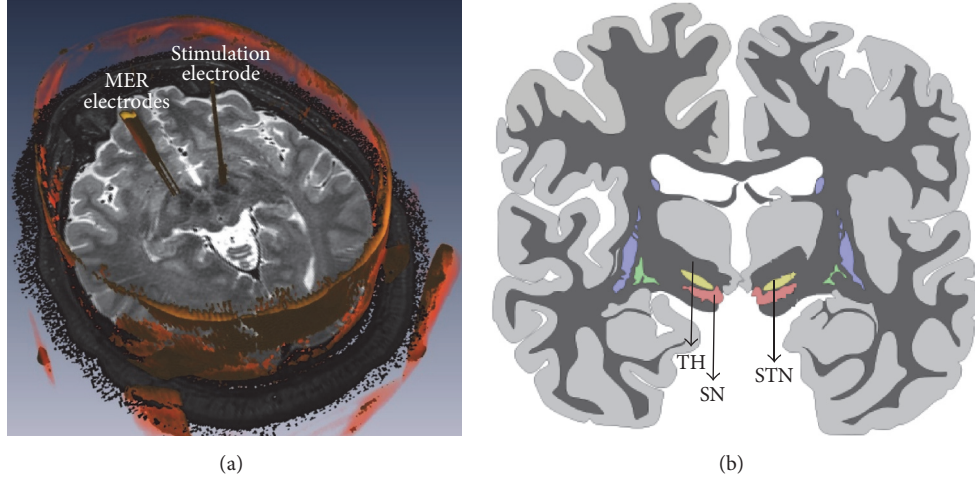


FIGURE 1: (a) MER and stimulation electrodes in STN during a DBS surgery. (b) Basal nuclei of the brain: TH: Thalamus, STN: Subthalamic Nucleus, and SN: Substantia Nigra.

validations, temporal characteristics of MER are used. That is, in order to locate the STN, MER signals are visually analyzed and it is sought to recognize the location where the electrode is located at each moment of the implantation surgery. This validation method requires a highly trained medical team.

Several researchers ([3–5]) demonstrated that STN's MER in humans with PD reveal a high power in the β band (frequencies between 13 Hz and 35 Hz), mainly in the dorsolateral region of that subcortical nucleus. In addition, this is the same region providing optimal therapeutic benefits for patients with PD who undergo DBS in the STN [4]. Therefore, research has been carried out to obtain frequency information, which could be valuable to locate the electrode implantation site [6]. Performing signal processing in the operating room to retrieve frequency information would imply having a complementary tool to those currently used, providing to the medical team more information for the selection of the best stimulation site.

From the mathematical point of view, in order to be able to retrieve frequency information from MER, and since the signals are random and only one segment of them is available, an estimation of the power spectrum must be considered [7]. There are different methods for power spectrum density (PSD) estimation of a random signal. In the literature, Welch's algorithm with 1 s Hamming window and 50% overlap is mostly used as the method for PSD estimation of MER signals ([5, 8–12]).

However, for β band power detection in real time during DBS surgery, it is necessary to explore algorithms that minimize PSD calculation time. In this work, different PSD methods were analyzed with the purpose of selecting the one that allows the calculation of the β band power of MER signals in real time during DBS electrodes implantation surgery. Section 2 describes the used data obtained from patients who were implanted with a brain stimulator and it details the followed signal processing methodology. Section 3 describes the obtained results. Finally, discussion and conclusions are given in Sections 4 and 5, respectively.

2. Materials and Methods

2.1. Patients and Data Collection. For this study, MER recordings obtained from bilateral surgery performed on 9 patients with PD undergoing the implantation of stimulation electrodes for DBS in the STN were used. The surgical interventions took place at La Fe Hospital, in Valencia, Spain.

The recordings were obtained with the “MicroGuide” system (AlphaOmega Engineering, Nazareth, Israel). Neurophysiological activity was recorded through polyamide-coated tungsten microelectrodes (Alpha Omega). The signal was amplified 10000 times and it was filtered with a bandpass filter between 200 and 6000 Hz, using a 4th order Butterworth filter for the low cutoff frequency and 2nd order for the high cutoff frequency. The sampling frequency was 12 kHz, and a 12-bit analog/digital converter was used.

Filtering the recordings with a high-pass filter with cutoff frequency at 200 Hz implies that these signals are MUA and not LFP. This selection of filters, however, is helpful to avoid the recording of electrical noise in the operating room [5]. Despite the fact that the recorded signals do not include low frequencies where β band is located, Section 3.2 describes the method used to analyze the β band.

During electrode implantation surgery, two parallel MERs in each brain hemisphere were moved in small discrete steps of 0.2 mm starting at 8 mm above the calculated target (center of the dorsolateral STN). The recording times in each depth were variable (between 0.43 s and 278.92 s). In the study conducted by [6] it was determined that, when using power spectral density for STN detection, recordings should not be shorter than one second. For this reason, recordings shorter than 1 s were discarded. Thus, recording times between 1.56 s and 278.92 s with a mean of 48.54 s and a standard deviation of 26.94 s were obtained.

2.2. Signal Processing. Signal processing and data analysis were performed with MATLAB software V8.5 R2015a (Mathworks, Natick, MA, USA) using *Signal Processing Toolbox*.

To compare the results of the different spectral estimators studied, a statistical analysis was performed using MATLAB *Statistics Toolbox*.

2.2.1. Signal Stability. As reported by other authors ([5, 6, 8]), due to surgical conditions such as electrode tip movements and/or neuronal lesions, it is necessary to select the most stable segment from the MER recording at each depth.

To assess signal stability, the strategy outlined by [5] was followed, but adding an energy threshold condition prior to RMS calculation.

First, signals values whose modulus exceeded $150 \mu\text{V}$ were replaced by zeros (the action potentials have typical values of $60 \mu\text{V}$, possibly reaching $100 \mu\text{V}$ [9], but there were long portions of signals with high energy in some particularly unstable recordings). Then, each signal was divided into consecutive segments of 50 ms and the RMS of each segment was calculated. A portion of the signal was considered stable when the RMS values of all of the segments fulfilled the following condition:

$$\text{RMS}_{50\text{ ms}} = \text{RMS}_{\text{median}} \pm 3\text{SD}, \quad (1)$$

where SD is the standard deviation of the RMS of all of the 50 ms segments of the signal.

This stability analysis rejects infrequent events, such as glitches (spurious electronic signals caused by peaks in electrical energy) or cell damage, but does not reject oscillatory activity greater than 1 Hz [5]. The longest stable portion of each signal was selected to continue the analysis, discarding the rest of the recording.

2.2.2. Rectification and Filtering. MER signals are produced by the superposition of multiple electrical sources corresponding to several neural processes. Since the acquisition was performed with a high-pass online filter with cutoff frequency at 200 Hz, the signals used in this work are MUA signals; that is, they are composed by background activity and action potentials from neurons close to the recording electrode.

Because of this acquisition strategy, it is impossible to perform a direct frequency analysis in ranges lower than 200 Hz, which are the ones of interest in this study (β band frequencies: 13 Hz to 35 Hz).

In [13], it is shown that MER signals acquired using a high-pass filter can recover its low frequency oscillatory components via the extraction of their envelope, since there is a low frequency modulation in the amplitude of the high frequency signals (MUA). In order to perform frequency analysis in lower frequency ranges, this modulation information needs to be retrieved.

In this study, the strategy proposed by [13] was followed. The low frequency envelope can be calculated following a two-step procedure: extraction of the instantaneous power of the signal by the absolute value operator and smoothing using a low-pass filter. In addition, the mean of the envelope signal was subtracted, given that some methods of power spectrum estimation assume that the signal has zero mean. The power spectrum of a nonzero mean signal has a zero

frequency pulse; if the mean is relatively large, it may obscure the components of the low amplitude and low frequency spectrum. Despite the fact the estimation is not an exact value, removing the mean value provides better estimation, especially for low frequencies [7].

Summarizing, to obtain the envelope, these steps were followed:

- (i) Full wave rectification: absolute value of each signal sample.
- (ii) Extraction of the mean.
- (iii) Smoothing to obtain the envelope: 4th order Butterworth low-pass filter: cutoff frequency at 100 Hz.

2.3. Power Spectrum Estimation. In studies where the β power of MER signals is obtained ([5, 8–12]), there is a systematic use of Welch's method with 1 s Hamming windows and 50% overlap. However, in order to be able to do an intraoperative validation of the electrode position during implantation surgeries, the β band power detection must be achieved in real time, that is, the shorter time possible. Thus, it is necessary to explore algorithms that minimize PSD calculation time.

In this work, different PSD methods were analyzed with the purpose of selecting the one that allows the calculation of the β band power of MER signals in real time during DBS electrodes implantation surgery.

First, it was decided to compare different power spectrum estimation methods in order to identify other methods that could also be used. For this, after performing spectral estimation with different methods, a statistical analysis was performed to find significant differences among them. Then the computation time of some of the methods was compared.

In all spectrum estimations, parameters were adjusted to achieve a frequency resolution of 0.1 Hz.

2.3.1. Nonparametric Estimation Methods. Nonparametric methods for power spectrum estimation are based exclusively on the available data, without making any assumptions about the system that generates them. Due to the analyzed signals characteristics, it seems appropriate to use such an estimation method.

In this study, three nonparametric techniques of PSD estimation were analyzed, which are described below.

Periodogram. This is the most basic nonparametric method based on the calculation of the Fourier Transform. By definition, the periodogram is not a consistent estimator [7]. Therefore, although the actual spectrum of the signal is unknown, it can be assumed that this estimation is not convenient. However, as it is the basis of other methods, it was decided to evaluate its results.

Welch's Method. Dividing the recordings into segments before calculating the periodogram reduces the estimation variance. Moreover, the length of those segments has an impact on the frequency resolution of the estimation [14]. Welch's method is based on this procedure: the overlap of the segments makes it possible to increase the number of segments (reducing

variance) without reducing its length in order to not lose resolution. If segments are shorter, the estimation has worse resolution but better (less) variance.

In this study, the results of three different window sizes were compared, always with an overlap of 50%:

- (i) 0.5-second Hamming window.
- (ii) 1-second Hamming window. This is the most used window length in the consulted bibliography.
- (iii) 1.5-second Hamming window.

Multitaper Method. This method reduces variance using different windows but all with the same length of the signal [7]. Since length is not reduced, the total bias is less than that obtained using signal segments. The time-bandwidth (NW) parameter balances this estimator resolution and variance. When NW increases, the variance decreases, but each estimate has higher spectral leakage and the resulting spectral estimator has more bias.

To use this method, it is necessary to define the set of windows used and the NW parameter, which is related to the number of windows. In this work, the DPSS set of windows, proposed by Thomson, was always used. In order to select NW value, the values used in the consulted bibliography ([15, 16]) were taken into account, where typical values were found to be between 2 and 6. It was decided to analyze the results of this estimator with typical extreme values of NW. Thus, the multitaper method was analyzed with NW = 2 and NW = 6.

2.3.2. Parametric Estimation Methods. Although MER signals characteristics do not seem to be described by a simple parametric model as they come from a system of great complexity, an autoregressive model (AR) was decided to be applied.

The order of the AR model provides a balance between bias and variance [17]. For a small order, the spectrum may not be well estimated (large bias) but it will have less variance. For a large order, the spectrum will exhibit lower bias but may have a lot of variances.

AR Model with Burg Coefficients. An AR model with the coefficients calculated by the Burg method was chosen. Regarding the order of the model, it was decided to compare AR models of two different orders. Two orders were selected within the margins of the values used in other studies ([18, 19]). The power spectrum was then estimated using AR model, 4th order, and AR model, 15th order.

2.4. Statistical Comparison of Spectral Estimators. A statistical analysis was performed to compare the results of the different spectral estimators studied. For this, all of the signals coming from the 28 trajectories were used (each trajectory contained several signals, each of a different recording depth). In total, 1010 signals were used.

Since there were few samples and the distribution of the samples was unknown, it was decided to work with Friedman's nonparametric method. This test was applied to two matrices. In both cases, each column represented a method

of power spectral estimation and each row represented one signal, which was recorded at a specific depth, with a specific microelectrode, in a specific hemisphere, and in a specific patient.

In one of the input matrices, each element of the matrix contained the average β band power. In the other case, instead of filling the matrix with power values, it was completed with the frequency values of the β band in which the highest power was obtained.

To obtain the significance value of the comparison between two methods, an ad hoc method for multiple comparisons, based on the Tukey-Kramer criterion, was used. The level of significance was $\alpha = 0.05$; that is, the confidence interval was 95%.

2.5. Computational Cost Comparison. Since the final goal of this work is to apply one of these estimation methods to an intraoperative validation of the stimulation electrode implantation optimal location, it is necessary that signal processing is done in real time. Thus, processing speed is an important factor to consider.

The computation time of four of the estimators were compared, using a computer with an Intel® Core™ i7-6700HQ Processor, 16 GB SDRAM DDR3L, and running Windows 10 home 64 bits. The methods chosen for the calculation of the computational cost were those that are shown to be more adequate for the calculation of the spectral estimation.

3. Results

3.1. Stability Analysis. An example of the stability analysis is shown in Figure 2. In this case a large increase in the amplitude of the original signal around second 18 can be observed. This segment is considered to be spurious by the algorithm since its RMS value is greater than the upper stability threshold as described above.

As a result of applying this stability analysis to all trajectories, stable portions were obtained from each of them. The length of the stable signals was 21.08 ± 12.18 s, being the minimum and maximum values of 1.55 s and 102.11 s, respectively.

3.2. Rectification and Filtering. To obtain the low frequency signal that modulates high frequency in the MER recordings, the method previously explained was applied over the stable segments of the signals.

As a result of full wave rectification, only positive values of the signal are present. However, the mean of the signal is then subtracted and then some samples may have negative values. Subsequent filtering, with a 4th order Butterworth low-pass filter with cutoff frequency at 100 Hz softens the signal, eliminating some of the original peaks. An example of this processing is illustrated in Figure 3.

3.3. Comparison of the Power Spectral Estimation Methods. Since the actual spectrum of the signals is unknown, the results can only be evaluated by doing a comparison between the estimations obtained by each of the methods. That is, the bias of an estimate cannot be assessed without knowledge of

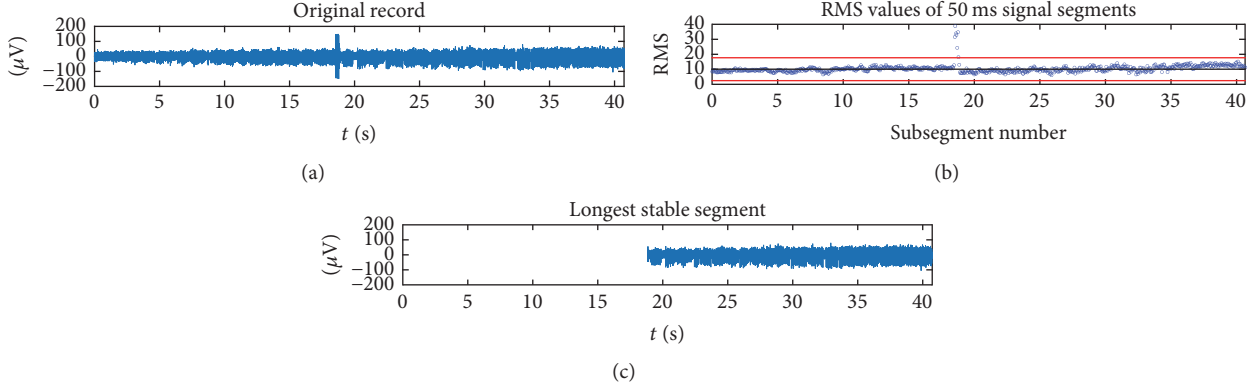


FIGURE 2: MER recording of patient 2, left hemisphere, central electrode, at a distance from target of 0.524 mm, processed to eliminate spurious data. (a) Original record. (b) RMS values of 50 ms signal segments; the red lines mark the limits corresponding to ± 3 standard deviations of the median. (c) Portion of signal considered stable by the algorithm.

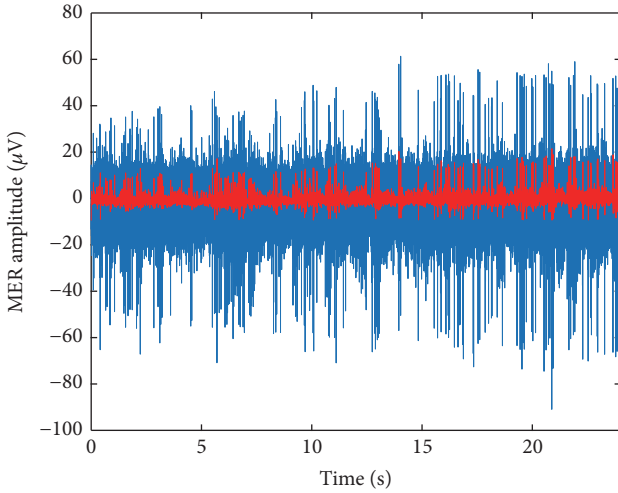


FIGURE 3: Low frequency modulation signal for patient 8, left hemisphere, central electrode (at a distance from the target of 1636 mm). Blue: stable MER segment. Red: rectified and filtered signal.

the actual spectrum, but the differences in the variability of the different methods or of the same method with different parameters can be seen. Given that in studies where the β power of MER signals is obtained ([5, 8–12]), there is a systematic use of Welch's method with 1 s Hamming windows and 50% overlap; that method is taken as a reference in this study.

The goal of this comparison is to identify other methods that could also be used for this application.

3.3.1. Qualitative Comparison. In order to perform a qualitative comparison, power spectral estimation of an example signal, calculated with the different methods, is shown in Figure 4. The goal is to make a visual comparison that will be helpful to understand the statistical results that will follow this section. The qualitative comparison provided these results compared with Welch method with Hamming windows of 1 s (Figure 4(d)):

- (i) *Periodogram.* Figure 4(a) shows the great variability of this estimation method compared with Figure 4(d).
- (ii) *Welch's Method.* In the case of 0.5 s Hamming windows (Figure 4(b)), it can be seen that the spectrum is very smooth; that is, it does not present great variability. This agrees with the fact that increasing the number of segments improves the variance of the estimate. However, this improvement implies some loss in frequency resolution. Increasing the length of the segments improves the frequency resolution. With 1.5 s Hamming windows (Figure 4(c)), the spectrum is less smooth, as expected.
- (iii) *Multitaper Method.* For multitaper $NW = 2$, the spectrum (Figure 4(e)) shows some variability. However, when compared with the periodogram, variability in this case is lower. Taking into account the fact that the number of windows used is $2 * NW - 1 = 3$, it can be thought that these are not sufficient to significantly reduce the variance of the spectral estimate. In case of multitaper $NW = 6$ (Figure 4(f)), the variance is smaller than $NW = 3$, which is consistent with the fact that increasing the number of windows improves this feature. The number of windows used is $2 * NW - 1 = 11$. However, this estimated variance is still considerably higher than that of Welch's estimators.

From the observation of these estimations, and concerning the AR model with Burg coefficients, in the case of the AR model, 4th order, the spectrum (Figure 4(g)) shows how the use of this parametric method implies an excessive simplification of the system under study. The estimated spectrum is completely smooth and has unlimited frequency resolution, but its shape does not match the one given by the other methods, which may indicate that bias is very large (although the actual spectrum is not known, it is more likely that it resembles the ones from nonparametric methods rather than that of this approach). For the AR model, 15th order (Figure 4(h)), the comparison shows an excessive simplification of the system under study.

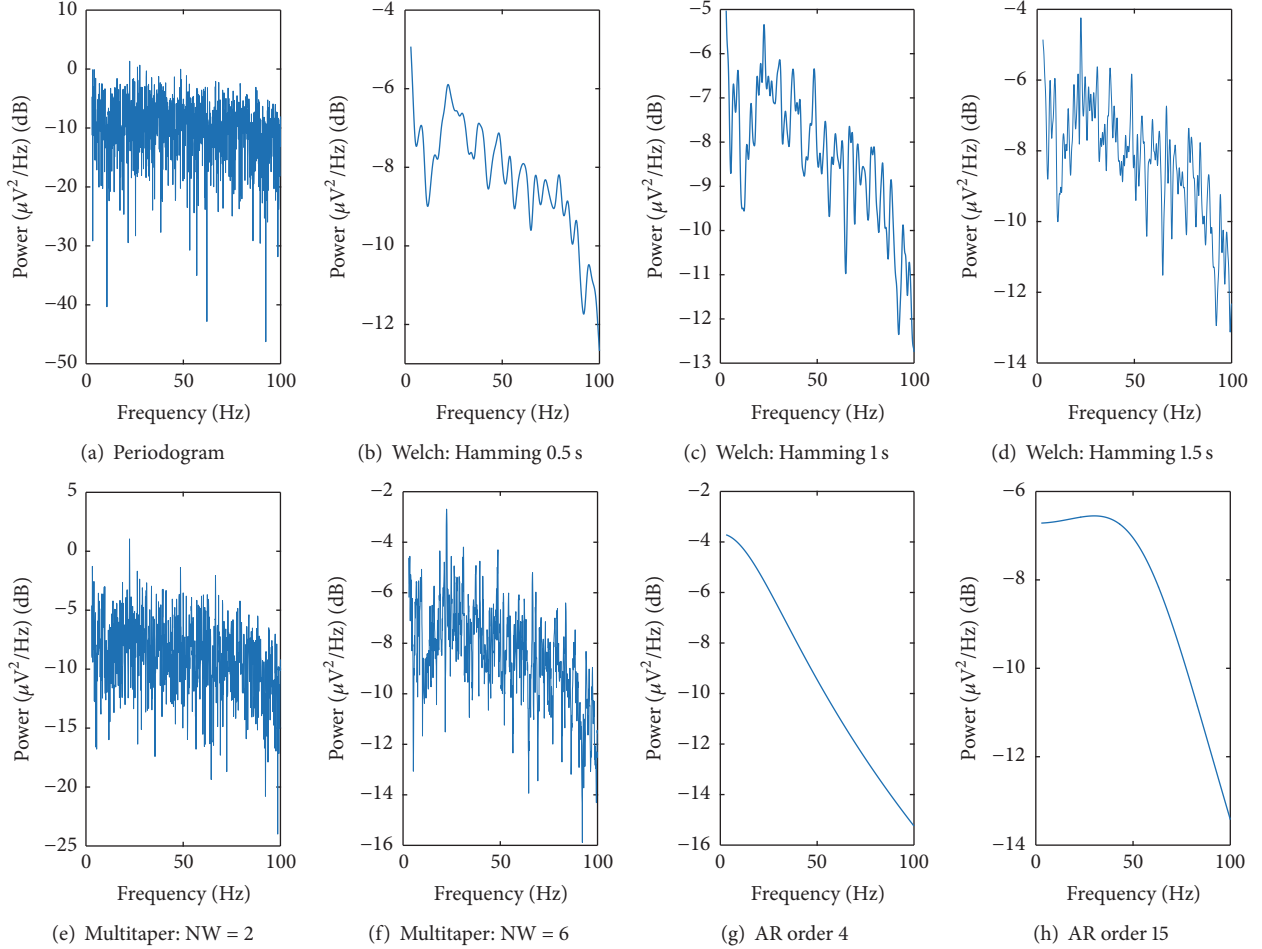


FIGURE 4: Results of different power spectral estimation methods apply to the signal from patient 5, left hemisphere, central electrode, at a distance from target of 2.235 mm.

3.3.2. Quantitative Comparison. Statistical comparisons of the spectral estimations were performed with two different datasets: average power and highest power.

Comparison of β Band Average Power. Figure 5 compares the different PSD estimation methods studied according to their estimations of β band average power. In this figure, the value corresponding to Welch's method with 1s window was selected. It can be seen that this method is significantly different to AR models, but not to the rest of methods.

Table 1 summarizes the p values of all of the pairs of the compared methods. It can be seen that several non-parametric PSD methods do not show significant differences among them. The calculation of the periodogram was not significantly different from those of Welch's method with 0.5 s window ($p = 0.9999$), 1 s window ($p = 0.2284$), and multitaper NW = 6 ($p = 0.3520$). On the other hand, for Welch's method, it can be emphasized that when using 1.5 s window, the estimations obtained are not significantly different from those obtained with 1 s window ($p = 0.6453$), but they are different from those obtained with 0.5 s window ($p = 0.0038$). On the other hand, the multitaper estimators did not show significant differences between each other ($p = 0.1697$)

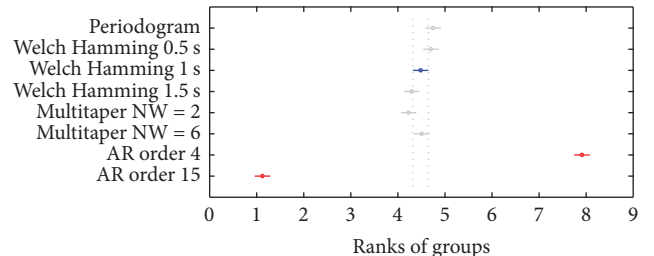


FIGURE 5: Comparison between Welch's method with 1s windows and the other estimators. Average power values in the β band are compared. Each circle represents the mean of one of the methods and is accompanied by the bars that define a 95% confidence interval. In blue, Welch's method with 1s windows; in red those methods with which a significant difference has been found; and in gray the methods that are not significantly different to the selected method.

and with Welch's method with 1 s window (MTNW = 2: $p = 0.2741$; MTNW = 6: $p = 1.0000$) and 1.5 s window (MTNW = 2: $p = 0.9992$; MTNW = 6: $p = 0.4884$).

With regard to parametric estimators, as expected, after visual inspection of the obtained spectra, the estimations

TABLE 1: Statistical results (p values) from the multiple comparisons of the PSD methods regarding average β band power values. In bold, significant values for $\alpha = 0.05$.

	PGRM	Welch 0.5 s	Welch 1 s	Welch 1.5 s	Mult. 2	Mult. 6	AR 4	AR 15
PGRM	-	0.9999	0.2284	$7.3461 * 10^{-4}$	$5.2344 * 10^{-5}$	0.3520	$5.9881 * 10^{-8}$	$5.9881 * 10^{-8}$
Welch 0.5 s	0.9999	-	0.4637	0.0038	$3.4350 * 10^{-4}$	0.6205	$5.9881 * 10^{-8}$	$5.9881 * 10^{-8}$
Welch 1 s	0.2284	0.4637	-	0.6453	0.2741	1.0000	$5.9881 * 10^{-8}$	$5.9881 * 10^{-8}$
Welch 1.5 s	$7.3461 * 10^{-4}$	0.0038	0.6453	-	0.9992	0.4884	$5.9881 * 10^{-8}$	$5.9881 * 10^{-8}$
Mult. 2	$5.2344 * 10^{-5}$	$3.4350 * 10^{-4}$	0.2741	0.9992	-	0.1697	$5.9881 * 10^{-8}$	$5.9881 * 10^{-8}$
Mult. 6	0.3520	0.6205	1.0000	0.4884	0.1697	-	$5.9881 * 10^{-8}$	$5.9881 * 10^{-8}$
AR 4	$5.9881 * 10^{-8}$	-	$5.9881 * 10^{-8}$					
AR 15	$5.9881 * 10^{-8}$	-						

TABLE 2: Statistical results (p values) from multiple comparisons of the PSD methods regarding β band frequency values in which the maximum power is reached. In bold, significant values for $\alpha = 0.05$.

	PGRM	Welch 0.5 s	Welch 1 s	Welch 1.5 s	Mult. 2	Mult. 6	AR 4	AR 15
PGRM	-	$5.9881 * 10^{-8}$	$7.4812 * 10^{-6}$	0.0037	0.9238	0.5155	0.9554	$5.9881 * 10^{-8}$
Welch 0.5 s	$5.9881 * 10^{-8}$	-	0.0487	$3.0526 * 10^{-4}$	$5.9961 * 10^{-8}$	$7.1982 * 10^{-8}$	$5.9913 * 10^{-8}$	$5.9881 * 10^{-8}$
Welch 1 s	$7.4812 * 10^{-6}$	0.0487	-	0.8801	0.0023	0.0306	0.0014	$5.9881 * 10^{-8}$
Welch 1.5 s	0.0037	$3.0526 * 10^{-4}$	0.8801	-	0.1680	0.5895	0.1262	$5.9881 * 10^{-8}$
Mult. 2	0.9238	$5.9961 * 10^{-8}$	0.0023	0.1680	-	0.9963	1.0000	$5.9881 * 10^{-8}$
Mult. 6	0.5155	$7.1982 * 10^{-8}$	0.0306	0.5895	0.9963	-	0.9906	$5.9881 * 10^{-8}$
AR 4	0.9554	$5.9913 * 10^{-8}$	0.0014	0.1262	1.0000	0.9906	-	$5.9881 * 10^{-8}$
AR 15	$5.9881 * 10^{-8}$	-						

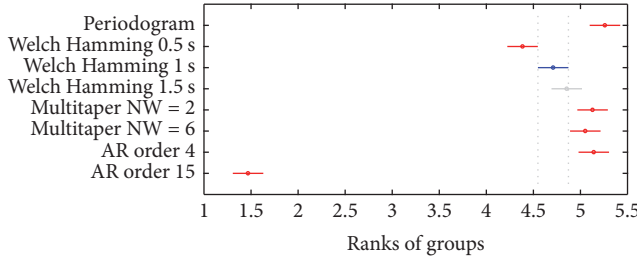


FIGURE 6: Comparison between 1 s windows Welch's method and the other estimation methods. The values of the frequencies in which the maximum energy in the β band is obtained are compared. Each circle represents the mean of one of the methods and is accompanied by the bars that define a 95% confidence interval. In blue, Welch's method with 1 s windows; in red, those methods with which a significant difference has been found; and in gray, the methods that are not significantly different to the selected one.

based on AR models presented significant differences with all of the other methods and between each other ($p = 5.9881 * 10^{-8}$).

Comparison of the β Band Frequency Value with the Highest Power. Figure 6 compares the different PSD estimation methods studied according to the frequency of the β band in which the highest power appears. In this figure, once again, the value corresponding to Welch's method with 1 s window was selected.

Table 2 summarizes the p values of the paired comparisons among all of the methods. In this comparison, the

periodogram did not have significant differences with the multitaper methods (MTNW = 2: $p = 0.9238$; MTNW = 6: $p = 0.5155$) and with the 4th order AR model ($p = 0.9554$), but it provided significant differences with all of the others methods. Welch's method with 1 s window was not significantly different from Welch's method with 1.5 s window ($p = 0.8801$), but it was significantly different to all others. The multitaper estimations, as in the previous comparison, did not present significant differences between each other ($p = 0.9963$) nor with Welch's method with 1.5 s window (MTNW = 2: $p = 0.1680$; MTNW = 6: $p = 0.5895$), but it shows differences with Welch's method with 1 s window (MTNW = 2: $p = 0.0023$; MTNW = 6: $p = 0.0306$).

Regarding parametric estimators, as in the previous comparison, AR models presented significant differences between each other ($p = 5.9881 * 10^{-8}$).

3.3.3. Computational Cost Comparison. Since the final goal of this work is to apply one of these methods for intraoperative validation of the implantation's optimal location, it is necessary that signal processing is done in real time. Thus, processing speed is a factor to consider.

The computation time of four of the estimators was compared. The methods chosen for the calculation of the computational cost were those that, from the previous comparisons, showed to be more suitable for the calculation of the spectral estimation, that is, Welch's method with 1 s and 1.5 s window and multitaper method with NW = 2 and NW = 6. The evaluation of the computation time was done in the signals from patient 1, left hemisphere, posteromedial electrode, whose duration was 27.9987 ± 11.9316 s.

TABLE 3: Computation times for the trajectory corresponding to patient 1, left hemisphere, posteromedial electrode, whose duration is 27.9987 ± 11.9316 s.

Method	Computation times
Welch 1 s windows	1.1137 ± 0.4831 s
Welch 1.5 s windows	0.7253 ± 0.3168 s
Multitaper NW = 2	2.3227 ± 0.8811 s
Multitaper NW = 6	4.4735 ± 1.8008 s

The computational times required by each of these methods for the PSD estimation are summarized in Table 3.

4. Discussion

Comparisons were done in order to choose the best method to perform an intraoperative validation that takes into account frequency characteristics of MER recordings from PD patients to be performed in real time.

First, it was necessary to compare different power spectrum estimation methods in order to identify methods that could be used for this application. Since the actual power spectrum of the analyzed signals is unknown, it is not possible to evaluate an estimator by how close it is to the ideality. Therefore, a comparison was made between different estimators, taking as a reference the mostly used method in the consulted bibliography ([5, 8–12]), which is Welch's method with 1 s Hamming window and 50% overlap.

The bias of an estimate cannot be assessed without knowledge of the real spectrum, but the differences in the variability of the different methods or of the same method with different parameters can be seen. Here parametric and nonparametric methods were considered.

Regarding parametric methods, the results obtained by the AR models confirm the previous assumption that, without making a much deeper study, these are not optimal for processing MER recordings. Their results are not only significantly different from the results of the other methods, but they are also different from each other.

Regarding nonparametric estimates, although qualitative comparisons showed certain morphological similarities between all methods, the quantitative analysis shows that they may be significantly different from each other.

For the particular case of the periodogram, it presented similarities with other nonparametric methods in the comparisons; however, it must be remembered that this is not a consistent estimator and a high variance was observed in the qualitative analysis. Although some of its results may not be significantly different from those of other estimators, we consider that it is not convenient to continue this work with an inconsistent estimator, since other options are available.

On the other hand, regarding the mostly used method in the consulted bibliography (Welch's method with 1 s Hamming windows and 50% overlap), the results of our comparisons show that there are significant differences, at least in one of the two comparisons, with all of the other tested methods, except for Welch's method with 1.5 s windows. This means that it does have significant differences with the case

of 0.5 s windows, but—taking into account the qualitative comparison—a reason for these differences can be found. Welch's method with 1 s window is a method with little variance but sufficient resolution so as not to lose all of the peaks. Estimations obtained with the same method but other window sizes are morphologically similar, but the 0.5 s windows provided a spectrum with no peaks. Having shorter windows allows the method to further soften the spectrum, but this can lead to missed peaks that should be taken into account. This could explain why the results with 0.5 s windows do not match those of the other window sizes when comparing the frequency values in which the maximum power in the β band is obtained.

So, for Welch's method, the results indicate that 1 s and 1.5 s windows provide results that are not significantly different from each other. Since this method with 1 s windows is the most used in the consulted bibliography and given that there are no significant differences with the one with 1.5 s windows, the possibility of working with one of these estimators indistinctly could be considered.

As for the multitaper method, in first place, these estimators do not present significant differences between them in any of the two comparisons. On the other hand, in the qualitative comparisons, it can be seen that these methods give more variable results than Welch's method. The quantitative comparison reveals that they do not present significant differences with Welch's method with 1.5 s windows. If this result is analyzed taking into account the explanation in the previous paragraph, the use of multitaper methods for the study of MER recordings could also be considered.

According to the statistical analysis performed, the methods that could be considered for PSD estimation in MER recordings are multitaper with NW = 2 and NW = 6 and Welch's with Hamming windows of 1 s and 1.5 s.

However, in order to be able to do an intraoperative validation of the electrode position during implantation surgeries, the β band power detection must be achieved in real time, that is, the shorter time possible. Thus, it is necessary to explore algorithms that minimize PSD calculation time.

In order to select a single method, then, the computational cost of each of them was considered. The results show that multitaper methods are computationally more expensive than those of Welch. In addition, the comparison suggests that Welch's method with 1.5 s windows is the fastest: 35% faster than Welch with 1 s windows and 617% faster than Multitaper_{NW=2}.

5. Conclusion

In this study, a comparison was made between different PSD estimation methods, taking into account a particular application. MER signal processing and particularly its frequency information can serve as an intraoperative validation tool for best electrode placement during DBS electrode implantation surgery in PD patients. The most used method for spectral estimation in the literature is that of Welch with 1 s Hamming windows and 50% overlap.

In this study we compared different spectral estimators and also the computational costs involved were taken into

account. Finally, according to the discussion, we propose Welch's method with 1.5 s Hamming windows and 50% overlap as the most appropriate real-time PSD estimator for MER signals of PD patients.

Even though the selection was based on the idea of performing an intraoperative validation in real time, the methods were not applied online. To further test the utility of the selected method, it would be appropriate to generate a hardware set, in which the registration of the signals could be simulated as if it was on the actual operating room, and the β band power detection could be achieved in real time, while the signals are being read. Moreover, it would be necessary to ideate a convenient way to show this frequency information, so that it could be easily read and understood by the medical team.

Conflicts of Interest

The authors declare that they have no conflicts of interest.

References

- [1] G. Suarez-Cedeno, J. Suescun, and M. C. Schiess, "Earlier intervention with deep brain stimulation for Parkinson's disease," *Parkinson's Disease*, vol. 2017, Article ID 9358153, 9 pages, 2017.
- [2] A.-S. Moldovan, S. J. Groiss, S. Elben, M. Südmeier, A. Schnitzler, and L. Wojtecki, "The treatment of Parkinson's disease with deep brain stimulation: current issues," *Neural Regeneration Research*, vol. 10, no. 7, pp. 1018–1022, 2015.
- [3] C. C. Chen, A. Pogosyan, L. U. Zrinzo et al., "Intra-operative recordings of local field potentials can help localize the subthalamic nucleus in Parkinson's disease surgery," *Experimental Neurology*, vol. 198, no. 1, pp. 214–221, 2006.
- [4] A. Zaidel, A. Spivak, L. Shpigelman, H. Bergman, and Z. Israel, "Delimiting subterritories of the human subthalamic nucleus by means of microelectrode recordings and a hidden Markov model," *Movement Disorders*, vol. 24, no. 12, pp. 1785–1793, 2009.
- [5] A. Zaidel, A. Spivak, B. Grieb, H. Bergman, and Z. Israel, "Subthalamic span of β oscillations predicts deep brain stimulation efficacy for patients with Parkinson's disease," *Brain*, vol. 133, no. 7, pp. 2007–2021, 2010.
- [6] R. R. Shamir, A. Zaidel, L. Joskowicz, H. Bergman, and Z. Israel, "Microelectrode recording duration and spatial density constraints for automatic targeting of the subthalamic nucleus," *Stereotactic and Functional Neurosurgery*, vol. 90, no. 5, pp. 325–334, 2012.
- [7] D. Manolakis, V. Ingle, and S. Kogon, *Statistical and Adaptive Signal Processing: Spectral Estimation, Signal Modeling, Adaptive Filtering, and Array Processing*, vol. 46, Artech House Norwood, 2005.
- [8] A. Moran, H. Bergman, Z. Israel, and I. Bar-Gad, "Subthalamic nucleus functional organization revealed by parkinsonian neuronal oscillations and synchrony," *Brain*, vol. 131, no. 12, pp. 3395–3409, 2008.
- [9] P. Novak, S. Daniluk, S. A. Elias, and J. M. Nazzaro, "Detection of the subthalamic nucleus in microelectrographic recordings in Parkinson disease using the high-frequency (> 500 Hz) neuronal background: Technical note," *Journal of Neurosurgery*, vol. 106, no. 1, pp. 175–179, 2007.
- [10] P. Novak, A. W. Przybyszewski, A. Barborica, P. Ravin, L. Margolin, and J. G. Pilitsis, "Localization of the subthalamic nucleus in Parkinson disease using multiunit activity," *Journal of the Neurological Sciences*, vol. 310, no. 1-2, pp. 44–49, 2011.
- [11] M. Rosa, G. Giannicola, D. Servello et al., "Subthalamic local field beta oscillations during ongoing deep brain stimulation in Parkinson's disease in hyperacute and chronic phases," *Neurosignals*, vol. 19, no. 3, pp. 151–162, 2011.
- [12] D. Whitmer, C. de Solages, B. Hill, H. Yu, J. M. Henderson, and H. Bronte-Stewart, "High frequency deep brain stimulation attenuates subthalamic and cortical rhythms in Parkinson's disease," *Frontiers in Human Neuroscience*, no. 2012, article no. 155, 2012.
- [13] A. Moran and I. Bar-Gad, "Revealing neuronal functional organization through the relation between multi-scale oscillatory extracellular signals," *Journal of Neuroscience Methods*, vol. 186, no. 1, pp. 116–129, 2010.
- [14] P. Djuric and S. Kay, "Spectrum estimation and modeling," in *Digital Signal Processing Handbook*, CRC Press LLC, 2009.
- [15] K. J. Rahim, *Applications of Multitaper Spectral Analysis to Non-stationary Data*, 2014.
- [16] K. Rahim, W. Burr, M. Rahim, and W. S. Burr, *Package Multitaper*, 2016, Package Multitaper.
- [17] P. Mitra, *Observed Brain Dynamics*, Oxford University Press, 2007.
- [18] P. J. Franaszczuk, K. J. Blinowska, and M. Kowalczyk, "The application of parametric multichannel spectral estimates in the study of electrical brain activity," *Biological Cybernetics*, vol. 51, no. 4, pp. 239–247, 1985.
- [19] O. M. Manzanera, J. W. Elting, J. H. Van Der Hoeven, and N. M. Maurits, "Tremor detection using parametric and non-parametric spectral estimation methods: A comparison with clinical assessment," *PLoS ONE*, vol. 11, no. 6, Article ID e0156822, 2016.